MEMBRANE BASED DEHUMIDIFICATION AND EVAPORATIVE COOLING USING WIRE MESH MEDIA

by

JARED R. GOODNIGHT

B.S., Kansas State University, 2007

A THESIS

submitted in partial fulfillment of the requirements for the degree

MASTER OF SCIENCE

Department of Mechanical Engineering
College of Engineering

KANSAS STATE UNIVERSITY
Manhattan, Kansas

2011

Approved by:

Major Professor
Dr. Steven Eckels

Abstract

Membrane dehumidification and evaporative cooling applications have the potential to significantly improve the energy efficiency of air conditioning equipment. The use of wire mesh media in such membrane applications is feasible but has not been studied extensively. Therefore, the aim of this work is to investigate the heat and mass transfer performance of several different wire mesh media in membrane based dehumidification and evaporative cooling. There were six wire mesh membranes tested in an experimental facility. The wire mesh membranes vary with respect to percent open area, wire diameter, pore size and material. Two non-permeable, solid membranes were also tested in the facility and compared with the wire mesh membranes. The test section of the experimental facility consists of a narrow air duct and a plate apparatus. The membrane samples were fashioned into rectangular plates and installed into the test section. The plate membranes separate liquid water and air flow streams. The inlet air temperature and humidity are altered to produce condensation or evaporation at the membrane surface.

The average convective heat and mass transfer coefficient of the air boundary layer is measured for each of the experimental plates. Membrane based dehumidification and evaporative cooling were accomplished using the wire mesh media. However, the wire mesh membranes did not exhibit any significant differences in their performance. The mesh plates were compared with the solid plate membranes and it was discovered that the solid plates exhibited significantly higher heat transfer coefficients during condensation conditions. This result most likely is due to the formation of large water droplets on the solid plates during condensation. The experimental data is then compared to analytical predictions of the heat and mass transfer coefficients developed from several heat transfer correlations and by invoking the heat and mass transfer analogy. The experimental data is also compared directly with the heat and mass transfer analogy. It was found that the data did not compare well with the heat and mass transfer analogy. This result is attributed to the fact that the membrane surface limits the amount of direct exposure to the gas-liquid interface.

Table of Contents

List of Figures

List of Tables

Nomenclature

A	Area	h_{fg}	Latent heat of vaporization
A_1	Air mass flow rate invariant constant	h_l	Liquid height
A_c	Cross sectional area	I	Current
A_s	Experimental plate surface area	i	Enthalpy
A_{open}	Percent open area	k	Thermal conductivity
C	Discharge coefficient	L	Duct entry length
C_s	Surface curvature	Le	Lewis number
Cp	Specific heat at constant pressure	M	Molecular weight
D	Diameter	$\dot{m}$	Mass flow rate
D_{AB}	Diffusivity of water vapor in air	mf	Mass fraction
D_h	Hydraulic diameter	N	Mesh count
d	Orifice diameter	Nu	Nusselt number
dq	Infinitesimal change in heat rate	$\bar{N}_H$	Average horizontal opening length
d_w	Wire diameter	$\bar{N}_V$	Average vertical opening length
dx	Infinitesimal change in position	n	Arbitrary exponent
E	Internal energy	n_p	Number of pixels
F	Force	P	Pressure
f	Moody friction factor	Pr	Prandtl number
f_v	Frequency	P_{wet}	Wetted perimeter
g	Gravitational acceleration	$\bar{p}_h$	Mean horizontal zero string length
H_{pix}	Horizontal pixel length	$\bar{p}_v$	Mean vertical zero string length
$\bar{h}_a$	Average air-side heat transfer coefficient	Q	Total heat transfer rate
h_d	Duct height	q	Heat transfer rate
$\bar{h}_m$	Average air-side mass transfer coefficient	R	Gas constant

R_x	Electrical resistance
Re	Reynolds number
r	Radius
S	Capillary square size
S_H	Horizontal capillary opening length
S_V	Vertical capillary opening length
S_x	Standard deviation
Sc	Schmidt number
Sh	Sherwood number
T	Temperature
t	Experimental plate thickness
t_{est}	T-estimator
U	Overall heat transfer coefficient
u	Uncertainty
u_m	Mean air velocity
V	Volume
V_0	Voltage
V_{pix}	Vertical pixel length
v	Velocity
w_d	Duct width
X	Molar concentrations
x	Arbitrary distance
x^*	Dimensionless length
z	Elevation
α	Thermal diffusivity
β	Diameter ratio
γ	Surface tension
ΔP	Pressure difference
ΔT	Temperature difference
$\Delta\rho$	Density difference
ε	Surface roughness
ε_x	Expansibility factor
ζ	Arbitrary coefficients
η	Number of molecules
θ	Contact angle
κ	Isentropic coefficient
λ	Convergence factor
μ	Dynamic viscosity
ν	Specific volume
ρ	Density
ϕ	Relative humidity
Ψ	Arbitrary property
ω	Humidity ratio

Subscripts

a	Air
atm	Atmosphere
ave	Average
c	Condensate
CF	Curve fit
CV	Control volume
D	Diameter
DAQ	Data acquisition unit
da	Dry air
fd	Fully developed
G	Gas
h	Hydraulic
in	Inlet
L	Liquid
LM	Log mean
m	Mean
man	Manufacturer
mix	Moist air mixture
out	Outlet
s	Surface
sat	Saturation
SG	Solid-gas
SL	Solid-liquid
w	Water
wv	Water vapor

Acknowledgements

I would like to thank Dr. Eckels for the opportunity to take on this project and his continued guidance throughout my time in graduate school. I would also like to thank Dr. Evraam Gorgy for being a good colleague, mentor, friend and brother. I am grateful for the IER staff and students who assisted me with my project. Thank you for your help and camaraderie. I am thankful for the professors whom I was privileged to learn from. Especially, Dr. Beck and his intermediate heat transfer course which profoundly inspired my thirst for knowledge. I would like to thank the faithful of St. Mary Magdalene Orthodox Church for their fellowship and prayers. A special thanks to Dr. Stan Ehler for many edifying spiritual conversations and for teaching me that education is really formation of the soul. I am grateful to my closest friends Sam Ford and Jonna Reinhardt for their encouragement and military service. Last but not least, I would like to thank my Father, Mother, Sister and extended family for their unconditional love, support, encouragement and prayers.

Dedication

This work is dedicated to God the Father, Son, and Holy Spirit. May Your will be done on earth as it is in heaven. Truly, I can do nothing without You.

Chapter 1 Introduction

1.1 Energy Crisis

The advent of central air conditioning in the late 20th century revolutionized humanity's ability to populate areas with extreme climates, some of which were previously uninhabitable. In the United States there are many large urban centers which could not thrive without central air conditioning. The social, economic, political, and population development of such regions was made possible by central air conditioning but did not come to fruition without cost. The rise of inexpensive central air conditioning beginning in the 1970's and continuing today led to a massive increase in the consumption of electrical energy. At present, central air conditioning remains one of the leading sources of energy expenditure in the common American household. The U.S. Department of Energy reports that "the share of households with central air conditioning rose from 27 percent in 1980 to 55 percent in 2001" (DOE). Furthermore, the Department of Energy also reports that Heating, Ventilation and Cooling (HVAC) equipment accounted for 356 billion kWh or about 31% of the total electricity consumed by U.S. households in 2001(DOE). Out of the 356 billion kWh approximately 183 billion kWh came solely from the use of air conditioning equipment. The amount of energy expended by air conditioning equipment in 2001 alone is approximately equivalent to the energy generated by 108 million barrels of crude oil or about 20 million tons of coal.

Humanity has entered an age where the consumption of natural resources used in the production of energy has raised some serious concerns. Alternate and sustainable energy sources must be realized in order to address this growing issue. There has already been a significant movement within the political and scientific communities to discover alternate renewable energy sources through the emerging concept of "green" technologies. Green technology is focused on creating innovative and energy efficient solutions to curb humanities exploitation of natural resources. One of the central tenants of green technology is energy conservation. By creating devices and products which expend less electrical energy it follows that fewer natural resources will be consumed. It would be of great benefit to pursue green technologies for air conditioning equipment given its high usage of electrical energy. One possible avenue for green ideas applied to air conditioning equipment is found in membrane technology. More specifically, the ideas of

membrane based dehumidification and evaporative cooling have great potential to create energy saving solutions for air conditioning equipment. Both ideas are centered around a semi-permeable membrane which is used to separate liquid water and air flow streams. The unique properties of the membrane allow water to transport from one fluid medium to the other while minimizing their direct contact. Membrane based dehumidification involves the simultaneous removal of heat and water vapor from a moist air stream using a semi-permeable membrane. Membrane based evaporative cooling entails the evaporation of liquid water through a semi-permeable membrane in order to cool and add moisture to a dry air stream. The advantage of these membrane based concepts comes from their ability to use the latent energy accompanying a phase change in order to create a more energy efficient processes when conditioning air. The concept of membrane based dehumidification and evaporative cooling are further explored in the remainder of this chapter.

It is the aim of this research to construct a facility in order to study the performance of different wire mesh media in the application of membrane based dehumidification and evaporative cooling. A variety of wire mesh samples with different characteristics will be tested and their performance with respect to heat and mass transfer will be evaluated by calculating the average convective air-side heat and mass transfer coefficients.

1.2 Membrane Based Dehumidification

1.2.1 Concept Overview

Membrane based dehumidification can be defined as the removal of water vapor from a humid air stream using a semi-permeable membrane. The membrane creates a physical barrier between cool liquid water and warm, moist air flow streams. The liquid water is kept below the dew point temperature of the moist air stream which causes the water vapor in the air stream to condense at the membrane surface. The difference in the partial pressure of the liquid water and water vapor in the moist air establishes the driving potential for mass transport. The membrane consists of a material with a vast array of microscopic pore openings. The capillary forces within the pores arising from the surface tension of the liquid maintain an interface between the gas and liquid phases and keep them from infiltrating one another. At the same time, the capillary pore openings enable the molecular transport of water vapor from the moist air stream

to the liquid water through the membrane surface. The capillary forces within the pore openings of the membrane are used to overcome gravity forces or an imposed pressure difference at the gas-liquid interface. The water vapor which condenses at the membrane surface is either directly absorbed through the gas-liquid interface within the capillary pores or collects on the membrane surface and coalesces into droplets. Ideally, the droplets then migrate to the capillary pores and are also absorbed into the liquid water. Figure 1-1 depicts a membrane cross section operating during dehumidification.

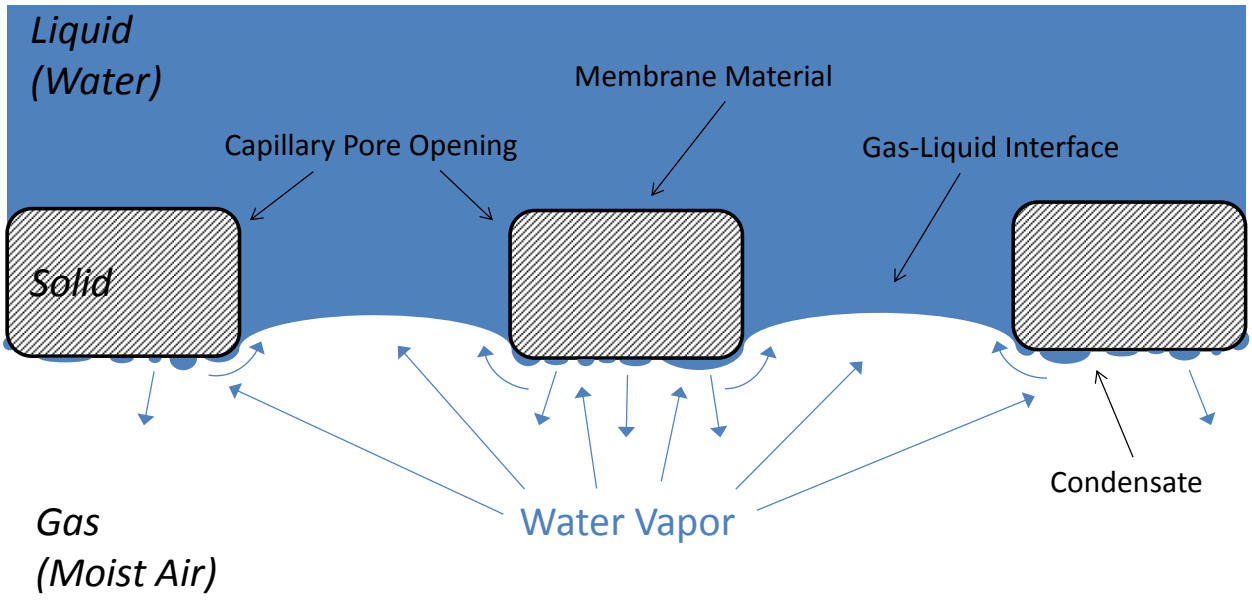

Figure 1-1 Membrane Cross Section during Dehumidification

In Figure 1-1, the liquid water is kept at a lower pressure than the air which causes the meniscus at the gas-liquid interface to protrude into the liquid side of the membrane. The force created by the pressure difference between the liquid and gas phases is balanced by the capillary forces created within the pore openings. Figure 1-1 also illustrates the various paths the water vapor can follow when it condenses at the membrane surface. The water vapor is shown to either be directly absorbed into the air-water interface or condense on the membrane material. The condensate at the solid surface of the membrane forms into droplets which coalesce into increasingly larger droplets. The droplets grow in size until they come into contact with the gas-liquid interface at which point the pressure difference between the droplet and the liquid medium causes the droplet to become absorbed. It is also possible for some of the water vapor which condenses at the solid surface to either be reflected by the membrane's surface or re-evaporate

into the air flow stream. The exact behavior of the liquid condensate on the membrane surface is unknown.

Membrane based dehumidification systems have several unique advantages when compared to conventional humidity removal systems. The most pragmatic application of dehumidification is to remove moisture from a humid air stream for climate control in a building or structure. In hot, humid climates the air temperature must be reduced well below the dew point temperature in order to sufficiently remove enough moisture from the air. In conventional systems, the air usually becomes too cool to be directly introduced into the building and must be re-heated to an acceptable temperature. Re-heating the air also adjusts the relative humidity of the air to a level suitable for human comfort. Figure 1-2 illustrates a simplified model of a conventional dehumidification system and tracks the path of the air temperature and humidity ratio on a psychometric chart.

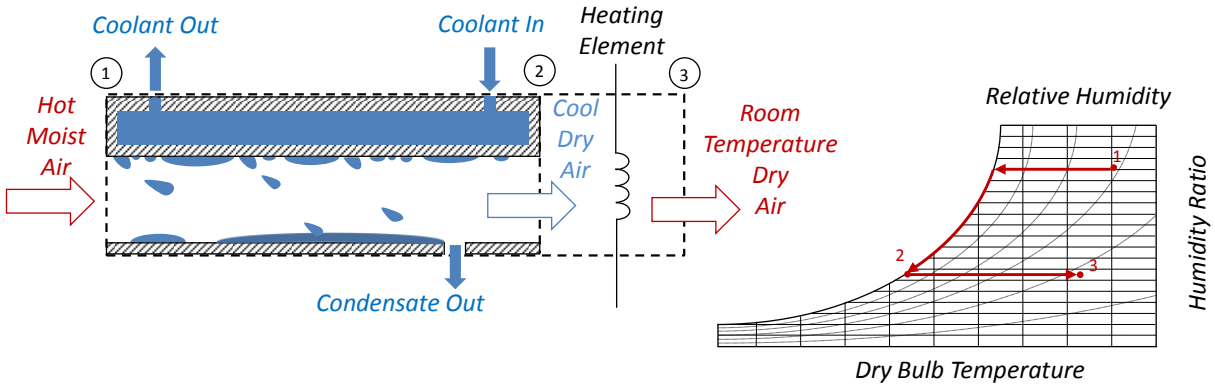

Figure 1-2 Convention Dehumidification System

In Figure 1-2 air is shown entering a duct at an elevated temperature and humidity. The humid air stream comes into contact with a solid surface which is kept below the dew point temperature of the air by a liquid coolant. In this example the coolant is considered to be water. Water vapor in the air stream condenses at the solid surface and forms into large droplets. When the droplets become large enough they are overcome by gravity and fall to the bottom of the duct where the liquid condensate exits through a drain. The air exiting the duct is now at the desired relative humidity for human comfort but is too cool to be delivered into a building. Thus, the air is heated until it is at the desired temperature. The psychometric chart demonstrates the changes in the air temperature and humidity as it travels through the conventional system.

In a membrane based system the bulk fluid air temperature does not need to be reduced below the dew point temperature. Figure 1-3 pictures a simplified model of a membrane based dehumidification system comparable to the conventional system shown in Figure 1-2.

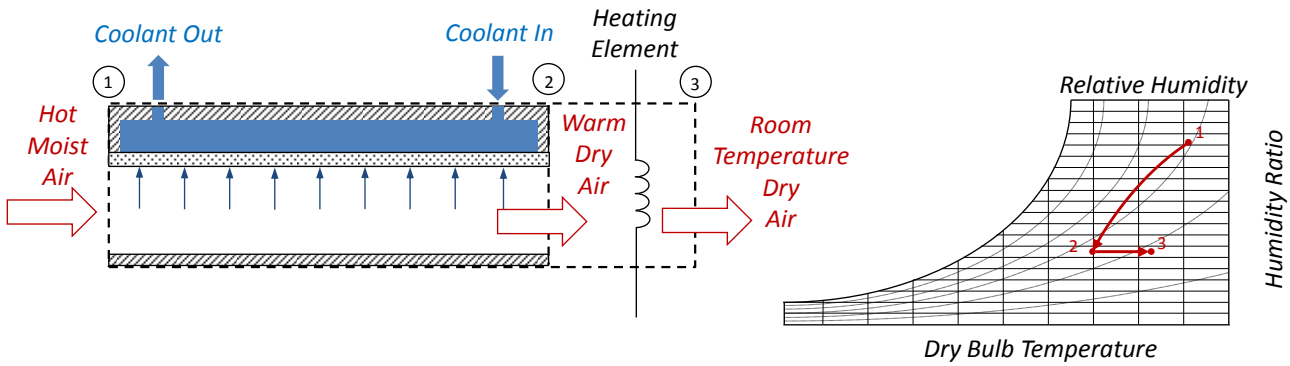

Figure 1-3 Membrane Based Dehumidification System

In Figure 1-3 moist air enters the membrane system at an elevated temperature and humidity. The water vapor in the air condenses at the membrane surface which is cooled by liquid water. The condensate is then absorbed directly through the membrane by the previously described phenomena. Figure 1-1 depicts the mechanisms by which the water vapor is transported through the membrane surface. The bulk fluid air stream leaves then exits the duct at a lower temperature but significantly above the dew point temperature at the exit humidity ratio. The air is then slightly heated to the desired supply temperature and relative humidity.

The membrane based dehumidification system has several distinct advantages when compared to the conventional system. The advantages of the membrane based system are centered on its ability to immediately absorb the liquid condensate and minimize its contact with the air flow stream. This allows moisture to be removed from the air stream without requiring the air temperature to be below the dew point. In the conventional system, the air must remain below the dew point temperature while moisture is being removed because the liquid condensate remains in direct contact with the air stream. Therefore, the air which exits the duct in the conventional system will be at a much lower temperature when compared to the air exiting the duct from the membrane based system. This means more energy is required to re-heat the exit air from the conventional system when compared to the membrane based system. Thus, the membrane based system presents a great opportunity to save energy by limiting the need to re-heat the treated air. Furthermore, in conventional systems the condensate which forms on the

solid interfacial surface creates an additional resistance to heat transfer. Condensation on a solid surface is generally characterized as dropwise or film by definition. During dropwise condensation, water droplets form on the solid surface and grow in size until overcome by gravity. In film condensation, a thin film forms over the solid surface. In both cases the condensate at the surface impedes the molecular transport of heat from the air to the liquid water. However, the membrane surface does not allow condensate to collect into large droplets or form a film at the heat transfer interface and therefore does not experience an added resistance. Therefore, it can be assumed that the membrane based system will possess a higher thermal efficiency than the conventional system. Additionally, the condensate which forms at the heat transfer interface in the conventional system will increase the viscous drag and consequently the power required to move air through the system. The absence of the condensate droplets or film on the membrane surface should also theoretically lessen the viscous drag. The advantages of the membrane based system stem from the elimination of the liquid condensate formation on the interface of heat and mass transfer. These advantages all serve to reduce the energy required to dehumidify the air.

1.2.2 Previous Work

From the available literature, it is apparent that the inception of membrane based dehumidification is linked to the pursuit of a device which could cool and dehumidify moist air in a zero gravity environment. In earth based dehumidification, condensate removal is generally accomplished by gravity. However, in a zero gravity environment the task of managing condensate becomes extremely challenging. Membrane based dehumidification provided a precise solution to this problem since it directly absorbs the condensate and because its operation is governed by forces which arise from capillarity instead of gravity. Several years later it was realized that the benefits of membrane based dehumidification are not limited to microgravity environments but pose many improvements to earth based applications as well. One such application came by applying membrane based dehumidification technology to a residential clothes dryer in an attempt to improve its energy efficiency. A review of the available literature pertaining to these works is summarized in the remainder of this section.

Newbold (Newbold 1993) produced an analytical model for a membrane-based heat exchanger designed to control the temperature and humidity of a spacecraft cabin in a zero

gravity environment. The device was aptly named a condensate recovery heat exchanger (CRX). The design of the CRX is similar to a shell and tube heat exchanger. Warm, humid air is passed through the shell side of the CRX and travels through a semi-permeable hollow fiber membrane. The hollow fiber membrane is composed of an array of tiny hollow fiber tubes which are aligned perpendicular to the air flow through the shell. Cool liquid water flowing through the fibers causes the water vapor from the air to condense on its surface. The condensate is then absorbed into the liquid flow stream within the hollow fibers through tiny capillary openings. Thus, the air is simultaneously cooled and dehumidified by the hollow fiber membrane as it passes through the CRX. A computer simulated model was developed to estimate the heat and mass transfer performance of the CRX. Various correlations were used to estimate the overall heat and mass transfer coefficients. These predicted values were then used to model the performance of the CRX. The correlations used to predict the heat and mass transfer coefficients in the gas-phase boundary layer are of particular interest to this work. The heat transfer coefficient in the gas-phase boundary layer was estimated to be 300 $^{W}/_{m^2-K}$ and the mass transfer coefficient in the gas-phase boundary layer was approximated to be 30 $\frac{cm}{s}$. Various operating conditions were simulated using the computer model including a scenario with high temperature and humidity input. The model predicted that for an inlet air temperature of 40°C and 80% relative humidity the CRX would be capable of reducing the air temperature to 10°C and 96% relative humidity. The inlet water temperature for this simulation was 8.5°C and the total condensate recovered from the humid air stream was approximated at 420 $^{Liters}/_{Day}$. From the analytical model used to estimate the performance of the CRX it was concluded that it would be capable of maintaining the desired temperature and humidity within a spacecraft cabin.

Noyes (Noyes 1993) describes the characteristics of the hollow fiber membrane which is proposed to be used in the CRX. The hollow fibers used to construct the membrane are made from pure crystalline polypropylene. The inner diameter of a single hollow fiber is 240 μm and the outer diameter is 300 μm. The size of the microscopic capillary pores in the hollow fiber surface are approximately 0.05 μm. The pore size creates an open area of about 30% per unit area of membrane surface. The pores in the fiber surface can withstand a pressure difference of about 60 psi between the liquid water and air. These properties of the hollow fibers are ideal for a membrane based dehumidification application.

Newbold et al. (Newbold et al. 1996, 268-277) constructed an apparatus to experimentally evaluate the performance of the CRX. Two CRX modules were tested in the experimental facility named BKL5 and BKL6. Both modules contained four panels constructed from the hollow fiber membrane with a surface area of $0.07\ m^2$. Both modules measured $10\ cm$ x $10\ cm$ x $8\ cm$ and weighed $0.8\ kg$. The only difference between the modules was in the spacing of the fiber panels. The panels of module BKL6 were spaced $1.0\ cm$ apart and the panels of BKL5 were spaced $0.2\ cm$ apart. The CRX is then enclosed in a climactic chamber where the air temperature can be controlled with precision. The inlet air to the CRX is treated outside the chamber using a heater and humidification column. Once the air is at the desired temperature and humidity it is delivered to the CRX using a blower. The temperature and humidity of the air are measured at the inlet and outlet of the CRX. The volumetric flow rate of the air is measured after it exits the CRX. The temperature and pressure of the liquid water are measured at the inlet and outlet of the CRX. The water is maintained at a desired temperature before entering the CRX using a chiller. The water is pulled through the CRX by a variable speed pump and a flow meter measures the mass flow rate of water exiting the CRX. A collection vessel is used to measure condensate captured from the humid air stream through the hollow fiber membranes.

Using the measurements collected from the experimental facility the overall heat and mass transfer coefficients were determined. A mass and energy balance were performed on the CRX in order to calculate the amount of water vapor and heat which were transferred from the humid air stream to the liquid water. The heat transfer from the air to the water includes a sensible and latent component. The sensible component comes from molecular transport and bulk fluid motion. The latent component occurs when the water vapor condenses on the hollow fiber surface. It is assumed that the energy required to change the water vapor from gas to liquid is absorbed into the liquid water stream. The log mean temperature difference is calculated from the inlet and outlet temperature of the air and water. The total heat transfer from the air to the water is divided by the log mean temperature difference and surface area to produce the overall heat transfer coefficient. The log mean partial pressure difference of the water vapor is calculated from the inlet and outlet temperatures of the air and water. The overall mass transfer coefficient is calculated from the amount of water vapor transferred from the air to the water divided by the log mean partial pressure difference and the membrane area. During each experiment the inlet air

temperature, humidity and flow rate are fixed. The inlet temperature and flow rate of the water are also held constant. Data was taken while these variables remained at steady state. The overall heat and mass transfer coefficient were then determined from the collected data. Data points were taken for a varying range of air flow rates. Plots of the data points are made which display the overall heat and mass transfer coefficients as a function of the air flow rate. By investigating these plots it is apparent that the overall heat and mass transfer coefficients increase as the air flow rate is increased. A data point for Module BKL6 is given to communicate the operating conditions during a typical experiment. The inlet air to the CRX is set at 29.6°C and 50% relative humidity while the flow rate is maintained at about 170 $^{m^3}\!/_{s}$. The inlet water is circulated through the CRX at a temperature of 8.2°C and a flow rate of 35 $^{ml}\!/_{\min}$. The overall heat transfer coefficient calculated for this data point is 195 $^{W}\!/_{m^2-K}$ and the overall mass transfer coefficient is 15.6 $\frac{cm}{s}$. It was concluded that the experimental data agrees well with the analytical model developed to predict the performance of the CRX. The experimental performance of the CRX proves that it is a viable method for climate control in a spacecraft cabin. The CRX was compared with several non-membrane based methods of humidity removal and showed significant advantages. The design and operation of the CRX proves that membrane based dehumidification is a legitimate concept for removing moisture from a humid air stream.

Scovazzo et al. (Scovazzo et al. 1998, 69-81) built upon the existing research involving the hollow fiber membranes. The motivation for this work was to design a membrane based dehumidification system to control the humidity in a plant growth chamber aboard a spacecraft. The hollow fiber membranes would be compared with metal and ceramic membranes and the performance of each would be evaluated to determine the optimum membrane material. The different membranes were tested in an experimental facility much like the one used to test the CRX. An apparatus which simulated a plant growth chamber was constructed and the air exiting the mock plant chamber was circulated to a membrane module. Three membrane modules were fabricated based on the size and weight constraints of spaceflight hardware. The hollow fiber membrane module consists of 40 mixed cellulose ester fibers with a length of 13 cm and a surface area of 100 cm^2. The inner diameter of a single fiber is 0.06 cm. The pore size of hollow fiber membrane is 0.1 μm and the porosity is 0.85. Porosity is the ratio of the volume of void space to the total volume of the membrane. Essentially, the porosity gives a measure of the

percentage of open area at the surface of the membrane. The ceramic membrane (α-Al_2O_3) is constructed from a single tube which is 25.4 cm long and with an inner diameter of 0.635 cm. The surface area of the ceramic membrane is 50 cm^2, the pore size is 0.2 μm, and the porosity is 0.33. The metal membrane is fabricated from 316 stainless steel sintered metal. The metal membrane consist of a single tube with the same inner diameter as the ceramic membrane. The length of the metal membrane is 15.24 cm and the surface area is 30 cm^2. The pore size of the sintered metal is 0.5 μm and the porosity is 0.33. Water was circulated through the membrane modules at around 5°C and also at about 10°C. Data was collected for a range of air flow rates through the module and the overall mass transfer coefficient was calculated for each data point. The hollow fiber membrane module outperformed the ceramic and metal membranes with respect to mass transfer. The reason for the better performance of the fiber module was uncertain but it was speculated that it could be due to either its higher porosity or its geometry. Although, the fiber module displayed superior mass transfer it was far less durable than the ceramic and metal membranes. It was concluded that the metal membrane was the best candidate for use in the plant growth chamber due to its high durability and because it exhibited slightly better mass transfer performance than the ceramic membrane.

There are several notable observations and hypothesis made in this research with respect to membrane based dehumidification. The first is that the transmembrane pressure did not have an effect on the condensation rate. This means the pressure difference between the gas –liquid interface at the membrane surface does not have influence on the rate at which mass is transferred through the membrane. Thus, the pressure difference is needed only to maintain separation between the gas and liquid phases and is not treated as a variable in the experiment. This observation also leads to the conclusion that the membrane does not pose any significant resistance to the mass transport. Therefore, the overall mass transfer coefficient is entirely dependent on the resistance present in the gas phase boundary layer. It is hypothesized in this work that the overall mass transfer coefficient is equal to the mass transfer coefficient of the gas phase boundary layer multiplied by a dimensionless parameter called the "sticking coefficient." The sticking coefficient represents the probability that a molecule of water vapor which comes into contact with the membrane surface will adhere and become absorbed. The sticking coefficient is believed to be a function of the membrane porosity, the probability of a water

vapor molecule sticking to the membrane material and the probability of a water molecule sticking to the liquid interface.

Scovazzo et al. (Scovazzo, Hoehn, and Todd 2000, 217-225) continued their previous research by testing a variety of membranes with identical geometries. The main objective of this work was to examine how the different surface properties of the various membranes affect their mass transfer performance while eliminating surface geometry as a variable in the experiment. It is reasonable to assume that the performance of the membrane would be directly related to the ratio of solid to liquid area at the membrane surface. It is surmised that condensate which interacts directly with the liquid interface has a higher probability of being absorbed than condensate which interacts with the solid surface (sticking coefficient). The ratio of liquid surface to the total surface area is believed to be expressed by the membrane porosity. The various membranes are fashioned into flat plate geometries and tested in an experimental facility. The membrane plates are inserted into a narrow rectangular air duct. Humid air is passed on one side of the membrane and cool liquid water on the other. The necessary measurements were made to determine the overall mass transfer coefficient for each of the membranes. The membranes were constructed from four different materials; each with a unique porosity. The membrane materials include: polyvinylidene fluoride, polyethersulfone, mixed cellulose ester, and 316 stainless steel. All of the membranes have a pore size of approximately 0.22 μm except for one of the stainless steel membranes which has a pore size of 0.5 μm. Data was collect for each membrane subjected to similar operating conditions. The overall mass transfer coefficient was determined for each of the membranes and compared with the others. It was found that the differences in the performance of the membranes varied by less than 20%. This result allowed the researchers to conclude that the membrane performance showed no distinct correlation with respect to the membrane's porosity.

Cochran et al. (Cochran et al. 2009, 723-731) applied membrane based dehumidification to a residential clothes dryer in an attempt to improve its energy efficiency. Typical condensing dryers utilize an air-to-air cross flow heat exchanger to remove water vapor from moist air circulated from the dryer's drum in a closed loop configuration. The air exiting the drum is usually around 55°C and 100% relative humidity. Thus, room temperature air is well below the dew point within the dryer drum and can be used to remove condensation. The liquid condensate which forms on the heat exchanger surface within the dryer air loop is removed by gravity and

vapor shear forces. The condensate collects in a holding tank where it freely drains or is manually emptied. It is hypothesized that by replacing the air-to-air design with a membrane based heat exchanger the overall energy efficiency of the dryer will improve. Therefore, a membrane based heat exchanger was constructed and tested in the dryer and compared with the dryer's air-to-air heat exchanger. The membrane based heat exchanger operates by circulating liquid water at room temperature causing moisture from dryer air stream to condense at the membrane surface. The condensate which forms on the membrane surface is then directly absorbed through the membrane into the liquid flow loop. This minimizes the interaction between the humid air stream and the free liquid condensate which theoretically improves the thermal efficiency of the moisture removal process. The material used in the membrane heat exchanger is called wire mesh. The wire mesh is comprised of small diameter wires woven into mesh structure. The wire mesh used in membrane heat exchanger is 500 x 500 twilled weave. The wire material is 316 stainless steel. The capillary openings in the mesh have a micron rating of approximately 55 μm. Multiple experiments were conducted to compare the two systems and it was concluded that using the membrane based heat exchanger improved the energy efficiency of the dryer. In fact, by implementing membrane based technology the IEC energy rating was increased from class C to class B. Therefore, membrane based dehumidification is shown to exhibit significant advantages in conventional dehumidification systems and is not limited to space craft applications.

1.3 Membrane Based Evaporative Cooling

1.3.1 Concept Overview

Evaporative cooling takes place when the energy required to change a substance from a liquid to a gas is exploited to reduce the temperature of another fluid medium or object. Membrane based evaporative cooling is simply the application of a semi-permeable membrane to promote evaporation. Perhaps the most readily available example of membrane based evaporative cooling is demonstrated within the thermoregulation system of the human body. Evaporative cooling keeps the surface temperature of the human body lower than the internal core body temperature. This is the primary mechanism through which human beings regulate

their core body temperature at the standard 98.6°F. The ideal temperature of human skin is around 92°F which provides the necessary temperature gradient to make heat loss from the core possible. Remarkably even when the ambient air temperature greatly exceeds the ideal skin temperature, evaporative cooling can maintain the skin temperature lower than the core body temperature. Human skin is essentially a semi-permeable membrane with a vast number of capillary pore openings. The diameter of the pore openings are around 50 μm and are distributed over the surface of the human body. Typically, each human is equipped with between 2 and 3 million pore openings. These capillary pore openings are more commonly referred to as sweat glands. The sweat glands excrete a dilute aqueous solution known as sweat. Largely through capillary action, the sweat is delivered to the surface of the skin through the sweat glands where it evaporates to produce the desired cooling effect. In essence, man trades mass for energy loss through the process of membrane based evaporative cooling.

The same principles of membrane based evaporative cooling present in the thermoregulation of the human body can easily be replicated in mechanical devices. A semi-permeable membrane with small capillary openings used to separate liquid water from dry air can produce evaporative cooling at the membrane surface. Figure 1-4 depicts a semi-permeable membrane with capillary pore openings. Water vapor evaporates from the liquid water into the dry air at the gas-liquid interface. Evaporative cooling at the gas-liquid interface cools the temperature of the liquid water as long as the sensible heat gain from the ambient air is less than the heat lost from evaporative cooling.

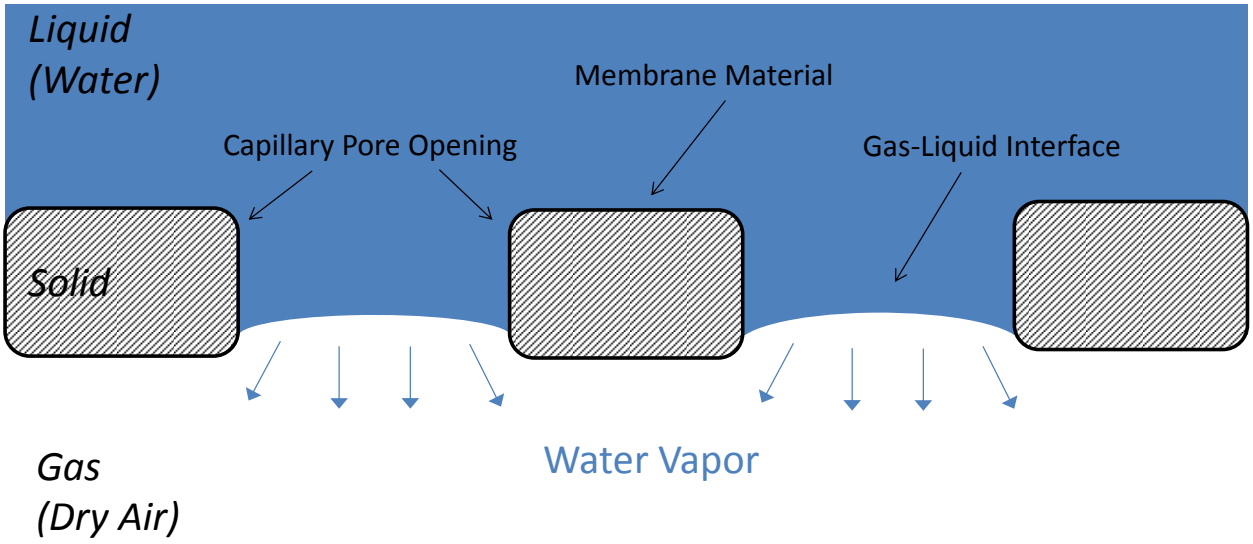

Figure 1-4 Membrane Based Evaporative Cooling

The advantages of evaporative cooling are not limited to the temperature reduction of the liquid phase. In fact, the temperature of the gas phase is also lowered during evaporative cooling. When evaporation occurs at a gas-liquid interface, the air in contact with interface is cooled if it is initially at a higher temperature than the interface. The cooled air also picks up moisture from the evaporation process. Thus, by passing air over a gas-liquid interface where evaporation is taking place the air is simultaneously cooled and humidified. Evaporative cooling has been used successfully for centuries as a primitive air conditioning technique in arid climates. In modern times some evaporative cooling devices are often referred to as swamp coolers. A swamp cooler generally consists of a fan which blows air through a wicking material saturated with water. As the air flow moves through the wicking material, liquid water evaporates which simultaneously cools and humidifies the air stream. Swamp coolers are perhaps the most efficient devices for cooling air because they usually require very little energy input. Usually the only power required is a fan which is used to force air through the device. Swamp coolers are ideal for regions with hot dry climates because more moisture can be added to the air flow stream which produces a greater cooling effect. In humid climates evaporative cooling is difficult to promote due to the already high moisture content of the air. The concept of membrane based evaporative cooling can also be applied to the operation of a swamp cooler. Figure 1-5 illustrates a swamp cooler device which employs membrane based evaporative cooling.

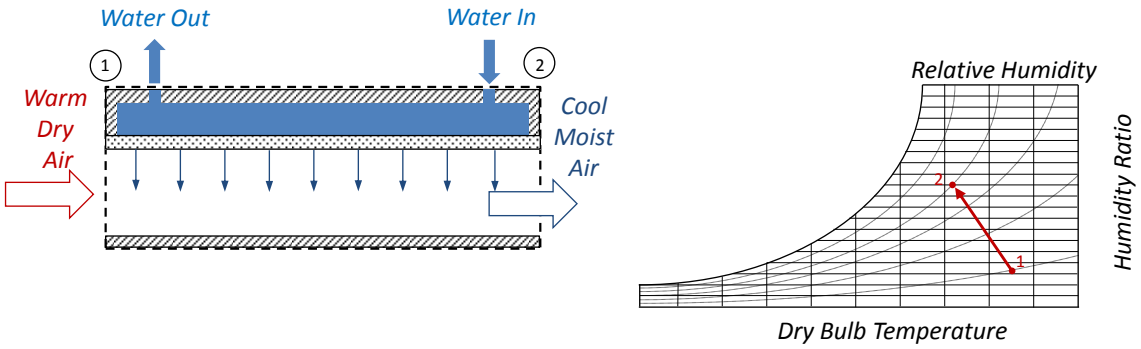

Figure 1-5 Membrane Based Swamp Cooler

Figure 1-5 depicts warm dry air entering a duct where it comes into contact with a membrane surface which separates the air from liquid water. Evaporation occurs at the membrane interface which simultaneously cools and adds moisture to the air stream. A psychometric chart illustrates the properties of the air as it passes through the duct.

Membrane based evaporative cooling can be used in a variety of applications which take advantage of the latent energy required to change water from a liquid to a gas phase. The concept is especially relevant to HVAC devices and could be utilized to create equipment with low energy usage and high efficiency.

1.3.2 Previous Work

Membrane based evaporative cooling is generally applied in one of two ways. It is either employed to cool a liquid medium or it is used to simultaneously cool and humidify a gaseous medium. Both of these cases are found in the available literature and the two most pertinent examples are considered in the remainder of this sub-section.

Loeb (Loeb 2003, 515-527) investigates the use of three microporous hydrophilic membranes used to chill water within a container in a desert climate. The cooled water could be used for the storage of perishable food goods in the harsh desert environment. Three different membranes are tested in an experimental facility and their overall heat and mass transfer coefficients are determined. The performance of the membranes are then compared to a canvas material, which is typically used in the desert water cooler. The facility basically consists of a blower which directs air flow at a rectangular container of water. The surface which the flow is impinged upon is vertically oriented and houses one of the three microporous membranes or the

canvas material. The remaining three sides of the container are non-porous and well insulated. The properties of the impinging air stream and its velocity are measured at the ambient conditions and at the surface of the container. During the experiments the water temperature inside the container was initially set to 30°C and measured at incremental time steps through the duration of the test. The heat and mass coefficients were then calculated from the collected data and results for each of the different materials were compared. The three membranes varied in material, thickness and pore size. The first membrane was fabricated from polytetrafluoroethylene and was 135 μm thick with a nominal pore size of 0.2 μm. The second membrane was made from polyurethane and was 73 μm thick with a nominal pore size of 0.2 μm. The third membrane was constructed from polypropylene and was 155 μm thick with a nominal pore size of 0.4 μm. The results from the experiments concluded that the canvas material allows the water inside the container to reach a temperature which is about 2.5°C lower than the water temperature reached by the membrane material. The canvas material also reduced the water temperature at a more rapid rate than the membranes. The microporous membrane's inferior performance is believed to arise from the large resistance to water vapor transport created in the small capillary openings of the membrane. The canvas material poses virtually no resistance to the transport of water vapor. Even though the canvas outperformed the membrane with respect to heat transfer, the canvas material had a mass transfer coefficient about 2 times larger than that measured from the membranes. Therefore, the membrane surface expends water from the container at a rate roughly half of that expended by the canvas giving the benefit of prolonged cooling. Additionally, the microscopic pores in the membrane surface make the container less susceptible to bacterial infiltration. Given that the membrane uses half as much water as the canvas and maintains the container water temperature within 2.5°C of that reached by the canvas; it proves to be a viable option for the evaporative water cooling application.

Johnson et al. (Johnson 2003, 159-171) examined the application of evaporative cooling of air in spacecraft cabin using hollow fiber membranes. The hollow fiber membranes were formed into bundles and arrays and mounted in a rectangular air duct. The aim of the work was to experimentally determine heat and mass transfer coefficients for the membrane modules and compare them with theoretical estimates obtained from the available literature. The experimental facility consists of a centrifugal fan which blows air through a rectangular duct. The membrane

module was installed into the air duct in a cross flow orientation. Distilled water was delivered to the membrane module from a vessel. The vessel was at a higher elevation than the membrane so the water flow was driven by gravity. The air temperature and humidity were measured upstream and downstream of the membrane module. The air velocity was also measured downstream of the membrane module. The temperature of the water was measured in the vessel before delivery to the membrane module. The water vessel rests on a mass balance so that the flow rate of the water supplied to the membrane module could also be measured. From these measurements the heat and mass transfer coefficients could be determined for each membrane module tested in the facility. There were two types of hollow fiber membranes considered in this work. The first type were manufactured from polypropylene and have an inner diameter of 200 μm. The outer diameter was 242 μm and the nominal pore size was 0.1 μm, which yields a porosity of 46.7%. Different fiber bundles were created from this membrane type consisting of 9, 19 and 29 fibers. The second type of fibers were manufactured from polypropylene with an inner diameter of 240 μm and an outer diameter of 300 μm. The nominal pore size was 0.03 μm and the porosity was 40%. The number of fibers in the membrane module consists of 21 fibers per centimeter. Data was taken for each of the different fiber bundles and the overall heat and mass transfer coefficients were determined. The experimentally determined coefficients were then compared to the theoretical approximations from the literature. It was found that the experimental data was slightly less than the values given from the theoretical correlations. It was also reasoned that the mass transfer through the membrane governed the overall mass transfer coefficient in the membrane modules. Thus, the membranes with larger pore size and thinner membrane walls sought to increase the mass transfer rates. It was concluded that the heat transfer in the air boundary layer governed the overall heat transfer coefficients in the membrane modules. Overall, the data collect from the various membranes allowed the researchers to conclude that the cooling potential generated by the membrane modules is sufficient for the spacecraft application. It was also concluded that membrane based evaporative cooling techniques could compete with conventional evaporative cooling air conditioning devices.

1.4 Thesis Outline

This document is divided into six chapters which are summarized by the following:

- Chapter 1 gives an overview of membrane based dehumidification and evaporative cooling and their potential application to create energy saving devices. This includes a brief literature review for each concept.
- Chapter 2 presents the wire mesh material and physical phenomena behind its operation and implementation as a semi-permeable membrane. The unique characteristics of each type of mesh are defined and summarized. An image analysis is also performed on each mesh sample in order to compare its properties with those listed by the manufacturer and the ones derived from theoretical equations.
- Chapter 3 gives a complete description of the experimental facility designed to test the wire mesh samples. The purpose, location and manufacturer of all the instrumentation and equipment is reported. A detailed account is given for the measurement instrumentation used in the facility.
- Chapter 4 displays how the data collected from the experimental facility is analyzed to produce the average convective heat and mass transfer coefficients for the experimental plates. This chapter also presents an analytical model used to theoretically predict the heat and mass transfer coefficients.
- Chapter 5 explores the experimental results determined from the data analysis. The heat and mass transfer performance of the experimental plates are considered with respect to several variables and discussed.
- Chapter 6 offers the major conclusions which can be drawn from this research. It also speculates on several improvements which could be made and applied to future work.

Chapter 2 Wire Mesh Media

2.1 Introduction

Wire mesh is found in a variety of industrial and practical applications. Large wire mesh media can be used to construct a fence or a screen for a window. Small wire mesh media can be used to build filters or to shield objects from radio waves. In this research the wire mesh has a unique application. The wire mesh is used as a semi-permeable membrane which separates air from liquid water in a heat exchanger apparatus. The wire mesh material used in this research looks and feels much like a fabric. In fact, it is referred to by various manufacturers as woven wire cloth or space cloth. It is constructed from small diameter wires woven into mesh grid which forms small square openings on the order of microns. The size of the square openings depends on the wire diameter and the spacing between the wires. The wire mesh in this research is fashioned from wires with diameters ranging from 25 – 100 μm. The square openings created by the mesh structure range from about 40 – 120 μm. These microscopic openings allow for some interesting behavior when the mesh is used an interface between air and liquid water. Figure 2-1 shows an image of one of the wire mesh samples used in this research. In order to provide some perspective on the size of the wire mesh, a human hair is placed on top of the mesh surface and pictured in the image. The average diameter of a human hair is approximately 60 μm.

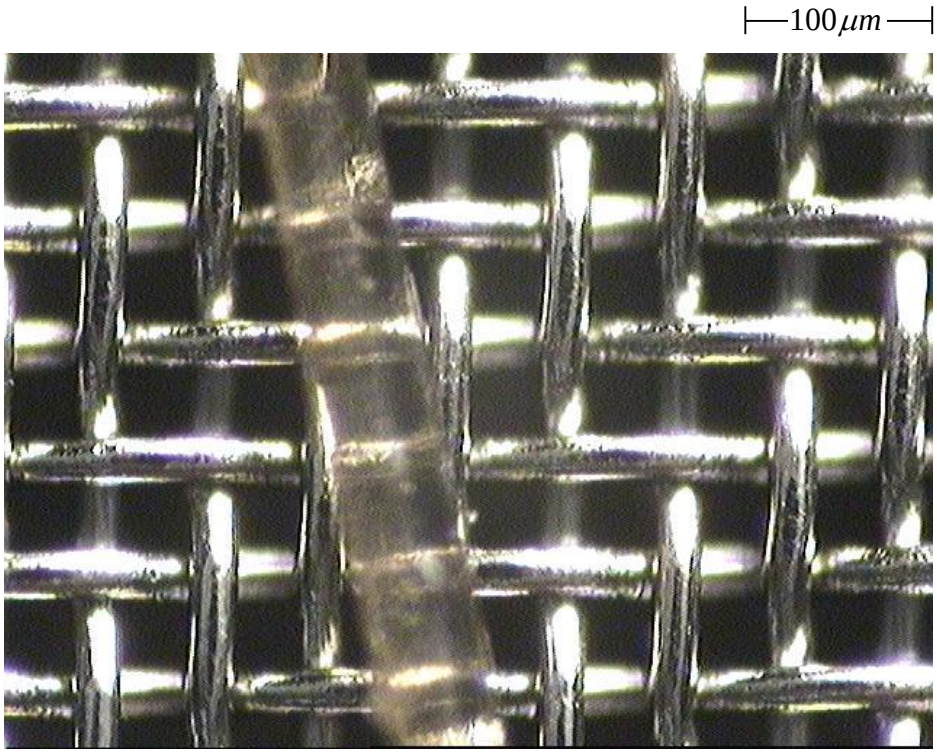

Figure 2-1 Human Hair on a Wire Mesh

The rest of this chapter is divided into three sections. The first section explains the scientific principles and physical phenomena which make the application of the wire mesh as a membrane possible. The second section is dedicated to describing and identifying the unique characteristics of each different type of wire mesh based on the manufacturer's specifications. The final section presents a computational analysis of microscopic images taken of the wire mesh in order to verify the information given by the manufacturer and predictions made from theoretical approximations.

2.2 Theory of Operation

This section describes the physical phenomena surrounding the application of the wire mesh as an interfacial boundary between air and liquid water in the presence of combined heat and mass transfer. The field which includes the phenomena of interest is dubbed Capillarity, and is defined as "the study of the interfaces between two immiscible liquids, or between a liquid and air"(De Gennes, Brochard-Wyart, and Quéré 2004). Of particular interest are the roles that surface tension and wetting play in the application of the wire mesh as a membrane. The

development of Capillarity as a scientific discipline was pioneered largely by Thomas Young and Pierre Simon de Laplace at the beginning of the 19th century. The main resource used in this section is a book published in the 21st century called *Capillarity and Wetting Phenomena* (De Gennes, Brochard-Wyart, and Quéré 2004). This book provides remarkable insight to the theories of Young and Laplace and how they apply to real world applications.

2.2.1 Surface Tension

Matter in a liquid state is free to change its shape based on molecular interactions with the surrounding environment. When a molecule is within a liquid medium it is surrounded by neighboring molecules which attracted it with equal cohesive forces. Thus, such a molecule is being pulled equally in all directions and finds itself in a balanced state. However, a liquid molecule at the surface of a gas-liquid interface loses approximately half of its neighboring molecules and hence the intermolecular forces become imbalanced. Thus, a molecule at a liquid gas-interface has a net force created by the imbalance in the direction of the bulk fluid. This imbalance in cohesive forces between molecules in a liquid is what causes a water droplet to form a curved surface as it seeks to minimize the number of molecules at its surface. This principle is illustrated in Figure 2-2.

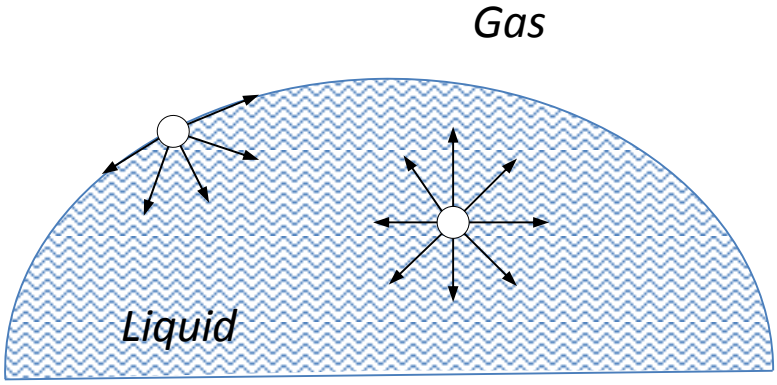

Figure 2-2 Intermolecular Forces in a Liquid Droplet

Matter in a liquid state will seek to minimize its surface area in order to reduce the number of imbalanced molecules at its surface. The stronger the intermolecular forces are between the molecules in a liquid the more it will be able to reduce its surface area. The surface tension of a liquid is a measure of the intermolecular forces between the molecules within that liquid. In fact, the surface tension of a given liquid can be defined and quantified as the amount

of energy required to increase the surface area by one unit. Therefore, surface tension (γ) has units of energy per unit area, which can be simplified to force per unit length. From a thermodynamic perspective the surface tension can be expressed as the derivative of internal energy of a liquid (E) with respect to surface area (A) at constant Temperature (T) and Volume (V) and without the number of molecules (η) changing.

$$\gamma = \left[\frac{dE}{dA}\right]_{T,V,\eta} \tag{2.1}$$

2.2.2 Wettability

When a liquid comes into contact with a solid it can be attracted or repelled to it by the intermolecular forces which arise between the two substances. The degree to which a liquid droplet spreads out on a given surface characterizes its wettability. In general, if a solid surface attracts a liquid it is said to be hydrophilic and if it repels the liquid it is called hydrophobic. A droplet of liquid on a solid surface creates three interfacial boundaries, each with accompanying surface tension interactions. There exists the surface tension of the solid surface in the presence of air (γ_{SG}), the surface tension of the solid surface in the presence of the liquid (γ_{SL}) and surface tension of the liquid in the presence of air (γ). In 1805, Thomas Young developed a relation which equates these three surface tensions based on a capillary force balance at the point where the three phases intersect and an angle is formed between the solid boundary and the liquid surface. The point of intersection of the solid, liquid and gas is called the triple line and the angle between the liquid and solid is known as the contact angle (θ). In Figure 2-3, the surface tension forces acting on the triple line are shown for a liquid droplet on a solid surface in the presence of air.

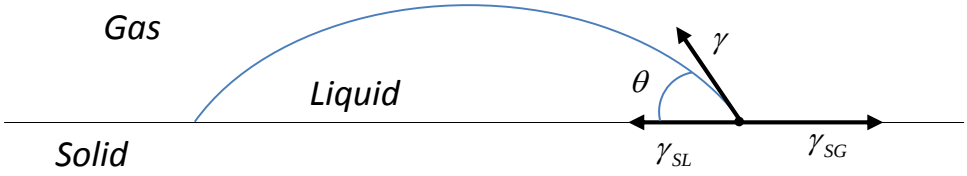

Figure 2-3 Young's Relation

By summing the components of surface tension and equating them to zero, Young derived the following equation.

$$\gamma \cos\theta = \gamma_{SG} - \gamma_{SL} \tag{2.2}$$

Equation (2.2) relates the forces which arise from the surface tensions between the solid, liquid and gas phases to the contact angle. Young's Equation demonstrates that surface tension interactions of the solid are of equal importance to surface tension of the liquid. In fact, solid surfaces can be grouped into categories based on their ability to promote wetting according to Zisman's rule (De Gennes, Brochard-Wyart, and Quéré 2004). Zisman's rule divides solids into high and low energy surface categories. High energy surfaces have a high chemical binding energy which means they are much more likely to attract a liquid which comes into contact with its surface. High energy surfaces include materials made from metal and exhibit solid-gas interfacial surface tensions $\left(\gamma_{SG}\right)$ approximately between 50-500 $\frac{mN}{m}$. Low energy surfaces have a low chemical binding energy and usually have a tendency to repel liquids. They include materials made from plastics and possess solid-gas interfacial surface tensions $\left(\gamma_{SG}\right)$ between about 10-50 $\frac{mN}{m}$. The different wire mesh media used in this research was chosen specifically to generate varying degrees of wettability in order to investigate its impact on mass transport.

2.2.3 Capillarity

The intermolecular forces between a liquid and a solid sometimes allow for the liquid to defy gravity. For example, one might notice while looking through a window on a rainy day that large raindrops rolling down the glass surface leave a trail of smaller droplets which stick to the window's surface. This could lead the observer to conclude that for the small droplets the intermolecular forces between the liquid droplet and the window are greater than the force acting on the droplet due to gravity. However, for the larger droplets the contrary is true and the forces of gravity overcome the intermolecular forces causing the droplet to fall. Therefore, there must be a critical size of the droplet where the forces of gravity overcome the capillary forces.

Capillary forces can also oppose the flow of liquid through a small orifice under the influence of gravity. Consider a small circular opening of diameter $\left(D\right)$ in the bottom of a container filled with liquid water to a height $\left(h_l\right)$. An equation can be developed which relates the gravity forces present in the hydrostatic pressure of the column of water above the circular

opening to the capillary forces which arise from the surface tension of the liquid. Figure 2-4 depicts a vessel containing liquid water with a small circular opening in the bottom. A water droplet protrudes from the opening creating a contact angle (θ) between the liquid and the solid and indicating that the pressure on the water side of the droplet is slightly greater than the atmospheric pressure.

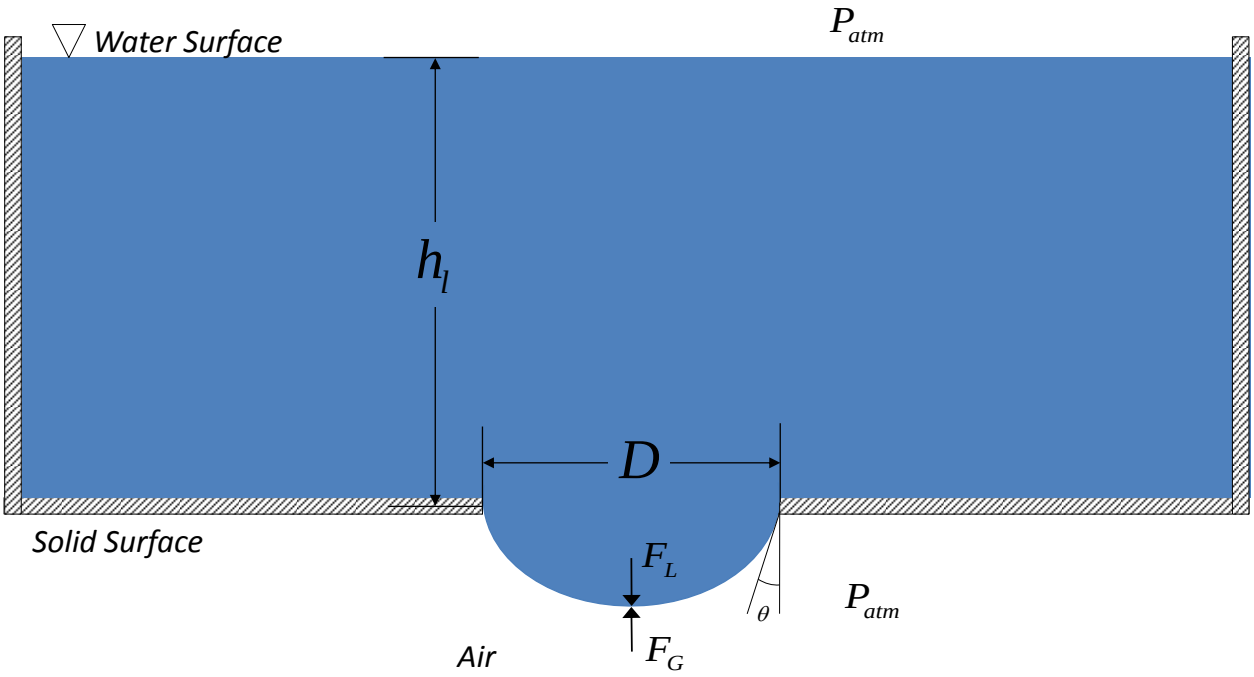

Figure 2-4 Circular Opening in the Bottom of a Container Holding Water

The force acting on the air-water interface from the liquid side (F_L) is the product of the hydrostatic pressure and the area of the opening. The hydrostatic pressure is determined by summing the atmospheric pressure with the product of the water density (ρ), the height (h_l) and the gravitational acceleration (g). Equation (2.3) demonstrates the force acting on the interface from the liquid side.

$$F_L = (P_{atm} + \rho g h_l)\frac{\pi}{4}D^2 \tag{2.3}$$

The forces acting from the air side of the interface (F_G) include the atmospheric pressure multiplied by the area of the opening and the surface tension multiplied by the circumference of the opening and the cosine of the contact angle. Equation (2.4) shows the force acting on the interface from the air side.

$$F_G = P_{atm}\frac{\pi}{4}D^2 + \pi D\gamma\cos\theta \tag{2.4}$$

The resultant forces acting along the air-water interface in Equations (2.3) and (2.4) can be equated and simplified to obtain the following equation.

$$F_L = F_G$$

$$(P_{atm} + \rho g h_l)\frac{\pi}{4}D^2 = P_{atm}\frac{\pi}{4}D^2 + \pi D\gamma\cos\theta$$

$$P_{atm}\frac{\pi}{4}D^2 - P_{atm}\frac{\pi}{4}D^2 + \rho g h_l\frac{\pi}{4}D^2 = \pi D\gamma\cos\theta$$

$$\rho g h_l\frac{\pi}{4}D^2 = \pi D\gamma\cos\theta$$

$$\rho g h_l = \frac{4\gamma\cos\theta}{D} \tag{2.5}$$

In Equation (2.5), the hydrostatic pressure appears on the left hand side. The hydrostatic pressure represents the force acting on the area of the opening due to weight of the liquid column under the influence of gravity. On the right hand side of the equation, the term which appears is referred to as a Laplace pressure. The Laplace pressure quantifies the force acting on the area of the opening due to the capillary force from the surface tension. Equation (2.5) shows that the forces from gravity and capillarity can be balanced given the right circumstances. Equation (2.5) can be further reduced to express the height of the water as a function of the other parameters.

$$h_l = \frac{4\gamma\cos\theta}{\rho g}\left(\frac{1}{D}\right) \tag{2.6}$$

The height of the water column as a function of the pore diameter can be plotted by assuming the following values for the surface tension and density of the water at room temperature.

$$\gamma = 0.07\frac{N}{m}$$

$$\rho = 1000\frac{kg}{m^3}$$

The gravitational acceleration is $9.8\,{}^{m}\!/_{s^2}$ and the contact angle is set at $0°$. A contact angle of zero represents the threshold value of the water height just before gravity overcomes the capillary force causing water to breach the opening. By making these assumptions the height of the water level is plotted as a function of the opening diameter in Figure 2-5.

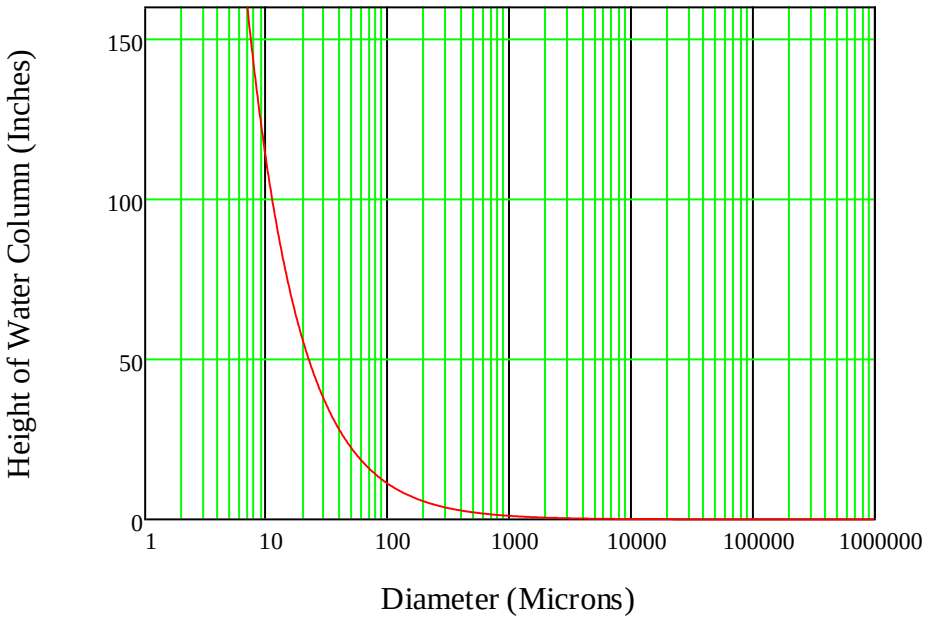

Figure 2-5 Height of Water Column vs. Pore Diameter

The opening diameter is shown in units of microns and the height of the water in inches. Figure 2-5 demonstrates that small pore diameters can withstand significantly large water columns. In fact, the capillary forces present in an opening diameter of 10 microns can withstand over 100 inches of water column!

It is apparent that capillary forces can overcome the hydrostatic pressure forces generated by gravity. It follows that the opposite must also be possible, when the gas pressure is greater than the liquid pressure. Consider a closed vessel filled with liquid water under a negative gage pressure. Instead of only one circular opening, imagine a surface filled with an array of capillary pores. Under these conditions the lower than atmospheric pressure of the liquid creates an air-water interface which protrudes into the liquid side of the apparatus. Thus, the air pressure is greater than the water pressure inside of the vessel and now the capillary forces compete with the forces generated from the pressure difference between the air and water. Figure 2-6 illustrates a water filled vessel under a negative pressure with an exposed capillary surface. The figure also depicts a zoomed view of an arbitrary pore of diameter (D).

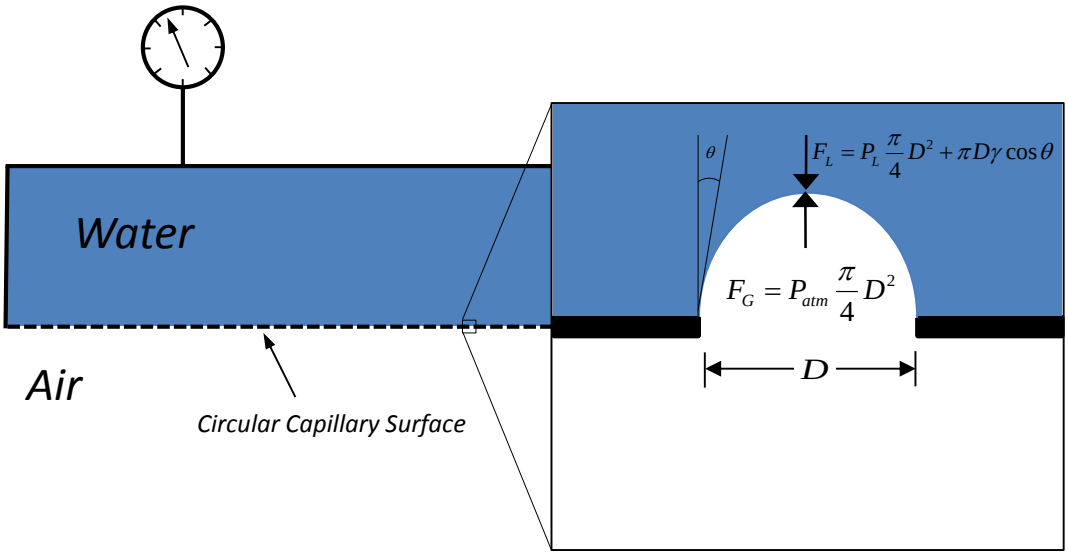

Figure 2-6 Water Filled Apparatus with a Capillary Surface

By examining the diagram in Figure 2-6, it is obvious that the capillary force now acts in the opposite direction than before as it opposes the infiltration of the air. In this case the pressure difference between the atmospheric pressure and the liquid pressure is defined as ΔP. If a force balance is conducted on the air-water interface the following result is obtained.

$$F_L = F_G$$

$$P_L \frac{\pi}{4} D^2 + \pi D \gamma \cos\theta = P_{atm} \frac{\pi}{4} D^2$$

$$\left(P_{atm} - P_L\right) \frac{\pi}{4} D^2 = \pi D \gamma \cos\theta$$

$$\Delta P \equiv P_{atm} - P_L$$

$$\Delta P = \frac{4\gamma \cos\theta}{D} \tag{2.7}$$

Equation (2.7) equates the force acting on the air-water interface from the generated pressure difference to the surface tension forces in the capillary pore. For a contact angle of $0°$, the pressure difference $\left(\Delta P\right)$ can be thought of as the maximum allowable difference between the liquid pressure in the vessel and the atmospheric pressure just before air begins to breach the interfacial boundary and flow freely into the apparatus. If the pressure difference is considered as a function of the pore diameter, it is expected to have the same shape as the previous case for the open vessel. In fact, since units of pressure can be expressed in the height of water column the

plot in Figure 2-5 is also valid for Equation (2.7) given the values chosen for the properties of the liquid water. Thus, this suggests that a capillary diameter opening of 10 microns can withstand a pressure difference in excess of 100 inches of water $\left(\approx 4\,psi\right)$ column before air would begin to infiltrate the apparatus.

Equation (2.7) turns out to be a special case of the equation Laplace developed in 1806 for the relation between change in pressure when traversing the interfacial boundary between two liquids or between liquid and air (De Gennes, Brochard-Wyart, and Quéré 2004). Laplace's theorem states that the change in pressure $\left(\Delta P\right)$ across a boundary separating two liquids is equal to the product of the surface tension $\left(\gamma\right)$ and the curvature of the surface $\left(C_s\right)$. Where the curvature of the surface is defined by the radii of curvature $\left(r_a, r_b\right)$, as shown in the Equation (2.8).

$$C_s = \left(\frac{1}{r_a} + \frac{1}{r_b}\right) \tag{2.8}$$

Thus, Laplace's equation is shown in Equation (2.9).

$$\Delta P = \gamma\left(\frac{1}{r_a} + \frac{1}{r_b}\right) \tag{2.9}$$

In the model used to derive Equation (2.7), the radii of curvature are equal and the contact angle is zero. By applying these assumptions to the Laplace equation we achieve the following result.

$$r = r_a = r_b$$

$$\Delta p = \gamma\left(\frac{1}{r} + \frac{1}{r}\right)$$

$$\Delta p = \gamma\frac{2}{r}$$

$$r = \frac{D}{2}$$

$$\Delta p = \frac{4\gamma}{D} \tag{2.10}$$

It is apparent that the result found in Equation (2.7) is simply a special case of Laplace's theorem shown in Equation (2.9).

2.2.4 Wire Mesh Application

The wire mesh material is used to create an interfacial membrane boundary which separates liquid water and air flow streams in an enclosed apparatus. Such a configuration can be likened to an air-water counter flow heat exchanger. The pressure of the liquid inside the apparatus is kept below atmospheric pressure to ensure that water does not leak through the wire mesh surface. However, the pressure difference is not large enough to allow air to infiltrate through the wire mesh into the liquid phase. Thus, each capillary opening in the wire mesh interface allows the liquid and gas mediums to be directly exposed to one another without infiltrating the other. This creates a unique situation with respect to heat and mass transfer between the air and the water mediums. Figure 2-7 depicts a cross sectional view of the wire mesh in an apparatus which separates air and water flow streams.

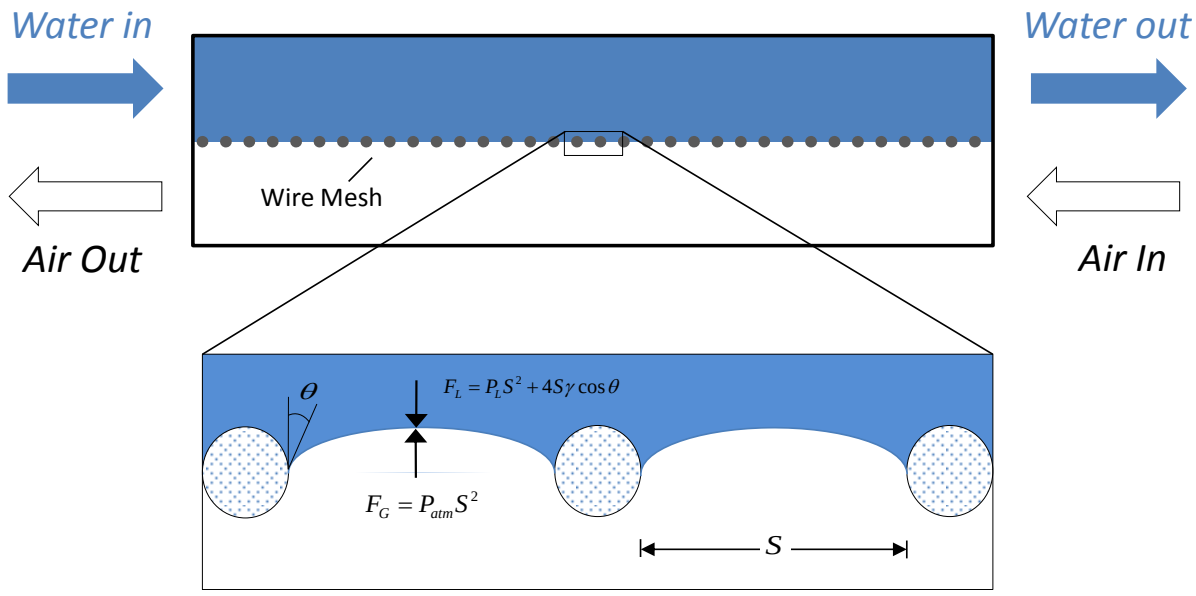

Figure 2-7 Wire Mesh Counter Flow Heat Exchanger Apparatus

The surface of the wire mesh material consists of a vast array of small capillary openings much like the one depicted in Figure 2-6. However, the wire mesh capillary openings are of a square geometry instead of a circular one. If a force balance is considered for a square capillary opening the area becomes S^2 and the perimeter becomes $4S$. A force balance on a square capillary opening is carried out to obtain the following.

$$F_L = F_G$$
$$P_L S^2 + 4S\gamma\cos\theta = P_{atm} S^2$$
$$\left(P_{atm} - P_L\right) S^2 = 4S\gamma\cos\theta$$
$$\Delta P \equiv P_{atm} - P_L$$

$$\Delta P = \frac{4\gamma\cos\theta}{S} \tag{2.11}$$

Equation (2.11) is identical to the result for a circular capillary opening in Equation (2.7) except that the diameter is replaced with the square size (S). It turns out that a square of width and length (S) can be equated to a circular opening of diameter (D). This is accomplished by inscribing a circle with the largest diameter possible into the square opening. Figure 2-8 shows a inscribed circle with the largest possible diameter (D) projected onto an image of the wire mesh and demonstrates how it can be equated to the width and length dimension of the square (S).

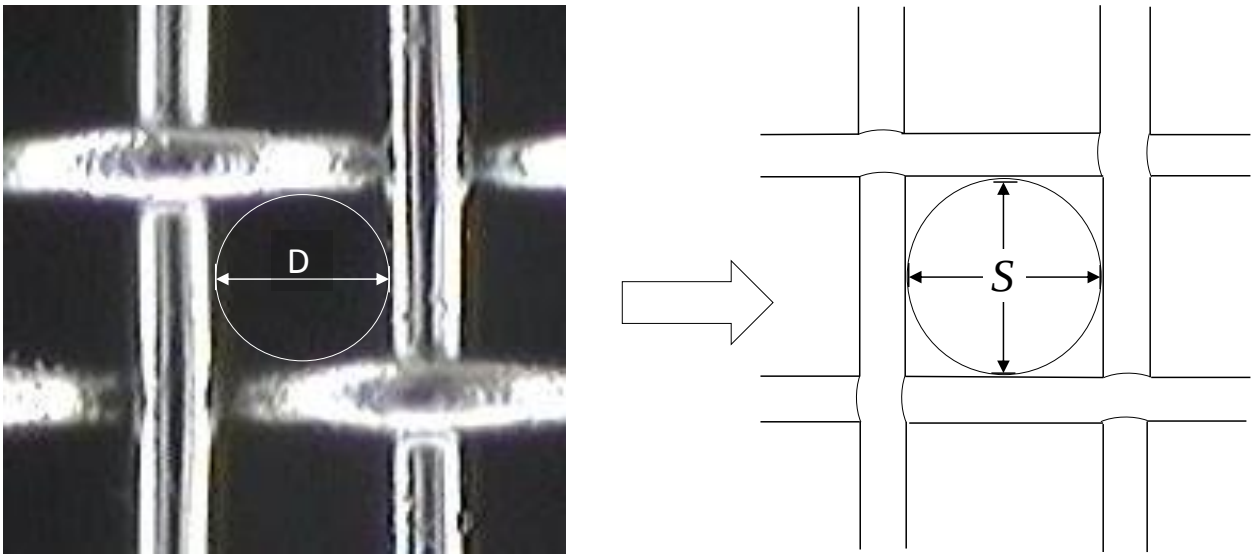

Figure 2-8 Square to Circular Geometry

The square capillary openings in the wire mesh do not allow air to pass into the water flow stream, nor does the liquid water leak into the air flow stream. Neither of the fluid mediums breach the interfacial boundary created by the wire mesh. However, mass transport of

water can occur through the mesh when a change of phase takes place. Water vapor in the air can condense at the wire mesh interface and become absorbed into the liquid water flow stream. Conversely, if the moisture content of the air flow stream is very low, the liquid water can evaporate and become entrained into the air flow stream as water vapor. A latent component of heat transfer accompanies the condensation or evaporation of water through the wire mesh surface. The driving force of condensation or evaporation is the difference in the partial pressure of the water vapor in the air and at the gas-liquid interface. This creates interesting possibilities for heat and mass transfer through the wire mesh media.

Condensation occurs at the wire mesh interface when the air flow stream has a high moisture content and the temperature of the liquid water is kept below the dew point temperature of the air. These conditions cause the water vapor in the air stream to condense onto the wire mesh surface. The water vapor in the air stream condenses either directly onto the air-water interface created in the capillary opening or condenses onto the wires of the mesh surface. It is assumed that the water vapor condensate which comes into direct contact with the air-water interface is immediately absorbed into the liquid water side. The condensate which comes into contact with the wire mesh is assumed to form droplets on the wire surface. The droplets then coalesce with neighboring droplets and continue to grow larger until they also contact the air-water interface at which point they also become absorbed into the liquid flow stream. However, the exact phenomena which occur at the membrane surface are unknown. It is possible that some of the condensing water vapor is reflected off the wire surface. It is also possible that some condensate droplets on the wire mesh surface might evaporate and put water vapor back into the air stream. It is assumed that the energy required to change the water vapor into a liquid is transmitted with the condensate to the liquid water. Thus, there is simultaneous heat and mass transfer to the liquid water during condensation conditions at the wire mesh interface. Figure 2-9 illustrates the transport of the condensate and the accompanying latent heat transfer to the liquid water through the capillary openings in the mesh surface.

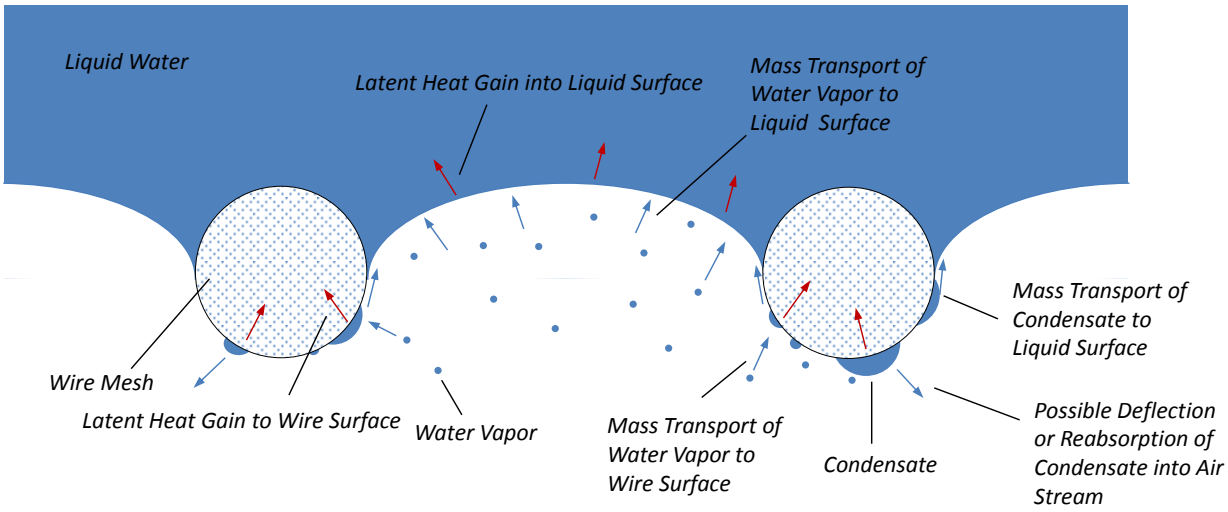

Figure 2-9 Condensation on the Wire Mesh Interface

Evaporation occurs through the wire mesh interface when the moisture content of the air is low. Molecules of liquid water at the air-water interface evaporate into water vapor and are carried away by the air stream. The energy required to change the liquid molecules into water vapor is lost from the liquid water. Thus, the transport of water vapor and the accompanying latent heat transfer are lost from the liquid water and transmitted to the air. Figure 2-10 depicts evaporation through the capillary openings of the wire mesh surface.

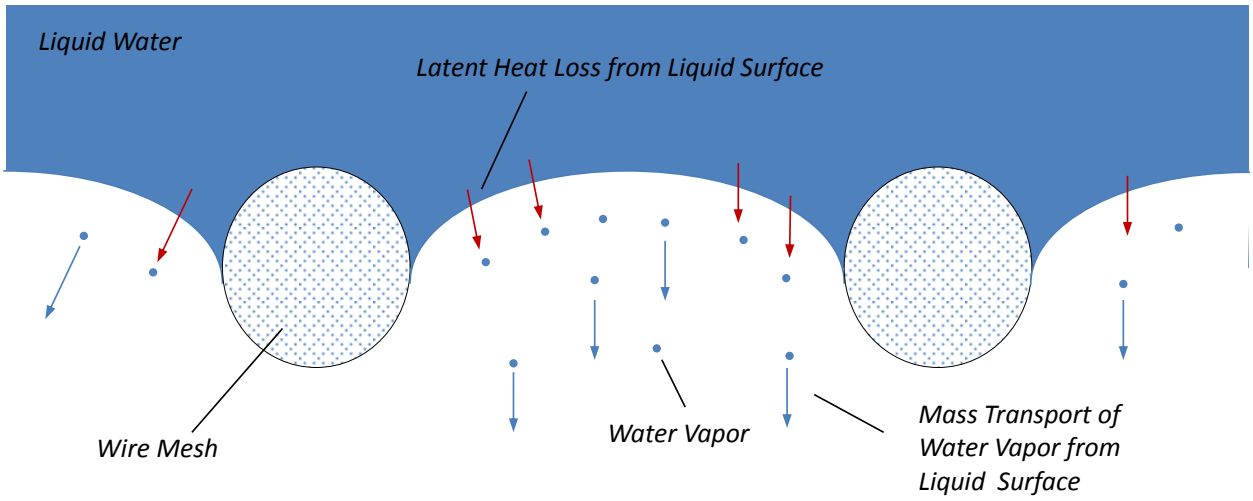

Figure 2-10 Evaporation through the Wire Mesh Interface

2.3 Defining Characteristics of the Wire Mesh

There are six different types of wire mesh media tested in this work. The wire mesh is cut into rectangular samples and installed into the test section of the experimental facility. When installed into the test section the wire mesh functions as a plate interface. Therefore, the different samples of wire mesh are named mesh plates (MP) and each is given a number between 1 and 6 to distinguish it from the others. There are also two plates which are not created from wire mesh. These plates are fabricated from metal shims and do not have any openings in their surface. Thus, these samples are named solid plates (SP) and numbered 1 and 2. In total there are eight experimental plates tested in the facility. The six mesh plate samples are depicted in Figure 2-2. The microscopic images shown in the figure are the same scale and illustrate the size differences between the wire mesh. The solid plates are not pictured.

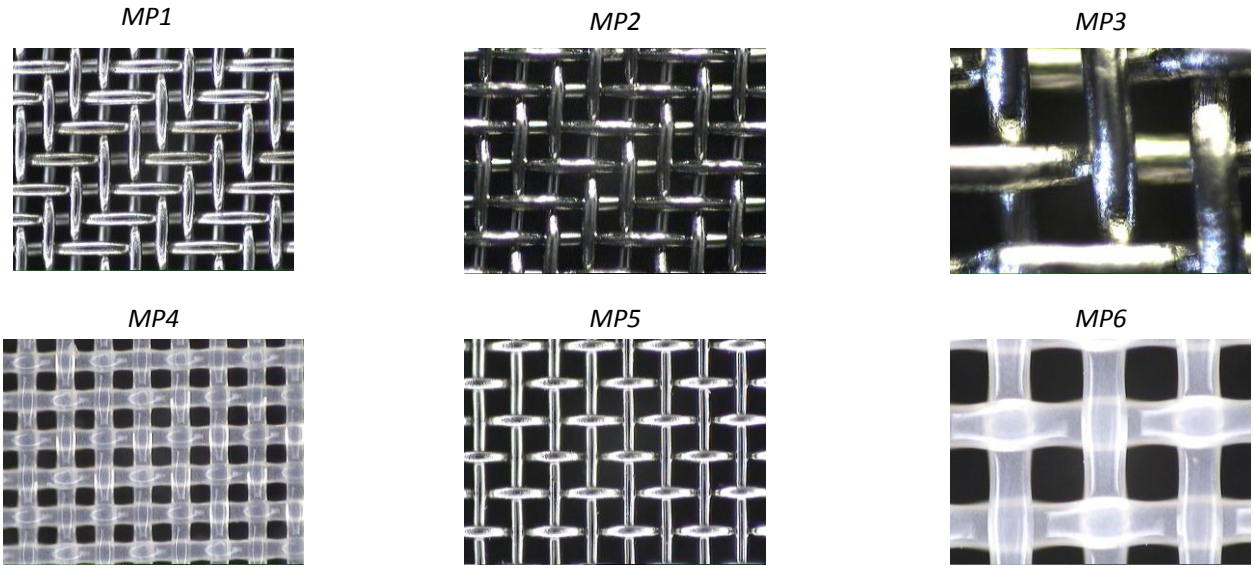

Figure 2-11 Microscopic Images of the Wire Mesh Plates

There are eight defining characteristics which make the experimental plates unique. The eight different parameters are as follows:

- Wire Diameter and Mesh Count
- Capillary Square Size and Percent Open Area
- Thickness and Surface Roughness
- Material and Relative Wettability

In the remainder of this section each pair of characteristics are defined and identified for each of the experimental plates.

2.3.1 Wire Diameter and Mesh Count

The diameter of the wire used to fabricate the mesh structure varies for each of the mesh plates. The wire diameter (d_w) is the most fundamental variable of the mesh plates and is also the most important. The wire diameter has a direct impact on the capillary square size (S), the percent open area (A_{open}), the thickness (t), and the surface roughness (ε) of the mesh plates. The variation of the wire diameter between the mesh plates can be observed in Figure 2-11. The wire diameter values for the mesh plates are obtained from the manufacturer and displayed in Table 2-1 below.

The mesh count (N) is defined as the number of openings in the mesh surface per unit length. The standard mesh count given by most manufacturers is the number openings per inch. As seen in Figure 2-11, the mesh structure forms square shaped capillary openings in the mesh surface. The capillary square openings appear in a uniform array across the surface of the mesh. Thus, by starting at an arbitrary square opening and counting the number of openings parallel to the wires for a distance of one inch, the numbers of squares counted should be equivalent to the mesh count. The mesh count directly defines the size of the capillary squares and the percent open area. The mesh count for each of the mesh plates is also presented in Table 2-1.

Table 2-1 Wire Diameter and Mesh Count for the Experimental Plates

	Wire Diameter, $d_w\,(inches)$	**Mesh Count,** $N\ \left(\frac{openings}{inch}\right)$
MP1	0.0010	400
MP2	0.0014	325
MP3	0.0040	120
MP4	0.0016	320
MP5	0.0011	325
MP6	0.0035	122
SP1	*n/a*	*n/a*
SP2	*n/a*	*n/a*

2.3.2 Capillary Square Size and Percent Open Area

The capillary square size (S) is the distance which defines the width and length of a single square opening in the mesh surface. The capillary square size is calculated from the wire

diameter and mesh count. Figure 2-12 depicts a single row of capillary square openings for an idealized wire mesh surface.

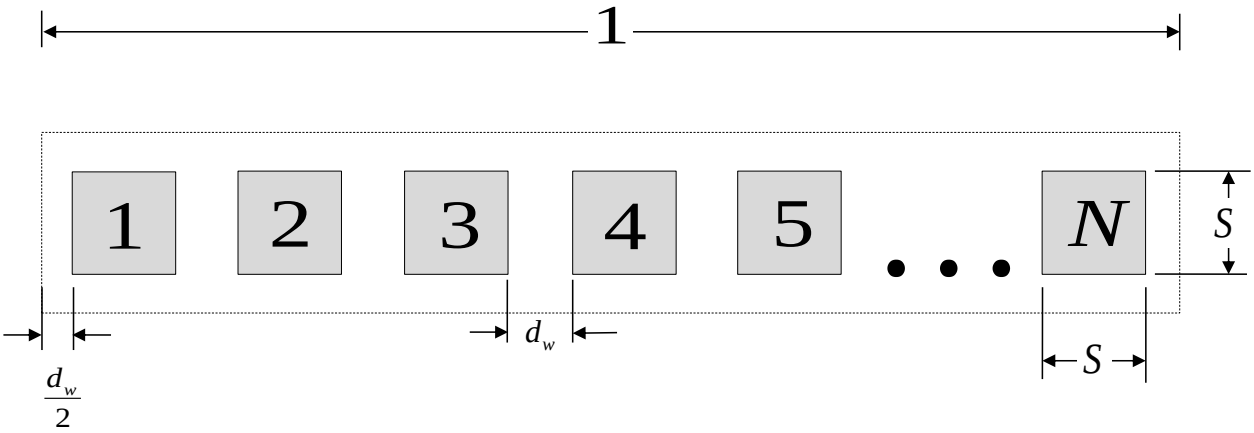

Figure 2-12 Single Row of Capillary Square Openings

In Figure 2-12, the capillary openings are separated by a distance equal to the wire diameter. It is assumed that the first capillary square opening is at a distance equal to half the wire diameter from the starting point of the row. Similarly, the row is assumed to end at a distance equal to half the wire diameter following the final square opening. If the total distance of the row is set to one unit of length, the number of square openings is equal to the mesh count. Using the model presented in Figure 2-12, the capillary square size is derived from the wire diameter and mesh count in the following manner.

$$1 = N \cdot S + N \cdot d_w$$
$$1 = N\left(S + d_w\right)$$
$$\frac{1}{N} = S + d_w$$
$$S = \frac{1}{N} - d_w \tag{2.12}$$

Equation (2.12) shows the theoretical calculation of the capillary square size as a function of the mesh count and wire diameter. It should be noted that unit of length used in the mesh count must be the same units used to describe the wire diameter. The capillary square size is a variable which is crucial to the operation of the plates. The capillary square size must be kept small enough so that the capillary forces present in the wire mesh remain significant.

The percent open area $\left(A_{open}\right)$ is defined as the ratio of the area created by the capillary square openings and the total area of the wire mesh surface. The total area includes the capillary

openings and the wires of the mesh structure. The percent open area of the wire mesh is theoretically determined by extending the model for the single row of capillary openings into two dimensions. Thus, the model is extended one unit of length in the vertical dimension creating an array of capillary square openings. A one by one unit of length area will contain a $N \times N$ matrix of capillary squares. Therefore, the percent open area is theoretically determined by multiplying the number of square openings $\left(N^2\right)$ by the area of a single square opening $\left(S^2\right)$ and then dividing by the total area $\left(1^2\right)$.

$$A_{open} = \frac{N^2 \cdot S^2}{1^2} \tag{2.13}$$

By substituting Equation (2.12) into Equation (2.13) and simplifying, the following equation is obtained.

$$A_{open} = \frac{N^2 \cdot \left(\frac{1}{N} - d_w\right)^2}{1^2}$$

$$A_{open} = N^2 \cdot \left(\frac{1}{N^2} - 2\frac{d_w}{N} + d_w^2\right)$$

$$A_{open} = \left(1 - 2Nd_w + N^2 d_w^2\right)$$

$$A_{open} = \left(1 - N \cdot d_w\right)^2 \tag{2.14}$$

Equation (2.14) expresses the percent open area as a function of wire diameter and mesh count. The percent open area is a variable of particular interesting in this work. It is anticipated that varying the percent open area will affect the heat and mass transfer performance of the mesh plates because it changes the area of the gas-liquid interface.

The capillary square size and the percent open area calculated from Equations (2.12) and (2.14) are regarded as purely theoretical approximations. In order to use these equations it is assumed that capillary openings in the mesh are perfectly square, spaced equally apart, and have the exact same area. These assumptions are highly idealized and therefore in the next section measures are taken to evaluate the actual capillary square size and percent open area of the mesh. The theoretical values for the capillary square size and the percent open area are shown for all the experimental plates in Table 2-2.

Table 2-2 Capillary Square Size and Percent Open Area of Experimental Plates

	Capillary Square Size, $(inches)$	**Percent Open Area,** $(\%)$
MP1	0.00150	36
MP2	0.00168	30
MP3	0.00433	27
MP4	0.00153	24
MP5	0.00198	41
MP6	0.00470	33
SP1	*n/a*	*n/a*
SP2	*n/a*	*n/a*

2.3.3 Thickness and Surface Roughness

The thickness and surface roughness of the wire mesh plates are attained from the wire diameter. The wire mesh is fabricated by weaving wires of equal diameter. Therefore, the maximum theoretical value for the thickness of the wire mesh (t) is assumed to be equivalent to twice the wire diameter. The roughness of a surface can be defined by a variety of methods. If the wire mesh is considered as a completely flat surface, then the maximum deviation in the profile of the wire mesh surface will be equivalent to the wire diameter. Therefore, the surface roughness of the wire mesh (ε) is approximated by the wire diameter. Figure 2-13 illustrates a cross sectional view of the wire mesh surface. The wire mesh thickness is depicted as twice the wire diameter.

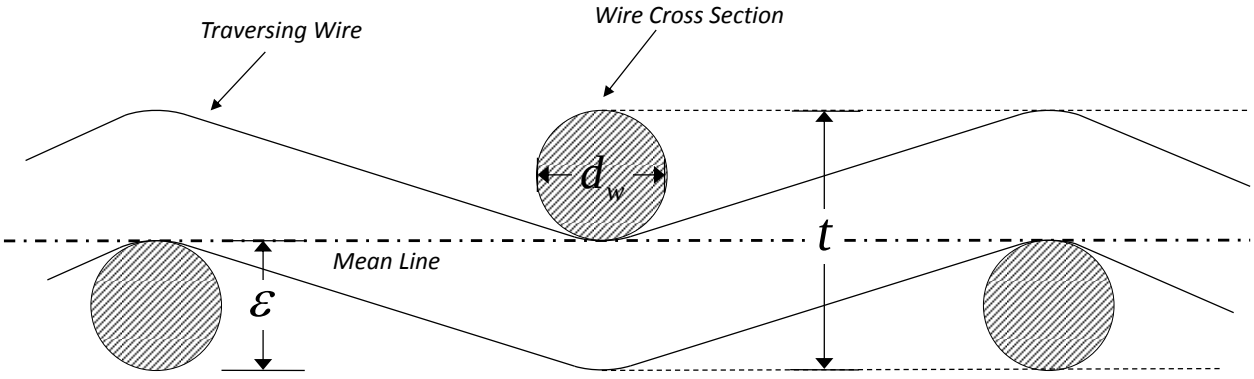

Figure 2-13 Cross Sectional View of Wire Mesh Surface

A line representing the mean of the wire mesh surface is depicted in Figure 2-13 and it is apparent that the maximum deviation from the mean line corresponds to the diameter of the wire.

The method used to determine the surface roughness of the wire mesh is admittedly ideal. The actual surface roughness could vary by orders of magnitude. This is due to the wire mesh's lack of rigidity; allowing the surface of the mesh to become deformed easily. Folds and wrinkles could form when the mesh is installed into the apparatus or during testing which would increase the apparent surface roughness of the wire mesh. The surface roughness of the solid plates is considered negligible when compared to the wire mesh and therefore no value is listed. The thicknesses of the solid plates were chosen so that it would be comparable to the mesh plates. Table 2-3 displays the values for the thickness and the surface roughness for the experimental plates.

Table 2-3 Thickness and Surface Roughness of the Experimental Plates

	Thickness, $t\ (\mu m)$	**Surface Roughness,** $\varepsilon\ (\mu m)$
MP1	51	25
MP2	71	36
MP3	203	102
MP4	81	41
MP5	56	28
MP6	178	89
SP1	51	*n/a*
SP2	76	*n/a*

A range spanning two orders of magnitude is chosen to represent the possible values for the surface roughness due to its high uncertainty. The lower limit of the range is set at $10\mu m$ which is chosen include the low surface roughness values of the solid plates. The upper limit is fixed at $1000\mu m$ to account for folds and wrinkles which might distort the surface of the wire mesh and increase its apparent surface roughness value. These values represent the minimum and maximum values for the surface roughness and are later used in analytical calculations of the heat and mass transfer coefficients.

2.3.4 Material and Relative Wettability

The experimental plates are fabricated from two distinct materials. Four of the mesh plates and both solid plates are made from the stainless steel 304 alloy (SS304). The remaining two mesh plates are constructed from polyester. The different materials are chosen because they are believed to possess varying degrees of wettability. According to Zisman's rule presented in

Section 2.2, the stainless steel is considered a high energy surface and should be hydrophilic relative to the polyester. Conversely, the polyester plates should be hydrophobic relative to the stainless steel plates. Thus, the different materials are chosen to test how their relative wettability affects the heat and mass transfer performance of the plates. Table 2-4 lists the material and relative wettability of the experimental plates.

Table 2-4 Material and Relative Wettability of the Experimental Plates

	Material	Relative Wettability
MP1	SS304	Hydrophilic
MP2	SS304	Hydrophilic
MP3	SS304	Hydrophilic
MP4	Polyester	Hydrophobic
MP5	SS304	Hydrophilic
MP6	Polyester	Hydrophobic
SP1	SS304	Hydrophilic
SP2	SS304	Hydrophilic

2.4 Image Analysis

The size of the square capillary openings in the mesh surface are calculated theoretically from the wire diameter and the mesh count using Equation (2.12). The percent open area can also be determined theoretically from the same parameters using Equation (2.14). These theoretical calculations are based on the ideal assumptions that the openings in the mesh are perfectly square and that each opening in the mesh is identical to the all the others. Furthermore, the manufacturer of the wire mesh lists a broad range for the percent open area indicating that the actual specifications of the mesh are most likely less than ideal. Thus, a method was sought to calculate the actual dimensions of the mesh in order to verify the theoretical calculations and manufacturer specifications. The method chosen to quantify the specifications of the wire mesh is based on the rigorous analysis of microscopic images. A series of microscopic images of each mesh are taken in the jpeg format and read into a computer program as an array of numbers. The wire mesh images are then reduced into a binary format where the wires and the capillary openings are distinguished from one another by numerical values of one or zero. The pixels in the image which represent the wires retain a value of zero and appear black while the pixels of the capillary openings possess a value of one and appear white. The average length of the

capillary openings and the percent open area of the wire mesh can then be evaluated by employing statistical techniques. The devices used to capture images of the wire mesh are a Sony CCD camera used in conjunction with a 10x microscope. The software used to analyze the image is Matlab 2010a. The Matlab script used to analyze the images is shown in Appendix D. The remainder of this section presents the details of the image analysis followed by a comparison of the results with the theoretically predicted values and the manufacturer's specifications.

2.4.1 Image Conversion

The initial image of the wire mesh taken from the digital microscope is in jpeg format. It is necessary to reduce the image to binary format so that it can be analyzed. The initial jpeg image is a RGB color image which consists of 640 x 480 pixels with a bit depth of 24. The RGB image is read by Matlab as an array of three separate 640 x 480 matrices. Each matrix corresponds to the red, green and blue components used to produce a color image. The elements within each matrix express the intensity of red, green or blue on a scale from 0 to 255. To simplify the analysis the RGB image is reduced to a grayscale image. This reduces the array of three matrices from the initial image to a single matrix of 640 x 480 pixels. The elements of the matrix have a value ranging from 0 to 255. In a grayscale image, a value of 0 appears as black and a value of 255 is white. The intermediate values appear as varying shades of gray. Figure 2-14 shows an example of the conversion of an RGB image to grayscale. The images in Figure 2-14 appear very similar to one another but this is due to the fact that the initial image lacks any significant coloring. The dialog box which appears in each image displays the value or values for a single pixel before and after the image is converted to grayscale. In the RGB image there are three distinct values corresponding to the red, green and blue components (97, 98, 102). After the image is converted to grayscale the value at the same pixel location is reduced to a single value (98).

RGB Image *Gray scale Image*

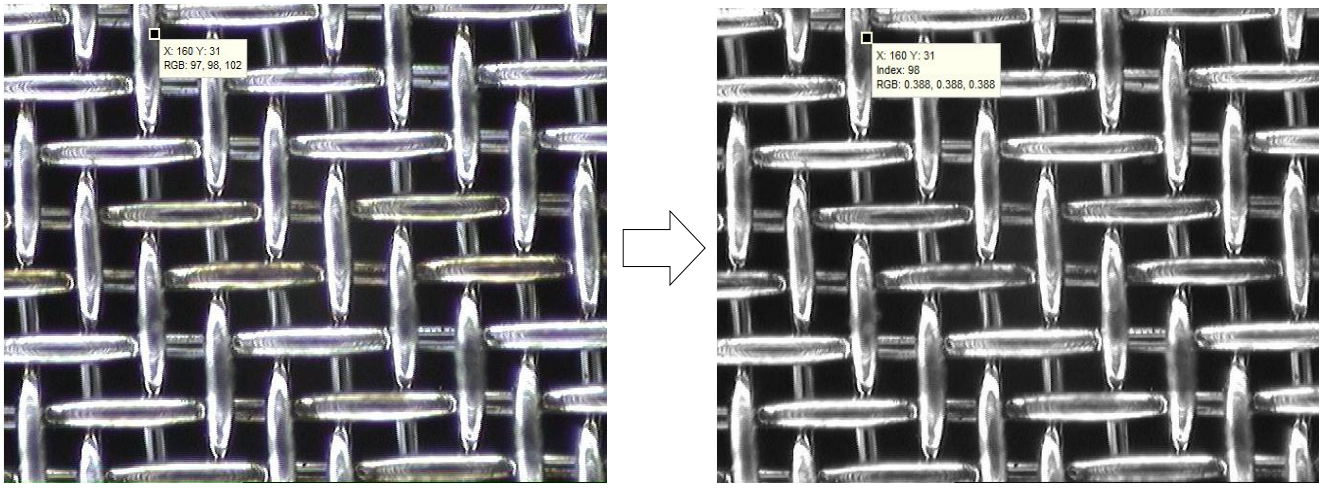

Figure 2-14 RGB Image Converted to Grayscale Image

Once the image is in grayscale format it can then be converted into binary format. A histogram plot of the grayscale image is produced in order to determine a threshold value. The threshold value is a user defined value which is input into Matlab function. The function then converts the grayscale image to a binary image. Every pixel less than or equal to the threshold value is set to zero and every pixel value greater than the threshold value is set to one. By selecting a reasonable threshold value a binary image can be created where the capillary openings in the mesh appear black and the wires appear white. The threshold value is determined by the user and may require several guesses before an accurate depiction of the wire mesh in binary form is achieved. Figure 2-15 displays a histogram plot of the grayscale image shown in Figure 2-14.

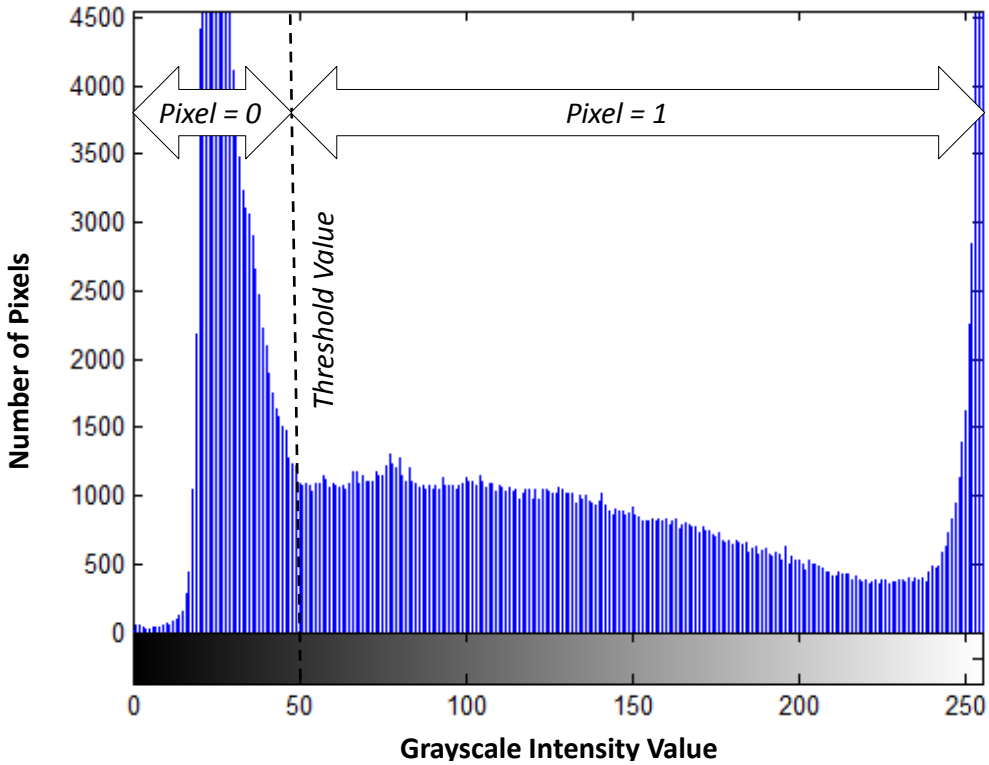

Figure 2-15 Histogram of Grayscale Image

By inspecting the grayscale image in Figure 2-14, it is apparent that there will be large number of pixels at the lower range of the grayscale intensity values. This is because the darker areas of the image correspond to the capillary openings. In Figure 2-15 there is a sharp increase in the number of pixels around the grayscale intensity value of about 50. Therefore, 50 is chosen as the threshold value for the grayscale image shown in Figure 2-14. The pixels to the left of the threshold receive a value of zero and those to the right are assigned a value of one. Once the binary image is created is necessary to immediately invert the image. This simply changes the zeros to ones and the ones to zeros. Therefore, in the inverted binary image the wires appear black and retain a value of zero and the capillary openings appear white and possess a value of one. The image is inverted so that two additional Matlab functions can be employed which enhance the quality of the inverted binary image. These functions require that the objects of interest retain a value of one. Since the capillary openings are the objects of interest the binary image must be inverted.

Binary Image *Inverted Binary Image*

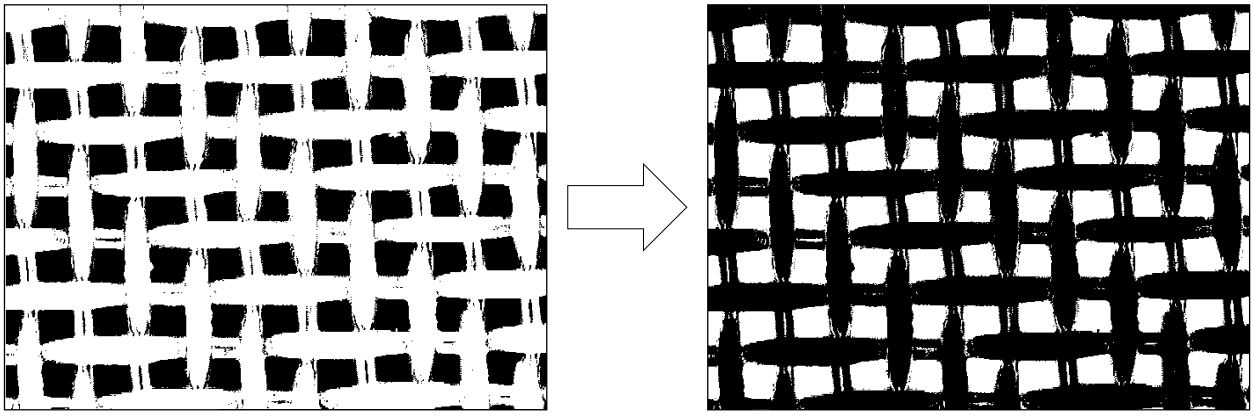

Figure 2-16 Binary and Inverted Binary Image

Figure 2-16 depicts the binary and the inverted binary image produced from the grayscale image in Figure 2-14 using a threshold value of 50. Upon inspection it is evident that there are some small patches of white on the wires in the inverted binary image. These patches were initally dark spots on the wires which were falsely identified as openings when the image was converted from the grayscale image to the binary image. A Matlab function is then used to remove false openings from the inverted binary image. The function identifies all the objects in the image which appear as groups of ones surrounded by zeros and eliminates them if they do not contain more than a certain number of pixels. The value which determines the size of the objects which are to be eliminated is selected by the user. Another Matlab function is used to remove objects which touch the border of the inverted binary image. This is done to remove the objects which only show a partial area of a single capillary opening. Figure 2-17 depicts the inverted binary image from Figure 2-16 after the two Matlab functions have been applied.

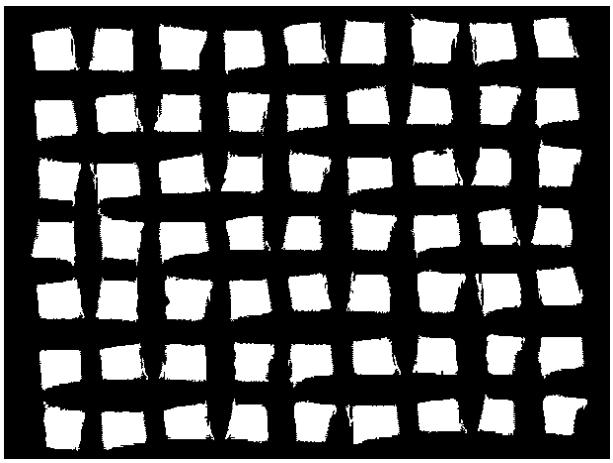

Figure 2-17 Inverted Binary Image after Modification

Figure 2-17 is the image used to determine the average opening distance of the capillary openings and the percent open area. In order to make accurate estimates for these variables in relevant units, a scaling factor must be obtained which expresses the dimensions of a single pixel in units of length. This is the subject of the following sub-section.

2.4.2 Pixel Dimensions

The size of a single pixel must be expressed in units of length in order to calculate the capillary square size and the percent open area. The wire diameter of each mesh is given by the manufacturer and is known to a high degree of accuracy. Therefore, a sufficient approximation of a pixel's size can be made by counting the number of pixels which correspond to the wire diameter in the inverted binary image and then divide by the known wire diameter given by the manufacturer in units of length. Thus, the wire diameter in the image gives the needed reference to determine the pixel size in an image. This method is executed by developing a pair of functions which read through the entire inverted binary image horizontally and vertically while counting the number of pixels which correspond to the width of the wire. The first function reads horizontally row by row and left to right through each pixel of the inverted binary image. When the function encounters an element which has a value of one and the element immediately to the right has a value of zero, the function begins counting the number of zero valued pixels in a row. When the function encounters a pixel with a value of zero followed by a pixel with a value of one the function then stops counting and the number of zero valued pixels which correspond to the wire diameter is recorded to a vector. Figure 2-18 demonstrates the operation

of the function which counts the number of zero valued pixels in a string. A consecutive number of zero valued pixels can be referred to as a zero string

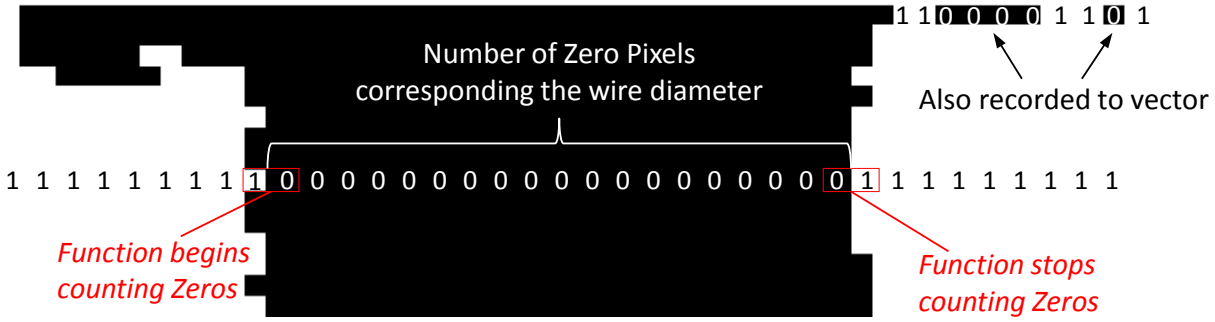

Figure 2-18 Illustration of Zero String Counting Function

Figure 2-18 also indicates that some zero strings which do not correspond to the wire diameter will also be recorded by the function to the output vector. In order to filter the unwanted zero strings, a histogram plot of the recorded vector is made and a range appropriate to the wire diameter is selected. There is a large quantity of zero strings which correspond to the wire diameter for a given image and therefore a peak will appear on the histogram. A range is selected around the peak and the zero strings which fall outside the selected range are eliminated from the recorded vector. The remaining zero strings in the vector are averaged to estimate the mean zero string length corresponding to the wire diameter.

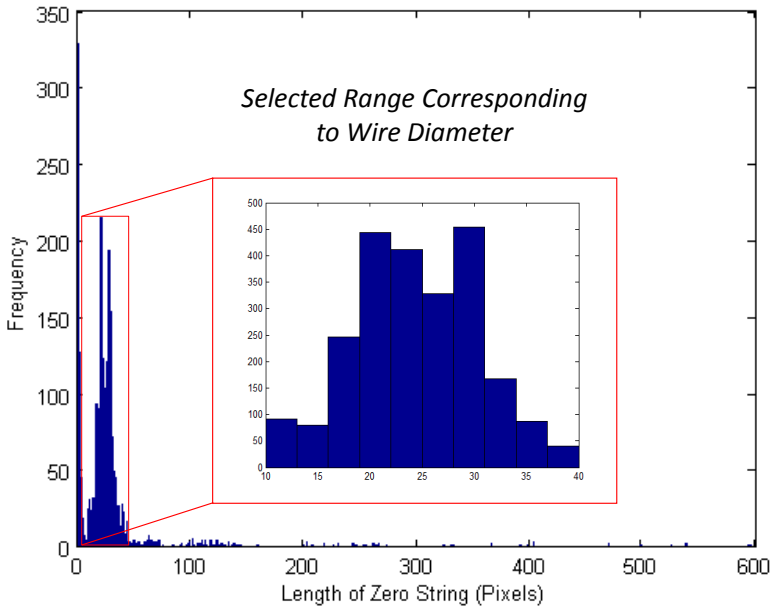

Figure 2-19 Histogram Plot of Zero String Length

Figure 2-19 shows a histogram plot of the zero strings from the inverted binary image pictured in Figure 2-17. A zoomed view is also shown in Figure 2-19 of the range selected to quantify the wire diameter. As expected, the selected range resembles a normal distribution. The known wire diameter $\left(d_w\right)$ is divided by the mean horizontal zero string length corresponding to the wire diameter $\left(\bar{p}_h\right)$ to produce the horizontal pixel length $\left(H_{pix}\right)$.

$$H_{pix} = \frac{d_w}{\bar{p}_h} \tag{2.15}$$

Equation (2.15) expresses the horizontal length of a single pixel in the same units of measurement as the wire diameter. A second function is created to read vertically from top to bottom an left to right through the inverted binary image and calculates the vertical pixel length employing the same method used to estimate the horizontal pixel length. Thus, the mean vertical zero string length of the wire diameter $\left(\bar{p}_v\right)$ is divided by the known wire diameter to calculate the vertical pixel length $\left(V_{pix}\right)$.

$$V_{pix} = \frac{\bar{p}_v}{d_w} \tag{2.16}$$

Equation (2.16) gives the vertical length of a single pixel in the same units of measurement chosen for the wire diameter. Once the horizontal and vertical pixel lengths have been established they can be used to calculate the capillary square size and the percent open area.

2.4.3 Calculation of Capillary Square Size and Percent Open Area

There are two methods used to determine the capillary square size $\left(S\right)$ and the percent open area $\left(A_{open}\right)$ of the wire mesh material. For simplicity, these methods are referred to as Method A and Method B. Method A employs the use of a built-in Matlab function which identifies and quantifies the capillary openings in the inverted binary image as unique objects. The function determines the exact number of pixels in each object which can be used to directly approximate the area and capillary square size. For Method B a more direct approach is taken and a sub-routine is developed which scans through the entire inverted binary image and counts the number of pixels corresponding to the horizontal and vertical openings in each capillary

square object. The horizontal and vertical pixel lengths are then averaged and utilized in the calculation of the capillary square size and the percent open area.

The Matlab function applied in Method A uses the inverted binary image as an input. The function takes the inverted binary image and creates a new RGB color image which defines each of the capillary square openings within as unique objects and assigns each one a distinct color. A sub-routine is constructed to project the new image from Method A onto the original image taken for analysis. This allows the user to ensure that the analysis captures the area of the capillary openings with precision. Figure 2-20 displays the Method A image using the inverted binary image from Figure 2-17 as an input. The Method A image is also shown project onto the original image shown in Figure 2-14.

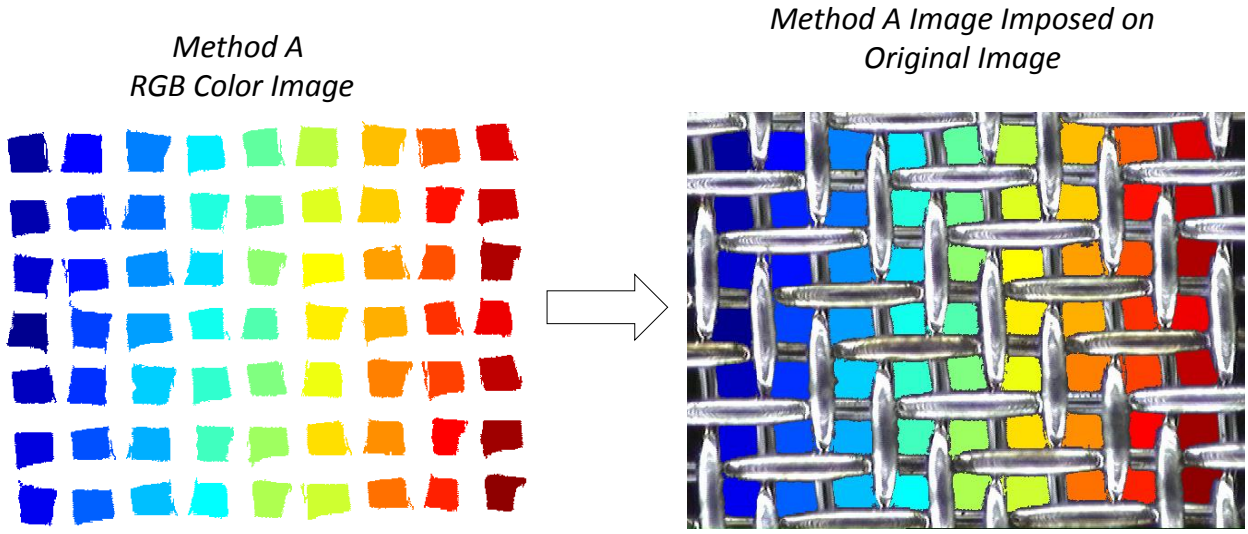

Figure 2-20 Method A Image Project onto Original Image

The Matlab function used in Method A counts the number of pixels (n_p) in each capillary square object and records them to a vector. The capillary square size (S) can then be estimated by taking the square root of the product of the number pixels and the horizontal and vertical pixel lengths calculated in Equations (2.15) and (2.16).

$$S = \sqrt{n_p \cdot H_{pix} \cdot V_{pix}} \tag{2.17}$$

Equation (2.17) is used to determine the capillary square size for each of the objects which appear in the inverted binary image. It should be mentioned that the use of Equation (2.17) assumes that the capillary objects are perfectly square. The mean value of the capillary square

size $\left(S_{ave}\right)$ is then calculated by averaging all the capillary square objects which appear in the Method A image. At least 30 capillary square objects collected from multiple images are used to calculate the mean value of the capillary square size for each wire mesh sample. The mean capillary square size and the wire diameter are then used to approximate the percent open area $\left(A_{open}\right)$.

$$A_{open} = \frac{S_{ave}^2}{\left(S_{ave} + d_w\right)^2} \tag{2.18}$$

Equation (2.18) calculates the percent open area for the wire mesh based on the mean capillary square size. The percent open area and capillary square size are determined for each wire mesh type using Method A and are compared to the theoretical predictions and manufacture's specifications in the following sub-section.

Method B utilizes a technique similar to the one developed to calculate the horizontal and vertical pixel lengths. In fact, the sub-routines used to count the horizontal and vertical zero strings are modified to instead count the number of pixels corresponding to the horizontal and vertical capillary opening lengths. The capillary opening pixel lengths are recorded to a vector and a histogram plot is made in order to select the appropriate pixel range. Figure 2-21 shows a histogram plot of the horizontal opening pixel lengths from the inverted binary image shown in Figure 2-17.

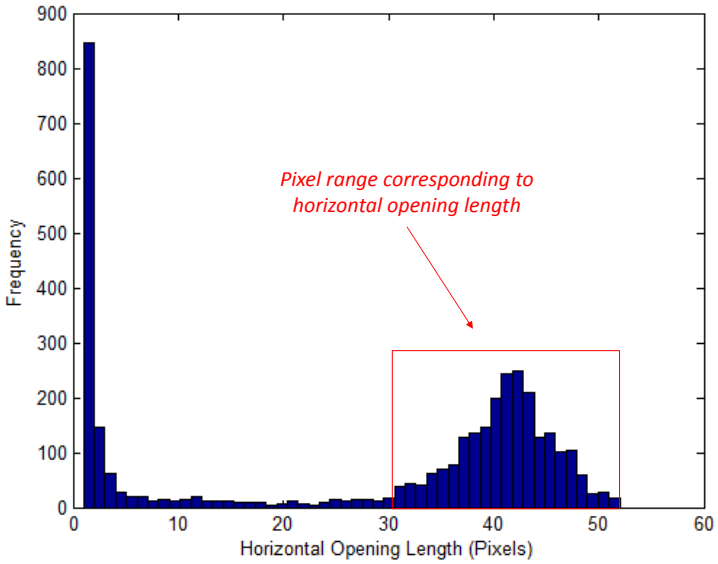

Figure 2-21 Histogram Plot of Horizontal Opening Length

A region appears in the histogram plot where the pixel lengths appear normally distributed. This region corresponds to the pixel lengths of the horizontal capillary openings. A range which encompasses the normally distributed pixel lengths is selected and the remaining elements in the vector are eliminated. The remaining values are then averaged to estimate the mean horizontal opening length in pixels $\left(\bar{N}_H\right)$. The mean horizontal opening length is multiplied by the horizontal pixel length $\left(H_{pix}\right)$ to produce the average horizontal capillary opening length $\left(S_H\right)$.

$$S_H = \bar{N}_H \cdot H_{pix} \tag{2.19}$$

The same procedure described above is executed to determine the average vertical capillary opening length $\left(S_V\right)$ using the mean vertical opening length in pixels $\left(\bar{N}_V\right)$ and the vertical pixel length $\left(V_{pix}\right)$.

$$S_V = \bar{N}_V \cdot V_{pix} \tag{2.20}$$

The average of the mean horizontal and vertical opening lengths is taken to estimate the mean capillary square size $\left(S_{ave}\right)$. The mean capillary square size is then used in Equation (2.18) to determine the percent open area for Method B.

Methods A and B both give reasonable approximations for the capillary square size and the percent open area. Method A is slightly more idealistic than Method B because it assumes the capillary cells are perfect squares. Method B presents a more rigorous procedure but also requires subjective inputs from the user because an arbitrary range must be selected in the histogram plots. In the following sub-section the results from the image analysis are compared to the theoretical predictions and the manufacturer specifications for the capillary square size and percent open area.

2.4.4 Comparison to Theoretical Calculations and Manufacturer Specifications

The results from the image analysis are compared to the theoretical predictions and the manufacturer specifications for the capillary square size and the percent open area of the wire mesh plates. Table 2-5 summarizes the results of the image analysis carried out for each mesh plate tested in facility. The image analysis results include the capillary square size and percent open area calculated from each of the methods described in this section.

Table 2-5 Results of the Image Analysis

Mesh	Capillary Square Size, S (μm)				Percent Open Area , A_{open} (%)			
Plate	*Theoretical*	*Manufacturer*	*Method A*	*Method B*	*Theoretical*	*Manufacturer*	*Method A*	*Method B*
MP1	38	38	39	38	36	30-39	36	36
MP2	43	43	50	49	30	30-39	34	34
MP3	110	109	122	119	27	20-29	30	29
MP4	39	41	37	37	24	25	23	23
MP5	50	51	56	56	41	40-49	45	45
MP6	119	119	104	104	33	34	29	29

By inspecting Table 2-5 it becomes apparent that the predicted values from Method A and Method B are nearly identical. There are a few instances where the values deviate slightly. In these instances it seems that Method B is closer to theoretical values which might lead to the conclusion that it is marginally better when comparing the accuracy of the two methods. As expected, the theoretical values appear nearly identical to the manufacturer's specifications for the capillary square size. The manufacturer list a range of possible values for the percent open area of the stainless steel mesh plates (MP1, MP2, MP3, MP5). This indicates that the uncertainty in the percent open area could be substantial. For each of the stainless steel plates the theoretical value does not necessarily fall in the center of the given range, rather it can appear at the high or low end. The manufacturer's specifications for the percent open area of the polyester mesh plates (MP4, MP6) does not list a range but a single value. For the polyester plates the value given from the manufacturer is within 1% of the theoretical value.

The results from Method A and B compare well with the theoretical predications. In Table 2-6 the percent difference between the results from both methods of the image analysis and the theoretical values are shown. The percent difference is calculated by Equation (2.21). The "actual" value which appears in Equation (2.21) is the predicted value from the image analysis using Method A or B.

$$Percent\ \ Difference = \frac{|Theoretical - Actual|}{Theoretical} \tag{2.21}$$

Table 2-6 Percent Difference from Theoretical Values

Mesh	**Percent Difference, S (%)**		**Percent Difference, A_{open} (%)**	
Plate	*Method A*	*Method B*	*Method A*	*Method B*
MP1	1.2%	0.5%	0.9%	0.4%
MP2	17%	15%	15%	13%
MP3	11%	8%	10%	8%
MP4	5%	4%	5%	4%
MP5	12%	12%	8%	8%
MP6	13%	13%	12%	11%

Table 2-6 shows that the values for the capillary square size and the percent open area obtained from the image analysis generally fall within approximately 5-15% from the theoretical values. MP1 is an exception to this generalization and displays a percent difference which is orders of magnitude lower than the other plates. The largest percent difference is found in the prediction of the capillary square size using Method A. In fact, MP2 shows the largest percent difference from the theoretical when compared to the other plates. It should be noted that the quality of the images taken for MP2 was poor and made analyzing the images more difficult. This is likely the cause of the deviation from the theoretical values, which would suggest that image quality is a crucial factor to a successful image analysis. Overall, the agreement between the results from the image analysis and the theoretical values implies that the theoretical predictions of the capillary square size and percent open area are reasonable. It is difficult to discern whether the inaccuracy in these parameters of the wire mesh are caused by distortions in the mesh structure or from the uncertainty in the methods used to measure them. For all practical purposes it is assumed that the theoretically predicted values give adequate measures of the capillary square size and the percent open area.

Chapter 3 Experimental Facility

3.1 Introduction

This Chapter describes the design of the experimental facility and presents the components which contribute to its operation. The purpose of the facility is to investigate the heat and mass transfer performance of the experimental plates in an air-water heat exchanger. The facility is divided into three main systems:

1. The Test Section
2. The Water Flow Loop
3. The Air Flow Loop

Figure 3-1 displays a schematic of the entire facility and identifies the three main systems. Figure 3-1 also depicts the location of the instrumentation used to collect the temperature, pressure and relative humidity measurements. The test section is essentially an air-water heat exchanger where the experimental plate surface serves as the interface between the air and liquid water mediums. The temperature of the water is measured at the inlet and outlet of the test section. The temperature of the plate surface, the water pressure, the inlet air temperature and the inlet relative humidity of the air are also measured in the test section. The water flow loop uses two positive displacement gear pumps to control the flow rate of the water delivered to the test section. A constant temperature bath regulates the temperature of the water. In the water flow loop, the mass flow rate of the water is measured before it enters the test section. The equipment shown in Figure 3-1, except for the constant temperature bath, is enclosed in a temperature and humidity controlled climactic chamber. The climactic chamber is considered a part of the air flow loop because it delivers air at a specified temperature and humidity to the test section. The air leaving the test section travels through a circular PVC duct in which the temperature and relative humidity are measured downstream of the test section. In the air flow loop, the pressure drop across an orifice plate is measured to determine the mass flow rate of the air. The air is drawn through the test section and PVC duct by a centrifugal radial blower. In the following sections each of the systems within the experimental facility are further examined. In the final section, the measurement instrumentation used in the experimental facility is presented.

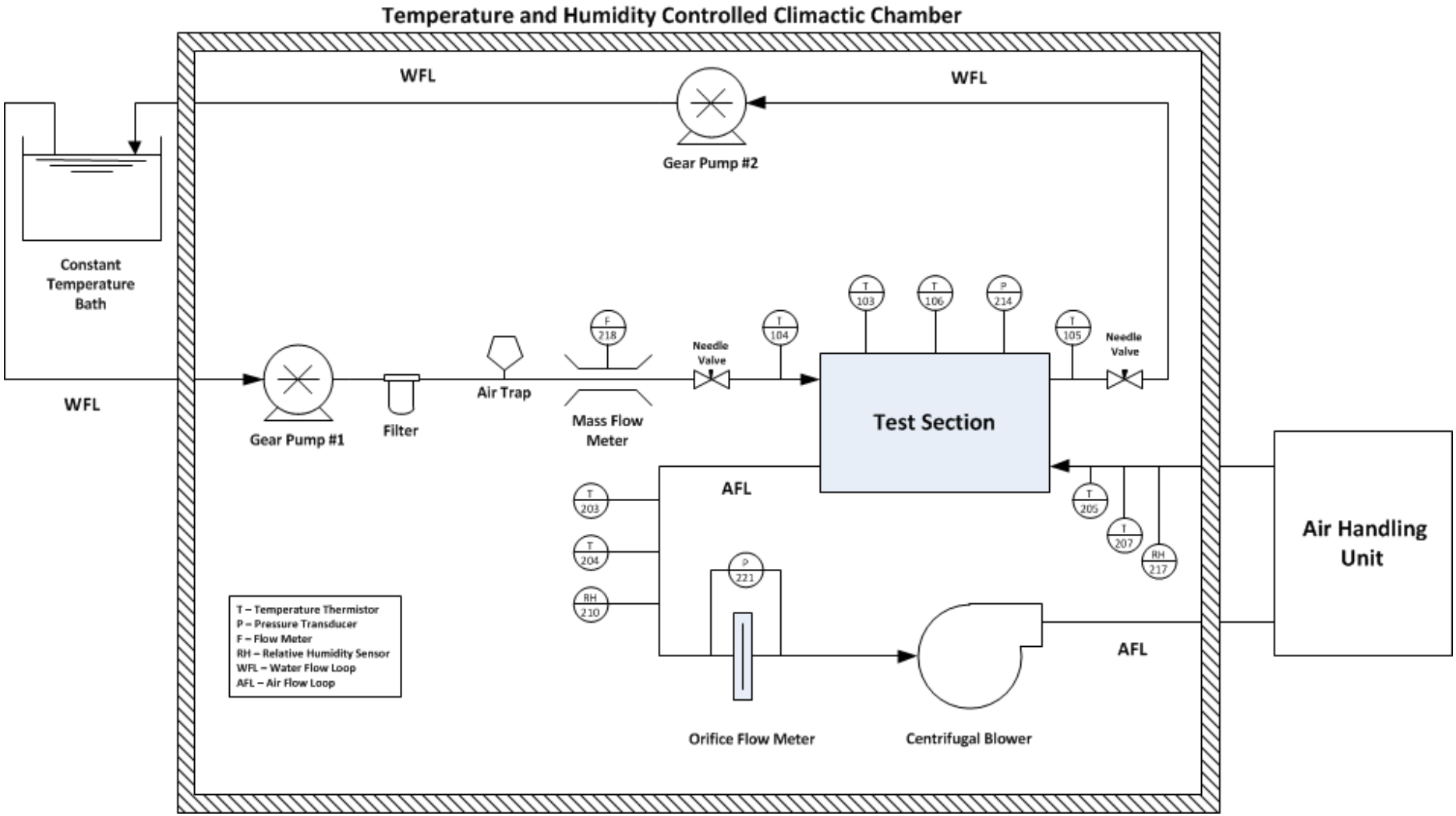

Figure 3-1 General Schematic of the Experimental Facility

3.2 Test Section

The purpose of the test section is to create an environment where simultaneous heat and mass transfer occur through a wire mesh membrane. The interface created by the wire mesh separates flowing streams of liquid water and air. This arrangement is accomplished by constructing a narrow rectangular air duct with a rectangular area on the inside of the duct where the wire mesh material separates the liquid water from the air passing through the duct. This design can be likened to a flat plate heat exchanger with only a single plate. The test section consists of two main features. The first is the plate apparatus, which is responsible for the water-side of the heat exchanger. The plate apparatus is constructed from two machined polymer plates that when bolted together form a cavity for water to flow through as it passes across the surface of wire mesh membrane. The second component is the rectangular air duct which is responsible for the air-side of the heat exchanger. The plate apparatus is inserted into the test section to create the top boundary of the air duct. The air duct is constructed from an existing rectangular wind tunnel. For the remainder of this section, the plate apparatus and air duct are examined in greater detail. Figure 3-2 and Figure 3-3 illustrate cross sectional views of the test section viewed from the side and the front. These Figures also identify the key features of the test section.

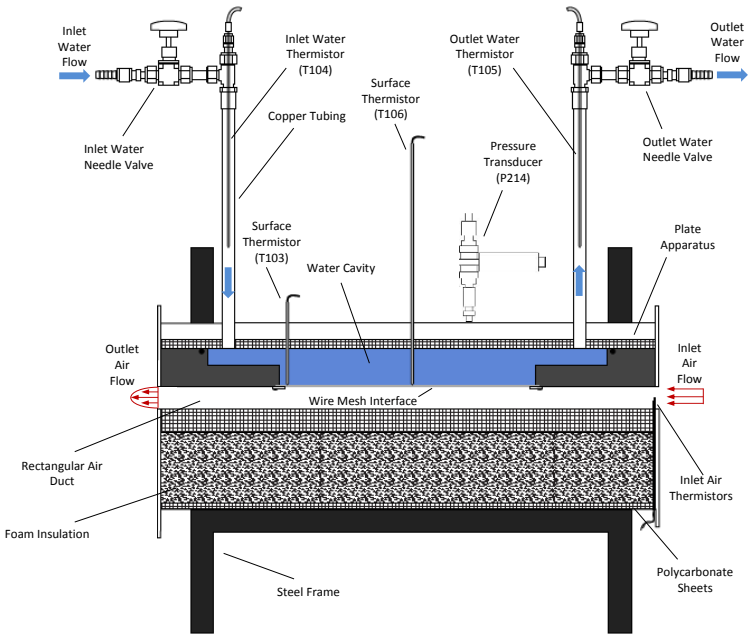

Figure 3-2 Cross Sectional View of the Test Section from Side

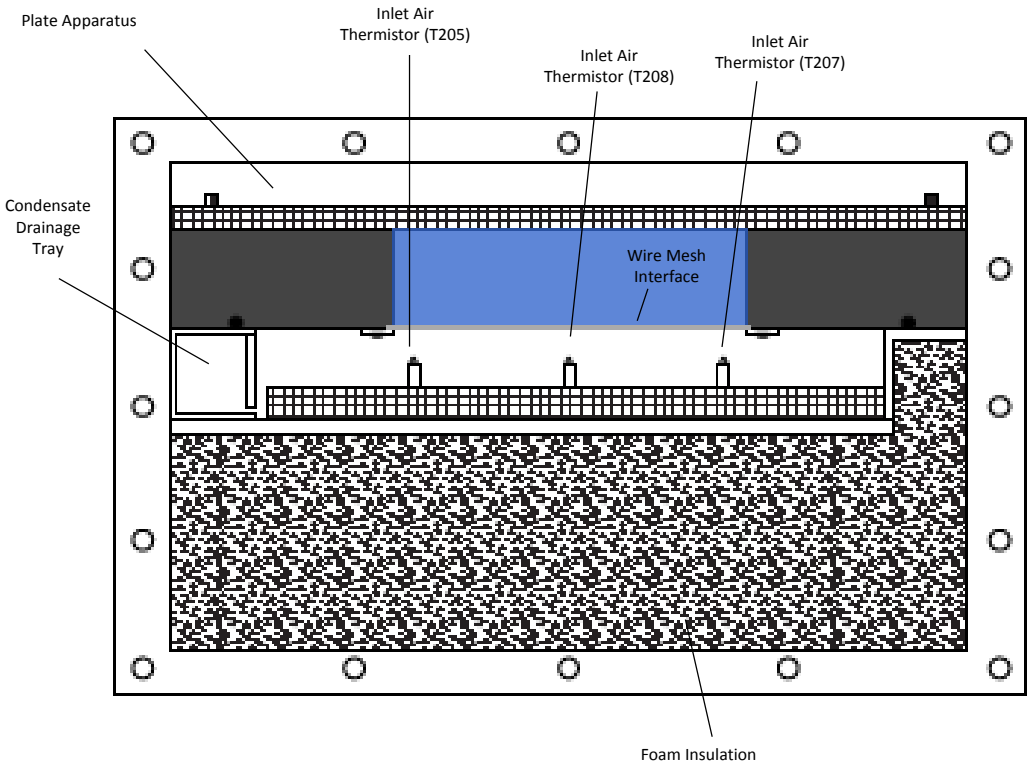

Figure 3-3 Cross Sectional View of the Test Section from Front

Figure 3-2 and Figure 3-3 depict the flow of the water and air through the test section and show the location of the air, water and surface thermistors. In Figure 3-2 surface thermistor T103 is pictured, however the data from this thermistor is not used in the data analysis because the thermistor was found to be out of calibration. Similarly, thermistor T208 in Figure 3-3 was out of calibration and its data was not used. Therefore, these thermistors can be disregarded.

3.2.1 Plate Apparatus

The plate apparatus is an assembly of two rectangular plates which are bolted together to form a cavity through which water can flow. The assembly of the two plates also has a rectangular opening where the experimental plate is attached. Figure 3-4 shows an exploded assembly drawing of the plate apparatus.

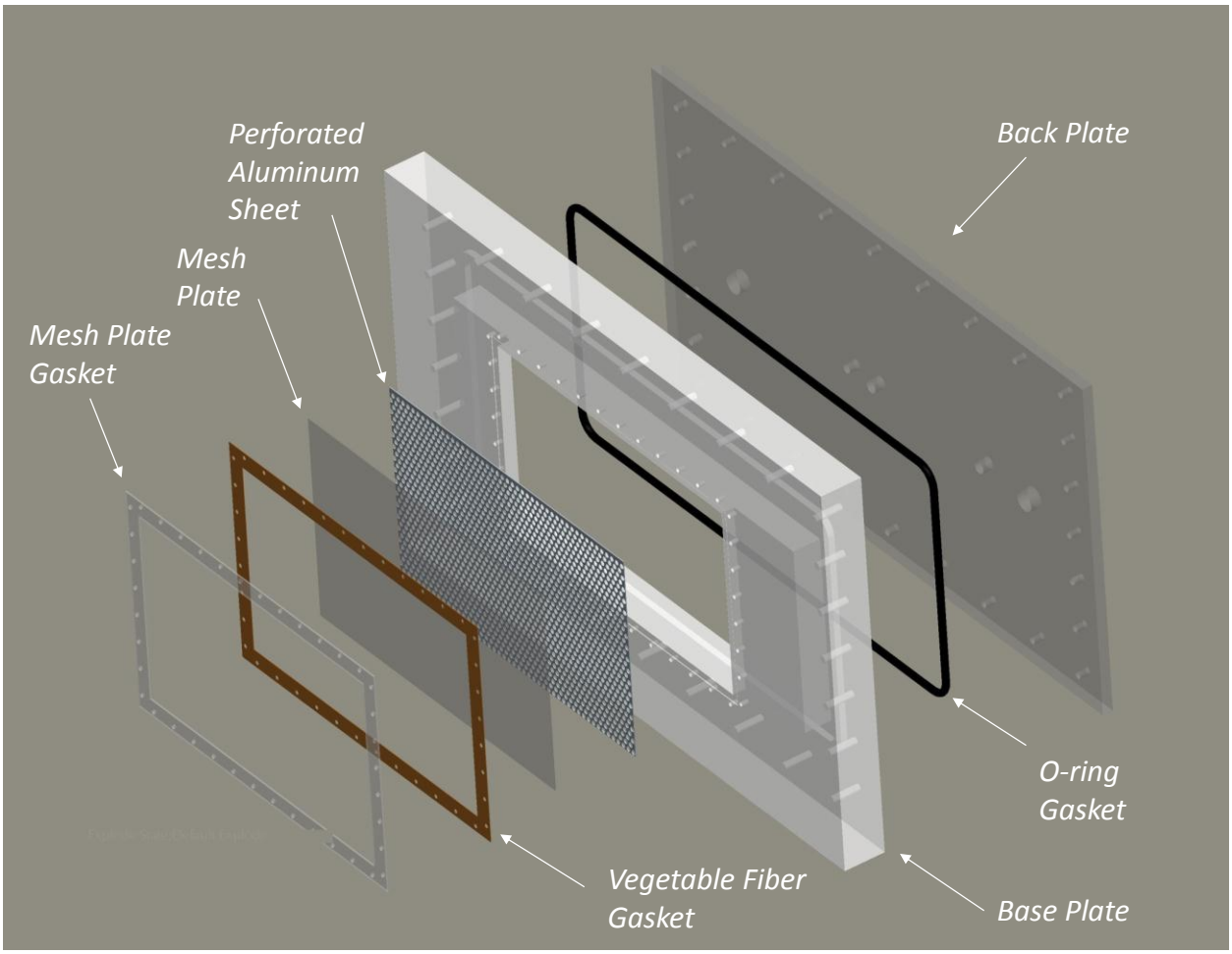

Figure 3-4 Exploded Assembly of the Plate Apparatus

The base plate is the main feature of the plate apparatus. The base plate is fabricated from a rectangular block of polypropylene which is approximately $22'' \times 14'' \times 1.5''$. A large rectangular cavity is machined into the back surface of the plate with a depth of $1''$. A gland is machined around the rectangular cavity to house an o-ring gasket fashioned from $0.25''$ diameter rubber cord stock. Surrounding the o-ring gland are a pattern of 28 bolt holes which are tapped to accept $\frac{1}{4}'' - 20$ socket cap screws. On the front surface of the base plate a rectangular area is removed to create an opening through the entire plate. This opening is where the mesh plate membrane is mounted. The wire mesh interface separates the water that flows through the plate from the air flowing on the outside of the plate. This opening has the same width of the cavity machined into the back surface but its length is less than that of the cavity. This prevents the inlet water flow from impinging directly on the mesh plate surface. Around the opening where

the mesh plate is mounted a 0.032" deep section is removed from around the opening to allow a perforated sheet to be placed in the same plane as the base plate surface. A bolt hole pattern is constructed around the opening in the front surface consisting of 40 holes which are tapped to receive $6-32\times\frac{3}{8}''$ machine screws. A transparent polycarbonate gasket is attached to the surface of the base plate using the bolts and the mesh is secured between the gasket and the base plate surface creating the interface where heat and mass transfer take place. Appendix B contains detailed part drawings of the base plate.

A second plate fabricated from polycarbonate is designed to attach to the back surface of the base plate. The back plate has approximately the same dimensions as the base plate except its thickness is $0.375''$. When the back plate is bolted to the base plate a water tight boundary is created by the o-ring gasket. There are five tapped holes along the centerline of the back plate. There are two ½" NPT holes which serve as the inlet and outlet ports for the water. There are also two $\frac{1}{4}''$ NPT holes which are used to house the thermistors which measure the surface temperature of the mesh plate. There is also one $\frac{1}{8}$" NPT hole where the apparatus pressure transducer is attached. Appendix B contains a detailed part drawing of the back plate with the dimensions of the five NPT holes.

The gasket used to attach the mesh plate to the surface of the base plate is machined from a $0.063''$ thick transparent polycarbonate sheet. The mesh plate gasket is bolted to the surface of the base plate using the 6-32 machine screws. There are several items placed between the mesh plate gasket and the surface of the base plate which should be mentioned. A $\frac{1}{64}''$ thick piece of vegetable fiber board is cut to the exact dimensions of the mesh plate gasket and placed between the mesh plate gasket and the base plate. The vegetable fiber gasket helps to create a watertight seal between the mesh and the plate apparatus. The mesh plate is then secured between the vegetable fiber gasket and the base plate. Lastly, a perforated sheet of aluminum which is $0.032''$ thick is placed between the mesh plate and the base plate. The perforated sheet has $0.1875''$ diameter holes which are in a staggered pattern and where the center axes of the circles are $0.25''$ apart from one another. The perforated sheet provides a rigid support for the mesh plate so that its surface does not deform during testing. A thin bead of silicone sealant is used to ensure that there are no gaps between the mesh plate and base plate. Figure 3-5 shows images

of the front and back surface of the plate apparatus when it is fully assembled. It should be noted that two black lines that appear on the front surface of the apparatus are gaskets which were added to ensure that the plate apparatus creates an air tight seal when installed into the air duct.

Figure 3-5 Image of Front and Back Surface of Plate Apparatus

3.2.2 Air Duct

The plate apparatus is installed into a wind tunnel to form a narrow air duct. The wind tunnel's original cross sectional area was $8'' \times 14''$. The wind tunnel is modified by inserting polycarbonate sheets and foam insulation to reduce the cross sectional area of the duct inlet to approximately $0.8'' \times 10.7''$. Figure 3-6 and Figure 3-7 illustrate the dimensions of the air duct and the locations of the air and water thermistors.

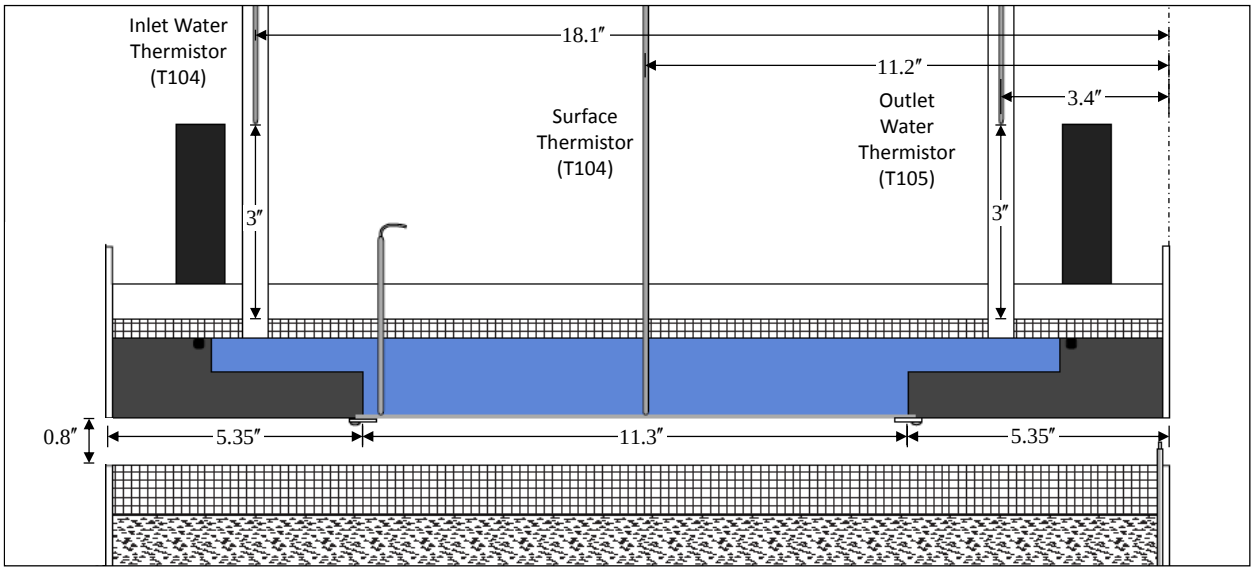

Figure 3-6 Dimensions of the Air Duct Length and Thermistor Locations

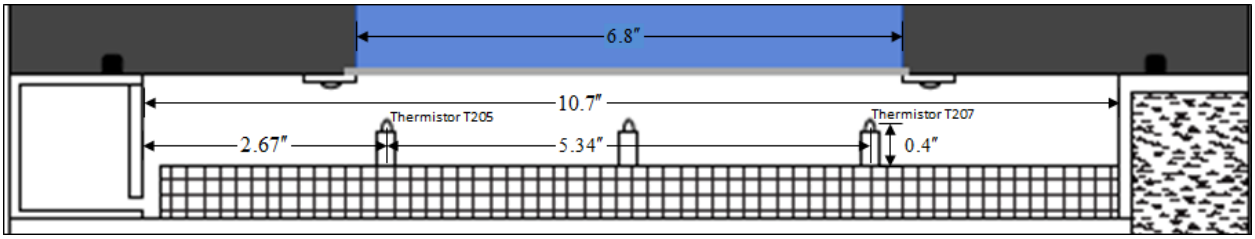

Figure 3-7 Dimensions of the Air Duct Width and Thermistor Locations

The air duct cross section is decreased in order to reduce the mass flow rate of air which in turn generates larger changes in the temperature and humidity of the air as it passes through the test section. Modifications were also made to the left side of the air duct to form a drainage system. This was accomplished by fabricating a tray from sheet metal and installing it on one side of the air duct. The drainage system was designed to remove condensate from the wind tunnel if it was inclined at an angle. It was orginally intended that the air duct be inclined to several different angles and data be taken so that it could be compared to the data from the horizontal orientation. However, the wire mesh was not able to maintain a seal when moved to an inclined position. Thus, this set of experiments was abandon but the drainage system was kept in the duct for the horizontal experiments. The condensate drainage tray is also depicted in Figure 3-3. At the end of the wind tunnel a transition connects the rectangular shape of the wind tunnel to a circular section of 6″ diameter PVC duct.

3.3 Water Flow Loop

The water flow loop delivers distilled water to the test section at a specific temperature and mass flow rate. The components of the water flow loop are connected by $\frac{3}{8}''$ diameter Tygon tubing which is adequately insulated. The water flow loop and its components are depicted in the schematic diagram of Figure 3-1.

The constant temperature bath is used in the water flow loop to maintain the temperature of the water entering the test section at a specified value. The temperature bath used in this facility is chosen for its stability and high cooling capacity. The bath is able to supply approximately 700 Watts of cooling at an operating temperature of around 10°C and the stability of the bath is ±0.01°C. The temperature range of the bath is between -30°C to 200°C and the reservoir of the bath is 13L (3.3 gal). The temperature of the bath is manipulated using an advanced digital controller. The bath is equipped with a circulating pump which has a pumping capacity of 15 L/min (250 g/s) at 0 psig. The bath's circulating pump is run during testing but does not regulate the flow rate supplied to the test section. This responsibility is placed on the gear pumps.

There are two positive displacement gear pumps utilized in the water flow loop. Gear pump #1 is located before the inlet of the test section and its speed is varied to control the mass flow rate of water supplied to the test section. Gear pump #2 is located after the test section and its primary function is to maintain a negative pressure inside the plate apparatus. The negative pressure is necessary to keep the mesh plate membrane from leaking water into the duct. It is important to keep the mass flow rate from fluctuating excessively because the mass flow rate of water measurement is used in the calculation the average convective heat and mass transfer coefficient. The positive displacement pumps working in tandem are able maintain the inlet mass flow rate of water within about ±1 $\frac{g}{s}$. The pressure inside the plate apparatus must be maintained within a narrow pressure range (0.1 - 0.2 psig) when testing a mesh plate membrane. If the pressure in the plate apparatus is too high, water will leak into the air duct through the mesh surface and conversely if the pressure is too low then air will leak into the water loop through the mesh surface. Each pump is driven by a magnetically coupled DC motor and the speed of the motor is adjusted by a DC controller.

The air trap removes any entrained air from the water flow loop before it enters the mass flow meter and test section. The air trap is constructed from copper tubing and an air release valve. The air trap operates by slowing the flow of water enough to allow the air to separate and escape through a one way valve which only allows air to pass through.

A filter is placed in the flow loop to mitigate contaminants in the water delivered to the test section. The filter is located between the air trap and gear pump #1. The filter is made from spun polypropylene and has a rating of 5 microns. The filter is cylindrical with an outer diameter of 2.375″ and a height of 4.875″. The filter is installed into a compact 5″ inch housing.

There are two needle valves in the water flow loop. Their purpose is to allow for fine tune adjustments to control the mass flow rate and pressure of the water in the test section. The valves are located at the inlet and outlet ports of the test section.

A list of all the components documenting their manufacturer and their model number is shown in Table 3-1. In Figure 3-8 the water flow loop components are depicted in a compilation of images from the facility. The white arrows are used to indicate the direction of the water flow.

Table 3-1 Water Flow Loop Components

Item	Description
Constant Temperature Bath	*Cole-Parmer* Polystat R13L Circulating Bath
Gear Pump #1	*Tuthill* Control-Mate TXCM series Magnet Drive Gear Pump
Gear Pump #1 Motor	*Scott Motors* (Unknown)
Gear Pump #1 DC Controller	*Dart Controls* Model 253G-200 DC Motor Speed Control
Filter Housing	*Pentek* #5 Opaque Slim Line Filter Housing
Filter	*Pentek* P5-478 Spun Polypropylene Filter Cartridge
Air Trap Release Valve	*MAID - O'- MIST* No. 71 Auto-Vent Automatic Air Elimanting Valve
Needle Valves	*Swagelok* SS Integral Bonnet Needle Valve
Gear Pump #2	*Liquflo* Model 35R Rotogear sealed pump 3-Series
Gear Pump #2 Motor	*BALDOR* CDP3330 General Purpose DC Motor
Gear Pump #2 Controller	*KB* Penta Power Multi-Drive DC Motor Speed Controller

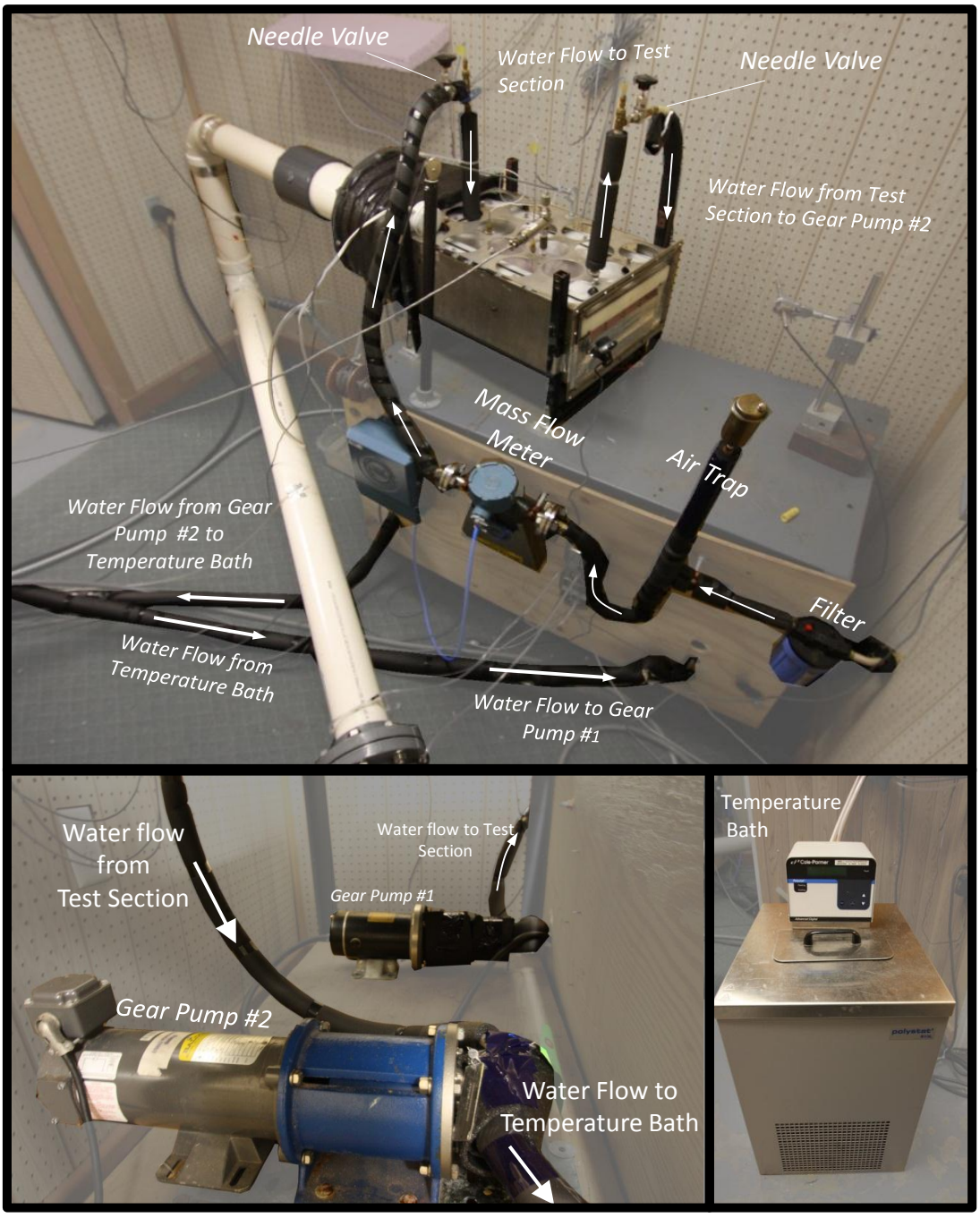

Figure 3-8 Image Compilation of Water Flow Loop Components

3.4 Air Flow Loop

The air flow loop supplies air to the test section at a specific temperature and humidity. The treated air is delivered to the climactic chamber by the chamber's air handling unit. The air is then drawn through the test section and into a transition where it is forced into a circular duct. The duct is constructed from schedule 40 PVC pipe with a 4″ inch inner diameter. The material of the pipe is Coextruded Poly Vinyl Chloride (PVC) with a cellular core. Downstream of the test section the pipe has two 90° bends. Between the two bends the air is assumed to be well mixed and the temperature and humidity is measured. After the 90° bends, the air enters a long straight section of pipe where it passes through two flow straighteners and is assumed to reach fully developed conditions. The air then passes through an orifice plate where the pressure drop is measured and then exits after passing through the centrifugal blower. After the air exits the blower it is directed to the return duct in the climactic chamber and travels back to the air handling unit. Figure 3-9 displays a schematic of the air flow loop components found within the climactic chamber.

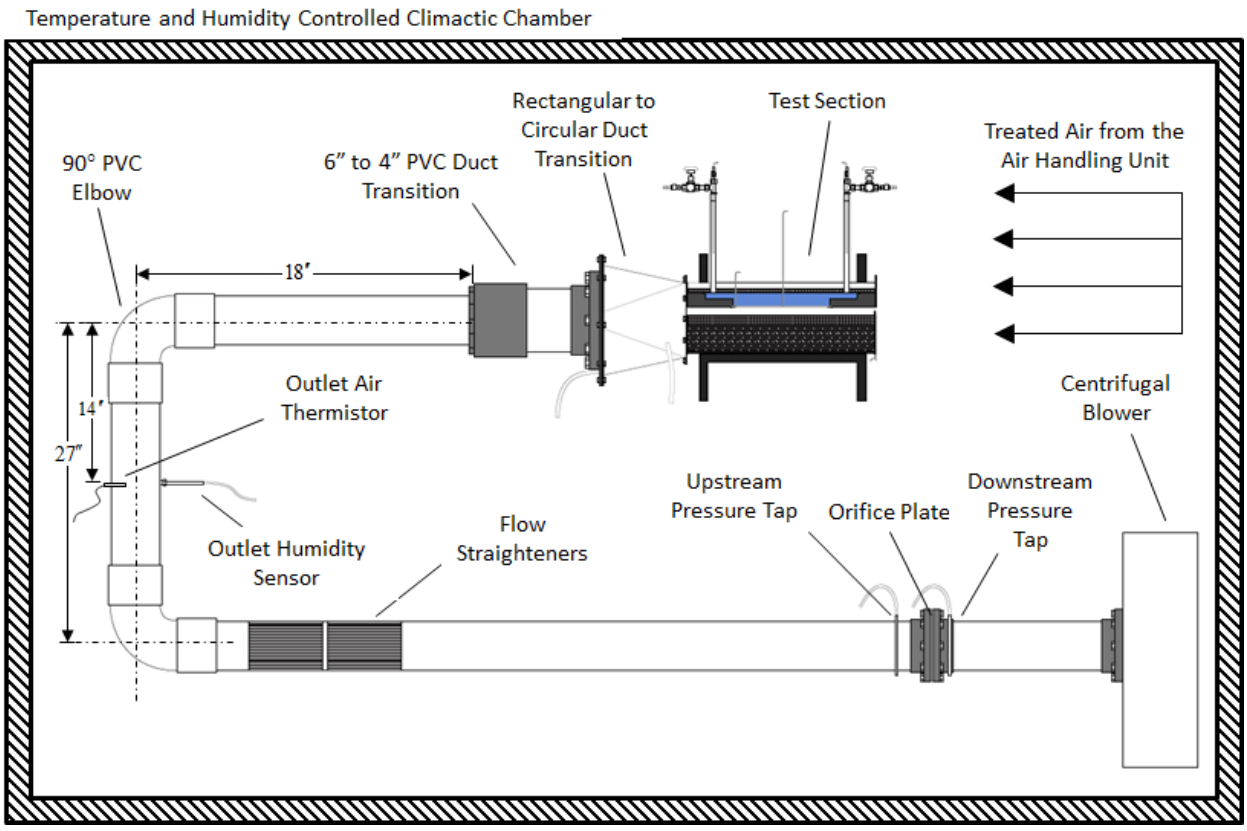

Figure 3-9 Schematic of Air Flow Loop Components

All the components of the facility exist within the climactic chamber except for the constant temperature bath, the DC gear pump controllers and the data acquisition equipment. The climactic chamber is designed to simulate a wide range of air temperature and humidity. During the condensation tests, the chamber reaches an air temperature of about 47°C and approximately 78 % relative humidity. For the evaporation tests, the steam injector is disabled and a desiccant wheel de-humidifier is used to reduce the relative humidity to less than 10% at about 35°C.

At the entrance to the long straight section containing the orifice plate, a pair of non-concentric honey comb matrix flow straightens are inserted into the duct to make the air flow uniform. In (Sprenkle 1945, 345-360) it is reported that for the given flow situation the flow straighteners should be 6 duct diameters upstream of the orifice face and the total length of the straight section should be 10 diameters. As shown in Figure 3-10, the dimensions of the key features in the straight section of duct are given in duct diameters. The distance to the flow straighteners and the length of the straight section are about 2 times greater than the specifications given in (Sprenkle 1945, 345-360). Therefore it is reasonable to assume the air flow reaches fully developed conditions before reaching the orifice plate.

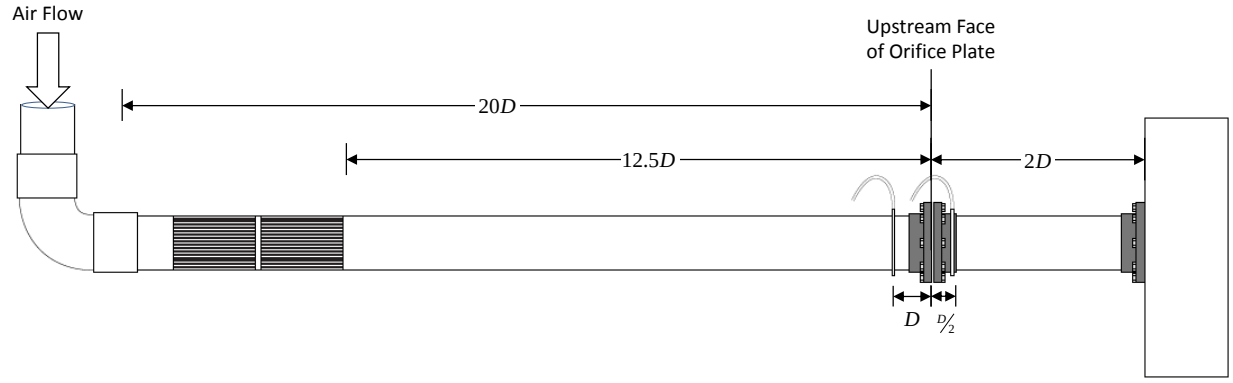

Figure 3-10 Dimensions for the Section of PVC Duct with Orifice Plate

The orifice plate is used in the air flow loop to generate a measurable pressure drop from which the mass flow rate of air can be calculated. The orifice plate is made from 316 stainless steel with a thickness of $\frac{1}{8}''$. The diameter of orifice is $2.1665''$ which gives a diameter ratio (β) of 0.542. The dimensions of the orifice plate are in compliance with the specifications outlined in (ASME 2004). The orifice plate is mounted between two class 150 PVC flanges. A small diameter cord stock is used to create o-ring gaskets to form an airtight seal plate between the orifice plate and the flanges.

The centrifugal blower creates the pressure difference which is required to draw the air through the air flow loop. The blower used in the air flow loop is chosen for its ability to handle the high pressure drop induced by the test section, the PVC duct, and the orifice plate. It is also chosen for its ability to control the mass flow rate of the air with precision. The blower is powered by a 5 h.p. motor which operates on 3-phase power. A variable frequency drive is used to control the current delivered to the motor which in turn allows the blower speed to be regulated with precision. Table 3-2 gives the make and model of the components in the air flow loop. In Figure 3-11 an image of the air flow loop is presented and illustrates the flow of air through each component.

Table 3-2 Air Flow Loop Components

Item	Description
PVC duct	*JM Eagle* 4"IPS SCH40 Series Coextruded Cellular Core PVC DWV PIPE ASTM F891-07
PVC Elbows	*UPC* ASTM D2665 90° PVC Elbow
Orifice Plate	*Imperial Flange and Fitting* PT-10 Series Paddle Type Orifice Plate
PVC Flanges	*LASCO* Class 150 SCH80 CPVC Flange
Centrifugal Blower	*Peerless Electric* Model PW-14 Radial Blade Blower
Centrfugal Blower Motor	*BALDOR* M3613T General Purpose AC Motor
Variable Frequency Drive	*Magnetek* GPD 506 Variable Frequency Drive

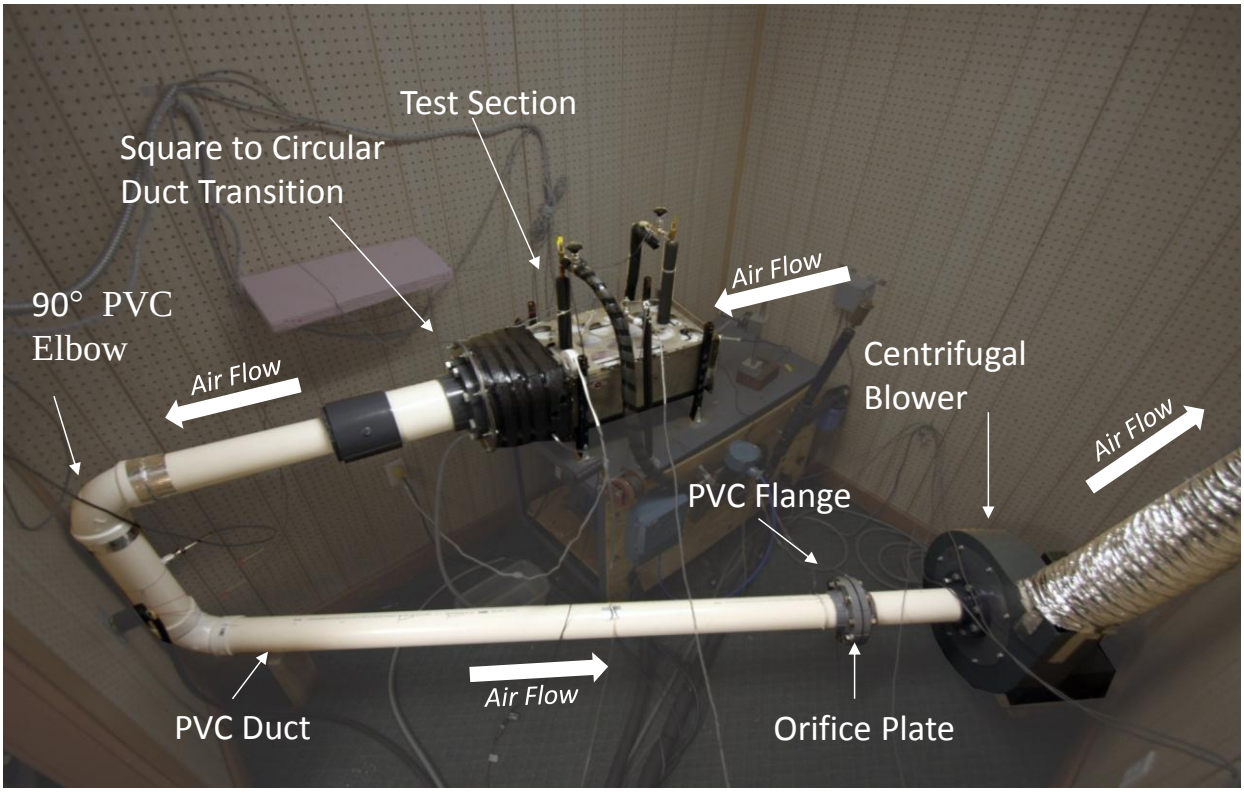

Figure 3-11 Image of Air Flow Loop Components

3.5 Instrumentation

This section identifies the measurement instrumentation used to collect data from the experimental facility. Information regarding the instrument's location, calibration and uncertainty is given for each device.

3.5.1 Data Acquisition Unit

The Data Acquisition Unit (DAQ) collects electrical signals from the measurement instrumentation and records them to an output file. The DAQ used in this experimental facility is an Agilent 34970A and is connected to the measurement instrumentation through two 20-Channel Multiplixer cards. A three digit number is associated with each measurement device which specifies the card and channel to which it is attached. The first digit indicates whether it is in card #1 or card #2. The next two digits indicate the channel number. For example thermistor T104 is found in card #1 channel 4. The DAQ communicates with a PC via the National Instruments software program named LabVIEW 8.5. LabVIEW employs the use of virtual instruments (VI) to manage the raw data signals and converts them into accurate measurements. The VI displays the measurement data graphically in real-time and also records them to a coma separated values file (.csv) at the will of the user. During a test, samples are collected from the measurement instrumentation at 10 second intervals for a time period of 10-15 minutes. This produces anywhere between 100-150 samples per data point. The resolution of the raw signal measurements is 6.5 digits. This is achieved by taking 10 power line cycles per sample measurement to increase the integration time and noise rejection. The accuracy specifications for the DAQ differ depending on the type of signal that is being measured. Table 3-3 lists the DAQ accuracy for the different type of measurements collected from the experimental facility.

Table 3-3 Accuracy of the DAQ for the Measurement Instrumentation

Instrument	Function	Time	Range	Accuracy (% of Reading + % of Range)
Humidity Sensors	DC Voltage	90 days	10 V	0.002 ± 0.0005
Plate Pressure Transducer	DC Voltage	1 year	10 V	0.0035 + 0.0005
Thermistors	Resistance	1 year	100 kΩ	0.008 + 0.001
Orifice Pressure Transducer	DC Current	1 year	100 mA	0.05 + 0.005

3.5.2 Water Instrumentation

The water instrumentation consists of three thermistors, a flow meter and a differential pressure transducer. The thermistors are used to measure the temperature of the water at specific locations. The flow meter measures the mass flow rate of water before it enters the test section and the pressure transducer measures the pressure inside the plate apparatus.

3.5.2.1 Water Thermistors

The water thermistors are manufactured by Omega and read around 30kΩ at room temperature (22°C). The thermistors are 12″ in length and their locations relative to the leading edge of the test section are shown in Figure 3-6. Thermistor T104 measures the inlet water temperature to the test section and thermistor T105 measures the outlet water temperature. Thermistor T106 measures the temperature at the interfacial boundary between the air and water at the plate surface. As shown in Figure 3-6, thermistor T106 extends through the water side of the plate apparatus until it touches the plate surface. Although thermistor T106 is listed with the water thermistors, it is assumed that it measures the surface temperature of the boundary between the air and water and not only the water temperature. In Figure 3-6 an additional surface thermistor is shown (T103). This thermistor was found to be out of calibration after performing the experiments in this work and therefore the data collected from it is not used. The thermistors are calibrated using a Fluke 7321 Calibration Temperature Bath with an accuracy of ±0.01°C. Using the temperature bath, the thermistors are calibrated over a temperature range of 5-25°C using 1°C increments. Once the temperature bath reaches steady state at a given temperature increment, 120 samples of the thermistor's resistance are collected over a time period of 10 minutes. The 120 samples of resistance are then averaged for each temperature increment. Thus, for each temperature increment between 5°C and 25°C there is a corresponding measure of the thermistor's electrical resistance $\left(R_x\right)$. Using the Steinhart-Hart Equation (Steinhart and Hart 1968, 497-503), shown in Equation (3.1), the temperature measured by the thermistor can be expressed as a function of the resistance. A 3rd order polynomial regression is carried out to solve for the unknown coefficients *a*, *b*, *c* and *d*.

$$\frac{1}{T} = a + b\ln(R_x) + c\ln(R_x)^2 + d\ln(R_x)^3 \tag{3.1}$$

Once the regression coefficients have been determined for each thermistor, Equation (3.1) is rearranged to express the temperature measured by the thermistor as a function of resistance.

$$T(R_x) = \frac{1}{\left(a + b\ln(R_x) + c\ln(R_x)^2 + d\ln(R_x)^3\right)} \tag{3.2}$$

Equation (3.2) gives the thermistor temperature in degrees Kelvin as a function of its resistance read in Ohms. The coefficients are determined for each of the water thermistors and are displayed in Table 3-4.

Table 3-4 Regression Coefficients for Water Thermistors

	Water Thermistors		
Coefficients	**T104**	**T105**	**T106**
a	2.119E-03	2.109E-03	2.072E-03
b	-1.134E-04	-1.093E-04	-9.176E-05
c	3.152E-05	3.095E-05	2.879E-05
d	-8.640E-07	-8.378E-07	-7.593E-07

There are three sources of uncertainty in the water thermistors. The total uncertainty for the water thermistors is a combination of the uncertainty in the constant temperature bath, the calibration curve-fit, and the DAQ. The temperature bath's accuracy (u_{TB}) is reported by the manufacturer to be ±0.01°C. The DAQ's accuracy specifications are listed in Table 3-3. The accuracy specification of the DAQ (u_{DAQ}) includes measurement error, switching error and transducer conversion error. The curve-fit uncertainty (u_{CF}) is determined by multiplying the t-estimator (t_{est}) and the standard deviation (S_x) obtained from the calibration regression statistics. The t-estimator is a function of the degrees of freedom and the probability. For the water thermistors the degrees of freedom is 19 and the probability is selected at 95%. Thermistor T104 possesses the highest curve-fit uncertainty among the three water thermistors and is therefore chosen to represent (u_{CF}) for all three water thermistors. The derivative of the thermistor temperature as a function of resistance is evaluated where it is at its largest magnitude in order to determine the highest value of uncertainty generated by the DAQ. By examining the thermistor temperature as a function of resistance, given in Equation (3.2), it is apparent that it will closely resemble the function of one over the resistance $\left(\frac{1}{R}\right)$. Therefore, the slope of the function will decrease in magnitude as the resistance is increased. The thermistor temperature is

inversely proportional to the resistance and thus the highest temperature of the thermistor calibration range will always yield the highest absolute value of the derivative. This idea is further discussed for the air thermistors and illustrated graphically in Figure 3-12. For the water thermistors, the highest value for the calibration temperature is at 25°C which corresponds to a resistance of approximately 30 kΩ $\left(\frac{dT}{dR}\Big|_{R=30k\Omega}\right)$. Thermistor T105 is chosen to represent the uncertainty in the water thermistors because it gives the highest absolute value of the derivative at 30 kΩ for all three thermistors. The propagation of error method is used to calculate the uncertainty in the water thermistors. Equation (3.3) shows the calculation of the uncertainty in the water thermistors using the propagation of error method develop from (Figliola and Beasley 2006).

$$u_{TB} = \pm 0.01°C$$

$$u_{DAQ} = \pm\left[(0.00008)(30k\Omega) + (0.00001)(100k\Omega)\right] = \pm 3.4\Omega$$

$$\left.\frac{dT}{dR_x}\right|_{R_x=30k\Omega} = -0.000776\frac{°C}{\Omega}$$

$$u_{CF} = \pm t_{est} S_x = \pm(2.093)(0.000000629°C) = \pm 1.83\times10^{-7}°C$$

$$uT_w = \pm\sqrt{{u_{TB}}^2 + {u_{CF}}^2 + \left(\left.\frac{dT}{dR_x}\right|_{R_x=10k\Omega} u_{DAQ}\right)^2} = \pm 0.0103°C \approx \pm 0.01°C \qquad (3.3)$$

From Equation (3.3) it is apparent that the dominant uncertainty in the water thermistors comes from the inaccuracy of the temperature bath. The uncertainty contribution from the DAQ and the curve fit are practically negligible. The uncertainty presented in Equation (3.3) is used for both the inlet and outlet water thermistors temperatures (T104 & T105). However, the surface temperature thermistor (T106) will most likely have a higher value for the uncertainty then what is calculated in Equation (3.3). This is because it is difficult to know if the surface temperature thermistor is positioned in the location to measure the exact temperature of the air – water interface. Therefore, the uncertainty of the surface thermistor temperature is increased to ±1°C in order to give a more realistic value for the surface temperature uncertainty.

$$uT_s = \pm 1°C \qquad (3.4)$$

3.5.2.2 Water Mass Flow Meter

The mass flow meter operates by detecting the frequency of vibration generated in a curved tube. This type of mass flow meter is known as a coriolis flow meter. A transmitter is used to send the frequency signals to the DAQ. The frequency signal is converted into a mass flow rate by dividing the signal frequency value by 100. The mass flow rate of water in grams per second $\left(\frac{g}{s}\right)$ is given as a function of the frequency $\left(f_v\right)$ in Hertz shown in the following equation.

$$\dot{m}_w(f_v) = \frac{f_v}{100} \tag{3.5}$$

The mass flow meter used in the facility is manufactured by Mirco Motion. The mass flow meter is located before the inlet to the test section. Figure 3-8 shows the mass flow meter in experimental facility. Before the water enters the flow meter it passes through an air trap to ensure that the presence of air in the flow stream is minimized. The flow accuracy plus zero stability is listed by the manufacturer as ±0.2% of rate ± 0.0667 $\frac{g}{s}$. The accuracy of the DAQ is assumed to be negligible. Therefore, the accuracy specifications listed by the manufacturer are used to calculate the uncertainty in the mass flow rate of water. The rate for the data collected in this work is around $50\frac{g}{s}$. Equation (3.6) shows the calculation of the uncertainty in the water mass flow rate measurement.

$$u_{\dot{m}_w} = \pm\left[(0.002)\left(50\frac{g}{s}\right) + 0.06667\frac{g}{s}\right] = \pm 0.167\frac{g}{s} \tag{3.6}$$

3.5.2.3 Plate Apparatus Pressure Transducer

The plate apparatus pressure transducer measures the differential pressure between the chamber atmosphere and the internal pressure of the plate apparatus. This pressure difference is also referred to as the bubble point pressure. The pressure transducer used in the facility is a Sensotec Model FDW/G081-04 differential pressure transducer. The device is supplied 24 Volts from an external power supply and outputs a voltage signal of 0-5 V. The range of the transducer is 0-15 psi. The pressure transducer is mounted directly to the plate apparatus of test section between the inlet and outlet water ports (see Figure 3-2). The transducer is attached to

the plate apparatus with a $\frac{1}{8}''$ NPT fitting. The transducer is calibrated using a dead weight tester. The transducer is calibrated from 0-15 psi using 1 psi increments. At each pressure increment 100 readings of the output voltage are collected and averaged. Using the measured voltages and corresponding pressures, a 3rd order polynomial regression is created to express the pressure as a function of the output voltage. Equation (3.7) shows the calibration equation with regression coefficients used to convert the voltage signals (V_0) from the DAQ into useful pressure measurements.

$$P(V_0) = 0.014798 + 3.011726 \cdot V_0 - 0.008726 \cdot V_0^2 + 0.000970 \cdot V_0^3 \tag{3.7}$$

The pressure measurements are in units of pounds per square inch (psi). The sources of uncertainty in the pressure transducer are derived from the manufacturer's listed accuracy, the calibration curve fit error, and the accuracy of the DAQ. The manufacturer reports an accuracy of 0.25% of the full scale output. The uncertainty of the transducer according to the manufacturer's specifications (u_{man}) is therefore about ±0.0375 psi. The uncertainty from the DAQ (u_{DAQ}) is shown in Table 3-3. The voltage reading which is used to calculate the DAQ accuracy is 0.075 Volts. This value corresponds to the normal operating range of the transducer during testing. The derivative of the pressure with respect to voltage is also determined at 0.075 volts $\left(\frac{dP}{dV_0}\Big|_{V_0=0.075V}\right)$. The uncertainty from the 3rd order curve fit (u_{CF}) is calculated by multiplying the t-estimator based on a 95 % confidence interval with 14 degrees of freedom and the standard deviation (S_x) obtained from the calibration regression statistics. Using the propagation of error the total uncertainty of the pressure transducer (u_{PT}) is evaluated in Equation(3.8).

$$u_{man} = \pm 0.0375\, psi$$
$$u_{DAQ} = \pm\left[(0.000035)(0.075V) + (0.000005)(5V)\right] = \pm 0.00003V$$
$$\frac{dP}{dV_0}\Big|_{V_0=0.075V} = 3.01\,\frac{psi}{V}$$
$$u_{CF} = \pm t_{est} S_x = \pm(2.145)(0.0011 psi) = \pm 0.0024\, psi$$
$$u_{pt} = \pm\sqrt{u_{man}{}^2 + u_{CF}{}^2 + \left(\frac{dP}{dV_0}\Big|_{V_0=0.075V} u_{DAQ}\right)^2} = \pm 0.03757\, psi \tag{3.8}$$

3.5.3 Air Instrumentation

The air measurement instrumentation consists of four 10 kΩ thermistor elements, a differential pressure transducer, and two relative humidity sensors. The thermistors are used to measure the air temperature at the inlet and outlet of the test section. The differential pressure transducer is used to measure the pressure drop across the orifice plate which is used to calculate the mass flow rate of air. The relative humidity sensors measure the humidity of the air at the inlet and outlet of the test section.

3.5.3.1 Air Thermistors

The air thermistors are 2.4 mm diameter epoxy coated precision thermistor elements manufactured by Omega. The thermistors were coated in an addition layer of epoxy to ensure that they were water tight during calibration in the constant temperature bath. The thermistors are sheathed in aluminum tubing and installed into the facility. The inlet air thermistors are placed at the inlet to the test section (see Figure 3-2 & Figure 3-3). The outlet air thermistors are located in the PVC duct downstream of the test section. More specifically, the outlet air thermistors and in the vertical section of pipe immediately following the first 90 elbow (see Figure 3-8). The outlet thermistors are installed through the pipe wall perpendicular to the flow stream approximately 1" from the inner pipe wall. The thermistors were calibrated in the same manner as the water thermistors using the calibration temperature bath. The calibration temperature range for the air thermistors is from 30– 50°C, using increments of 1 °C. The resistances are collected at each temperature increment in the same manner as the water thermistors. A 3rd order polynomial regression is implemented to solve for the unknown coefficients of the Steinhart-Hart equation. Table 3-5 lists the regression coefficients for each of the air thermistors.

Table 3-5 Regression Coefficients for Air Thermistors

	Air Thermistors			
Coefficients	**T203**	**T204**	**T205**	**T207**
a	6.018E-04	-2.887E-04	9.679E-04	9.377E-04
b	4.214E-04	7.369E-04	2.906E-04	3.059E-04
c	-2.218E-05	-5.934E-05	-6.616E-06	-8.904E-06
d	9.613E-07	2.418E-06	3.459E-07	4.528E-07

The method used to calculate the uncertainty in the air thermistors is identical to the method used for the water thermistors. The only significant difference lies in the value for the curve fit uncertainty $\left(u_{CF}\right)$, or more specifically, in the derivative of the temperature with respect to resistance $\left(\frac{dT}{dR_x}\right)$. The lowest resistance corresponding to the upper limit of the calibration temperature range (50°C) is about 3.6 kΩ. Thus, the derivative of the temperature with respect to resistance used to determine the uncertainty for the air thermistors is evaluated at 3.6 kΩ $\left(\left.\frac{dT}{dR_x}\right|_{R_x=3.6k\Omega}\right)$. Air Thermistor T207 gives the largest magnitude of the derivative when evaluated at 3.6 kΩ. In Figure 3-12 the air and water thermistors with the largest magnitude of the derivative (T207 & T105) are plotted on a graph which displays temperature versus the resistance. The calibration data points are shown with the respective curve fit function for each thermistor. It is obvious that the absolute value of the temperature derivative will be higher for the air thermistors because the slope of the curve fit function is much greater at the lower resistances. Figure 3-12 also illustrates that the magnitude of the temperature derivative will be greatest at the highest temperature calibration point. Thus, for the water thermistors it is apparent that at 25°C the resistance is approximately 30kΩ and for the air thermistors at 50°C the corresponding resistance is at 3.6kΩ.

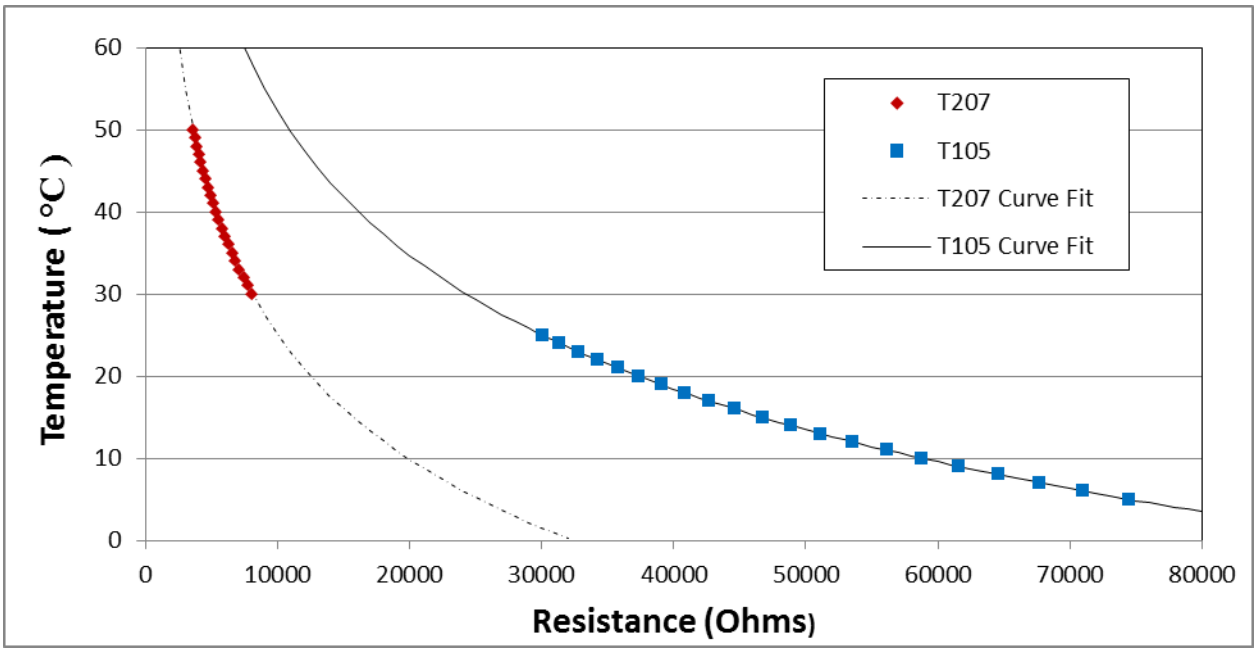

Figure 3-12 Plot of Thermistors T105 and T207

Air thermistor T204 has the highest curve fit uncertainty and is therefore used to calculate the total uncertainty for the other air thermistors. The propagation of error is used to calculate the total uncertainty in the air thermistors. Equation (3.9) shows the calculation of the total uncertainty in the air thermistors.

$$u_{TB} = \pm 0.01°C$$

$$u_{DAQ} = \pm\left[\left(0.00008\right)\left(10k\Omega\right) + \left(0.00001\right)\left(100k\Omega\right)\right] = \pm 1.8\Omega$$

$$\left.\frac{dT}{dR_x}\right|_{R_x = 3.6k\Omega} = -0.0073\frac{°C}{\Omega}$$

$$u_{CF} = \pm t_{est} S_x = \pm(2.093)(0.000000652°C) = \pm 1.37\times 10^{-7}°C$$

$$uT_a = \sqrt{{u_{TB}}^2 + {u_{CF}}^2 + \left(\left.\frac{dT}{dR_x}\right|_{R_x = 10k\Omega} u_{DAQ}\right)^2} = \pm 0.017°C \approx \pm 0.02°C \qquad (3.9)$$

The uncertainty in the air thermistors is nearly twice that of the water thermistors. This is due to the higher absolute value of the slope shown in Figure 3-12. The dominant uncertainty in the air thermistors is not from the temperature bath but comes from the temperature derivative used to calculate the uncertainty from the DAQ. The curve fit uncertainty is so small that it can be neglected.

3.5.3.2 Orifice Pressure Transducer

A differential pressure transducer measures the pressure drop across the orifice plate and is used to calculate the mass flow rate of air. The transducer used in the experimental facility is a Dwyer Model 607-8 Differential Pressure Transmitter. The device measures a range from 0 – 10 inches of water column pressure difference and is supplied with 24VDC from an external power supply. The transducer emits a 4-20 mA output signal which is sent to the DAQ and converted into a differential pressure measurement. The following equation expresses the pressure difference $\left(\Delta P\right)$ in inches of water column as a function of the current $\left(I\right)$ measured in amps.

$$\Delta P\left(I\right) = 625\left(I - 0.004\right) \qquad (3.10)$$

The transducer is located in close proximity to the orifice plate and is connected to the pressure taps with small diameter Tygon tubing. The manufacturer reports that the transducer accuracy is

±0.5% of the full scale output. The total uncertainty in the pressure transducer is derived from this reported accuracy and from the accuracy specifications of the DAQ found in Table 3-3. Equation (3.11) shows the calculation of total uncertainty in the pressure transducer using propagation of error. A conversion factor of 249.09 $^{Pa}/_{"W.C.}$ is used to report the final uncertainty in units of Pascals.

$$u_{DAQ} = \left[\left(0.0005\right)\left(20mA\right) + \left(0.00005\right)\left(100mA\right)\right] = \pm 0.015mA$$

$$\frac{d\Delta p}{dI} = 0.625\frac{"W.C.}{mA}$$

$$u_{man} = \pm\left(0.005\right)\left(10"W.C.\right) = \pm 0.05"W.C.$$

$$u_{\Delta P} = \pm\sqrt{{u_{man}}^2 + \left(\frac{dp}{dI}u_{DAQ}\right)^2} = \pm 0.05087"W.C. = \pm 13Pa \tag{3.11}$$

3.5.3.3 Humidity Sensors

The humidity sensors are responsible for measuring the relative humidity at the inlet and outlet of the test section. The sensors used in the facility are Vaisala Model HMP-238 relative humidity sensors. The inlet sensor (RH217) is positioned on a stand upstream of the test section immediately before entering the air duct. The outlet sensor (RH210) is located downstream in the vertical section of PVC duct and in the same plane as the outlet air thermistors (see Figure 3-9). The sensors receive 24VDC from an external power supply and output a 0-5VDC signal to the DAQ. The output voltage signal corresponds to a 0 – 100 % RH measurement. Therefore, the relative humidity displayed as a percentage is shown as a function of voltage $\left(V_0\right)$ in Equation (3.12).

$$\phi(V_0) = 20 \cdot V_0 \tag{3.12}$$

The sensors are calibrated yearly by the manufacturer to ensure that they are accurate and precise. The manufacturer reports an accuracy $\left(u_{man}\right)$ of about ±1% RH for the humidity range the sensors experience during testing. This reported accuracy coupled with the DAQ accuracy (u_{DAQ}) is used to calculate the total uncertainty of the sensors. The propagation of error method is used to determine the total uncertainty, as shown in Equation (3.13).

$$u_{DAQ} = \left[(0.00002)(3V) + (0.000005)(10V) \right] = \pm 0.00011V$$

$$\frac{d\phi}{dV} = 20 \frac{\%RH}{V}$$

$$u_{man.} = \pm 1\%RH$$

$$u_{\phi} = \pm \sqrt{u_{man}{}^2 + \left(\left. \frac{dH}{dV} \right|_{V=3V} u_{DAQ} \right)^2} = \pm 1.000\%RH \tag{3.13}$$

3.5.4 Auxiliary Instrumentation

There are two auxiliary measurement devices that were not used in conjunction with the DAQ. The first is a barometer which is used to measure the atmospheric pressure in the chamber while collecting data. The barometer that is used is an Omega DPI 740 Precision Pressure Indicator. This model is a digital handheld device and reads the absolute pressure of the atmosphere in Pascals (Pa). The unit is kept outside of the chamber during testing and a small diameter plastic tube is attached to the device and fed into the chamber to take measurements. The uncertainty in the device is listed by the manufacturer as 0.045 % of the full scale which is approximately ±52 Pa. The second auxiliary device is a digital angle gauge which is used to ensure that the plate apparatus is level before data is collected. The digital angle gauge is manufactured by Wiley and has a resolution of 0.1°. The gauge is zeroed using a bubble level.

There is one other auxiliary measurement device that is used by the DAQ. A model PX653 differential pressure transducer manufactured by Omega is used to estimate the pressure drop from the inlet of the test section to the pressure tap upstream of the orifice plate. The auxiliary pressure transducer (P213) outputs a 1-5 Volt signal corresponding to 0-5 inches of water column pressure difference. This device is used to produce a rough estimate for the value of the pressure drop from the duct inlet to the upstream face of the orifice plate. The measurement does not need to be exact and therefore the calculation of its uncertainty can be neglected.

Chapter 4 Data Analysis

4.1 Introduction

This Chapter presents the calculations used to experimentally and theoretically determine the average convective heat and mass transfer coefficients for each of the experimental plates. In the following section, a case is presented explaining why the average air heat transfer coefficient is chosen to rate the performance of the experimental plates instead of the overall heat transfer coefficient. In the following section, the major variables measured from the experimental facility are defined and serve as the basis for the data analysis. Using the major variables, the calculations for the moist air properties and air mass flow rate are shown in the next sections. The analytical methods used to predict the average convective heat and mass transfer coefficients are presented in the following section. These theoretical predictions of the heat and mass transfer coefficients are compared with the experimental data in Chapter 5. The last three sections present an energy rate balance on a control volume which encompasses the test section. The energy rate balance allows for the amount of mass transport to be quantified and also evaluates the sensible component of the heat transfer from the air to the water. Finally, the method used to determine the average convective heat and mass transfer coefficients from the experimental data is shown.

The uncertainties within the calculations made in this chapter are estimated using the propagation of error method. The uncertainties in the measurements collected by the experimental facility propagate through the calculations made in this chapter. The uncertainties of the measurement instrumentation are presented in Section 3.5 of Chapter 3. Appendix C contains a Mathcad worksheet which displays the uncertainty for every calculation presented in this chapter.

4.2 Overall vs. Air-Side Heat Transfer Coefficient

The test section was initially modeled as a counter-flow heat exchanger and the overall heat transfer coefficient (U) was determined for each of the experimental plates. The overall heat transfer coefficient is calculated from the following equation.

$$U = \frac{q_{net}}{A\Delta T_{LM}} \tag{4.1}$$

The heat transfer term, q_{net}, represents the total heat transfer from the air to the water and is determined from the product of the mass flow rate of water, the change in water temperature and the specific heat of water.

$$q_{net} = \dot{m}_w Cp_w \Delta T_w \tag{4.2}$$

The area term, A_s, is the total area of the experimental plate. The temperature difference term, ΔT_{LM}, is known as the log mean temperature difference. The log mean temperature difference is obtained from the inlet and outlet temperatures of the air and water as they enter or exit the test section. The log mean temperature difference is shown in the following equation.

$$\Delta T_{LM} = \frac{\left(T_{a,out} - T_{w,in}\right) - \left(T_{a,in} - T_{w,out}\right)}{\ln\left(\frac{T_{a,out} - T_{w,in}}{T_{a,in} - T_{w,out}}\right)} \tag{4.3}$$

The subscripts 'a' and 'w' indicate if the temperature measurement is for the air or water and the subscripts 'in' and 'out' signify inlet or outlet flow. Using Equations (4.1) and (4.3) the overall heat transfer is easily determined for each experimental plate.

The overall heat transfer coefficient appears to be a reliable way to evaluate the heat transfer performance of the different plates. However, it turns out that the use of the log mean temperature difference is invalid for cases where there is combined heat and mass transfer accompanying a partial phase change (i.e. condensation or evaporation) (Kern 1950). A phase change creates an additional latent component of heat transfer which renders the derivation of the log mean temperature difference invalid. Figure 4-1 illustrates a differential element of width dx in a generalized air-water counter-flow heat exchanger in which there is no change of phase in either fluid. The air is at a higher temperature than the water so there will only be a sensible component of heat transfer from the air to the water.

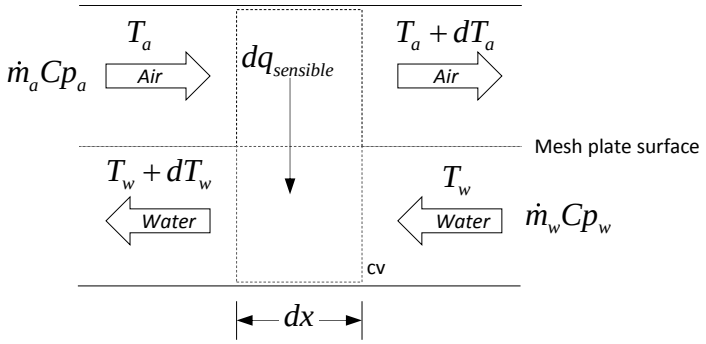

Figure 4-1 Differential Element of a Counter-Flow Heat Exchanger

The differential sensible heat transfer term, $dq_{sensible}$, can be expressed by either of the following equations.

$$dq_{sensible} = -\dot{m}_a Cp_a dT_a \tag{4.4}$$

$$dq_{sensible} = \dot{m}_w Cp_w dT_w \tag{4.5}$$

The first step when deriving the log mean temperature difference is to rearrange the equations above and substitute them into an equation which expresses the local temperature difference between the air and water in differential form.

$$\Delta T \equiv T_a - T_w$$

$$d(\Delta T) = dT_a - dT_w \tag{4.6}$$

Substituting Equation (4.4) and (4.5) into Equation (4.6) the following is obtained.

$$dT_a = -\frac{dq_{sensible}}{\dot{m}_a Cp_a}$$

$$dT_w = \frac{dq_{sensible}}{\dot{m}_w Cp_w}$$

$$d(\Delta T) = dT_a - dT_w$$

$$d(\Delta T) = -dq_{sensible}\left(\frac{1}{\dot{m}_a Cp_a} + \frac{1}{\dot{m}_w Cp_w}\right) \tag{4.7}$$

For the experiments conducted in this research there is always a phase change present in the form of condensation or evaporation. To achieve condensation the inlet air is heated and humidified. The inlet water temperature is then lowered below the dew point of the moist air and as a consequence water vapor from the air stream condenses into a liquid at the mesh plate surface. During condensation, the energy required to change the water vapor into a liquid is transferred

from the air to the water in the same direction as the sensible heat transfer. In the evaporation experiments the inlet air supplied to the test section is dehumidified until it reaches the lowest relative humidity possible. The dry air is then passed over the mesh plate surface where evaporation of the liquid water occurs through the mesh plate. The evaporation process creates a latent component of heat transfer in the opposite direction of the sensible heat transfer. As previously mentioned, the inlet air temperature is maintained above the inlet water temperature and therefore in all the experiments the sensible component of heat transfer is always from the air to the water. Figure 4-2 shows a counter flow heat exchanger where condensation or evaporation takes place creating a latent component of heat transfer $\left(dq_{latent}\right)$ in either in the same or opposite direction of the established sensible heat transfer component.

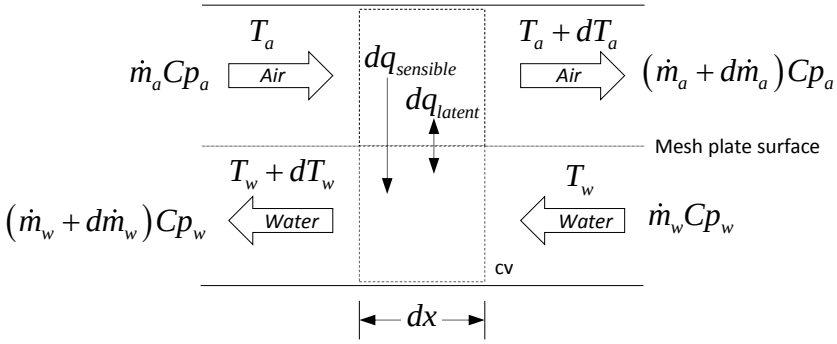

Figure 4-2 Differential Element of Counter Flow Heat Exchanger with Latent Component

The addition of the latent heat transfer term disrupts the conventional derivation of the log mean temperature difference. In particular, by adding the latent heat transfer term, the sensible component can no longer be factored out of the expression on the right hand side of Equation (4.7). Also because of the addition of latent heat transfer, the net heat rate shown in Equation (4.1) is changed to the sum of the latent and sensible components.

$$q_{net} = q_{sensible} + q_{latent} \tag{4.8}$$

Note that the latent component is assumed positive from the air to the water and therefore is added to the sensible component. However, when evaporation occurs the latent component of heat transfer is negative. Furthermore, if the latent component is larger in magnitude than the sensible component then the net heat transfer will yield a negative value. A negative value for the net heat transfer produces a negative value for the overall heat transfer coefficient and such a result is impractical. It should be noted that there is always mass transport of water that accompanies a change of phase for the experiments conducted on the mesh plates. Therefore, as

indicated in Figure 4-2, the mass flow rates of the air and water do not remain constant. This also renders Equations (4.4) and (4.5) invalid since they do not account for the change in mass.

Due to these complications, the use of the overall heat transfer coefficient as a means to quantify the performance of the experimental plates is abandoned. Instead, a simplified model employing Newton's law of cooling is used to determine the average convective air-side heat transfer coefficient for experimental plate. This is a reasonable alternative because the majority of the resistance to heat transfer in the experiments occurs in the gas phase boundary layer. Newton's law of cooling requires the knowledge of the sensible component of heat transfer, the surface area and the temperature difference between the air and surface temperature of the experimental plate. Section 4.8 explains the method used to obtain the average convective air-side heat transfer coefficients for each experimental plate. The mass transfer coefficient is calculated in a similar manner using the surface temperature measurement, the mass transport and the water vapor concentration gradient. The average mass transfer coefficient is presented in Section 4.9.

4.3 Major Variables

There are ten key variables obtained from the data collected by the experimental facility which serve as the foundation for the calculations presented in this chapter. Each of the ten variables is acquired either directly or indirectly from the measurement instrumentation of the experimental facility. The variables are listed in Table 4-1 along with a brief description and their units of measurement.

Table 4-1 Major Variables in the Data Analysis

Variable	*Description*	*Units*
$T_{w,in}$	Inlet Water Temperature	$°K$
T_s	Surface Temperature	$°K$
$T_{w,out}$	Outlet Water Temperature	$°K$
$T_{a,in}$	Inlet Air Temperature	$°K$
$T_{a,out}$	Outlet Air Temperature	$°K$
$\dot{m}_{w,in}$	Inlet Mass Flow Rate of Water	$\frac{g}{s}$
$\dot{m}_c$	Mass Flow Rate of Condensate	$\frac{g}{s}$
$\dot{m}_a$	Mass Flow Rate of Air	$\frac{kg}{s}$
ω_{in}	Inlet Humidity Ratio	$\frac{kg_{da}}{kg_{wv}}$
ω_{out}	Outlet Humidity Ratio	$\frac{kg_{da}}{kg_{wv}}$

4.3.1 Temperatures

The air and water temperatures are obtained directly from the thermistors described in Chapter 3 Section 3.5. The inlet water temperature $\left(T_{w,in}\right)$ is measured directly from thermistor T104. The outlet water temperature $\left(T_{w,out}\right)$ is taken from thermistor T105 and the plate surface temperature is estimated by thermistor T106. There are four air thermistors used to measure the inlet and outlet air temperature. Thermistors T205 and T207 are positioned at the inlet of the air duct. The average of the temperature readings from these thermistors are used to determine the inlet air temperature $\left(T_{a,in}\right)$.

$$T_{a,in} = \frac{T205 + T207}{2} \tag{4.9}$$

Similarly, thermistors T203 and T204 are averaged to evaluate the outlet air temperature $\left(T_{a,out}\right)$.

$$T_{a,out} = \frac{T203 + T204}{2} \tag{4.10}$$

4.3.2 Mass Flow Rates

The inlet mass flow rate of water $\left(\dot{m}_{w,in}\right)$ is taken directly from the coriolis flow meter positioned before the inlet of the test section. When a mesh plate is tested in the facility, mass transport of water occurs through the plate. In a condensation test, water vapor from a moist air stream condenses on the mesh surface and enters through the mesh plate into the liquid phase. This addition of mass to the water side means that the outlet mass flow rate $\left(\dot{m}_{w,out}\right)$ will be greater than the inlet mass flow. Conversely, in an evaporation test mass is lost through the plate into the air stream. Therefore, in an evaporation test the outlet mass flow rate of water will be less than the inlet mass flow. A variable, named the mass flow rate of condensate $\left(\dot{m}_c\right)$, is created to quantify the mass transfer through the plate. The mass flow rate of condensate into the plate is assumed positive. Therefore during a condensation test the mass flow rate of the condensate is positive and negative during an evaporation test. The mass flow rate of condensate is a critical variable because it is used to determine the average mass transfer coefficient. It should be noted that the mass flow rate of condensate is very small in magnitude when compared to the inlet mass flow rate of water. In fact, it is less than the uncertainty in the measurement of the mass flow rate of water given in Equation (3.6). Therefore, methods employed to physically measure the change in mass proved too difficult. Thus, mass flow rate of condensate is calculated by performing an energy balance on the test section. Section 4.7 shows the calculation of the mass flow rate of the condensate from the energy balance.

The mass flow rate of air $\left(\dot{m}_a\right)$ is calculated from the pressure drop measurement $\left(\Delta p\right)$ across the orifice plate. The orifice pressure transducer (P214) is used to determine the change in pressure across the orifice. An entire section (4.5) is devoted to the calculation of the mass flow rate of air because of its complexity. The mass flow rate of air is vital to the calculation of the average heat transfer coefficient and Reynolds number.

4.3.3 Humidity Ratios

The inlet and outlet humidity ratios $\left(\omega_{in} \,\&\, \omega_{out}\right)$ are calculated from the inlet and outlet relative humidity measurements $\left(\phi_{in} \,\&\, \phi_{out}\right)$ and the inlet and outlet air temperatures $\left(T_{a,in} \,\&\, T_{a,out}\right)$. The relative humidity is measured directly by the relative humidity sensors

RH217 and RH210. To determine the humidity ratios from the relative humidity and air temperature the water vapor saturation pressure $\left(P_{sat}\right)$ must be used and is given by the following equation (ASHRAE 2005).

$$P_{sat}(T) = e^{\left(\frac{C_8}{T} + C_9 + C_{10}T + C_{11}T^2 + C_{12}T^3 + C_{13}\ln(T)\right)} \tag{4.11}$$

The saturation pressure is a function of air temperature. Table 4-2 shows the values for the coefficients used in Equation (4.11).

Table 4-2 Coefficients for Water Vapor Saturation Equation

Coefficients	Value
C8	-5.8002206E+03
C9	1.3914993E+00
C10	-4.8640239E-02
C11	4.1764768E-05
C12	-1.4452093E-08
C13	6.5459673E+00

The saturation pressure of water vapor is then used to calculate the partial pressure of water vapor $\left(P_{wv}\right)$ in the air.

$$P_{wv}(\phi, T) = \phi \cdot P_{sat}(T) \tag{4.12}$$

The partial pressure is a function of the relative humidity and air temperature. The humidity ratio is calculated from the partial pressure in the following equation (ASHRAE 2005).

$$\omega = 0.62198 \frac{P_{wv}(\phi, T)}{P_{atm} - P_{wv}(\phi, T)} \tag{4.13}$$

The inlet and outlet humidity ratios are calculated from Equation (4.13) using the combination of the inlet or outlet air temperature and the corresponding relative humidity. The inlet and outlet humidity ratios are shown in the following equations.

$$\omega_{in} = 0.62198 \frac{P_{wv}(\phi_{in}, T_{a,in})}{P_{atm} - P_{wv}(\phi_{in}, T_{a,in})} \tag{4.14}$$

$$\omega_{out} = 0.62198 \frac{P_{wv}(\phi_{out}, T_{a,out})}{P_{atm} - P_{wv}(\phi_{out}, T_{a,out})} \tag{4.15}$$

4.4 Moist Air Properties

The properties of air can be heavily influenced by the presence of water vapor. The moisture content of the air in the experiments conducted in this work change dramatically between the evaporation and condensation operating conditions. During evaporation there is virtually no water vapor present in the air and its effects can essentially be neglected. However, during condensation testing the humidity ratio of the air is very large and the presence of water vapor has a significant effect on the air properties. Thus, it is necessary to characterize the properties of the moist air mixture. Moist air is treated as a binary mixture of dry air and water vapor. Both components are treated as separate ideal gases which combine to form the properties of the moist air mixture. The moist air properties are needed in order to determine the mass flow rate of the air and to generate the theoretically predicted values for the average convective heat and mass transfer coefficients. Three references are used extensively to calculate the moist air properties. The first is, *Thermophysical Properties of Humid Air* by (M. CONDE ENGINEERING 2007) and the second is the *2005 ASHRAE Fundamentals Handbook* (ASHRAE 2005). The third and final reference is *Fundamentals of Engineering Thermodynamics* (Moran and Shapiro 2004). The equations developed in this section are attained from each of these three sources.

The molar concentrations of dry air (X_a) and water vapor (X_w) are functions of the humidity ratio (ω) and are used to determine the molecular weight of the moist air mixture.

$$X_a = \frac{1}{1+1.607793\omega} \tag{4.16}$$

$$X_w = \frac{\omega}{0.62197058+\omega} \tag{4.17}$$

The molecular weight of the moist air mixture (M_{mix}) is calculated by summing the products of the molecular concentration and molecular mass for each component of the mixture. The molecular mass of the dry air (M_a) has a value of 28.9645 $\frac{g}{mol}$. The value of the molecular mass of water (M_w) is 18.016 $\frac{g}{mol}$.

$$M_{mix} = X_a M_a + X_w M_w \tag{4.18}$$

The ideal gas law is used to calculate the specific volume of the moist air mixture $\left(\nu_{mix}\right)$. The value used for the universal gas constant $\left(\bar{R}\right)$ is 8.314 $\frac{kJ}{kmol-K}$. The specific volume is a function of the atmospheric pressure $\left(P_{atm}\right)$, the air temperature $\left(T\right)$ and the gas constant for the moist air mixture $\left(R_{mix}\right)$.

$$R_{mix} = \frac{\bar{R}}{M_{mix}}$$

$$\nu_{mix} = \frac{R_{mix}T}{P_{atm}} \tag{4.19}$$

The reciprocal of the specific volume of the mixture gives the density of the moist air mixture $\left(\rho_{mix}\right)$.

The dynamic viscosity of the dry air $\left(\mu_a\right)$ and water vapor $\left(\mu_w\right)$, as well as the thermal conductivity of the dry air $\left(k_a\right)$ and water vapor $\left(k_w\right)$ are functions of temperature and are calculated from second order polynomial equations given by the following.

$$\Psi_x = \sum_{i=0}^{2} \zeta_i T^i \tag{4.20}$$

In Equation (4.20) the variable, Ψ, represents the desired property (μ or k) and the subscript 'x' is either 'a' for dry air or 'w' for water vapor. The coefficients $\left(\zeta_i\right)$ for each property are shown in Table 4-3.

Table 4-3 Coefficients for Dynamic Viscosity and Thermal Conductivity Equation

	Water Vapor		**Dry Air**	
i	**ζ_k**	**ζ_μ**	**ζ_k**	**ζ_μ**
0	-3.53760E-03	-9.74940E-07	6.69881E-04	1.43387E-06
1	6.54755E-05	3.59061E-08	9.42482E-05	6.56244E-08
2	1.74460E-08	2.41612E-13	-3.27450E-08	-2.99050E-11

After the properties for the dry air and the water vapor are determined separately it is necessary to evaluate the properties for the mixture of the two gases. The Mason and Saxena approximation equation (M. CONDE ENGINEERING 2007) is used to calculate the properties of the moist air mixture. The Mason and Saxena equation is generalized for a number of two

component gas mixtures but for the following analysis the equation is tailored specifically for the combination of dry air and water vapor.

$$\Psi_{mix} = \frac{\Psi_a}{1 + G_{a,w}\frac{X_w}{X_a}} + \frac{\Psi_w}{1 + G_{w,a}\frac{X_a}{X_w}} \tag{4.21}$$

Again, Ψ, indicates the property of interest which in this case is either the dynamic viscosity or thermal conductivity. The molar concentrations for dry air and water vapor are previously determined in Equation (4.16) and Equation (4.17). The variables $G_{a,w}$ and $G_{w,a}$ are functions of the dynamic viscosity of dry air and water vapor and are shown in following equations.

$$G_{w,a} = 0.277609\left[1 + 1.12605\left(\frac{\mu_w}{\mu_a}\right)^{1/2}\right]^2 \tag{4.22}$$

$$G_{a,w} = 0.2189366\left[1 + 0.8880603\left(\frac{\mu_a}{\mu_w}\right)^{1/2}\right]^2 \tag{4.23}$$

Therefore, the dynamic viscosity $\left(\mu_{mix}\right)$ and the thermal conductivity $\left(k_{mix}\right)$ of the moist air mixture are calculated using Equation (4.21).

$$\mu_{mix} = \frac{\mu_a}{1 + G_{a,w}\frac{X_w}{X_a}} + \frac{\mu_w}{1 + G_{w,a}\frac{X_a}{X_w}} \tag{4.24}$$

$$k_{mix} = \frac{k_a}{1 + G_{a,w}\frac{X_w}{X_a}} + \frac{k_w}{1 + G_{w,a}\frac{X_a}{X_w}} \tag{4.25}$$

The specific heat of the dry air, water vapor and the moist air mixture are evaluated in a different manner. The specific heat for the dry air and water vapor are a function of the air temperature and the molecular mass. A fourth order polynomial is used to determine the specific heat of the dry air $\left(Cp_a\right)$ and water vapor $\left(Cp_w\right)$.

$$Cp_x = \left(\alpha + \beta T + \gamma T^2 + \delta T^3 + \varepsilon T^4\right)\left(\frac{\bar{R}}{M_x}\right) \tag{4.26}$$

In the equation above the subscript, x, is set to 'a' for dry air and 'w' for water vapor. The coefficients for each case are reported in the following table.

Table 4-4 Coefficients for Specific Heat Equation

Gas	α	β	γ	δ	ε
Dry Air	4.070E+00	-1.108E-03	4.152E-06	-2.964E-09	8.070E-13
Water Vapor	3.653E+00	-1.337E-03	3.294E-06	-1.913E-09	2.763E-13

The specific heat of the moist air mixture is determined by multiplying the specific heat of the dry air with the mass fraction of the dry air $\left(mf_a\right)$ and then adding it to the specific heat of the water vapor multiplied by its mass fraction $\left(mf_w\right)$.

$$Cp_{mix} = mf_a Cp_a + mf_{wv} Cp_{wv} \tag{4.27}$$

The mass fractions of the air and water are calculated from their molar concentrations $\left(X\right)$ and their molecular weights $\left(M\right)$.

$$mf_a = \frac{X_a M_a}{X_a M_a + X_w M_w} \tag{4.28}$$

$$mf_w = \frac{X_w M_w}{X_a M_a + X_w M_w} \tag{4.29}$$

The diffusivity of water vapor in the air $\left(D_{AB}\right)$ is a function of the air temperature and atmospheric pressure. The diffusivity is used to predict the values of the average mass transfer coefficient.

$$D_{AB} = 104.91143 \times 10^{-6} \frac{T^{1.774}}{P_{atm}} \tag{4.30}$$

The approximation of the diffusivity in Equation (4.30) is valid for air temperatures less than or equal to 80°C.

The thermal diffusivity of the moist air mixture is evaluated from the mixture's thermal conductivity, density, and specific heat.

$$\alpha_{mix} = \frac{k_{mix}}{\rho_{mix} Cp_{mix}} \tag{4.31}$$

The Prandtl number for the moist air mixture is calculated from the mixture's specific heat, dynamic viscosity and thermal conductivity. The Prandtl number is equal to the ratio of the momentum and thermal diffusivities and is shown in Equation (4.32).

$$\Pr = \frac{Cp_{mix}\mu_{mix}}{k_{mix}} \tag{4.32}$$

The Schmidt number is calculated from the air mixture's dynamic viscosity, specific volume and diffusivity of water vapor in the air. The Schmidt number is the ratio of the momentum and mass diffusivities. It is used in the theoretical model to predict the average convective mass transfer coefficient.

$$Sc = \frac{\mu_{mix}v_{mix}}{D_{AB}} \tag{4.33}$$

4.5 Mass Flow Rate of the Air

The mass flow rate of air is determined by measuring the pressure drop across an orifice plate mounted in a circular duct. The ASME standard *Measurement of Fluid Flow in Pipes Using Orifice, Nozzle, and Venturi* (ASME 2004) is followed with precision to obtain the methodology for measuring the mass flow rate of air.

4.5.1 Derivation

In order to determine the mass flow rate of the air an equation is developed which expresses the increase in velocity created by the constricted area of the orifice as a function of the pressure drop. Such a function is derived from the Bernoulli and continuity equations. Before implementing the Bernoulli equation the underlying assumptions used in its derivation are considered. These four assumptions are found in (Munson, Young, and Okiishi 2002) and are as follows:

1. Viscous effects are assumed negligible
2. The flow is assumed to be steady
3. The flow is assumed to be incompressible
4. The equation is applicable along a streamline

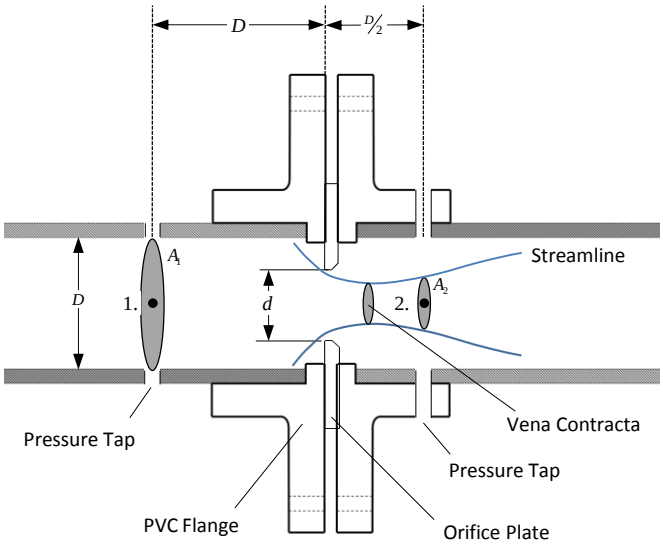

Figure 4-3 Orifice Plate in a Circular Duct

Figure 4-3 illustrates the orifice plate mounted in the PVC duct and also indicates the location of the pressure taps at points 1 and 2. To use the Bernoulli equation it is assumed that the flow is steady, inviscid and incompressible between points 1 and 2. Since the air flow is assumed to be incompressible the density of the air (ρ) is constant between points 1 and 2. It is also assumed that the mass flow rate $(\dot{m}_a)$ at points 1 and 2 are equivalent. Therefore using the continuity equation an expression is developed relating the respective cross sectional area (A) and the velocity (v) at points 1 and 2, as shown in Equation (4.34).

$$\rho = \rho_1 = \rho_2$$
$$\dot{m}_a = \dot{m}_1 = \dot{m}_2$$
$$\rho A_1 v_1 = \rho A_2 v_2$$
$$v_1 = v_2 \left(\frac{A_1}{A_2} \right) \tag{4.34}$$

The Bernoulli equation, as shown in Equation (4.35), allows the pressure (P) and the velocity at points 1 and 2 to be equated. It is assumed that the points are at the same elevation (z) which allows the potential energy term $(\rho g z)$ from the Bernoulli equation to be eliminated (g is the acceleration due to gravity). The Bernoulli equation relates the pressure difference between points 1 and 2 to the change in velocity.

$$P_1 + \tfrac{1}{2}\rho v_1^2 + \rho g z_1 = P_2 + \tfrac{1}{2}\rho v_2^2 + \rho g z_2$$
$$P_1 - P_2 = \tfrac{1}{2}\rho v_2^2 - \tfrac{1}{2}\rho v_1^2$$
$$\Delta p \equiv P_1 - P_2$$

$$\Delta p = \tfrac{1}{2}\rho\left(v_2^2 - v_1^2\right) \tag{4.35}$$

By substituting Equation (4.34) into Equation (4.35) an expression is obtained which relates the velocity at point 1 to the pressure difference.

$$\Delta P = \tfrac{1}{2}\rho\left(v_1^2\left(\tfrac{A_1}{A_2}\right)^2 - v_1^2\right)$$
$$v_1^2 = \frac{\Delta P}{\tfrac{1}{2}\rho\left[\left(\tfrac{A_1}{A_2}\right)^2 - 1\right]}$$
$$v_1 = \sqrt{\frac{\Delta P}{\tfrac{1}{2}\rho\left[\left(\tfrac{A_1}{A_2}\right)^2 - 1\right]}} \tag{4.36}$$

Equation (4.36) is multiplied by the air density and the area at point 1 to obtain the mass flow rate of the air $\left(\dot{m}_a\right)$ as a function of the pressure difference, as shown in Equation (4.37).

$$\left(\rho A_1\right)v_1 = \sqrt{\frac{\Delta p}{\tfrac{1}{2}\rho\left[\left(\tfrac{A_1}{A_2}\right)^2 - 1\right]}}\left(\rho A_1\right)$$
$$\dot{m}_a = \sqrt{\frac{\rho^2 \Delta p}{\tfrac{1}{2}\rho\left(\tfrac{1}{A_1}\right)^2\left[\left(\tfrac{A_1}{A_2}\right)^2 - 1\right]}} \tag{4.37}$$

It is beneficial to define the parameter β as the ratio of the orifice throat diameter $\left(d\right)$ to the upstream pipe diameter $\left(D\right)$. Using this definition the ratio of the areas $\left(\tfrac{A_2}{A_1}\right)$ can be expressed simply as β^2, as shown in Equation (4.38).

$$\left(\tfrac{1}{A_1}\right)^2\left[\left(\tfrac{A_1}{A_2}\right)^2 - 1\right] \Rightarrow \left(\tfrac{1}{A_2}\right)^2 \beta^4\left[\left(\tfrac{1}{\beta^4}\right) - 1\right] \Rightarrow \tfrac{1}{A_2^2}\left[1 - \beta^4\right]$$
$$\dot{m}_a = \sqrt{\frac{2\rho\Delta p A_2^2}{\left[1-\beta^4\right]}} = A_2\sqrt{\frac{2\rho\Delta p}{\left[1-\beta^4\right]}}$$
$$\dot{m}_a = \frac{\pi d^2}{4}\sqrt{\frac{2\rho\Delta P}{\left[1-\beta^4\right]}} \tag{4.38}$$

Equation (4.38) gives the mass flow rate of air as a function of the pressure drop between points 1 and 2. There are two dimensionless correction terms which must are included in Equation (4.38). These terms are known as the discharge coefficient (C) and the expansibility factor (ε_x) and are addressed separately in the following sub-sections. By adding these terms, the final expression of the mass flow rate of air is obtained and shown in Equation.

$$\dot{m}_a = C\varepsilon_x \frac{\pi d^2}{4}\sqrt{\frac{2\rho\Delta P}{\left[1-\beta^4\right]}} \tag{4.39}$$

4.5.2 Discharge Coefficient

The discharge coefficient (C) makes two corrections to the calculation of the mass flow rate of air. The first correction must be made because the cross sectional area of the air flow stream at point 2 is actually less than the diameter of the orifice. The area at point 2 is less than the orifice diameter because the fluid entering the orifice cannot make an exact 90° turn at the edge of the orifice opening and therefore must curve around the edge. This causes the air flow to constrict to a smaller diameter at a point downstream of the orifice. This phenomenon is known as the vena contracta effect and hence the point in the flow stream where the area is least is called the vena contracta. Figure 4-3 displays the vena contracta and illustrates that the area at point 2 (A_2) is in fact less than the orifice diameter (d). The second correction the discharge coefficient accounts for is due to head losses which occur as the air flows through the orifice. The discharge coefficient is primarily a function of β and the Reynolds number based on the pipe diameter upstream of the orifice (Re_D). The Reader-Harris / Gallagher equation (ASME 2004) is used to determine the discharge coefficient for the orifice plate and is shown in Equation (4.40).

$$C = 0.5961 + 0.0261\beta^2 - 0.216\beta^8 + 0.000521\left(\frac{10^6\beta}{\mathrm{Re}_D}\right)^{0.7} + \left(0.0188 + 0.0063A\right)\beta^{3.5}\left(\frac{10^6}{\mathrm{Re}_D}\right)^{0.3}$$

$$+\left(0.043 + 0.08e^{-10L_1} - 0.123e^{-7L_1}\right)\left(1 - 0.11A_x\right)\frac{\beta^4}{1-\beta^4} - 0.031\left(M_2' - 0.8M_2'^{1.1}\right)\beta^{1.3} \tag{4.40}$$

The addition parameters which appear in the equation are shown below:

$$L_1 = 1$$
$$L_2 = 0.47$$
$$M_2' = \frac{2L_2'}{1-\beta}$$
$$A_x = \left(\frac{19000\beta}{\mathrm{Re}_D}\right)^{0.8}$$

These parameters are specific to the pressure tap arrangement where the upstream tap is at a distance, D, from the orifice plate face and downstream tap is at a distance of $\frac{D}{2}$.

4.5.3 Expansibility Factor

The assumption of the Bernoulli equation which deems the flow incompressible raises minor concern since the density of the air could potentially change as it travels through the orifice. It is demonstrated in (Ower and Pankhurst 1977) that for air velocities below 60 $\frac{m}{s}$ the compressibility issue can be ignored. The highest mass flow rates collected in this research do not produce velocities in the orifice which exceed 60 $\frac{m}{s}$ and therefore the incompressibility assumption is upheld. Even though compressibility issues can be neglected, the effect of compressibility is still accounted for using a dimensionless correction parameter called the expansibility factor. This is done to maintain compliance with (ASME 2004). In (ASME 2004) an equation is given to estimate the expansibility factor which represents the effect of the minor change in air density on the mass flow rate. The expansibility factor is a function of the ratio of orifice diameter to upstream internal pipe diameter (β), the ratio of specific heat of the air at constant pressure to the specific heat of air at constant volume (κ), and the ratio of the absolute pressure at point 2 to the absolute pressure at point 1 $\left(\frac{P_2}{P_1}\right)$. The parameter (κ) is also known as the isentropic exponent and is typically assigned a value of 1.4 for air. The ratio of the pressures $\left(\frac{P_2}{P_1}\right)$ is estimated by measuring the pressure drop from the atmospheric pressure in the chamber to the pressure at point 1. Since the chamber pressure is known the absolute pressure at point 1 can then be determined. The pressure drop across the orifice is measured to estimate the absolute pressure at point 2. Thus, given the atmospheric pressure the absolute pressure at point

1 and point 2 can be determined. In Equation (4.41) the formula used to evaluate the expansibility factor is shown.

$$\varepsilon_x = 1-\left(0.351+0.256\beta^4+0.93\beta^8\right)\left[1-\left(\frac{P_2}{P_1}\right)^{\frac{1}{\kappa}}\right] \tag{4.41}$$

4.5.4 Iterative Solution

The discharge coefficient, determined by Equation (4.40) , is a function of the Reynolds number of the upstream internal pipe diameter $\left(\mathrm{Re}_D\right)$. However, in order to calculate this Reynolds number, the mass flow rate of air must already be known. Therefore, there are two unknowns in the equation used to determine the mass flow rate of the air and hence another equation which relates the two in unknowns must be established. Equation (4.42) defines the Reynolds number based on D as a function of the mass flow rate $\left(\dot{m}_a\right)$. Where ρ is the density of the air, u_m is the mean air velocity, D is the internal diameter of the duct upstream of the orifice, and μ is the absolute viscosity.

$$\mathrm{Re}_D = \frac{\rho u_m D}{\mu}$$

$$u_m = \frac{\dot{m}_a}{\frac{\pi}{4}D^2}$$

$$\mathrm{Re}_D = \frac{\rho\left(\frac{\dot{m}_a}{\frac{\pi}{4}D^2}\right)D}{\mu}$$

$$\mathrm{Re}_D = \frac{4\dot{m}_a}{\pi D\mu} \tag{4.42}$$

Using Equation (4.38) and Equation (4.42) the two unknowns can be solved by an iterative technique. First, the equations are re-arranged to gather the unknown variables on the left side and the known variables on the right.

$$\frac{\dot{m}_a}{C} = \varepsilon_x \frac{\pi d^2}{4}\sqrt{\frac{2\rho\Delta P}{\left[1-\beta^4\right]}} \tag{4.43}$$

$$\frac{\mathrm{Re}_D}{\dot{m}_a} = \frac{4}{\pi D\mu} \tag{4.44}$$

By multiplying Equation (4.43) and Equation (4.44) an expression is obtained which relates the two unknowns and isolates the invariant terms on the right hand side of the equation. The invariant terms are consolidated into a constant (A_1).

$$\frac{\dot{m}_a}{C}\frac{\mathrm{Re}_D}{\dot{m}_a} = \left(\frac{4}{\pi D\mu}\right)\left(\varepsilon_x \frac{\pi d^2}{4}\sqrt{\frac{2\rho\Delta P}{\left[1-\beta^4\right]}}\right)$$

$$\frac{\mathrm{Re}_D}{C} = \varepsilon_x \frac{d^2}{D\mu}\sqrt{\frac{2\rho\Delta P}{\left[1-\beta^4\right]}}$$

$$A_1 \equiv \varepsilon_x \frac{d^2}{D\mu}\sqrt{\frac{2\rho\Delta P}{\left[1-\beta^4\right]}}$$

$$\frac{\mathrm{Re}_D}{C} = A_1$$

$$\mathrm{Re}_D = CA_1 \tag{4.45}$$

Equation (4.45) is the iterative equation used to solve for the mass flow rate of air. The solver application in Microsoft Excel 2010 is used to search by iteration for the value of the mass flow rate which makes Equation (4.45) true. The precision of convergence (λ) is determined using the invariant term.

$$\lambda = \left|\frac{A_1 - \frac{\mathrm{Re}_D}{C}}{A_1}\right| \tag{4.46}$$

The typical value of λ for the calculated mass flow rates in this work is on the order of 1×10^{-16}, which indicates a very high degree of convergence for the calculation of the mass flow rate of air.

4.6 Analytical Model

4.6.1 Heat and Mass Transfer Correlations

This section presents the correlations used to predict the average convective heat and mass transfer coefficients. These correlations are found in (Incropera and Incropera 2007) and (Bird, Stewart, and Lightfoot 2002). The Gnielinkski and Dittus-Boetler correlations are implemented to predict the Nusselt number (Nu_D) for turbulent flow in circular tubes. The

correlations are functions of the Reynolds and Prandtl numbers. The Gnielinski correlation is also a function of the Moody friction factor (f) and is shown in the following equation.

$$Nu_D = \frac{\left(\frac{f}{8}\right)(\mathrm{Re}_D - 1000)\,\mathrm{Pr}}{1 + 12.7\left(\frac{f}{8}\right)^{\frac{1}{2}}\left(\mathrm{Pr}^{\frac{2}{3}} - 1\right)} \tag{4.47}$$

Where the valid range of conditions are as follows:

$$0.5 \le \mathrm{Pr} \le 2000$$
$$3000 \le \mathrm{Re}_D \le 5 \times 10^6$$

The Dittus-Boetler equation is used for smooth circular tubes and does not depend on the friction factor. The Dittus-Boetler equation is given by the following equation.

$$Nu_D = 0.023\,\mathrm{Re}_D^{\frac{4}{5}}\,\mathrm{Pr}^n \tag{4.48}$$

Where $n = 0.4$ for heating $(T_s > T_m)$ and $n = 0.3$ for cooling $(T_s < T_m)$. The Dittus-Boetler equation is valid for the following conditions.

$$0.7 \le \mathrm{Pr} \le 160$$
$$\mathrm{Re}_D \ge 10,000$$
$$\frac{L}{D} \ge 10$$

The Nusselt number obtained from these equations is used to estimate the average convective heat transfer coefficient so that it can be compared with the experimental data. In order to develop predictions for the average convective mass transfer coefficient, the heat and mass transfer analogy must be invoked invoked. The Sherwood number (Sh) is the mass transfer equivalent to the Nusselt number and is used to determine the average convective mass transfer coefficient. The Gnielinksi and Dittus-Boetler equations can be modified to produce the Sherwood number simply by replacing the Prandlt number with the analogous Schmidt number (Sc). Thus, by implementing this change in Equation (4.47) and Equation (4.48) the Sherwood numbers are predicted by the following modified correlations.

$$Sh_D = \frac{\left(\frac{f}{8}\right)\left(\mathrm{Re}_D - 1000\right)Sc}{1+12.7\left(\frac{f}{8}\right)^{\frac{1}{2}}\left(Sc^{\frac{2}{3}}-1\right)} \tag{4.49}$$

$$Sh_D = 0.023\,\mathrm{Re}_D^{\frac{4}{5}}\,Sc^n \tag{4.50}$$

Equation (4.49) gives the Sherwood number calculated from the Gnielinksi correlation and Equation (4.50) shows the Sherwood number evaluated from the Dittus-Boetler equation. The Sherwood number from each equation is later used to determine the average convective mass transfer coefficient.

4.6.2 Hydraulic Diameter

The inner diameter is the characteristic length used in the calculation of the Reynolds number for ducts with a circular cross section. However, in this research the internal flow is through a narrow rectangular duct. Therefore, an effective diameter is calculated from the duct dimensions and is commonly referred to as the hydraulic diameter. The hydraulic diameter $\left(D_h\right)$ is calculated from the cross sectional area $\left(A_c\right)$ and the wetted perimeter $\left(P_{wet}\right)$ in the following definition.

$$D_h \equiv \frac{4A_c}{P_{wet}} \tag{4.51}$$

The cross sectional area and wetted perimeter of the rectangular duct are determined from the width $\left(w_d\right)$ and height $\left(h_d\right)$ of the duct.

$$D_h = \frac{4w_d h_d}{2w_d + 2h_d} = \frac{2w_d h_d}{w_d + h_d} \tag{4.52}$$

The actual width of the rectangular duct in this work is 27.15cm and the height is 2.07cm. The value of hydraulic diameter for the air duct in the facility is calculated in Equation (4.53).

$$D_h = \frac{2w_d h_d}{w_d + h_d} = \left[\frac{2\left(27.15\right)\left(2.07\right)}{\left(27.15+2.07\right)}\right]cm = 3.85cm \tag{4.53}$$

The value for the hydraulic diameter shown in Equation (4.53) is the characteristic length used to determine the Reynolds number. The mean air velocity $\left(u_m\right)$ is also used to calculate the

Reynolds number and can be approximated by dividing the mass flow rate of the air $\left(\dot{m}_a\right)$ by the cross sectional area of the duct and the air density. Using this definition of the mean air velocity the calculation of the Reynolds number can be simplified to the result shown in Equation (4.54).

$$\mathrm{Re}_{Dh} = \frac{\rho u_m D_h}{\mu} = \frac{\rho\left(\frac{\dot{m}_a}{\rho w_d h_d}\right)\left(\frac{2w_d h_d}{w_d + h_d}\right)}{\mu}$$

$$\mathrm{Re}_{Dh} = \frac{2\dot{m}_a}{\mu\left(w_d + h_d\right)} \tag{4.54}$$

Equation (4.54) is used to calculate the Reynolds number for the experimental data and is shown to be a function of the mass flow rate of air, the dynamic viscosity of air and the sum of the duct width and the duct height.

4.6.3 Moody Friction Factor

The Moody friction factor is used in the Gnielinski correlation to produce a Nusselt number. The friction factor is a function of the Reynolds number and surface roughness. The Moody friction factor is closely linked with the pressure drop for internal flow situations. The Moody friction factor is calculated from the Colebrook formula (Munson, Young, and Okiishi 2002) and is shown in Equation (4.55).

$$\frac{1}{\sqrt{f}} = -2\ln\left(\frac{\varepsilon/D_h}{3.7} + \frac{2.51}{\mathrm{Re}_{Dh}\sqrt{f}}\right) \tag{4.55}$$

The Colebrook equation cannot be solved analytically and therefore requires the use of an iterative solution. The solver application in Microsoft Excel 2010 is employed to solve for the unknown friction factor given a specific Reynolds number and surface roughness value. Two values of the surface roughness are used to calculate the corresponding friction factors for a large range of Reynolds numbers. The values chosen to the surface roughness for the experimental plate surfaces are $\varepsilon = 10\mu m$ and $\varepsilon = 1000\mu m$. For detailed information on how these values were selected see Section 2.3 of Chapter 2.

4.6.4 Entry Length Correction

The hydrodynamic entry length $\left(x_{fd,h}\right)$ is the approximated position in the duct where the velocity profile becomes fully developed. For turbulent flow the entry length is given by the following inequality (Incropera and Incropera 2007).

$$10 \le \left(\frac{x_{fd,h}}{D_h}\right)_{turb} \le 60 \tag{4.56}$$

Utilizing the hydraulic diameter for the rectangular duct in this work $\left(D_h = 3.85cm\right)$, the minimum hydrodynamic entry length is estimated by the following expression.

$$x_{fd,h} \ge 10 D_h \tag{4.57}$$

The minimum entry length from the entrance of the duct is 38.5 centimeters or about 15.14 inches. The distance from the entrance of the duct to end of the mesh plate is 16.64 inches. Therefore, at best, only 1.5 inches of the mesh plate surface is in the fully developed region. Thus, it is reasonable to assume that heat and mass transfer take place within the entrance region of the duct where the flow is still developing. Figure 4-4 depicts the entry length region in a cross sectional view of the air duct. The location of the hydrodynamic entry length $\left(x_{fd,h}\right)$ and the distance from the leading edge of the duct to the end of the mesh plate surface $\left(L\right)$ are given in units of inches.

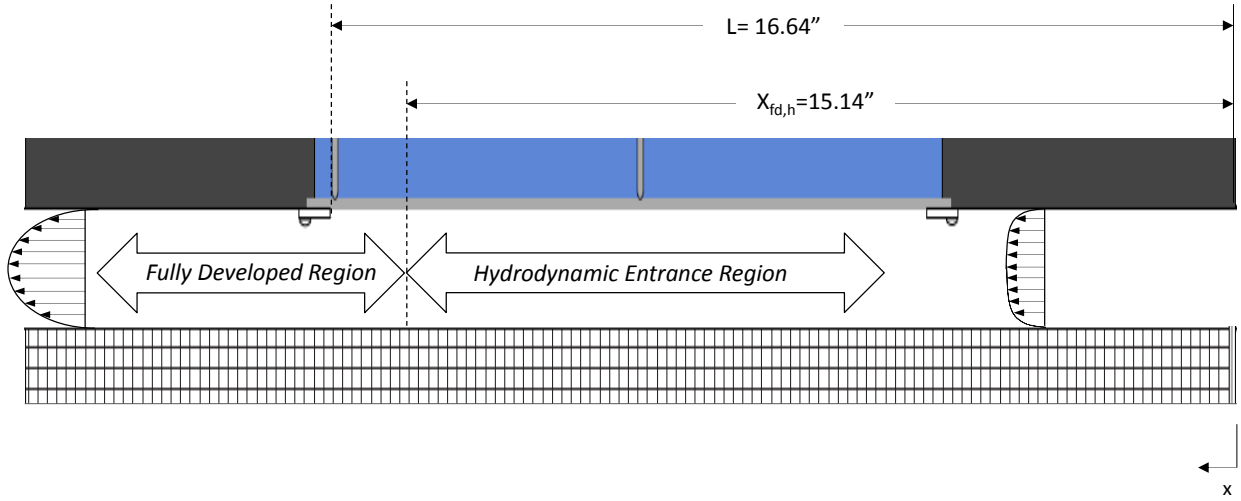

Figure 4-4 Hydrodynamic Entry Length Region

For entry length flow conditions a correction must be applied to the Nusselt and Sherwood numbers predicted by the Gnielinski and Dittus-Boetler correlations. For long ducts which extend well into the fully developed region it is often adequate to assume that the average Nusselt number is approximately equal to the Nusselt number calculated at fully developed conditions $\left(\overline{Nu_D} \approx Nu_{D,fd}\right)$. However, for short ducts the average Nusselt number is often significantly larger than the Nusselt number based on fully developed conditions. The Molki and Sparrow correlation (Molki and Sparrow 1986, 482-484) is used to calculate the corrected average Nusselt number for short length ducts.

$$\frac{\overline{Nu_D}}{Nu_{D,fd}} = 1 + \frac{a}{\left(x/D\right)^b} \tag{4.58}$$

Where a and b are functions of the Reynolds number.

$$a = 23.99\,\mathrm{Re}_D^{-0.230} \tag{4.59}$$

$$b = -2.08\times10^{-6}\cdot\mathrm{Re}_D + 0.815 \tag{4.60}$$

The parameters a and b are developed for the case where the duct inlet is sharp-edged, which is the scenario for the air duct used in this research. In Equation (4.58) the distance, x, is taken as the length from the leading edge of the duct entrance to the end of the mesh plate. This distance is equivalent to the dimension, L, depicted in Figure 4-4. The hydraulic diameter D_h is used in the place of the diameter D. The Nusselt number based on fully developed flow $\left(Nu_{D,fd}\right)$ is obtained from either the Gnielinski or Dittus-Boetler correlation. The average convective heat transfer coefficient is then determined using Equations (4.58), (4.47) and (4.48). Finally, by applying the heat and mass transfer analogy the average convective mass transfer coefficients are evaluated for each correlation. The calculations of the average heat and mass transfer coefficients are presented in the next sub-section.

4.6.5 Predicted Values for the Average Heat and Mass Transfer Coefficients

The predicted values for the average heat and mass transfer coefficients are calculated from the average Nusselt and Sherwood numbers which are obtained from Equation (4.58). The average Nusselt number is defined as the product of the average convective air-side heat transfer

coefficient $\left(\bar{h}_a\right)$ and hydraulic diameter $\left(D_h\right)$ divided by the thermal conductivity of moist air mixture $\left(k_{mix}\right)$.

$$\overline{Nu_D} = \frac{\bar{h}_a D_h}{k_{mix}} \tag{4.61}$$

The average Nusselt number is calculated from both the Gnielinski and Dittus-Boetler correlations by applying the entry length correction. The average convective air-side heat transfer coefficient is determined by rearranging Equation (4.61) .

$$\bar{h}_a = \frac{\overline{Nu_D} D_h}{k_{mix}} \tag{4.62}$$

Equation (4.62) shows how the average convective air-side heat transfer coefficient is determined. The Sherwood number is defined as the product of the average convective air-side mass transfer coefficient $\left(\bar{h}_m\right)$ and the hydraulic diameter $\left(D_h\right)$, divided by the diffusivity of water vapor in air $\left(D_{AB}\right)$.

$$\overline{Sh_{Dh}} = \frac{\bar{h}_m D_h}{D_{AB}} \tag{4.63}$$

The Sherwood number is derived from the heat transfer correlations using the heat and mass transfer analogy. The entry length correction is then applied to find the average Sherwood number shown in Equation (4.63). Once the average Sherwood number is obtained, Equation (4.63) is rearranged to solve for the average mass transfer coefficient. Equation (4.64) shows the predicted convective air-side mass transfer coefficient.

$$\bar{h}_m = \frac{\overline{Sh_{Dh}} D_{AB}}{D_h} \tag{4.64}$$

4.6.6 Heat and Mass Transfer Analogy

When two processes are governed by dimensionless equations of the same form the processes are said to be analogous (Incropera and Incropera 2007). Therefore, since the differential equations and boundary conditions for the thermal and concentration boundary layers are of the same form, an analogy can be constructed between them. It also stands to reason that

for a particular geometry the heat and mass transfer relations are interchangeable (Incropera and Incropera 2007). The only difference between the thermal and concentration boundary layer is the identity of a dimensionless parameter. For the thermal boundary layer equation, the dimensionless Prandtl number is used and for the concentration boundary layer equation the dimensionless Schmidt number is employed. Thus, for any heat transfer correlation the Schmidt number can replace the Prandtl number to convert it into a mass transfer correlation. This idea constitutes the basis of the heat and mass transfer analogy and has already been implemented in this section whenever the Gnielinski and Dittus-Boetler heat transfer correlations are transformed into mass transfer correlations by replacing the Prandtl number with the Schmidt number. The heat and mass transfer analogy can also be used to formulate an equation which calculates the ratio of the average heat and mass transfer coefficients. The average Nusselt number and average Sherwood number are both functions of dimensionless length $\left(x^*\right)$ and Reynolds number and can therefore be directly related to one another.

$$\overline{Nu} = f(x^*, \mathrm{Re})\,\mathrm{Pr}^n \tag{4.65}$$

$$\overline{Sh} = f(x^*, \mathrm{Re})Sc^n \tag{4.66}$$

By equating the dimensionless function of length and Reynolds number in Equation (4.65) and Equation (4.66), the following expression is obtained and shown in Equation (4.67).

$$\frac{\overline{Nu}}{\mathrm{Pr}^n} = \frac{\overline{Sh}}{Sc^n} \tag{4.67}$$

By substituting the previous definitions of the average Nusselt and Sherwood numbers found in Equation (4.61) and Equation (4.63), the following expression is obtained and shown in Equation (4.68).

$$\frac{\bar{h}_a D_h \big/ k_{mix}}{\mathrm{Pr}^n} = \frac{\bar{h}_m D_h \big/ D_{AB}}{Sc^n} \tag{4.68}$$

The ratio of the Schmidt number to the Prandtl number is known as the Lewis number $\left(Le\right)$. The Lewis number can be thought of as the ratio of thermal to mass diffusivities. By simplifying the above expression and introducing the Lewis number the following equation is developed which expresses the ratio of the average heat and mass transfer coefficients as a function of the thermal conductivity, the diffusivity of water vapor in air, and the Lewis number.

$$\frac{\bar{h}_a}{\bar{h}_m} = \frac{k_{mix}}{D_{AB}}\left(\frac{\Pr}{Sc}\right)^n$$

$$\frac{\bar{h}_a}{\bar{h}_m} = \frac{k_{mix}}{D_{AB}}\left(Le\right)^{1-n} \tag{4.69}$$

Where the Lewis number is given by:

$$Le = \frac{\alpha_{mix}}{D_{AB}}$$

Equation (4.69) shows the ratio of the average convective air-side heat and mass transfer coefficeints as a function of the thermal conductivity, the diffusivity of water vapor in air, the Lewis number and the exponent n. The exponent n which appears in Equation (4.69) is typically given a value between 0 and 1. In (Incropera and Incropera 2007) it is reported that a value of $\frac{1}{3}$ is a reasonable approximation for most applications and therefore is assumed as such in this work. Equation (4.69) is used to generate predications for the ratio of the average heat and mass transfer coefficients which is compared with the experimental data in Chapter 5.

4.7 Energy Rate Balance on Test Section

In this section an energy rate balance is carried out for a control volume which encompasses the entire test section. The conservation of energy is applied to the test section control volume in order to solve for the mass flow rate of the condensate $\left(\dot{m}_c\right)$ and also to determine the sensible component of heat transfer from the air to the water $\left(q_{sensible}\right)$. The energy balance analysis is conducted with the assumption that a mesh plate is installed into the test section and therefore allows mass transfer of water from the gas to liquid phase and vice versa. The analysis is carried out with the assumption that condensation occurs on the mesh surface. In the condensation case, water vapor from the air condenses on the mesh plate surface and is absorbed into the liquid water flow stream. Thus for condensation, the mass flow rate of the condensate is assumed positive into the mesh plate. The energy balance analysis is also valid for the evaporation case. In the evaporation case, mass transfer occurs out of the mesh plate when liquid water evaporates into the air flow stream. Therefore, evaporation data will possess negative values for the mass flow rate of the condensate.

It was originally anticipated that the mass flow rate of the condensate could be determined directly by measuring the change between the values of the inlet and outlet air humidity ratios and then multiplying that difference by the mass flow rate of air. Equation (4.70) shows the mass flow rate of condensate as a function of variables measured in the facility.

$$\dot{m}_c = \dot{m}_a(\omega_{in} - \omega_{out}) \tag{4.70}$$

Although this equation is valid, the uncertainty in the measurement of the humidity ratio difference is so large that it renders the calculation of the mass flow rate of the condensate useless. The uncertainty in the mass flow rate of the condensate using this method is between 60 - 100% for most of the data collected in this work. The calculation of both the heat and mass transfer coefficient depends directly on the mass flow rate of the condensate so an alternate method must be developed for estimating the mass flow rate of the condensate. In this work, the most accurate way to determine the mass flow rate of the condensate is to perform an energy balance on the test section and solve for the mass flow rate of the condensate. The energy balance also enables the heat transfer between the air and the water to be divided into its sensible and latent components. This is desirable because the sensible component of the total heat transfer (q_{total}) is used to evaluate the average convective heat transfer coefficient. Figure 4-5 illustrates the energy balance conducted on the test section. Figure 4-5 shows the entry and exit of the air and water flow streams and the properties which fix their states. Also shown within the control volume are the assumed directions for the heat transfer and the mass transfer across the mesh plate surface during condensation conditions.

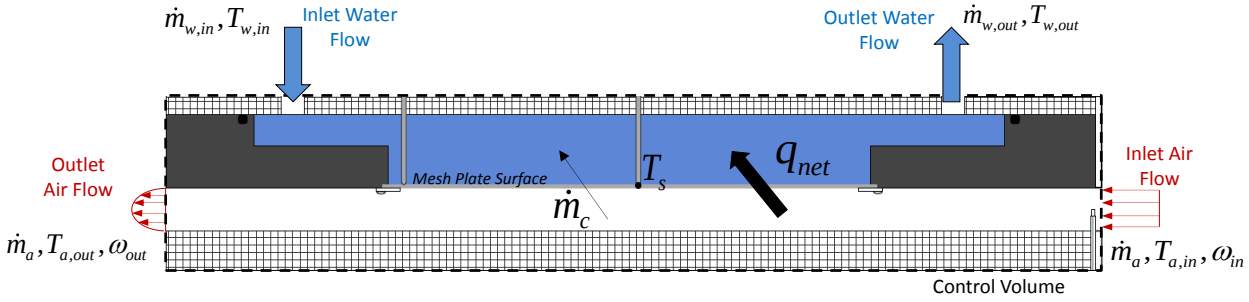

Figure 4-5 Energy Rate Balance on Test Section

The general equation expressing the conservation of energy for control volumes is found in (Moran and Shapiro 2004) and is shown in Equation (4.71).

$$\frac{dE_{CV}}{dt} = \dot{Q}_{CV} - \dot{W}_{CV} + \sum_{in} \dot{m}_{in}\left(i_{in} + \frac{V_i^2}{2} + gz_i\right) - \sum_{out} \dot{m}_{out}\left(i_{out} + \frac{V_{out}^2}{2} + gz_{out}\right) \tag{4.71}$$

The time rate of change of energy within the control volume $\left(\frac{dE_{CV}}{dt}\right)$ can be set to zero since it is assumed that the system is operating at steady state conditions. The rate at which energy is being transferred by heat transfer $\left(\dot{Q}_{CV}\right)$ and by work $\left(\dot{W}_{CV}\right)$ are considered negligible and can also be eliminated from the equation. In addition, the kinetic $\left(\frac{V^2}{2}\right)$ and potential $\left(gz\right)$ energy terms within the mass flow energy terms can be neglected. This leaves the sum of the energy transfer entering the control volume from the mass flow $\left(\sum_{in} \dot{m}_{in} i_{in}\right)$ minus the sum of the energy transfer exiting the control volume $\left(\sum_{e} \dot{m}_{out} i_{out}\right)$. The equation is re-written in terms of the inlet and outlet mass flow rates with respect to air and water and their accompanying enthalpies.

$$\dot{m}_{w,in} i_{w,in} + \dot{m}_a i_{mix,in} - \dot{m}_{w,out} i_{w,out} - \dot{m}_a i_{mix,out} = 0 \tag{4.72}$$

The outlet mass flow rate of water, shown in Equation (4.73), can be expressed as the sum of the inlet water flow rate and the mass flow rate of the condensate.

$$\dot{m}_{w,out} = \dot{m}_{w,in} + \dot{m}_c \tag{4.73}$$

By rearranging Equation (4.72), the water energy terms are isolated on the left hand side and the air energy terms on the right. By substituting Equation (4.73) into Equation (4.72) the following is obtained in Equation (4.74).

$$\left(\dot{m}_{w,in} + \dot{m}_c\right) i_{w,out} - \dot{m}_{w,in} i_{w,in} = \dot{m}_a i_{mix,in} - \dot{m}_a i_{mix,out}$$

$$\dot{m}_c i_{w,out} + \dot{m}_{w,in}\left(i_{w,out} - i_{w,in}\right) = \dot{m}_a\left(i_{mix,in} - i_{mix,out}\right) \tag{4.74}$$

The enthalpy of humid air is determined by the individual components of the moist air mixture, namely the enthalpy of the dry air $\left(i_{da}\right)$ and the enthalpy of the water vapor $\left(i_{wv}\right)$. The enthalpy of the water vapor is multiplied by humidity ratio so that it can be combined with the enthalpy of

the dry air to express the total enthalpy of the moist air mixture $\left(i_{mix}\right)$, as shown in Equation (4.75).

$$i_{mix} = i_{da} + \omega i_{wv} \tag{4.75}$$

The change in enthalpy of the water between the inlet and outlet of the test section can be expressed as specific heat $\left(Cp_w\right)$ multiplied by the change in water temperature from the inlet and outlet of the test section $\left(\Delta T_w\right)$, as shown in Equation (4.76).

$$\Delta T_w \equiv T_{w,out} - T_{w,in}$$

$$\left(i_{w,out} - i_{w,in}\right) = Cp_w \Delta T_w \tag{4.76}$$

The specific heat of water is a function of temperature and is determined by a fourth order polynomial curve fit to a set of tabulated data obtained from NIST Refprops software. The function used to approximate the specific heat of water is shown in Equation (4.77).

$$\begin{aligned} Cp_w(T) = &\left(4.21988722026695\right) - \left(3.43222872936659\times10^{-3}\cdot T\right) + ... \\ &\left(1.21034144183641\times10^{-4}\cdot \mathrm{T}^2\right) - \left(2.35526177066008\times10^{-6}\cdot T^3\right) + ... \\ &\left(2.21941695954213\times10^{-8}\cdot T^4\right) \end{aligned} \tag{4.77}$$

In this analysis it becomes necessary to express the outlet enthalpy of the water in terms of the enthalpy of the surface of the mesh plate. This allows the surface temperature $\left(T_s\right)$ to be introduced into the analysis. Equation (4.78) introduces the enthalpy at the plate surface.

$$i_{w,out} = i_{w,s} + \left(i_{w,out} - i_{w,s}\right) \tag{4.78}$$

By applying Equations (4.75),(4.76) and (4.78) to Equation (4.74) the following is result is achieved and shown in Equation (4.79) .

$$\begin{aligned} \dot{m}_{w,in} Cp_w \Delta T_w + \dot{m}_c \left[i_{w,s} + \left(i_{w,out} - i_{w,s}\right)\right] &= \dot{m}_a \left[\left(i_{da,in} + \omega_{in} i_{wv,in}\right) - \left(i_{da,out} + \omega_{out} i_{wv,out}\right)\right] \\ \dot{m}_{w,in} Cp_w \Delta T_w + \dot{m}_c i_{w,s} + \dot{m}_c \left(i_{w,s} - i_{w,out}\right) &= \dot{m}_a \left[\left(i_{da,in} - i_{da,out}\right) + \left(\omega_{in} i_{wv,in} - \omega_{out} i_{wv,out}\right)\right] \end{aligned} \tag{4.79}$$

By rearranging Equation (4.70), an expression is developed which states the inlet humidity ratio in terms of the outlet humidity ratio, the mass flow rate of air and the mass flow rate of the condensate.

$$\omega_{in} = \frac{\dot{m}_c}{\dot{m}_a} + \omega_{out} \tag{4.80}$$

By substituting Equations (4.80) into Equation (4.79) and simplifying the following result is attained and shown in Equation (4.81).

$$\dot{m}_{w,in} Cp_w \Delta T_w - \dot{m}_c i_{w,s} + \dot{m}_c \left(i_{w,out} - i_{w,s} \right) = \dot{m}_a \left[\left(i_{da,in} - i_{da,out} \right) + \left(\left(\frac{\dot{m}_c}{\dot{m}_a} + \omega_{out} \right) i_{wv,in} - \omega_{out} i_{wv,out} \right) \right]$$

$$\dot{m}_{w,in} Cp_w \Delta T_w - \dot{m}_c i_{w,s} + \dot{m}_c \left(i_{w,out} - i_{w,s} \right) = \dot{m}_a \left(i_{da,in} - i_{da,out} \right) + \dot{m}_c i_{wv,in} + \dot{m}_a \omega_{out} i_{wv,in} - \dot{m}_a \omega_{out} i_{wv,out}$$

$$\dot{m}_{w,in} Cp_w \Delta T_w - \dot{m}_c i_{w,s} + \dot{m}_c \left(i_{w,out} - i_{w,s} \right) = \dot{m}_a \left(i_{da,in} - i_{da,out} \right) + \dot{m}_c i_{wv,in} + \dot{m}_a \omega_{out} \left(i_{wv,in} - i_{wv,out} \right) \tag{4.81}$$

The change in enthalpy of the dry air $\left(i_{da,in} - i_{da,out} \right)$ and of the water vapor $\left(i_{wv,in} - i_{wv,out} \right)$ can be expressed in terms of the specific heat for each component and the change in air temperature between the inlet and outlet of the test section. The specific heats of the dry air and water vapor are previously determined in Section 4.4.

$$\Delta T_a \equiv T_{a,in} - T_{a,out}$$

$$\left(i_{da,in} - i_{wv,out} \right) = Cp_a \Delta T_a \tag{4.82}$$

$$\left(i_{wv,in} - i_{wv,out} \right) = Cp_{wv} \Delta T_a \tag{4.83}$$

Equation (4.82) and (4.83) are inserted into Equation (4.81) to yield Equation (4.84).

$$\dot{m}_{w,in} Cp_w \Delta T_w - \dot{m}_c i_{w,s} + \dot{m}_c \left(i_{w,out} - i_{w,s} \right) = \dot{m}_a Cp_{da} \Delta T_a + \dot{m}_c i_{wv,in} + \dot{m}_a \omega_{out} Cp_{wv} \Delta T_a \tag{4.84}$$

The inlet water vapor enthalpy term $\left(i_{wv,in} \right)$ is re-written in Equation (4.85) to introduce the water vapor enthalpy at the surface into the analysis.

$$i_{wv,in} = i_{wv,s} + \left(i_{wv,in} - i_{wv,s} \right) \tag{4.85}$$

Equation (4.85) is substituted into Equation (4.84) and several terms are re-arranged to result in Equation (4.86).

$$\dot{m}_{w,in} Cp_w \Delta T_w - \dot{m}_c i_{w,s} + \dot{m}_c \left(i_{w,out} - i_{w,s} \right) = \dot{m}_a Cp_{da} \Delta T_a + \dot{m}_c \left[i_{wv,s} + \left(i_{wv,in} - i_{wv,s} \right) \right] + \dot{m}_a \omega_{out} Cp_{wv} \Delta T_a$$

$$\dot{m}_{w,in} Cp_w \Delta T_w + \dot{m}_c \left(i_{w,out} - i_{w,s} \right) = \dot{m}_a Cp_{da} \Delta T_a + \dot{m}_c i_{wv,s} - \dot{m}_c i_{w,s} + \dot{m}_c \left(i_{wv,in} - i_{wv,s} \right) + \dot{m}_a \omega_{out} Cp_{wv} \Delta T_a$$

$$\dot{m}_{w,in} Cp_w \Delta T_w + \dot{m}_c \left(i_{w,out} - i_{w,s} \right) = \dot{m}_a Cp_{da} \Delta T_a + \dot{m}_c \left(i_{wv,s} - i_{w,s} \right) + \dot{m}_c \left(i_{wv,in} - i_{wv,s} \right) + \dot{m}_a \omega_{out} Cp_{wv} \Delta T_a \quad (4.86)$$

The change in enthalpy of the liquid condensate between the mesh plate surface and the outlet water flow from the test section $\left(i_{w,out} - i_{w,s} \right)$ can be expressed as the specific heat of water multiplied by the change in temperature between the two locations. Similarly, the change in enthalpy of the water vapor condensate from the inlet air to the plate surface $\left(i_{wv,in} - i_{wv,s} \right)$ can be expressed in the same manner. Equation (4.87) and (4.88) show these change in enthalpies as a function of the specific heat and temperature difference.

$$\left(i_{w,out} - i_{w,s} \right) = Cp_w \left(T_{w,out} - T_s \right) \quad (4.87)$$

$$\left(i_{wv,in} - i_{wv,s} \right) = Cp_{wv} \left(T_{a,in} - T_s \right) \quad (4.88)$$

The term $\left(i_{wv,s} - i_{w,s} \right)$ which appears in Equation (4.86), represents the energy required to change the water vapor in the air into liquid condensate at the mesh plate surface. This quantity is also known as the latent heat of vaporization $\left(h_{fg} \right)$ and is equal to the energy required to change the liquid water into water vapor. The latent heat of vaporization is a function of temperature. A linear approximation of the latent heat of vaporization is developed from data listed in (ASHRAE 2005) and shown explicitly in Equation (4.89).

$$h_{fg} \left(T \right) = \text{-2.38725} \cdot \text{T+ 2501.45125} \quad (4.89)$$

Therefore, the latent heat of vaporization term in Equation (4.86) is rewritten as the following in Equation (4.90).

$$\left(i_{wv,s} - i_{w,s} \right) = h_{fg} \left(T_s \right) \quad (4.90)$$

Finally, by substituting Equation (4.87),(4.88) and (4.90) into Equation (4.86) the energy rate equation is presented in its optimal form. Equation (4.91) displays the final form of the energy rate balance on the test section control volume.

$$\dot{m}_{w,in} Cp_w \Delta T_w + \dot{m}_c Cp_w \left(T_{w,out} - T_s \right) = \dot{m}_a Cp_{da} \Delta T_a + \dot{m}_c h_{fg} \left(T_s \right) + \dot{m}_c Cp_{wv} \left(T_{a,in} - T_s \right) + \dot{m}_a \omega_{out} Cp_{wv} \Delta T_a \quad (4.91)$$

The mass flow rate of the condensate is the only unknown in Equation (4.91). Therefore, the equation is rearranged to solve for mass flow rate of the condensate.

$$\dot{m}_c = \frac{\dot{m}_{w,in} Cp_w \Delta T_w - \dot{m}_a \omega_{out} Cp_{wv} \Delta T_a - \dot{m}_a Cp_{da} \Delta T_a}{h_{fg}\left(T_s\right) + Cp_{wv}\left(T_{a,in} - T_s\right) - Cp_w\left(T_{w,out} - T_s\right)} \tag{4.92}$$

Equation (4.92) is used to determine the mass flow rate of the condensate for the case where a mesh plate is installed in the test section. The mass flow rate of the condensate is directly used to calculate the average convective mass transfer coefficient. It is also used to determine one of the terms in the sensible component of heat transfer. The sensible component of heat transfer is then used to determine the average convective heat transfer coefficient. However, two of the plates tested in the facility are solid plates and do not allow mass transfer to occur. Thus, Equation (4.92) must be modified to calculate the mass flow rate of the condensate for the solid plates. When using a solid plate in condensation conditions, water vapor condenses into droplets at the plate surface. However, instead of passing though the plate, the condensate droplets eventually fall from the plate surface and collect in the air duct. The vapor shear from the air flow then pushes the condensate out of the test section control volume and it is removed from the system by a condensate drain (see Figure 3-9). It is reasonable to assume that the condensate leaves the test section at the plate surface temperature (T_s). By making this assumption, the energy balance analysis is nearly identical to the case for mesh plate. The only difference is that the outlet mass flow rate of water is equal to the inlet mass flow rate instead of including the mass flow rate of the condensate as in Equation (4.73). By making this simplification and carrying it through the analysis the same result given by Equation (4.92) is obtained except the $Cp_w\left(T_{w,out} - T_s\right)$ term is omitted. Thus, the mass flow rate of condensate for a solid plate in condensation is given by the Equation (4.93).

$$\dot{m}_c = \frac{\dot{m}_{w,in} Cp_w \Delta T_w - \dot{m}_a \omega_{out} Cp_{wv} \Delta T_a - \dot{m}_a Cp_{da} \Delta T_a}{h_{fg}\left(T_s\right) + Cp_{wv}\left(T_{a,in} - T_s\right)} \tag{4.93}$$

In the case of evaporation for a solid plate there is no mass transfer from one medium to the other and hence no need to calculate of the mass flow rate of the condensate.

The terms which appear in Equation (4.91) can be grouped into categories which identify the type of heat transfer they represent. The terms which describe the heat gained or lost by the water $\left(Q_{water}\right)$ as it passes through the test section appear on the left hand side of the equation.

Similarly the heat gained or lost by the air $\left(Q_{air}\right)$ is shown on the right. The air heat transfer terms can be further divided into the sensible and latent components of heat transfer. Figure 4-6 illustrates the various heat transfer terms of the air and water.

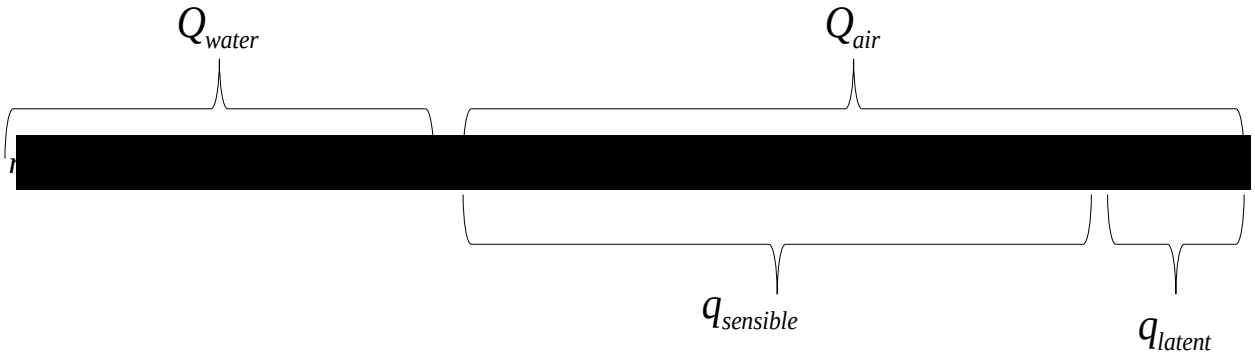

Figure 4-6 Equation (4.91) with Heat Transfer Labels

The sensible component of the air heat transfer is of particular interest since it is used to calculate the average convective heat transfer coefficient. The sensible component of the heat transfer is given by Equation (4.94).

$$q_{sensible} = \dot{m}_a Cp_{da} \Delta t_a + \dot{m}_c Cp_{wv} \left(T_{a,in} - T_s\right) + \dot{m}_a \omega_{out} Cp_{wv} \Delta t_a \tag{4.94}$$

The sensible component of the air heat transfer shown in Equation (4.94) consists of three terms. The first term $\left(\dot{m}_a Cp_{da} \Delta t_a\right)$ represents the sensible heat transfer from the dry air. The next term $\left(\dot{m}_c Cp_{wv} \left(T_{a,in} - T_s\right)\right)$ represents the sensible heat transfer associated with the change in water vapor temperature at the plate surface and the final term $\left(\dot{m}_a \omega_{out} Cp_{wv} \Delta T_a\right)$ quantifies the sensible heat transfer from the water vapor in the air as it passes through the test section.

The sensible component of the air heat transfer could also be calculated by the difference between the water heat transfer and the latent component of the air heat transfer, as shown in Equation (4.95). However, Equation (4.94) yields less uncertainty in the calculation of the sensible component of heat transfer and therefore is preferred.

$$q_{sensible} = Q_{water} - q_{latent}$$

$$q_{sensible} = \dot{m}_{w,in} Cp_w \Delta T_w + \dot{m}_c Cp_w \left(T_{w,out} - T_s\right) - \dot{m}_c h_{fg} \left(T_s\right) \tag{4.95}$$

In the following sub-section the sensible component of the air heat transfer is used to determine the average convective heat transfer coefficient.

4.8 Average Convective Heat Transfer Coefficient

The average convective air-side heat transfer coefficient is derived from Newton's law of cooling and is shown below in Equation (4.96).

$$\bar{h}_a = \frac{q_{sensible}}{A_s\left(T_m - T_s\right)} \tag{4.96}$$

$q_{sensible}$ is the sensible component of heat transfer from the air to the experimental plate surface and is determined from Equation (4.94). The mean air temperature $\left(T_m\right)$ is defined as the average of the inlet and outlet air temperatures. Equation (4.97) shows the mean air temperature as a function of the inlet and outlet air temperature.

$$T_m = \frac{T_{a,in} + T_{a,out}}{2} \tag{4.97}$$

For all the data collected in this work, the mean air temperature is always greater than the surface temperature $\left(T_m > T_s\right)$. Therefore, it follows that the sensible component of heat transfer will always be positive into the experimental plate for condensation as well as evaporation.

The area of heat transfer $\left(A_s\right)$ is the entire area of the experimental plate in contact with the moist air stream and liquid water. For mesh plates this includes the open area within the capillary openings and the area created by the wires. Therefore, the mesh and the solid plate area is assumed to be the same. The value used for the surface area of the experimental plates is given in Equation (4.98).

$$A_s = 0.0436212837 m^2 \tag{4.98}$$

4.9 Average Convective Mass Transfer Coefficient

The average convective mass transfer coefficient is shown in Equation (4.99) and is calculated from the mass flow rate of the condensate, the mass density water vapor gradient and the surface area.

$$\bar{h}_m = \frac{\dot{m}_c}{A_s\left(\rho_{wv,m} - \rho_{wv,s}\right)} \tag{4.99}$$

The mass flow rate of the condensate is calculated in Section 4.7 for the mesh and solid plates in condensation or evaporation. The mass density of the water vapor in air is determined by application of the ideal gas law. For the inlet and outlet air streams the mass density is

calculated from the partial pressure of water vapor $\left(P_{wv}\right)$, the air temperature and the gas constant of water vapor $\left(R_{wv}\right)$. The gas constant of water vapor is obtained from the universal gas constant divided by the molecular mass of water vapor and is shown in Equation (4.100). The values of these constants are given in Section 4.4.

$$R_{wv} = \frac{\bar{R}}{M_{wv}} \tag{4.100}$$

The partial pressure of water vapor is given in Equation (4.12) and is a function of the relative humidity and saturation pressure. Therefore, the mass densities of water vapor for the inlet and outlet air streams are given by the following expressions and shown in Equations (4.101) and (4.102).

$$\rho_{wv,in} = \frac{\phi_{in} P_{sat}(T_{a,in})}{R_{wv} T_{a,in}} \tag{4.101}$$

$$\rho_{wv,out} = \frac{\phi_{out} P_{sat}(T_{a,out})}{R_{wv} T_{a,out}} \tag{4.102}$$

The mean mass density of water vapor in the air $\left(\rho_{wv,m}\right)$ is calculated from the average of the inlet and outlet mass densities and shown in Equation (4.103).

$$\rho_{wv,m} = \frac{\rho_{wv,in} + \rho_{wv,out}}{2} \tag{4.103}$$

The mass density of the water vapor at the plate surface is calculated from the saturation pressure $\left(P_{sat}\right)$, as shown in Equation (4.104).

$$\rho_{wv,s} = \frac{P_{sat}(T_s)}{R_{wv} T_s} \tag{4.104}$$

The area of mass transfer $\left(A_s\right)$ is the same area shown in Equation (4.98). It is apparent that mass transfer through the mesh plates can only occur through the open area created by the capillary pores. Therefore, it is expected that this will cause some inconsistences in the results.

Chapter 5 Experimental Results

5.1 Introduction

This Chapter presents the data collected from the experimental facility and offers a discussion of the significant results obtained from the data. The information in this Chapter is divided into two main sections. The first section explains how the data is organized, identifies the major variables in the experiment, and describes the operating conditions in which the data is collected. This section also briefly mentions the attributes of the solid and mesh experimental plates. Finally, this section presents the average convective heat and mass transfer coefficients for all the experimental data collected in this research.

The second section examines in detail the results inferred from the data. In this section comparisons are made between the solid and mesh plates as well as between the condensation and evaporation conditions. Parameters such as percent open area, wire diameter, and material are also considered. Finally, the data is compared with the Gnielinski and Dittus-Boetler correlations and then measured against the heat and mass transfer analogy.

5.2 Experimental Data

The purpose of the experimental data is to evaluate the performance of the solid and mesh plates with respect to heat and mass transfer. The data is separated into two major factions based on whether the operating conditions promote condensation or evaporation. In order to achieve the condensation and evaporation conditions, six experimental variables must be manipulated. The six experimental variables are:

1. Inlet air temperature
2. Inlet air humidity
3. Mass flow rate of air
4. Mass flow rate of water
5. Inlet water temperature
6. Bubble point pressure

In general, the condensation test conditions are achieved by setting the inlet water temperature lower than the dew point of the inlet air. The evaporation test conditions are obtained by

reducing the humidity of the inlet air to its lowest possible level and ensuring that the inlet water temperature does not fall below the dew point of the inlet air. The experimental variables must be adjusted to reach these conditions and are further discussed in the following sub-section.

Multiple data points are collected for a given plate that is subjected to either the condensation or evaporation conditions. A data point is defined as a single test run at steady state with the experimental variables fixed at specific states. For each data point 60 samples are collected from every measurement device in the experimental apparatus. The specific states of the experimental variables are either replicated or changed in order to formulate comparisons between the data points and to see how the heat and mass transfer coefficients are affected. In order to ensure that accurate comparisons could be made between the data points, it became necessary to further divide the data into groups based on the inlet air temperature and inlet air humidity. This further classification allows the data to be more accurately compared to the heat and mass transfer correlations and to the heat and mass transfer analogy. Therefore, data points with similar values for inlet air temperature and humidity are organized into four data groups and denoted by the following: (Ta_1,ω_1), (Ta_2,ω_2), (Ta_3,ω_3), (Ta_4,ω_4). The first two data groups contain the data points from condensation tests and the remaining two data groups contain the data points from the evaporation tests.

5.2.1 Experimental Variables and Operating Conditions

This sub-section describes the experimental conditions under which the data is collected. The condition of the experimental variables is unique for each data point. The inlet air temperature and inlet air humidity ratio proved to be the most difficult variables to control and much effort was taken to replicate the inlet air conditions for each data point. Within each data group the values of the inlet air temperature and inlet air humidity ratio for each data point are averaged. The standard deviation of the inlet air temperature and inlet air humidity ratio are also calculated for each data point in order to give a measure of the variation between the data points within each data group. Table 5-1 shows the average inlet air temperature and the average inlet air humidity ratio for each data group. It also displays the 95 % confidence interval for each group which is determined from the standard deviation.

Table 5-1 Average Air Temperature and Absolute Humidity for all Data Groups

k	Ta_k (°C)	± 2σ (°C)	ω_k (kg_{wv} / kg_{da})	± 2σ (kg_{wv} / kg_{da})
1	46.38	0.90	0.0447	0.0058
2	39.12	4.99	0.0313	0.0053
3	32.49	0.67	0.0033	0.0005
4	32.51	2.21	0.0032	0.0012

The inlet water temperature and the mass flow rate of water are the experimental variables which directly control the surface temperature of the experimental plate. Table 5-2 provides the average inlet water temperature and average mass flow rate of water for each data group. It also shows the variation between the data points within each data group by showing the 95 % confidence interval for each data group.

Table 5-2 Average Inlet Water Temperature and Mass Flow Rate of Water for Data Groups

Data Group	Inlet Water Temperature (°C)	± 2σ (°C)	Mass Flow Rate of Water (g/s)	± 2σ (g/s)
(Ta_1,ω_1)	12.11	0.11	51.50	1.27
(Ta_2,ω_2)	10.86	1.91	51.49	1.33
(Ta_3,ω_3)	24.44	0.06	51.21	1.29
(Ta_4,ω_4)	14.61	0.08	50.50	1.01

The experimental variable which has the greatest effect on the heat transfer coefficient is the mass flow rate of air. The mass flow rate of air is used to calculate the Reynolds number. Thus, the Reynolds number is changed by increasing or decreasing the mass flow rate of air. Once the other experimental variables are set, each plate is subjected to a low, medium and high mass flow rate of air. The three intensities of the mass flow rate of air create three distinct data points during an experiment where the operating conditions are fixed. The Reynolds numbers for all the data points collected in this work are found within a range of 10,000 to 30,000. Table 5-3 shows the average Reynolds number based on hydraulic diameter for all the data points at each of the three levels for the mass flow rate of air.

Table 5-3 Average Reynolds Number (Hydraulic Diameter) for all Data Points

Range	Average Re_{Dh}	$\pm 2\sigma$
Low	13047	623
Medium	18419	577
High	25801	887

The pressure difference between the gas-liquid interface must be maintained so that no liquid leaks into the gas phase or vice versa. This pressure difference is called the bubble point pressure. It is desirable that no air enters into the water side of the interface through the mesh plate surface, however this condition is very difficult to achieve. Thus, for nearly all tests performed on the mesh plates there was a small amount of air infiltration into the water side. However, it was discovered that the air leakage into the water side did not have a significant effect on the test results and is considered negligible.

Table 5-4 reports the average bubble point pressure and 95 % confidence interval for all the mesh plate data points and for all the solid plate data points.

Table 5-4 Average Bubble Point Pressure for Mesh and Solid Plates

Plate Type	Average Bubble Point Pressure (psi)	$\pm 2\sigma$ (psi)
Mesh	0.135	0.063
Solid	0.291	0.313

The variation in the mesh plates is much smaller due to the need to maintain the gas-liquid interface in quasi-equilibrium. The solid plates do not allow any gas or liquid to cross the interface and therefore have a much larger range of operation.

Steady state conditions are easily reached for all the experimental variables except for the inlet air temperature. Thus, steady state conditions are assumed to be reached when the inlet air temperature varies less than 1°C between the minimum and maximum sample value for a time period of 600 seconds. Also the standard deviation of the inlet air temperature measurements must be less than 0.5 °C for a time period of 600 seconds. If these conditions are met then a data point is taken.

5.2.2 Experimental Plates

Eight different experimental plates are tested in the experimental facility. The two plates fabricated from metal shims are named "solid" plates because they do not allow any mass transfer to occur. The remaining six plates are constructed from woven wire cloth and are called "mesh" plates. The mesh plates have varying amounts of percent open area that allows mass transfer to occur. The mesh plates also vary in thickness, material, and wire diameter. The solid plates only differ with thickness. Each plate is subject to condensation and evaporation conditions and once steady state conditions are obtained the mass flow rate of air is changed to produce data points for the low, medium and high Reynolds numbers. Approximately 12 data points were collected for each plate. In order to easily differentiate between the experimental plates, the mesh plates are named MP1, MP2, MP3, MP4, MP5, and MP6, where the "MP" stands for mesh plate. Similarly, the solid plates are labeled SP1 and SP2. Refer to Section 2.3 of Chapter 2 for detailed information on the experimental plates and their distinguishing characteristics.

5.2.3 Average Convective Heat Transfer Coefficient

This section presents the average air-side convective heat transfer coefficient for all the data points collected in this work plotted versus the Reynolds number based on hydraulic diameter. The plots are divided based on whether the experiment was conducted in condensation or evaporation conditions. Figure 5-1 displays the average convective heat transfer coefficient for the condensation data. This includes all the data points from data groups (Ta_1,ω_1) and (Ta_2,ω_2). The uncertainty associated with each data point is also depicted by error bars.

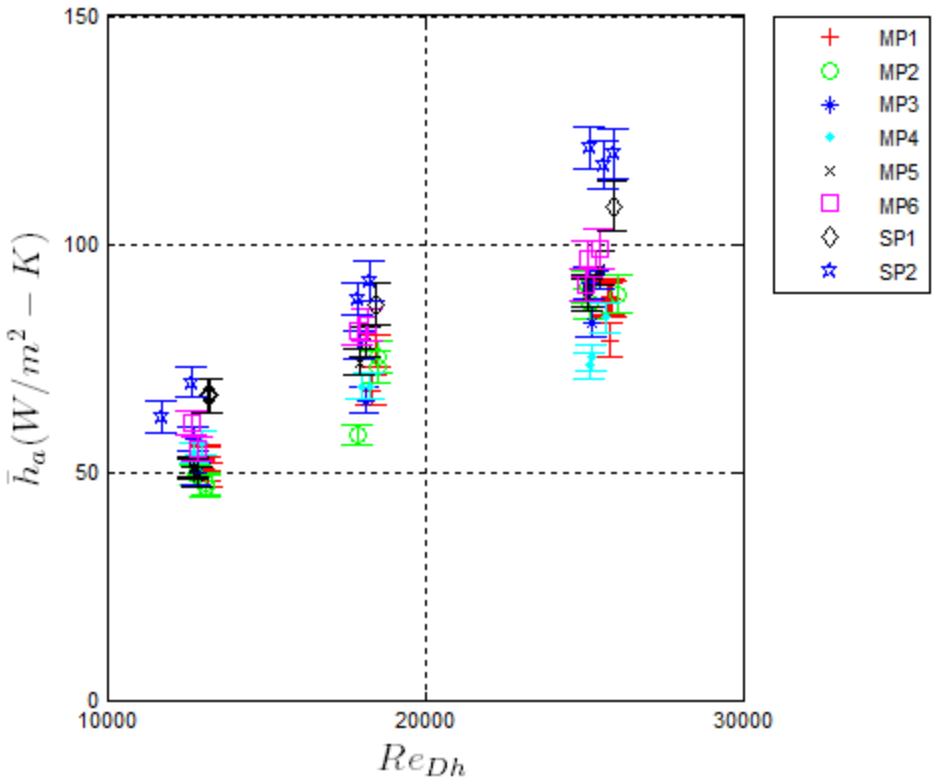

Figure 5-1 Average Heat Transfer Coefficient vs. Re_{Dh} for the Condensation Data

In this plot it is apparent that the average heat transfer coefficient is directly proportional to the Reynolds number and appears to increase linearly for all plates. The solid plates appear to possess slightly higher values than the mesh plates at each Reynolds number level. The mesh plates do not exhibit any significant distinction from one another. In Appendix A additional plots are given which picture the data points at each Reynolds number with better accuracy. In Table 5-1 it is evident that data group (Ta_1,ω_1) has a higher air temperature and humidity ratio than data group (Ta_2,ω_2). Given this fact, it is expected that data group (Ta_1,ω_1) would display a higher heat transfer coefficient, however the data does not indicate this result.

Figure 5-2 shows the average heat transfer coefficient plotted versus the Reynolds number for all evaporation data points collected from the experimental plates. This includes all the data points in data groups (Ta_3,ω_3) and (Ta_4,ω_4). The error bars for each data point are also shown in the plot to give a measure of the uncertainty.

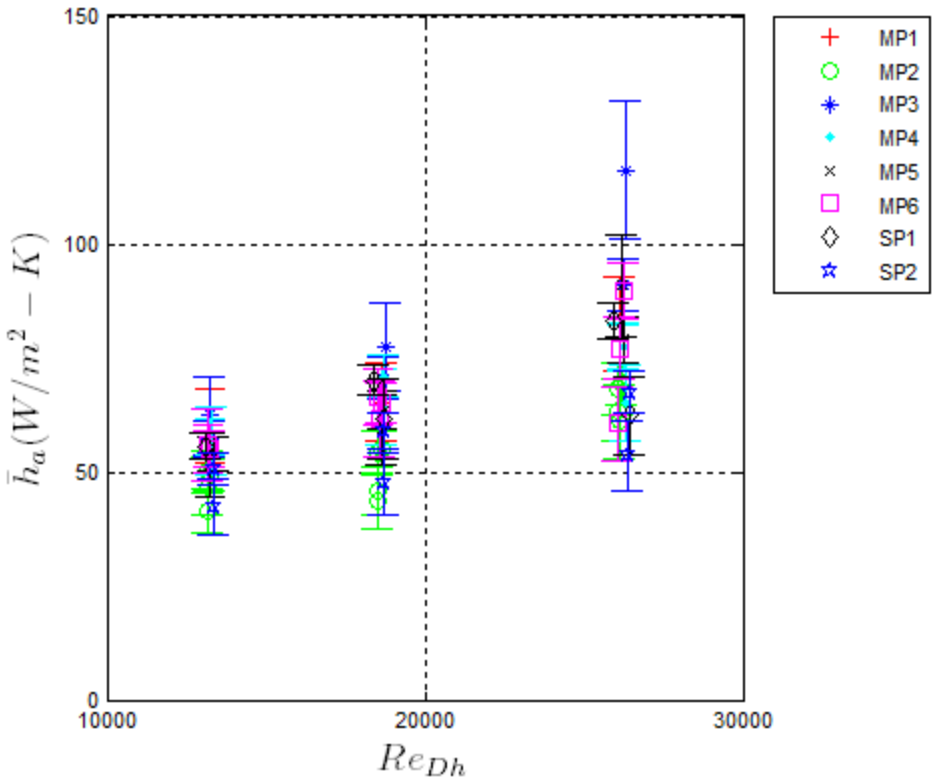

Figure 5-2 Average Heat Transfer Coefficient vs. ReDh for the Evaporation Data

In Figure 5-2 the average heat transfer coefficient increases with Reynolds number. The solid plates are no longer noticeably higher than the mesh plates and instead they appear to have the same value. As is the case for the condensation data, there is no apparent distinction between the mesh plates, however it is evident that as the Reynolds number increases so does the variation between the data points for each plate. Additional error bar plots for the data shown in Figure 5-2 are found in Appendix A. It should be noted that the uncertainty in the evaporation data is considerably higher than for the condensation data.

5.2.4 Average Convective Mass Transfer Coefficient

In this section the average air-side convective mass transfer coefficients are presented for all the data points collected in this work. The average convective mass transfer coefficient is plotted versus the Reynolds number based on the hydraulic diameter. The two plots shown in this section are divided based on whether the data was collected in condensation or evaporation conditions. Figure 5-3 shows the average mass transfer coefficient for the condensation data

points. This includes all the data points from data groups (Ta_1,ω_1) and (Ta_2,ω_2). Error bars are also shown for each data point.

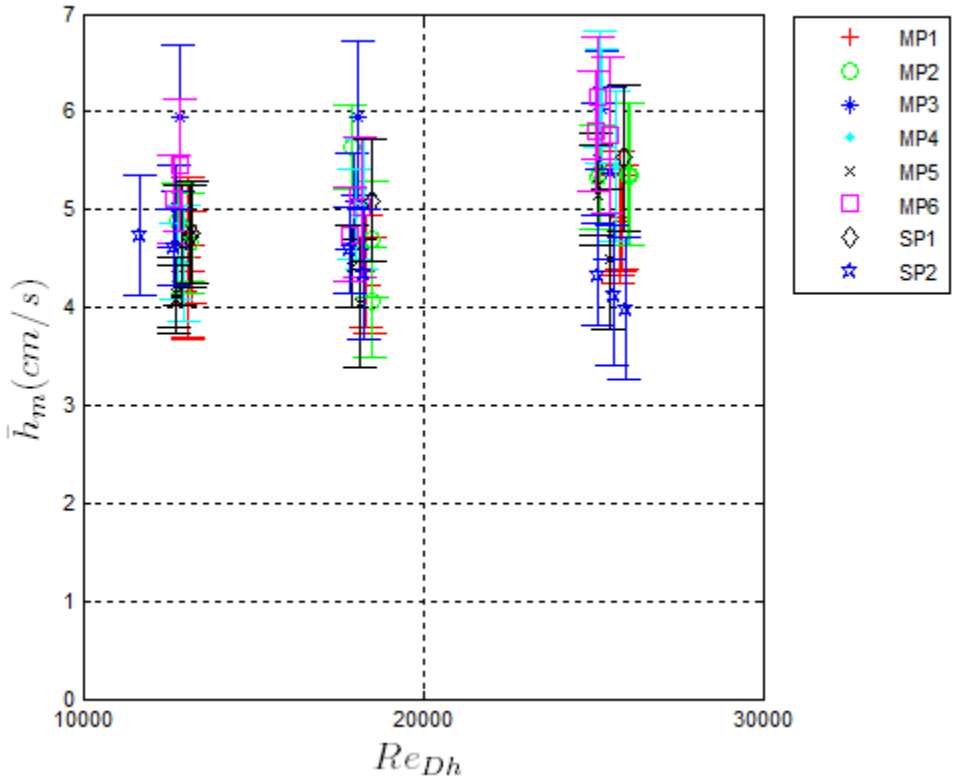

Figure 5-3 Average Convective Mass Transfer Coefficient for the Condensation Data

The data points in this figure show little distinction between one another. The average convective mass transfer coefficient does not appear to increase linearly with the Reynolds number and instead seems to remain constant for all plates as the Reynolds number is increased. The mesh and solid plates exhibit no obvious differences between one another. Additional error bar plots of the data points in Figure 5-3 can be found in Appendix A.

Figure 5-4 displays the average convective mass transfer coefficient for the evaporation data. This includes all the data points in (Ta_3,ω_3) and (Ta_4,ω_4) and a few additional data points which did not fit into either data group.

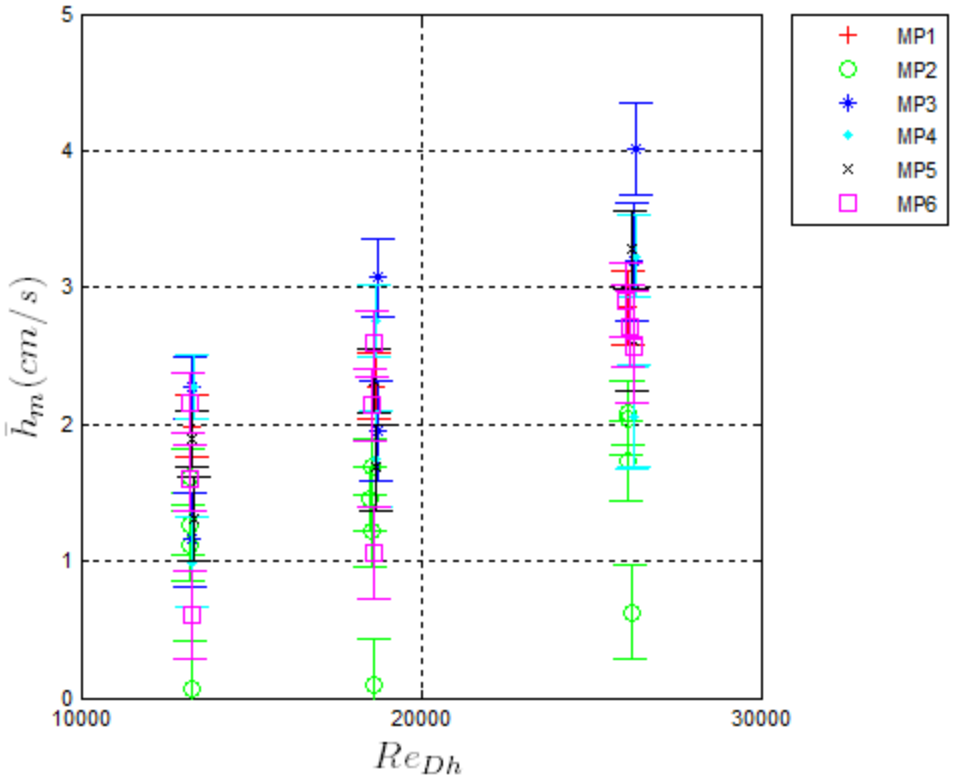

Figure 5-4 Average Mass Transfer Coefficient for Evaporation Data

It is immediately apparent that the data points in this figure span a wide range when compared to the condensation data points. The plates exhibit significant distinction between one another. The solid plates do not appear in this figure because they do not allow any mass to transfer. Additional error bar plots for the data shown in this figure are found in Appendix A.

These four plots summarize the heat and mass transfer performance of the experimental plates. The auxiliary plots in Appendix A illustrate the data with better accuracy by plotting the data points against smaller ranges for the Reynolds number. In the next section the results from the data are discussed at length.

5.3 Discussion of Results

In this section, observations made from the data are explored and discussed. In particular, comparisons are drawn between the condensation and evaporation data and between the mesh and solid plates. Varying characteristics of the different plates which might influence the data are also investigated. These characteristics include: percent open area, material, wire diameter and thickness. Lastly, the data is compared with analytical models derived from the two

heat transfer correlations. The four data groups are individually compared with the Gnielinski and Dittus-Boetler correlations (Incropera and Incropera 2007). For each data group, the predicted values for the average convective heat and mass transfer coefficients are calculated from the two correlations. The predicted values range from a Reynolds number of 10,000 to 30,000. The Gnielinski correlation is found to be a function of surface roughness. Thus, two surface roughness values are chosen which span two orders of magnitude and are selected to represent the theoretical limits of the surface roughness values for all the plates. It is a reasonable assumption that the actual surface roughness of all the plates fall within the selected values for surface roughness. The data is also compared to the heat and mass transfer analogy using the plate surface area and again using the percent open area. For each data group the analogy is invoked by calculating the ratio of the average convective heat transfer coefficient to the average convective mass transfer coefficient.

5.3.1 Comparison of Condensation and Evaporation Data

The condensation and evaporation data are compared by examining their average convective heat and mass transfer coefficients. The two figures presented in this section show the average air-side convective heat and mass transfer coefficients for the condensation and evaporation data points plotted versus the Reynolds number. The data groups are distinguished by whether they are condensation or evaporation data in an attempt to make any comparisons easily visible. Figure 5-5 displays the average convective heat transfer coefficient for the condensation and evaporation data groups plotted against the Reynolds data points within the evaporation data groups have more variation than the condensation data groups. This is largely due to the difference in the areas used to calculate the mass transfer coefficients for the condensation and evaporation data. For the case of evaporation it is assumed that mass transfer only occurs through the capillary openings in the mesh plate surface. Thus, the percent open area is used to calculate the mass transfer coefficient for the evaporation data. In the case of condensation it is assumed that mass transfer occurs not only through the capillary openings but on the wire surface as well. Therefore, the entire area of the plate is used to calculate the mass transfer coefficient for the condensation data. The mesh plates vary signifigantly with respect to their percent open area so it is anticipated that the data points within the evaporation data groups

will demonstate this fact. It is also evident that the evaporation data points seem to increase with Reynolds number while the condensation data points remain relatively the same.

Data points within the evaporation data groups have more variation than the condensation data groups. This is largely due to the difference in the areas used to calculate the mass transfer coefficients for the condensation and evaporation data. For the case of evaporation it is assumed that mass transfer only occurs through the capillary openings in the mesh plate surface. Thus, the percent open area is used to calculate the mass transfer coefficient for the evaporation data. In the case of condensation it is assumed that mass transfer occurs not only through the capillary openings but on the wire surface as well. Therefore, the entire area of the plate is used to calculate the mass transfer coefficient for the condensation data. The mesh plates vary signifigantly with respect to their percent open area so it is anticipated that the data points within the evaporation data groups will demonstate this fact. It is also evident that the evaporation data points seem to increase with Reynolds number while the condensation data points remain relatively the same.

Data points within the evaporation data groups have more variation than the condensation data groups. This is largely due to the difference in the areas used to calculate the mass transfer coefficients for the condensation and evaporation data. For the case of evaporation it is assumed that mass transfer only occurs through the capillary openings in the mesh plate surface. Thus, the percent open area is used to calculate the mass transfer coefficient for the evaporation data. In the case of condensation it is assumed that mass transfer occurs not only through the capillary openings but on the wire surface as well. Therefore, the entire area of the plate is used to calculate the mass transfer coefficient for the condensation data. The mesh plates vary signifigantly with respect to their percent open area so it is anticipated that the data points within the evaporation data groups will demonstate this fact. It is also evident that the evaporation data points seem to increase with Reynolds number while the condensation data points remain relatively the same.

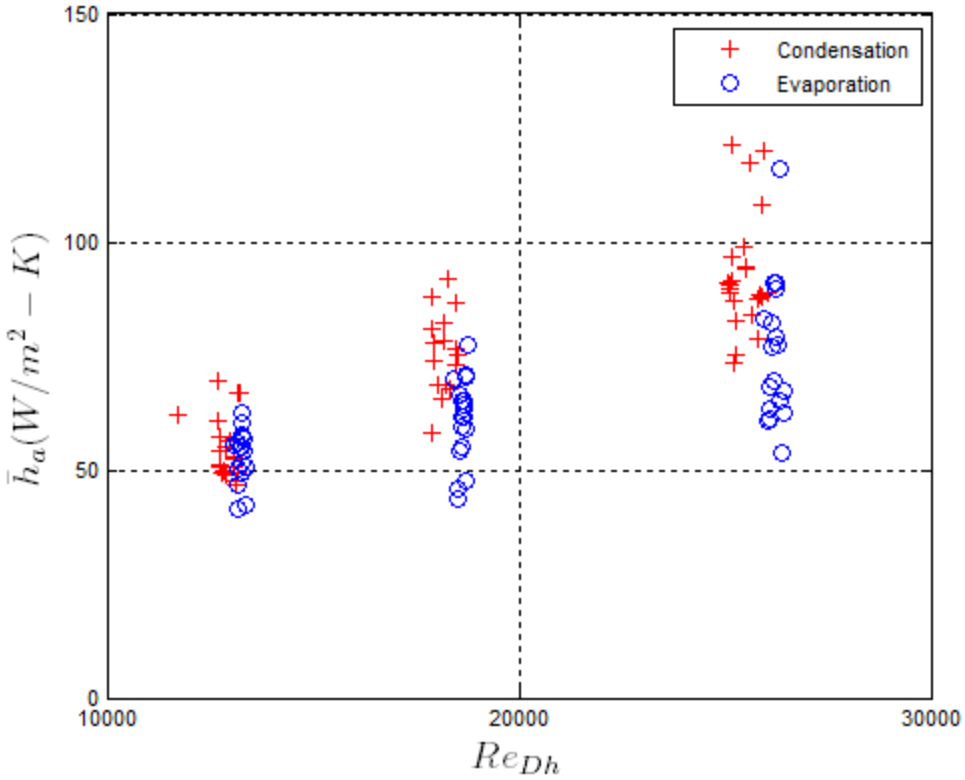

Figure 5-5 Average Convective Heat Transfer Coefficient versus Reynolds Number for all Condensation and Evaporation Data Points

In Figure 5-5 the heat transfer coefficients for the condensation and evaporation data do not display any significant differences although the condensation data points seem to have slightly higher values. This is probably due to the fact that the temperature difference between the air and plate surface temperature is much larger for the condensation data when compared to the evaporation data. The heat transfer coefficient should be independent of this temperature difference but could still instigate a small deviation like the one present in Figure 5-5. Overall, the difference between the heat transfer coefficients for the condensation and evaporation data is minimal.

The comparison of the average convective mass transfer coefficients for the condensation and evaporation data groups yields a striking difference. In Figure 5-6 the average convective mass transfer coefficient for the condensation and evaporation data groups are plotted versus the Reynolds number.

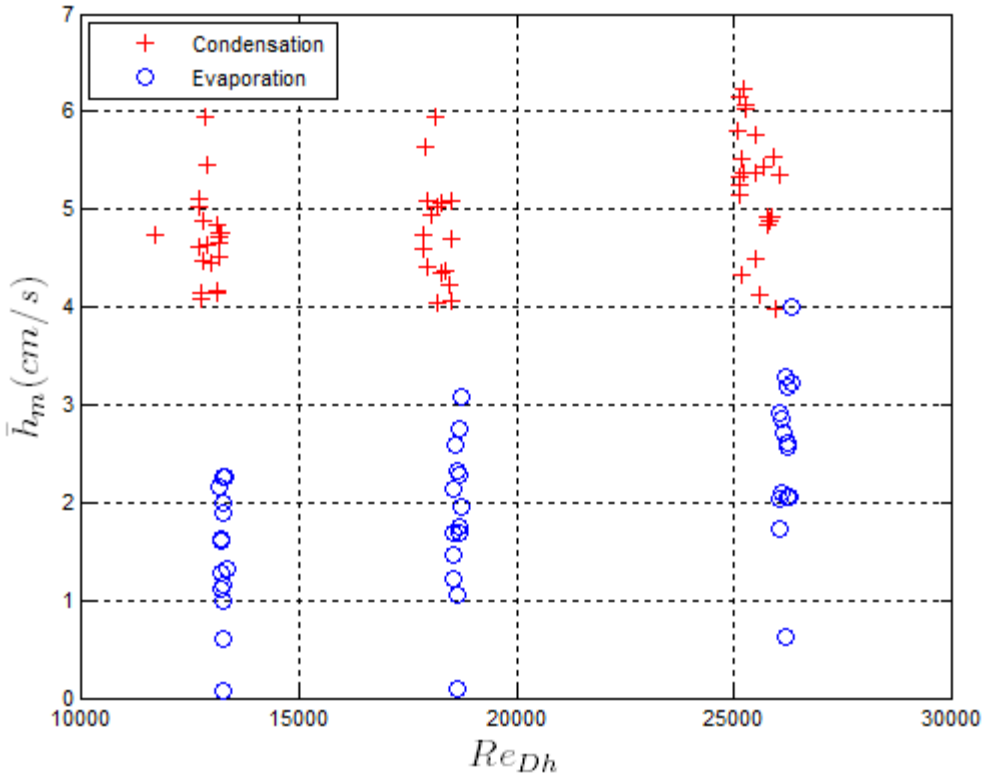

Figure 5-6 Average Convective Mass Transfer Coefficient for Condensation and Evaporation Data Points

In Figure 5-6 it is apparent that the condensation data points are substantially higher when compared to the evaporation data. This is probably due to the different way in which mass transport occurs through the wire mesh membrane during evaporation and condensation. During evaporation, mass transport only occurs through the capillary openings in the mesh plate surface. However, during condensation mass transfer occurs through the capillary openings and on the surface of the wires. The additional surface area of the wires allows for more water vapor to collect at the mesh plate surface and hence the values for the mass transfer coefficients for the condensation data will be higher. It is also pertinent to mention that the evaporation data points increase with respect to the Reynolds number while the condensation data points remain relatively constant.

5.3.2 Comparison of Solid Plates and Mesh Plates

This section investigates the differences between the mesh and solid plates. Figure 5-7 and Figure 5-8 display plots of the average convective heat transfer coefficients for the solid and mesh plates during condensation or evaporation conditions.

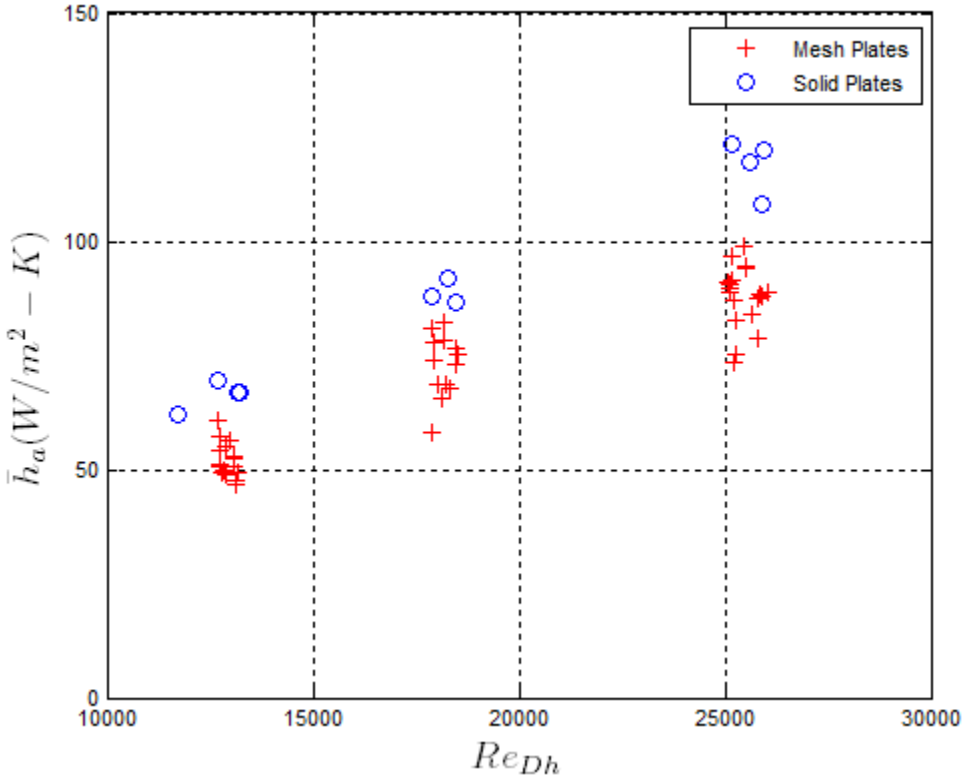

Figure 5-7 Average Convective Heat Transfer Coefficient of Mesh and Solid Plates for all Condensation Data Points

In Figure 5-7 it is apparent that the solid plate data points are higher than the mesh plate data points. A possible explanation for this is due to the presence of dropwise condensation on the solid plate surface. The formation of water droplets on the surface of the solid plates couldact as an enhancement to the surface by increasing the effective area and surface roughness. This is contrary to what might be anticipated, since the formation of water droplets on the plate surface would seem to create an additional resistance to heat transfer. However, the increase in surface area from the droplets could outweigh the added resistance and this is believed to be the result present in Figure 5-7. During condensation conditions large visible droplets are observed on the

solid plate surface. The droplets grow larger until overcome by gravity or vapor shear forces. The mesh plates do not form visible droplets on the plate surface during condensation. It is likely that very small droplets do form on the wires of the mesh plates but they would be many orders of magnitude smaller than the droplets which form on the solid plate surface. Therefore it is reasonable to assume that the mesh plates would not exhibit the same enhancement in heat transfer due to dropwise condensation as do the solid plates.

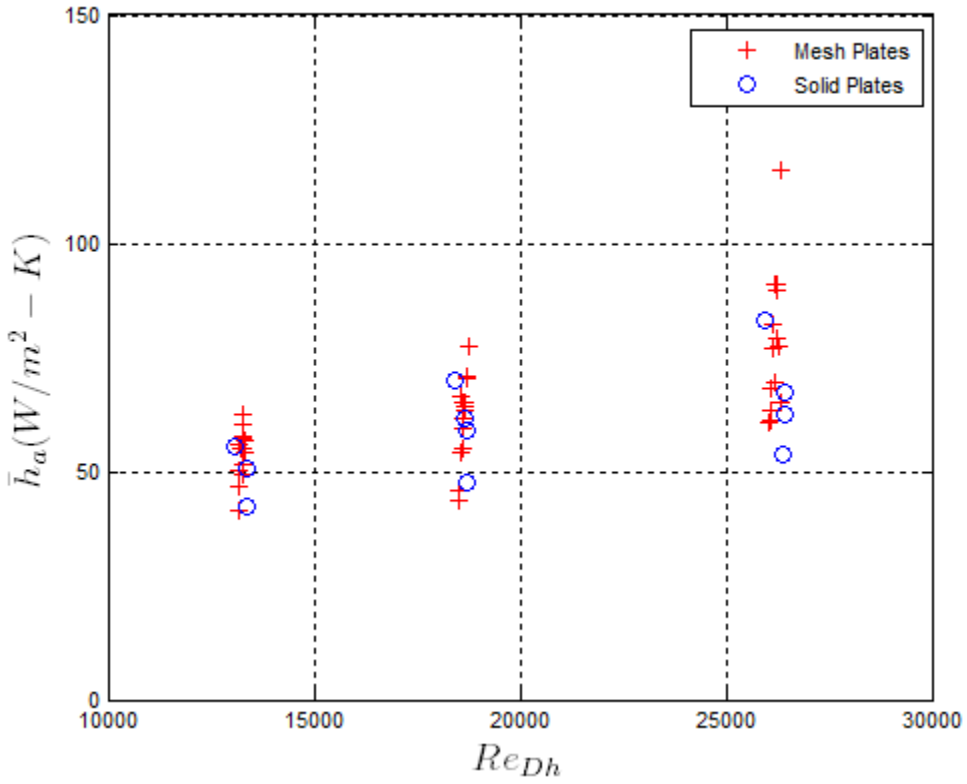

Figure 5-8 Average Convective Heat Transfer Coefficient of Mesh and Solid Plates for all Evaporation Data Points

Figure 5-8 shows the mesh and solid plate evaporation data points. It is obvious that the data collected from the solid and mesh plates is very similar. This indicates that mesh and solid plates exhibit the same behavior in the absence of condensate forming at the plate surface. It might be expected that the surface roughness of the mesh plates would produce higher values for the heat transfer coefficient when compared to the smooth surface of the solid plates. However, the data does not confirm this hypothesis and suggests that the difference in surface roughness

between the mesh and solid plates is not significant enough to manifest any differences in the heat transfer performance.

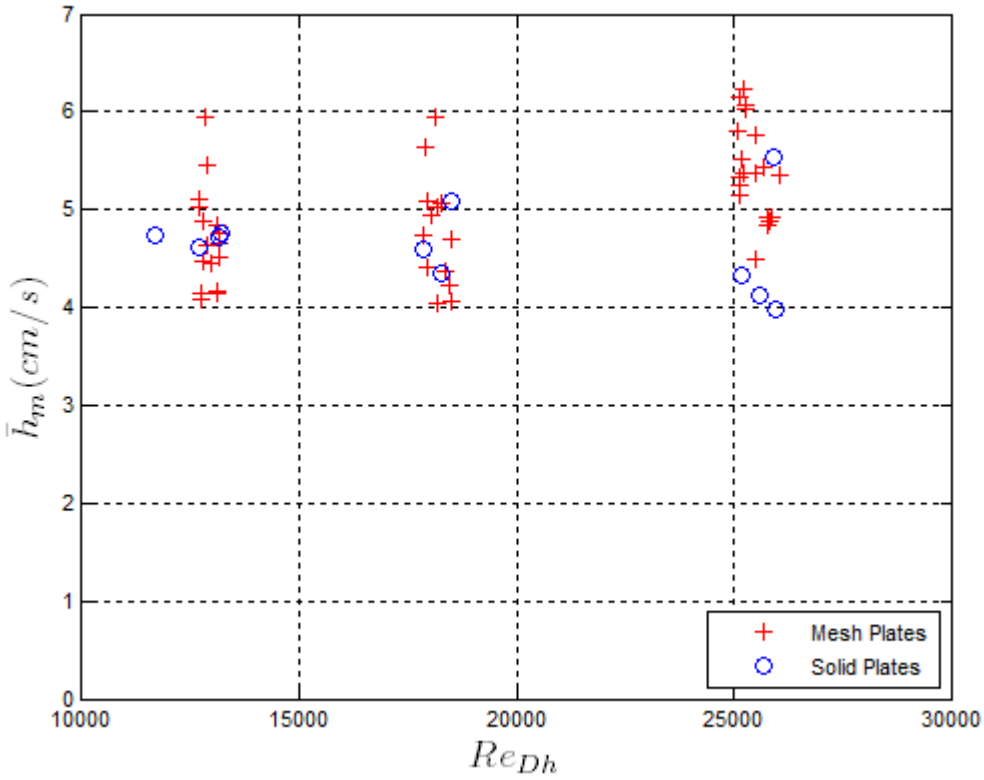

Figure 5-9 Average Convective Mass Transfer Coefficient of Mesh and Solid Plates for all Condensation Data Points

Figure 5-9 suggests that the rate of mass transfer to solid and mesh plates are nearly the same. This result indicates that the mesh plates do not increase the mass transfer rate significantly when compared to the solid plates. This evidence supports the theory of dropwise condensation enhancing the solid plate surface because the latent heat gain to the solid plate from the mass transport can be ruled out as the cause of the higher heat transfer present in Figure 5-7. If the solid plate data in Figure 5-9 would have shown higher mass transfer coefficients for the solid plates, then this could have been a reasonable explanation for the higher heat transfer coefficients of the solid plates in Figure 5-7. A plot of the mesh and solid plate data for the evaporation data is not shown because the solid plates do not allow mass transfer to occur.

5.3.3 Percent Open Area, Wire Diameter, Material and Plate Thickness

This section offers a discussion on several properties of the experimental plates which are believed to affect their performance. It was anticipated that the percent open area of the mesh plates would have a significant impact on the average convective heat and mass transfer coefficients. Plots of the average convective heat transfer coefficient for the condensation and evaporation data is shown versus the percent open area of the mesh plates in Figure 5-10 and Figure 5-11. The solid plates have zero percent open area and appear on the vertical axis of the plot.

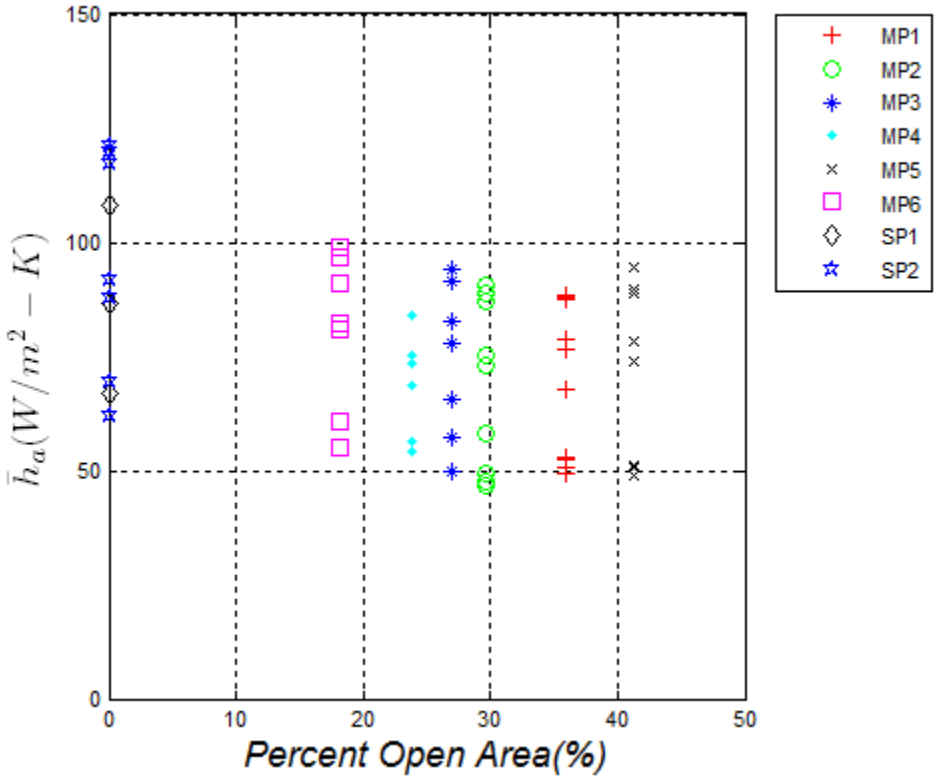

Figure 5-10 Average Convective Heat Transfer Coefficient vs. Percent Open Area for Condensation Data Points

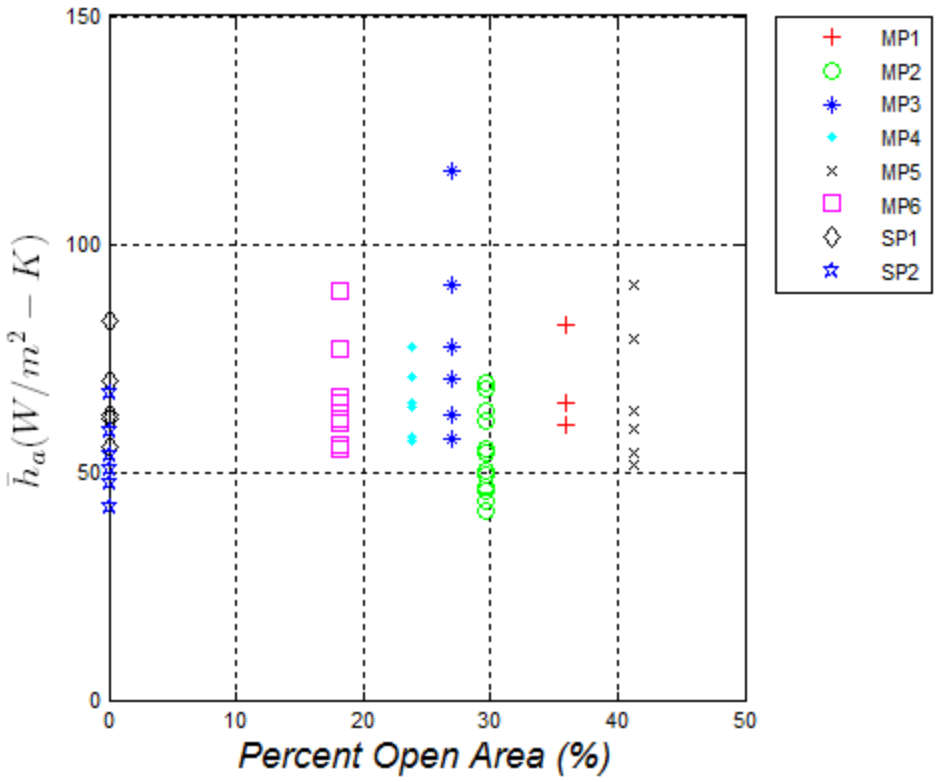

Figure 5-11 Average Convective Heat Transfer Coefficient vs. Percent Open Area for Evaporation Data Points

In Figure 5-10 there does not appear to be any indication of a significant trend present in the condensation data points. Nearly all the data points fall within the range of 50-100 $^{W}/_{m^2-K}$ If any observation can be made it would be that the heat transfer coefficient does not change with respect to the percent open area. This result is contrary to what is expected. It was hypothesized that mesh plates possessing a higher percent open area would exhibit higher heat transfer coefficients because they have more liquid surface area in direct contact with the air flow. In Figure 5-11 no trend is detected for the evaporation data. It should be noted that the data points for the solid plates display a noticeable shift between the condensation and evaporation data, again confirming the heat transfer enhancement from the presence of dropwise condensation.

In Figure 5-12 the average convective mass transfer coefficient is plotted versus the percent open area for the condensation data points and in Figure 5-13 the same is plotted for the evaporation data points.

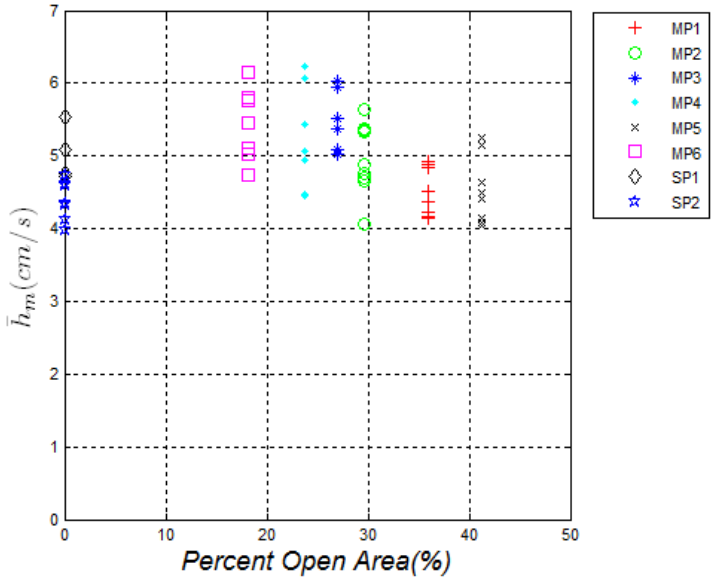

Figure 5-12 Average Convective Mass Transfer Coefficient vs. Percent Open Area for Condensation Data Points

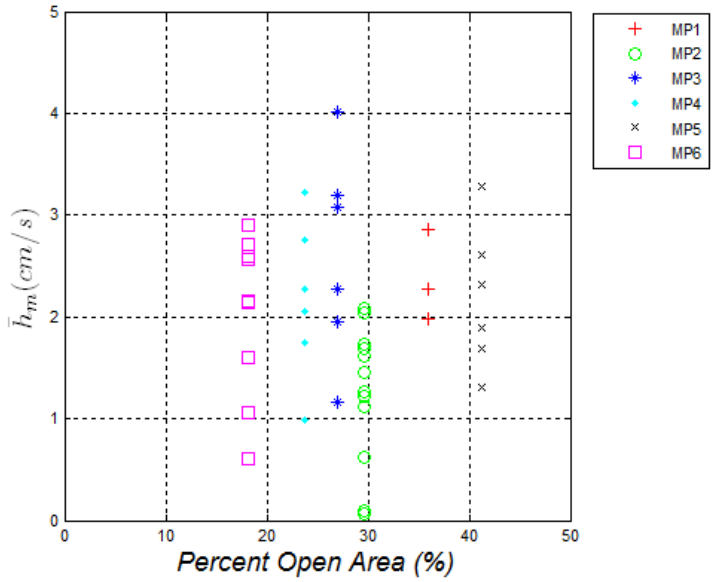

Figure 5-13 Average Convective Mass Transfer Coefficient vs. Percent Open Area for Evaporation Data Points

In Figure 5-12 a trend in the condensation data points is visible which indicates a decrease in the mass transfer coefficient as the percent open area is increased. It was assumed that the mass transfer coefficient for the condensation data would increase as percent open area was increased because more gas-liquid interface would be exposed at the mesh surface. However, the opposite result is observed from the data and could be explained by assuming that the wires of the mesh surface actually promote condensation better than the capillary openings in the mesh. The wires at the mesh surface could provide more surface area and hence more nucleation sites for condensate to form at the plate surface. In Figure 5-13 the evaporation data points do not display a noticeable trend. It is expected that the average convective mass transfer coefficient for the evaporation data points would increase noticeably as the percent open area is increased but this result is not evident.

The wire diameter of the mesh plates is directly tied to their percent open area and thickness. In general, as the wire diameter of the plates is increased the thickness of the plates increases and the percent open area decreases. It is conjectured that the larger wire diameters enhance the heat transfer by increasing the effective area at the mesh surface. Similarly, it is also hypothesized that the larger wire diameters create more surface area for liquid condensate to form and therefore should increase the rate of mass transfer. In Figure 5-14 the average convective heat transfer coefficient is plotted versus the wire diameter for the condensation data points. Figure 5-15 displays the average convective mass transfer coefficient versus the wire diameter for the condensation data points. In both of these plots the solid plate data does not have an effective wire diameter so the solid plate data is shown on the vertical axis.

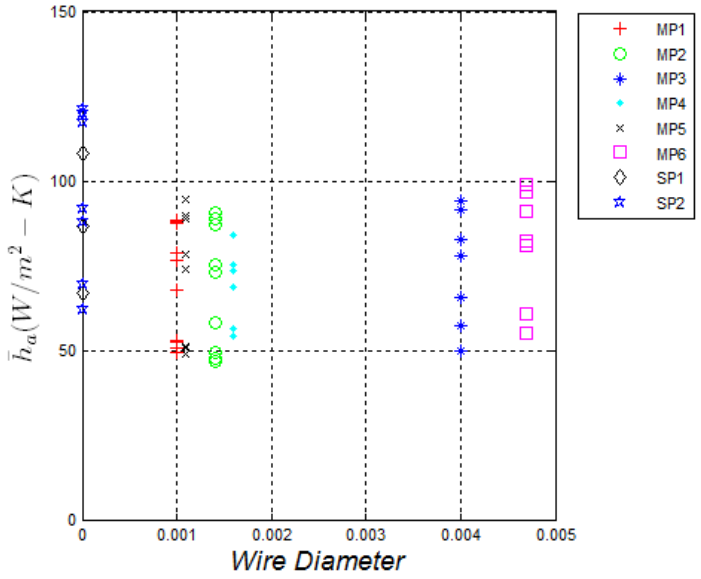

Figure 5-14 Average Convective Heat Transfer Coefficient vs. Wire Diameter for Condensation Data Points

In Figure 5-14 there does not appear to be an increase in the heat transfer coefficients as the wire diameter is increased. In fact, the data points seem to have nearly the same values with respect to wire diameter.

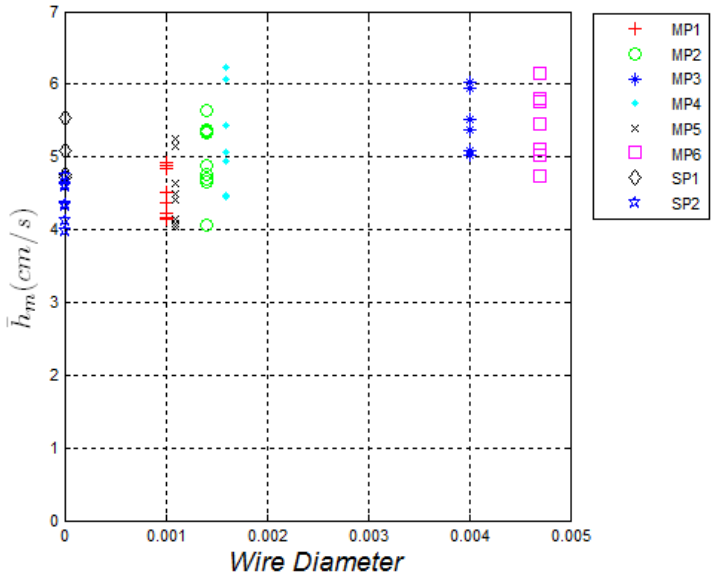

Figure 5-15 Average Convective Mass Transfer Coefficient vs. Wire Diameter for Condensation Data Points

In Figure 5-15 there is a slight increase in the convective mass transfer coefficient as the wire diameter becomes larger. This supports the hypothesis that the larger wire diameters promote mass transfer by providing more surface area and hence more nucleation sites for condensaiton to take place. The average heat and mass transfer coefficients versus the wire diameter for the evaporation data points do not display any tenable trends and therefore are not included in this sub-section. Plots of the evaporation data with respect to the wire diameter can be found in Appendix A.

It was hypothesized that the variation of the material of the plates would have some effect on their performance. This conjecture was based on the fact that the material of the plates can affect how it attracts liquid water. The polyester plates are considered to be a low energy material, thus it was assumed that condensing water vapor would adhere to this material better and improve the mass transfer. However, from all the collected data there is no definitive information which shows that the difference in the plate material affects their performance. In Appendix A, four figures are presented which plot the Stainless Steel plates against the Polyester plates displaying the average heat and mass transfer coefficients for the condensation and evaporation data points. It should be mentioned that the thickness of the plates, whether mesh or solid, has no impact on their performance. The thickness of all the plates is so small that its resistance to heat transfer is negligible. Therefore, based on this fact alone, it is reasonable to assume that the thickness of the plates has no significant impact on their performance.

5.3.4 Comparison with Heat Transfer Correlations

In this section the experimental data is compared to the Gnielinski and Dittus-Boetler heat transfer correlations (Incropera and Incropera 2007). These correlations are used to predict the average convective heat transfer coefficient as a function of Reynolds number for each of the four data groups. It is necessary to create separate correlation predictions for each data group because the correlations are functions of the inlet air temperature and humidity ratio. The Gnielinski correlation is also a function of surface roughness (ε). Therefore, two surface roughness values are chosen to represent the theoretical limits of the surface roughness for all the experimental plates. The lower value for surface roughness is set at 0.01 mm and the upper value is selected to be 1 mm. These values span two orders of magnitude and it is assumed that the actual surface roughness values of the mesh and solid plates are contained within these bounds.

The Dittus-Boetler correlation is based on the assumption that the surface roughness is negligible. Therefore, the Dittus-Boetler correlation is used to check the Gnielinski correlation to ensure that the prediction of the average convective heat transfer coefficient is accurate. Figure 5-16 presents the average convective heat transfer coefficients versus Reynolds number for the data points in data group (Ta_1,ω_1). Figure 5-17 displays the same data for group (Ta_2,ω_2). It is important to reiterate that the data in groups (Ta_1,ω_1) and (Ta_2,ω_2) contain the condensation data.

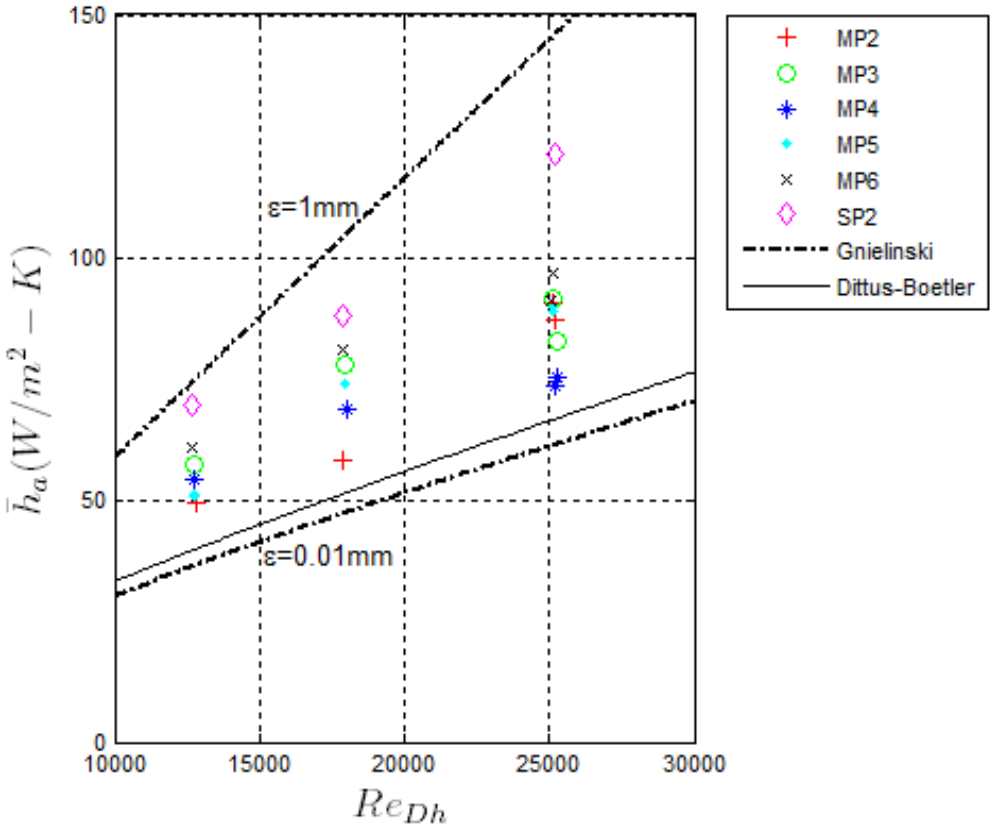

Figure 5-16 Average Convective Heat Transfer Coefficient vs. Reynolds Number for Data Group (Ta_1,ω_1)

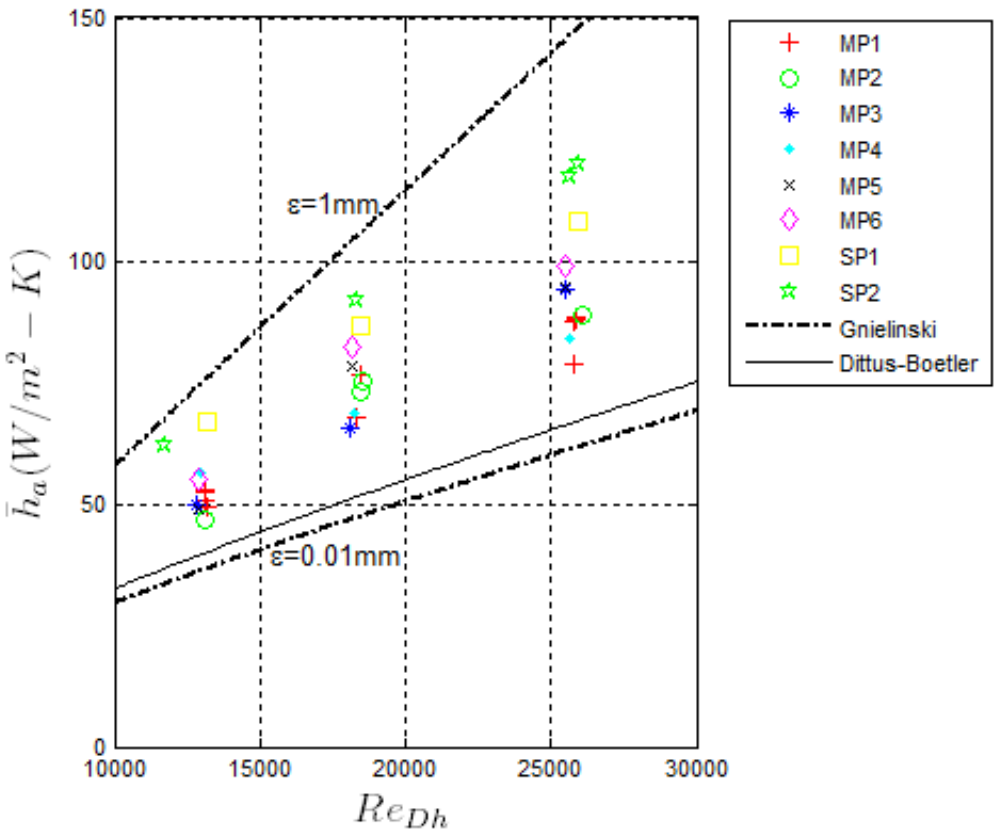

Figure 5-17 Average Convective Heat Transfer Coefficient vs. Reynolds Number for Data Group (Ta_2,ω_2)

In Figure 5-16 and Figure 5-17 it is apparent that the data points in each data group lie between the two Gnielinski correlation predictions for the average convective heat transfer coefficient. If the theoretical values for surface roughness of the plates are considered then the experimental data should be much closer to the Dittus-Boetler and Gnielinksi (with ε=0.01 mm) correlations. However, in both plots the average heat transfer coefficient data points in both groups are higher than the Dittus-Boetler and Gnielinksi (with ε=0.01 mm). There are two plausible explanations for why the data is higher than these correlations predict. The first reason is related to the surface temperature of the experimental plates. During condensation the experimental plate surface temperature is increased by the latent component of heat transfer accompanying the phase change of water vapor in the air. Therefore, the plate surface temperature is higher for the data points in Figure 5-16 and Figure 5-17 than for a scenario where no condensation takes place. An increase in plate surface temperature translates to a

direct increase in the heat transfers coefficient and hence explains why the data in the plots is higher than expected. The second explanation for the higher heat transfer coefficients is due to the presence of dropwise condensation on the mesh and solid plates. It is hypothesized that the water droplets which form on the plate increase the relative surface roughness of the plates which consequently enhances the heat transfer. It is also possible that irregularities in the mesh surface, such as folds or wrinkles, could also contribute to an increase in surface roughness. It is apparent that for both data groups the solid plates possess higher heat transfer coefficients than the mesh plates and thus are in closer proximity to the Gnielinski correlation with the higher value for surface roughness. This result is attributed to the fact that in dropwise condensation the solid plates have larger water droplets form on their surface. It is likely that the water droplets which form on mesh plates are several orders of magnitude smaller than those which form on the solid plates. Hence, the enhancement to heat transfer from these droplets is probably marginal. In Figure 5-16 the mesh plates MP3 and MP6 display the highest values for the heat transfer coefficients. This result is consistent with the observation that the heat transfer coefficient increases with surface roughness since the mesh plates MP3 and MP6 have the largest wire diameter and therefore should theoretically possess higher values for surface roughness. This result is not as evident in Figure 5-17 although it could be argued.

In Figure 5-18 and Figure 5-19 plots of the average convective heat transfer coefficient versus Reynolds number are shown for data groups (Ta_3,ω_3) and (Ta_4,ω_4). These data groups contain all the evaporation data points.

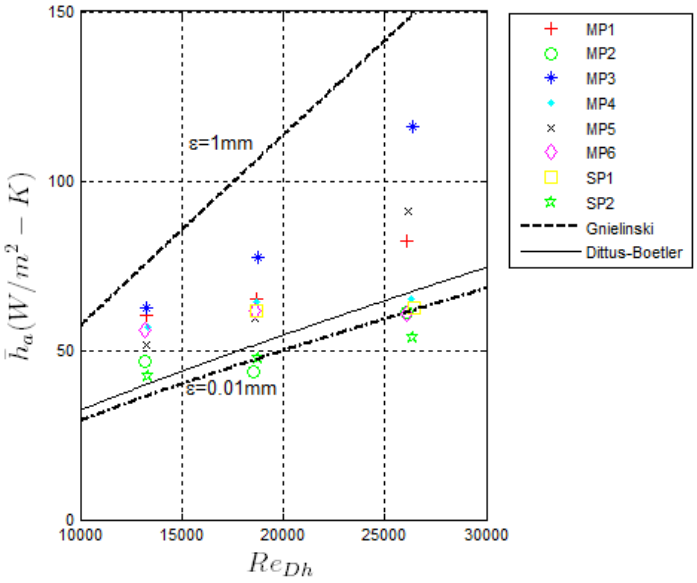

Figure 5-18 Average Convective Heat Transfer Coefficient vs. Reynolds Number for Data Group (Ta_3,ω_3)

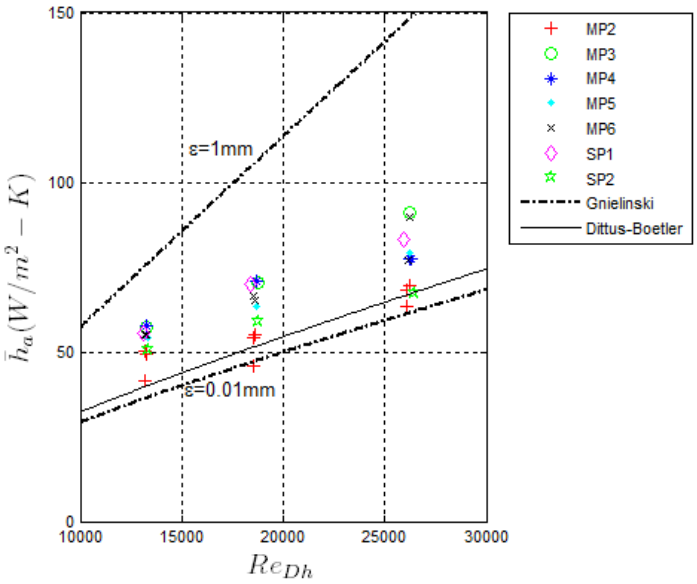

Figure 5-19 Average Convective Heat Transfer Coefficient vs. Reynolds Number for Data Group (Ta_4,ω_4)

In Figure 5-18 and Figure 5-19 it is observed that the data points exhibit lower heat transfer coefficients when compared to the plots of the condensation data groups (Ta_1,ω_1) and (Ta_2,ω_2). This apparent shift in the heat transfer coefficient data points can again be explained by the plate surface temperature. The surface temperature of the mesh plates is lowered due to the evaporation of liquid water at the plate surface. A decrease in the plate surface temperature creates a decrease in the heat transfer coefficient. In both of these plots the data points of the mesh plates lie much closer in proximity to the Dittus-Boetler and Gnielinsk (ε=0.01mm) correlations. This supplies evidence that the decrease in surface temperature of the mesh plates is likely responsible for the lower heat transfer coefficients. The solid plates do not experience evaporation at the plate surface and therefore the drastic change in the heat transfer coefficient is likely due to a different phenomenon. It is surmised that the absence of dropwise condensation on the solid plate surface is also responsible for the decrease in the heat transfer coefficient. The solid plate data points fall closer to Gnielinski (ε=1mm) for the condensation data groups and then appear closer to the Dittus-Boetler and Gnielinski (ε=0.01mm) for the evaporation data groups. This again shows that the absence of the droplets decrease the surface roughness and consequently the heat transfer enhancement. It should be noted that the difference in the inlet temperature of water varies by approximately 10°C between data groups (Ta3,ω3) and (Ta4,ω4). Despite this fact, the value of the heat transfer coefficient does not display a significant change between data groups. Therefore it is reasonable to assume that the average convective heat transfer coefficient is independent of the difference between the inlet air temperature and inlet water temperature.

5.3.5 Comparison with Mass Transfer Correlations

The mass transfer correlations are directly adopted from the heat transfer correlations by application of the heat and mass transfer analogy. Thus, the mass transfer correlations are developed by simply replacing the Nusselt and Prandtl numbers in the Gnielinski and Dittus-Boetler correlations with the analogous Sherwood and Schmidt numbers. These modifications to the Gnielinski and Dittus-Boetler correlations are used to predict the average convective mass transfer coefficient as a function of Reynolds number. The same surface roughness values are used in conjunction with the Gnielinski correlation are used for the calculation of the average

convective heat transfer coefficients. Figure 5-20 and Figure 5-21 show the average convective heat transfer coefficients versus Reynolds number for the data points in data groups (Ta_1,ω_1) and (Ta_2,ω_2).

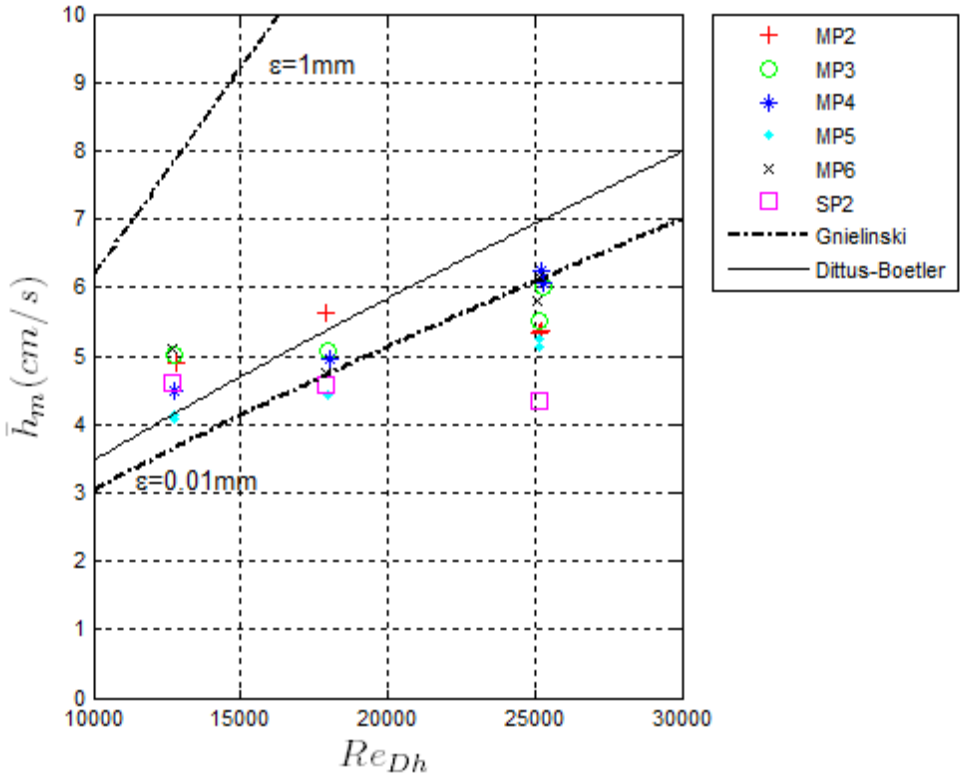

Figure 5-20 Average Convective Mass Transfer Coefficient vs. Reynolds Number for Data Group (Ta_1,ω_1)

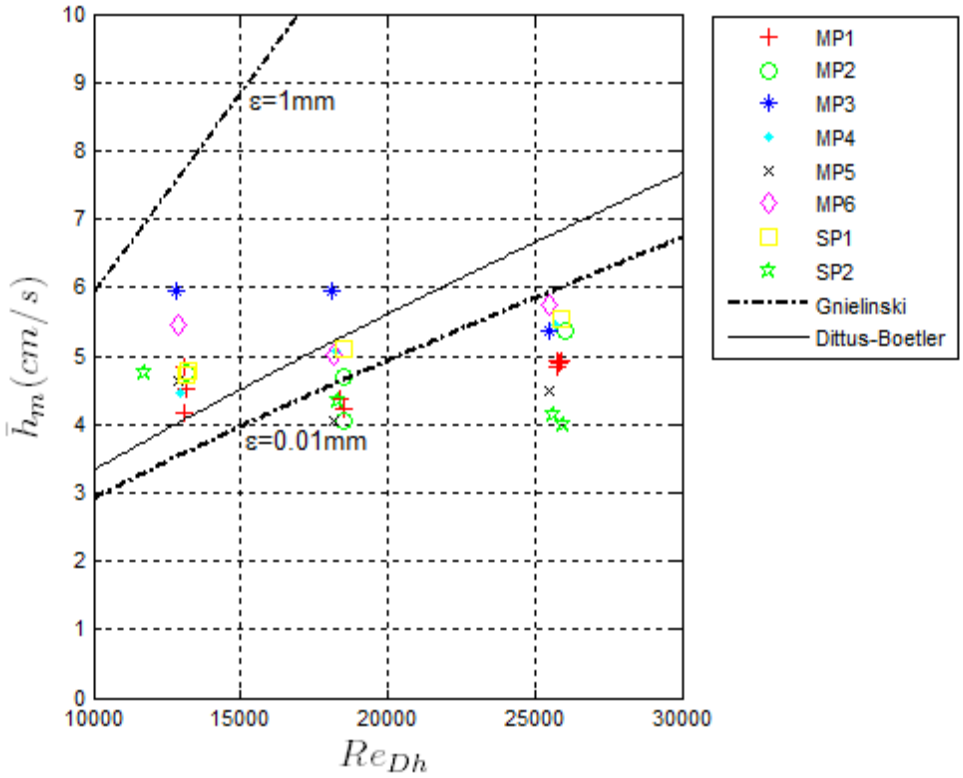

Figure 5-21 Average Convective Heat Transfer Coefficient vs. Reynolds Number for Data Group (Ta_2,ω_2)

In Figure 5-20 and Figure 5-21 the data points do not increase linearly as the correlations suggest. It is anticipated that the data points would be found in between the two Gnielinski predictions as is the case for the plots of the average convective heat transfer coefficient. However, the data points in these plots lie much closer to the Dittus-Boetler and Gnielinski (ε=0.01mm) correlations. At the low Reynolds number the data points are slightly above the Dittus-Boetler and Gnielinski (ε=0.01mm) correlations, at the mid-range Reynolds number they fall very close to the correlations, and at the high Reynolds number they fall slightly below. This indicates that the data points do not increase with respect to the Reynolds number but remain relatively constant. If the calculations of the mass transfer coefficients from the energy balance are accurate, then it is likely that the cause for the trend seen in these plots is due an inaccuracy in the heat and mass transfer analogy. In the next section the data is compared directly against the heat and mass transfer analogy to further investigate this proposition. Figure 5-22 and Figure

5-23 depict the average convective heat transfer coefficients versus Reynolds number for the data points in data groups (Ta_3,ω_3) and (Ta_4,ω_4).

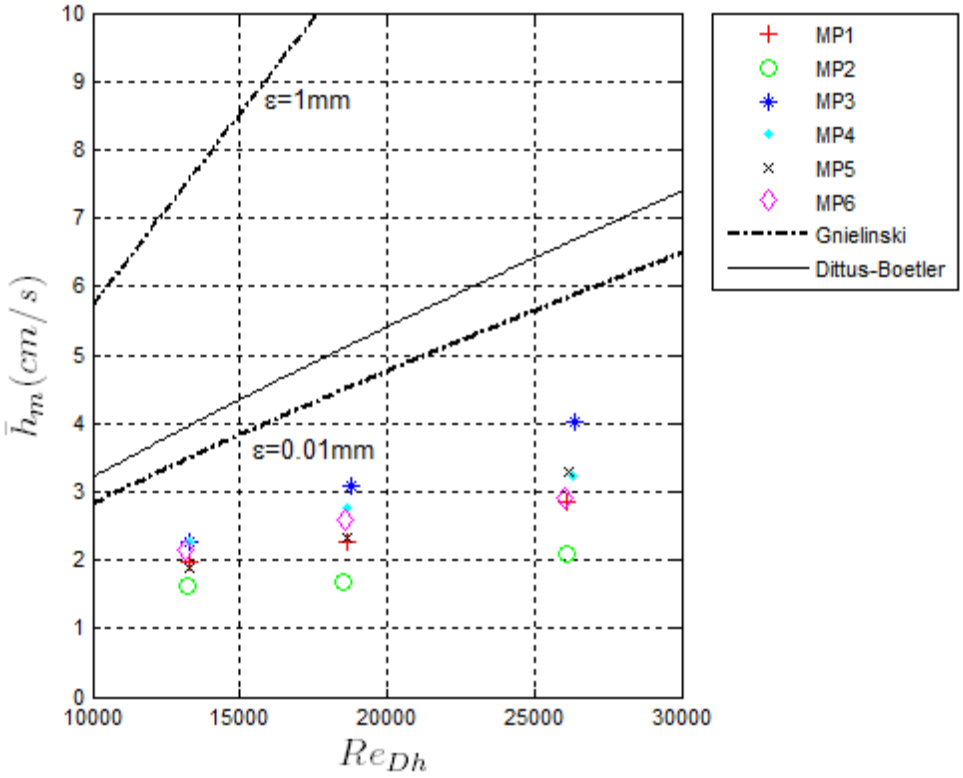

Figure 5-22 Average Convective Heat Transfer Coefficient vs. Reynolds Number for Data Group (Ta_3,ω_3)

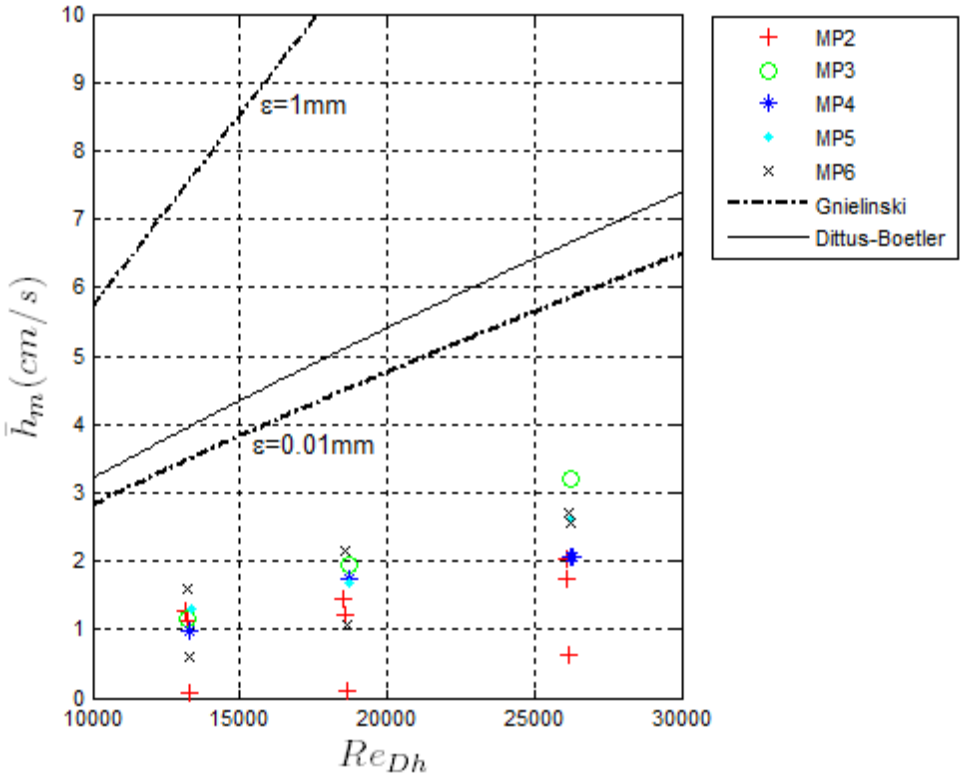

Figure 5-23 Average Convective Heat Transfer Coefficient vs. Reynolds Number for Data Group (Ta4,ω4)

In both plots the evaporation data points are much lower than what is predicted by the correlations. This could be due to the fact that during evaporation through the mesh plate mass transfer only occurs through the capillary openings in the mesh. The area for mass transfer is equal to the area of the gas-liquid interface which is clearly less than the total surface area of the mesh membrane. The heat and mass transfer analogy operates under the assumption that the area of the heat and mass transfer are equivalent. It is obvious that for the evaporation conditions these areas are not equal and therefore the mass transfer coefficients for the mesh plates will be less than what is predicted by correlation using the heat and mass transfer analogy. In the next section the experimental data is compared directly to the heat and mass transfer analogy.

5.3.6 Comparison with the Heat and Mass Transfer Analogy

The heat and mass transfer analogy is based on the premise that the dimensionless parameters which control the behavior of the thermal boundary layer have the same form as those which govern the concentration boundary layer. Hence, for a given geometry the heat and

mass transfer relations are interchangeable. This assumption has already been implemented in the previous section when determining the predicted values for the average convective mass transfer coefficient from the Gnielinski and Dittus-Boetler correlations. In this section, the ratio of the average convective heat transfer coefficient to the average convective mass transfer coefficient is plotted versus the Reynolds number. The theoretical ratio of the heat and mass transfer coefficients is derived from the heat and mass transfer analogy. The complete derivation is shown in detain in Sub-Section 4.6.6 of Chapter 4. The ratio of the actual heat and mass transfer coefficients is determined for data points and plotted with the theoretical values. The theoretical predictions of the ratio of heat and mass transfer coefficients are made separately for each data group since the groups are distinguished by the inlet air properties. Figure 5-24 and Figure 5-25 depict the actual and theoretical ratios of the average convective heat and mass transfer coefficients versus Reynolds number for the condensation data points in data groups (Ta_1,ω_1) and (Ta_2,ω_2).

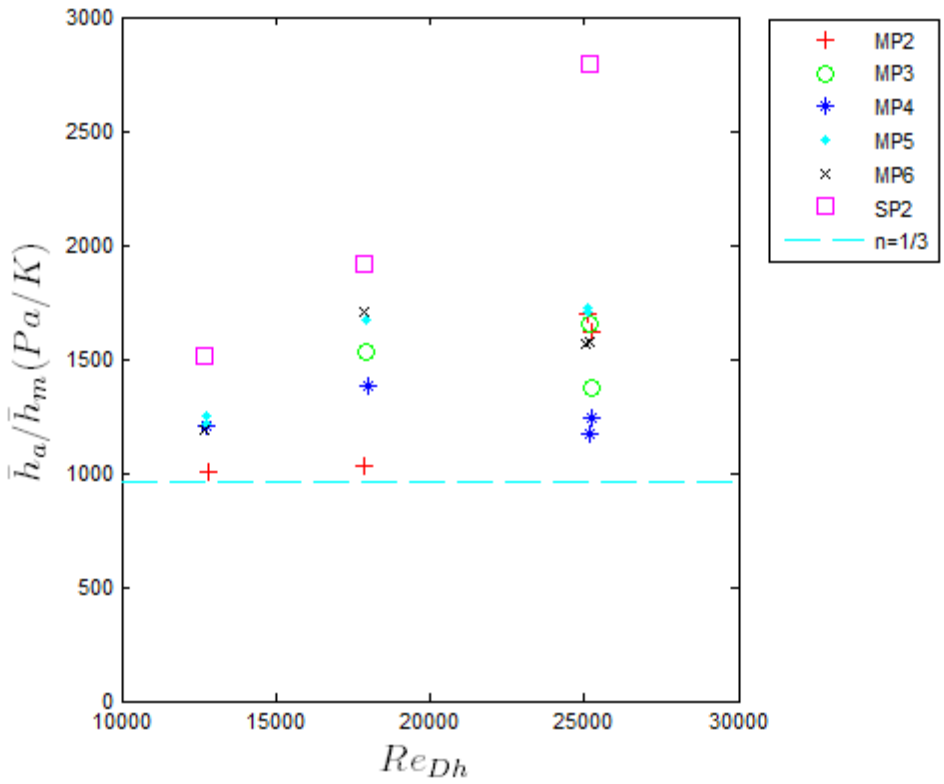

Figure 5-24 Ratio of Average Convective Heat and Mass Transfer Coefficients for Data Group (Ta_1,ω_1)

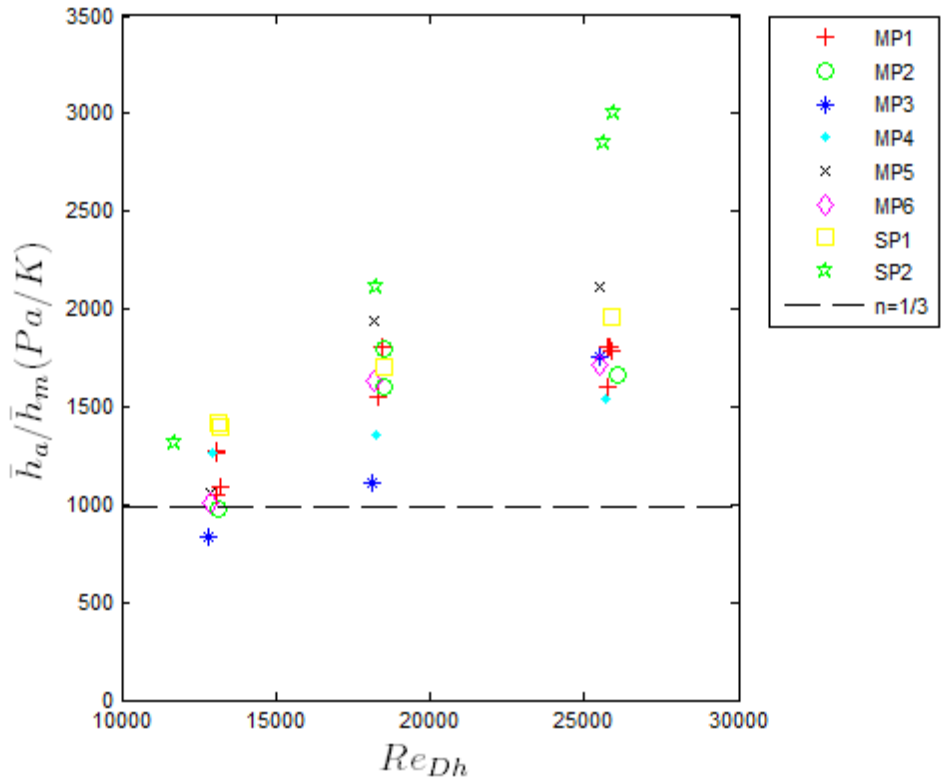

Figure 5-25 Ratio of Average Convective Heat and Mass Transfer Coefficients for Data Group (Ta_2,ω_2)

It is immediately apparent that the actual values for the ratio of heat and mass transfer coefficients are much larger than the theoretical values. In Figure 5-24 there are a few data points which lie close to the predicted ratio at the low Reynolds number but the majority of the data is well above. This result agrees with the observations made for the condensation data in the previous section. In the previous section the condensation data points for the average mass transfer coefficients appear to remain relatively constant and a slightly lower in value when compared to the correlations. This behavior of the mass transfer coefficient would cause us to expect the ratio of heat and mass transfer to be higher than expected and deviate more as the Reynolds number increases. Both these results can be observed for the condensation data plots. These plots confirm that there is clearly an issue with employing the use of the heat and mass transfer analogy. Figure 5-26 and Figure 5-27 displays the actual and theoretical ratios of the average convective heat and mass transfer coefficients versus Reynolds number for the evaporation data points in data groups (Ta_3,ω_3) and (Ta_4,ω_4).

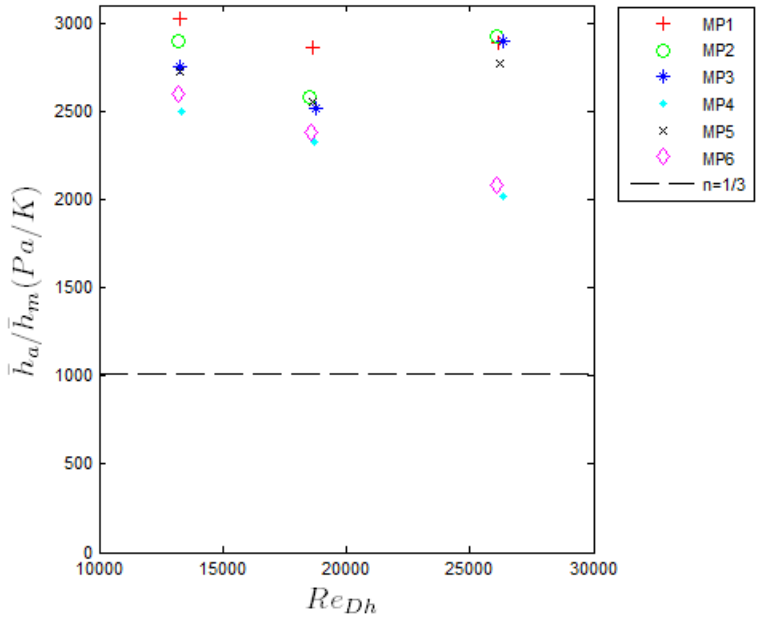

Figure 5-26 Ratio of Average Convective Heat and Mass Transfer Coefficients for Data Group (Ta_3,ω_3)

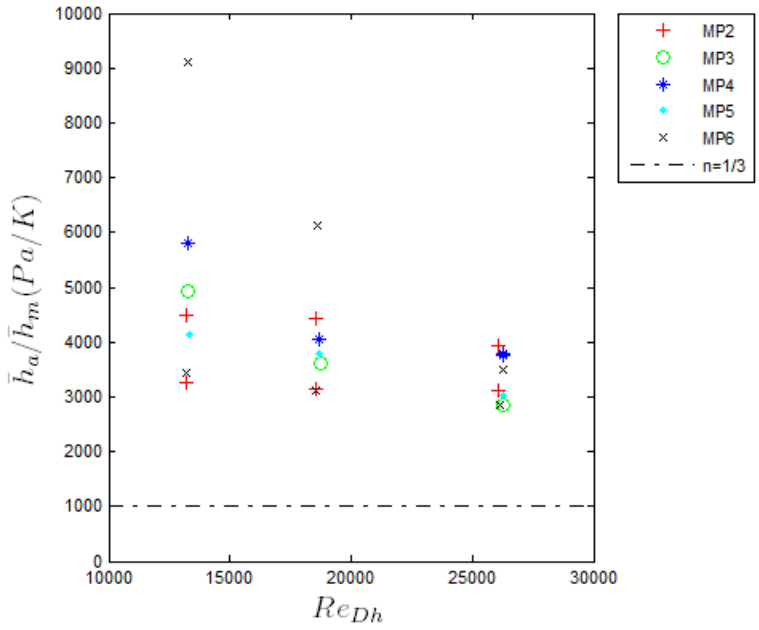

Figure 5-27 Ratio of Average Convective Heat and Mass Transfer Coefficients for Data Group (Ta_4,ω_4)

The evaporation data points lead to similar observations that are made from the condensation data points. Again, it is evident that the actual ratios of the heat and mass transfer

coefficient are much greater than the theoretical. The evaporation data points deviate even more from the theoretical than do the condensation data points. In the previous section the plots of the average convective mass transfer coefficients for the evaporation data points are found well below the correlations. Therefore, it would be expected that the ratio of heat and mass transfer would deviate more in magnitude than the condensation data points. The conclusion is reached that the heat and mass transfer analogy is not valid for the wire mesh membrane.

The reason the heat and mass transfer analogy breaks down is because the wire mesh membrane allows heat transfer to occur across the entire membrane area but limits the area where mass transfer can take place. The heat and mass transfer analogy operates under the assumption that these areas are equal. The condensation data fits the analogy better because mass transfer is believed to occur across the entire surface of the wire mesh. However, the condensate still must travel to the gas-liquid interface within a capillary opening to become absorbed into the liquid flow stream. Therefore, it is unknown whether all the condensate which forms on the membrane surface is transported to the liquid phase. The evaporation data deviates from the heat and mass transfer analogy even more than the condensation data. This is because mass transport can only occur at the gas-liquid interface within the capillary openings. If there were no membrane present it is likely that the data would agree much better with the theoretically predicted values from the heat and mass transfer analogy.

5.3.7 Comparison with the Heat and Mass Transfer Analogy using Percent Open Area

The heat and mass transfer analogy does not compare very well with the experimental data when using the plate surface area to calculate the ratio of heat and mass transfer coefficients. As previously mentioned, this is most likely due to the fact that the plate surface area does not adequately represent the actual area of mass transport. Therefore, in this sub-section, the percent open area of each wire mesh plate is used to determine the ratio of heat and mass transfer coefficients. It is surmised that the percent open area will give a better estimate of the actual area of mass transfer, especially in the case of evaporation, where the mass transport is known to occur only through the area defined by the percent open area. It is hypothesized that the actual area of mass transfer during condensation is greater than the percent open area, since liquid condensate can also form on the surface of the wires. It is expected that by using the percent open area to calculate the ratio of heat and mass transfer coefficients, the agreement

between the evaporation data with the heat and mass transfer analogy will be imporved. It also is expected that by using the percent open area the condensation data will appear below the theoretical predication from the heat and mass transfer analogy. Plots of the ratio of heat and mass transfer coefficients are given for each of the condensation and evaporation data groups. Figure 5-28 and Figure 5-29 display the ratio of heat and mass transfer coefficients versus Reynolds number for the condensation data groups. It should be mentioned that the solid plate data points do not possess a percent open area and therefore these data points are identical to those calculated from the plate surface area.

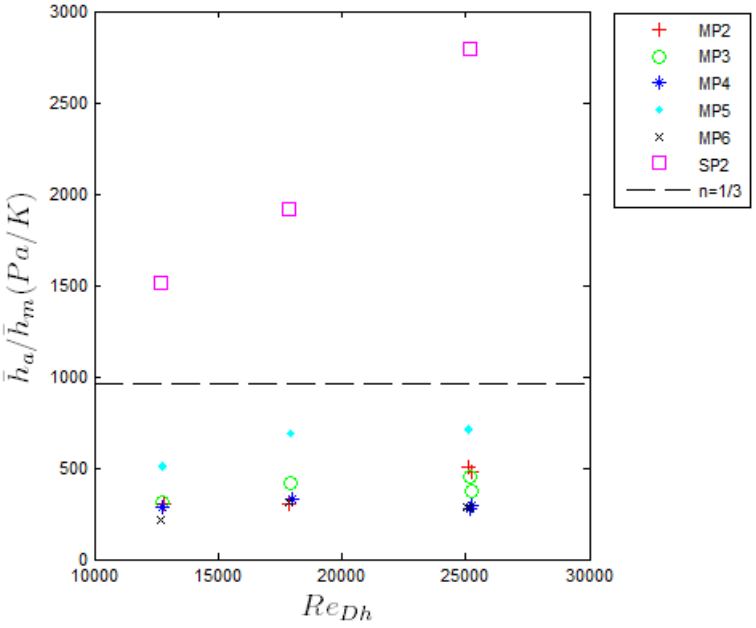

Figure 5-28 Ratio of Heat and Mass Transfer Coefficients using Percent Open Area for Data Group (Ta_1,ω_1)

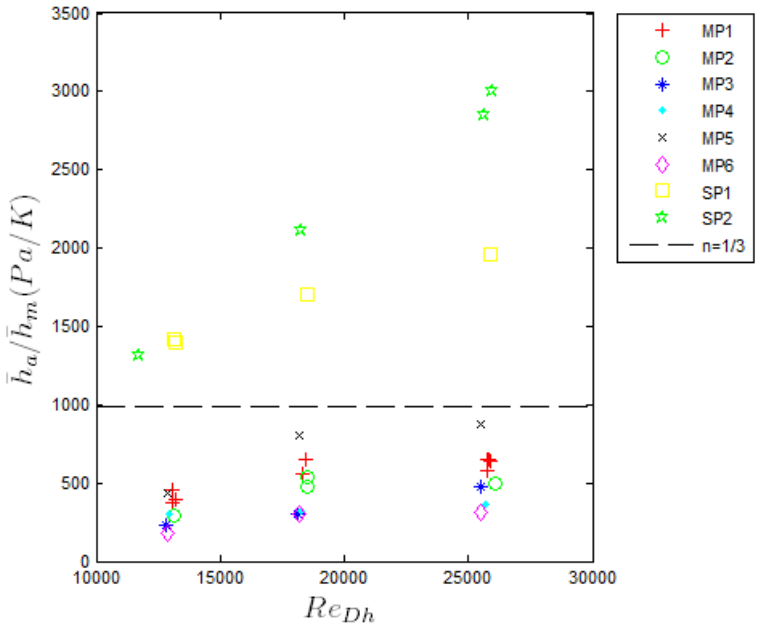

Figure 5-29 Ratio of Heat and Mass Transfer Coefficients using Percent Open Area for Data Group (Ta_2,ω_2)

It is apparent that the mesh plate data points for both condensation data groups appear below the theoretical predicted values from the heat and mass transfer analogy. This supports the hypothesis that the actual area of mass transfer is greater than the percent open area. If the data using the percent open area is compared with the data using the plate surface area (Figure 5-24 and Figure 5-25), it is evident that the data shifts from above to below the theoretical predicted values from the heat and mass transfer analogy. When using the plate surface area, the data generally falls above the theoretical value and when using the percent open area the data points fall below. Overall, the data points when using the percent open area lie closer to the predicted values from the heat and mass transfer analogy. Therefore, it is assumed that the actual area of mass transfer is found between the plate surface area and the percent open area. Furthermore, the value of the actual area of mass transfer is more than likely closer to the percent open area than the plate surface area.

Figure 5-30 and Figure 5-31 show the ratio of heat and mass transfer coefficients versus Reynolds number for the evaporation data groups. The plots are shown with the same dimensions of the plots using the plate surface area (Figure 5-26 and Figure 5-27).

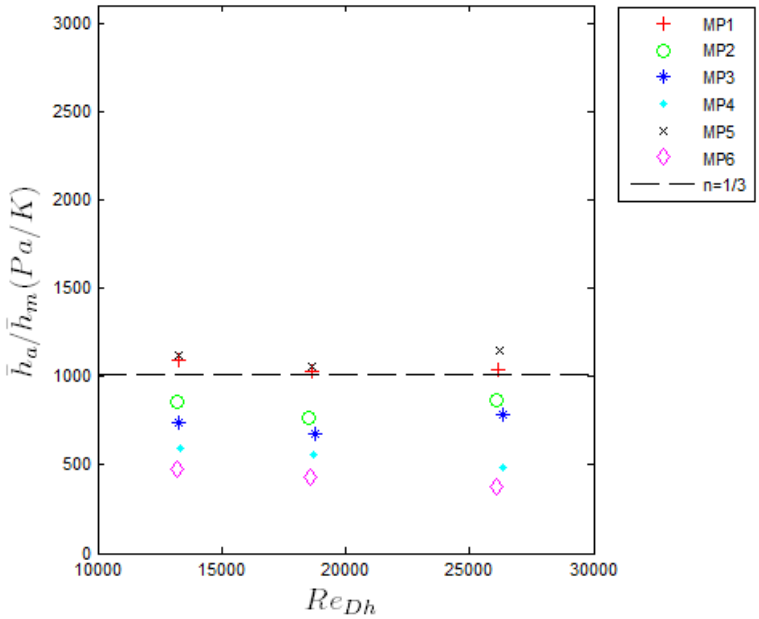

Figure 5-30 Ratio of Heat and Mass Transfer Coefficients using Percent Open Area for Data Group (Ta_3,ω_3)

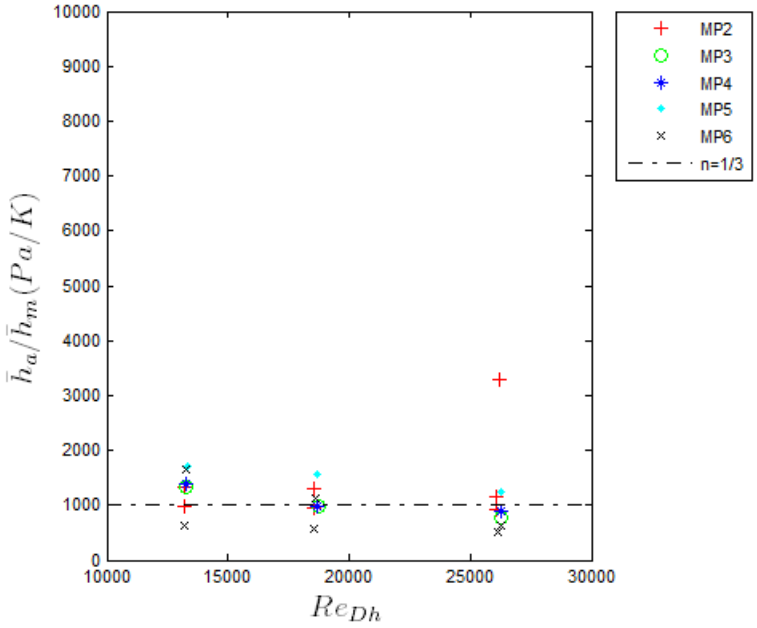

Figure 5-31 Ratio of Heat and Mass Transfer Coefficients using Percent Open Area for Data Group (Ta_4,ω_4)

It is immediately apparent that the data points fall much closer to the theoretically predicted values from the heat and mass transfer analogy when using the percent open area to calculate the heat and mass transfer coefficients. When using the plate surface area the data points deviated greatly from the theoretical values. Therefore, it is apparent that the percent open area is close to the actual area of mass transfer.

Overall, the experimental data compares more accurately with the heat and mass transfer analogy when using the percent open area versus the plate surface area. The evaporation data showed a great improvement with respect to the heat and mass transfer analogy. The condensation data showed that when using the percent open area the experimental data falls below the predicted values from the heat and mass transfer analogy. This result confirms the hypothesis that the actual area of mass transfer during condensation lies between the percent open area and the plate surface area but is likely closer to the percent open area.

Chapter 6 Conclusions

6.1 Introduction

In this work an experimental facility was designed to test the heat and mass transfer performance of wire mesh media in the application of membrane based dehumidification and evaporative cooling. Six square weave wire mesh plates were tested in the facility along with two solid plates. The wire mesh plates varied in wire diameter, mesh count, capillary square size, percent open area, thickness, surface roughness, and relative wettability. The impact of these properties on the heat and mass transfer performance were investigated. The wire diameter of the mesh membranes ranged from 25 – 100 μm and the capillary square size from about 40 – 120 μm. There were also two solid plates tested in the facility. The solid plates constructed from metal shims and simulated wire mesh membranes with zero percent open area. The solid plates supplied conventional data to which the mesh plates could be compared.

The test section of the experimental facility essentially functions as a flat plate heat exchanger in which the wire mesh membrane is used to separate liquid water and air flow streams. The test section consists of a narrow air duct and a plate apparatus. The test section is housed in a temperature and humidity controlled climactic chamber. There are two main operating conditions employed in the facility. The first is used to promote condensation on the wire mesh membrane. The condensation conditions are achieved by setting the air temperature to around 50°C and the relative humidity to about 80%. The liquid water temperature is then set below the dew point to ensure condensate forms at the membrane surface. The second operating condition allows for liquid water to evaporate through the wire mesh membrane and into the air. The evaporation conditions are reached by setting the air temperature to approximately 32°C and the relative humidity to about 10%. The liquid water temperature is maintained well above the dew point temperature of the air. During the condensation and evaporation operating conditions the air flow rate is varied to collect data for a range of increasing Reynolds numbers. Distilled water is circulated through the test section using two magnetically coupled gear pumps. A constant temperature bath maintains the water delivered to the test section at a desired temperature. A filter and air trap are used to remove contaminants and air bubbles from the liquid flow stream before it enters the test section. The temperature of the water is measured at the inlet and outlet of the test section using two 30kΩ thermistors. The surface temperature of the

wire mesh membrane is also measured using a single 30kΩ thermistor. The inlet water flow rate was measured using a coriolis mass flow meter. The air temperature was measured at the inlet and outlet of the test section using four 10 kΩ thermistors. The relative humidity of the air was also measured at the inlet and outlet of the test section. The mass flow rate of the air was determined by measuring the pressure drop across an orifice plate in a section of circular duct, downstream of the test section. Measurements were collected from the facility using a data acquisition unit and a PC running Labview 8.5 software. Using the measurements collected from the facility an energy balance was conducted on the test section to calculate the mass transported from the air to water (or vice versa) and the sensible component of heat transfer from the air to water. The average air-side convective heat transfer was calculated from the sensible component of the heat transfer, the difference between the air and surface temperatures, and the area of the membrane. The average convective mass transfer coefficient was determined from the mass transport, the difference between the air and surface concentrations, and the membrane area. The average convective heat and mass transfer coefficients were calculated for each of the experimental plates at a low, medium and high Reynolds number. The data falls within a Reynolds number range of 10,000-30,000.

The average convective heat and mass transfer coefficients were used to evaluate the performance of experimental plates. The data points were then compared to see how the various properties of the membranes affect their performance. The condensation and evaporation data were also compared to one another in order to investigate the behavior of the plates during the different phenomena. The mesh plate membranes were compared to the solid plates in order to see if any advantages were obtained by using the wire mesh. The experimental data was then compared to theoretical predictions of the heat and mass transfer coefficients developed from the Gnielinski and Dittus-Boetler heat transfer correlations and by invoking the heat and mass transfer analogy. The conclusions formulated by investigating the experimental data are summarized in the next section. In the final section several recommendations are made for future research into membrane based dehumidification and evaporative cooling using wire mesh media.

6.2 Conclusions from the Data

The conclusions drawn from examining the data collected in this work are summarized by the following:

- Membrane based dehumidification and evaporative cooling were achieved using the square weave wire mesh media. The wire mesh membrane with the largest pore openings was MP6 with a capillary square size of 119.4 μm.
- The average air-side convective heat transfer coefficients for the mesh plate data in condensation and evaporation, fall within a 50 – 100 $^{W}/_{m^2-K}$ range and increase linearly with respect to Reynolds number.
- The majority of the average convective mass transfer coefficients for the condensation data are found within a range of 4 – 6 $\frac{cm}{s}$ and do not increase linearly with respect to the Reynolds number.
- The majority of the average convective mass transfer coefficients for the evaporation data fall within a range of 1 – 4 $\frac{cm}{s}$ and increase linearly with respect to Reynolds number.
- The mass transfer coefficients are higher for the condensation data apparently because condensate can form on the entire membrane surface while during evaporation mass transport is limited to the gas-liquid interface created within the capillary openings of the mesh.
- The solid plates have higher heat transfer coefficients than the mesh plates during condensation because the condensate forms large liquid droplets which act as a surface enhancements.
- The mesh and solid plate data display similar values for the mass transfer coefficients during condensation and for the heat transfer coefficients during evaporation.
- The mesh plate data does not show any significant trends or correlations with respect to percent open area, wire diameter, material, or thickness. The only exception is the mass transfer coefficient data during condensation which decreases with respect to percent open area and increases with respect to wire diameter. Since the mesh plates with the lowest percent open area have the largest

wire diameter it is concluded that they provide more surface area for condensate to form and hence increase the mass transfer.

- The heat transfer coefficients from the condensation data are higher than expected when compared with the theoretical predictions from the Gnielinski and Dittus-Boetler correlations. It is hypothesized that the data is higher because of either the presence of dropwise condensation or the increase in the plate surface temperature from the latent component of heat transfer accompanying condensation.
- The heat transfer coefficients for the evaporation data compare better with the correlations. This is probably due to the absence of condensate on the plate surface.
- The mass transfer coefficients for the condensation data agree well with the theoretically predicted values from the correlations. However, the data does not increase linearly as the correlation suggests.
- The mass transfer coefficients for the evaporation data are significantly lower than the values predicted by the correlations. It is expected that this result comes from using the plate surface area instead of the percent open area to define the area of mass transfer.
- The condensation and evaporation data do not agree well with theoretical predictions from the heat and mass transfer analogy when using the plate surface area as the area of mass transfer. The experimental data agreed much better with the heat and mass transfer analogy when using the percent open area to define the area of mass transfer.
- The actual area of mass transfer during condensation is a value between the plate surface area and the percent open area, but closer to the percent open area. For the evaporation data the actual area of mass transfer is best estimated by the percent open area

6.3 Recommendations for Future Work

There are several recommendations and suggestions to be made for researchers who are pursuing membrane based applications:

- An array of temperature measurements should be taken across the entire membrane surface to produce a more accurate reading of the heat and mass transfer coefficients.
- It would be beneficial to study membrane based applications for laminar and turbulent flow conditions. It would also be practical to collect data in a test section which has hydrodynamic fully developed flow as opposed to entry length conditions.
- It would be good to physically observe the phenomena which take place at the membrane surface during condensation. Especially droplet formation and absorption through the gas-liquid interface
- It would further advance research in membrane based applications to test the wire mesh membrane for a variety of different geometries, orientations and weaves.
- It would be of benefit to study the durability and longevity of wire mesh media used in the application of dehumidification and evaporative cooling.
- It would be an improvement to develop a way to directly collect and measure the amount of mass transferred from one medium to the other in order to confirm the energy balance method.

References

ASHRAE. 2005. ASHRAE handbook. fundamentals.

ASME. 2004. Measurement of fluid flow in pipes using orifice, nozzle, and venturi: ASME standard MFC-3M-2004.

Bird, R. Byron, Warren E. Stewart, and Edwin N. Lightfoot. 2002. *Transport phenomena*. 2nd ed. New York: J. Wiley.

Cochran, Michael, Jared Goodnight, Bruce Babin, and Steve Eckels. 2009. Condensing dryers with enhanced dehumidification using surface tension elements. *Applied Thermal Engineering* 29 (4): 723-31.

De Gennes, Pierre-Gilles, Françoise Brochard-Wyart, and David Quéré. 2004. *Capillarity and wetting phenomena: Drops, bubbles, pearls, waves* [Gouttes, bulles, perles et ondes.]. New York: Springer.

DOE. U.S. household electricity uses: A/C, heating, appliances. [cited 6/8/2011 2011]. Available from http://www.eia.gov/emeu/reps/enduse/er01_us.html (accessed 6/8/2011).

Figliola, R. S., and Donald E. Beasley. 2006. *Theory and design for mechanical measurement*s. 4th ed. Hoboken, N.J.: John Wiley.

Incropera, Frank P., and Frank P. Incropera. 2007. *Fundamentals of heat and mass transfe*r. 6th ed. Hoboken, NJ: John Wiley.

Johnson, Drew. 2003. Analysis of heat and mass transfer phenomena in hollow fiber membranes used for evaporative cooling. *Journal of Membrane Scienc*e 227 (1): 159-71.

Kern, Donald Quentin. 1950. *Process heat transfe*r. 1st ed. New York: McGraw-Hill.

Loeb, S. 2003. Membrane evaporative cooling to 30° C or less. *Annals of the New York Academy of Science*s 984 (1): 515-27.

M. CONDE ENGINEERING. Thermophysical properties of humid air, models and background. 20072010]. Available from http://www.mrc-eng.com/Downloads/Moist%20Air%20Props%20English.pdf.

Molki, M., and E. M. Sparrow. 1986. EMPIRICAL CORRELATION FOR THE AVERAGE HEAT TRANSFER COEFFICIENT IN CIRCULAR TUBES. *Journal of Heat Transfe*r 108 (2): 482-4.

Moran, Michael J., and Howard N. Shapiro. 2004. *Fundamentals of engineering thermodynamic*s. 5th ed. Hoboken, NJ: Wiley.

Munson, Bruce Roy, Donald F. Young, and T. H. Okiishi. 2002. *Fundamentals of fluid mechanic*s. 4th ed. New York: Wiley.

Newbold, D. D., S. B. McCray, D. L. Millard, and R. Ray. 1996. Performance of a membrane-based condensate-recovery heat exchanger. *SAE Transaction*s 105 (1): 268-77.

Newbold, DD. 1993. Analysis of a membrane-based condesate recovery heat exchanger (CRX).

Noyes, G. 1993. Microporous hydrophobic hollow fiber modules for gas-liquid phase separation in microgravity. *NASA STI/Recon Technical Report* A 95 : 91664.

Ower, Ernest, and R. C. Pankhurst. 1977. *The measurement of air flo*w. 5th (in SI/metric units) ed. New York: Pergamon Press.

Scovazzo, P., A. Hoehn, and P. Todd. 2000. Membrane porosity and hydrophilic membrane-based dehumidification performance. *Journal of Membrane Scienc*e 167 (2): 217-25.

Scovazzo, Paul, Jedrick Burgos, Alex Hoehn, and Paul Todd. 1998. Hydrophilic membrane-based humidity control. *Journal of Membrane Scienc*e 149 (1) (10/14): 69-81.

Sprenkle, R. E. 1945. Piping arrangements for acceptable flowmeter accuracy. *Transactions of the ASM*E 67 (07): 345-60.

Steinhart, John S., and Stanley R. Hart. 1968. Calibration curves for thermistors. *Deep Sea Research and Oceanographic Abstract*s 15 (4) (8): 497-503.

Appendix A

Auxiliary Plots for Sub-Section 5.2.3

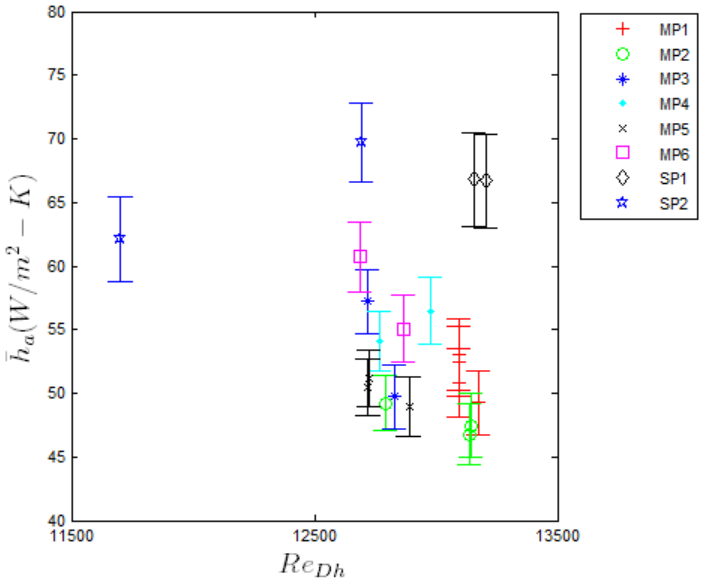

Figure A-1 Average Heat Transfer Coefficient vs. Reynolds number for Condensation Data (Re_{Dh}=11500 to 13500)

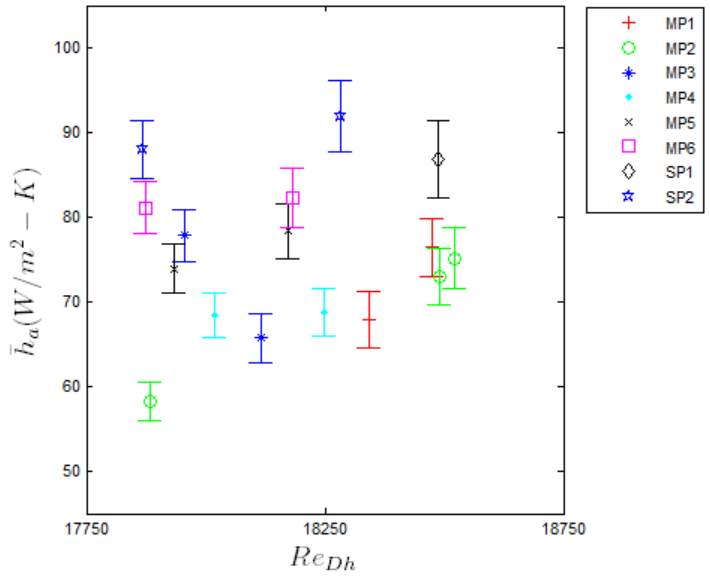

Figure A-2 Average Heat Transfer Coefficient vs. Reynolds number for Condensation Data (Re_{Dh}=17750 to 18750)

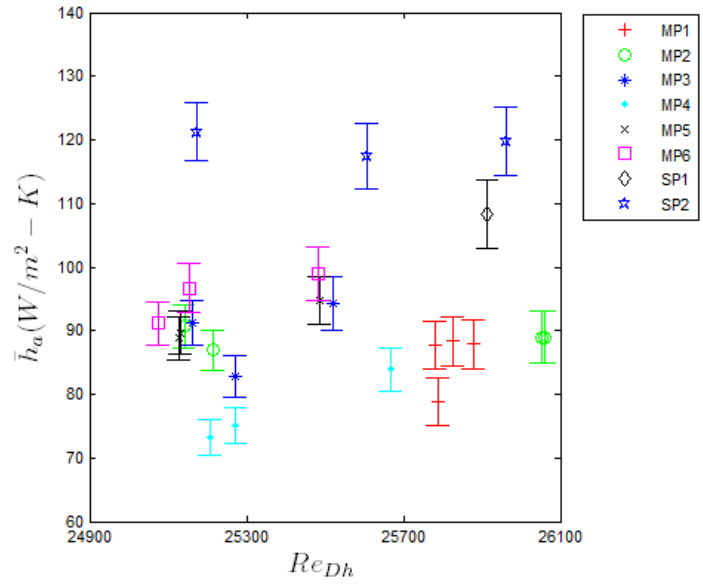

Figure A-3 Average Heat Transfer Coefficient vs. Reynolds number for Condensation Data (Re_{Dh}=24900 to 26100)

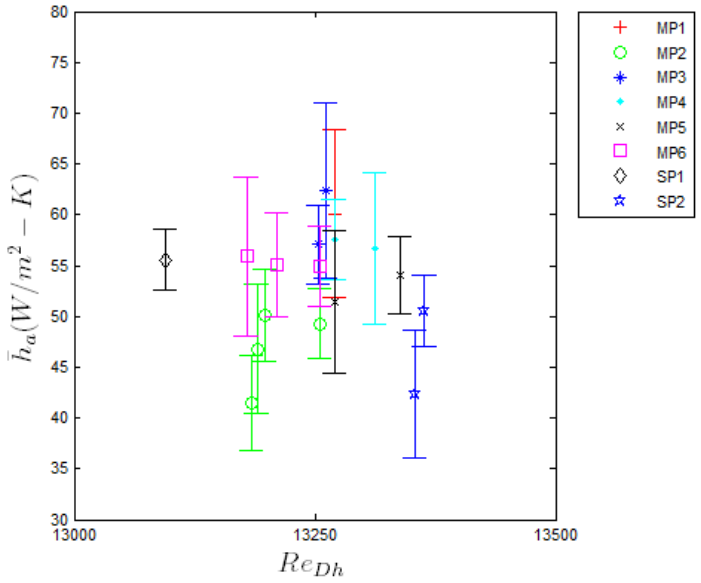

Figure A-4 Average Heat Transfer Coefficient vs. Reynolds number for Evaporation Data (Re_{Dh}=13000 to 13500)

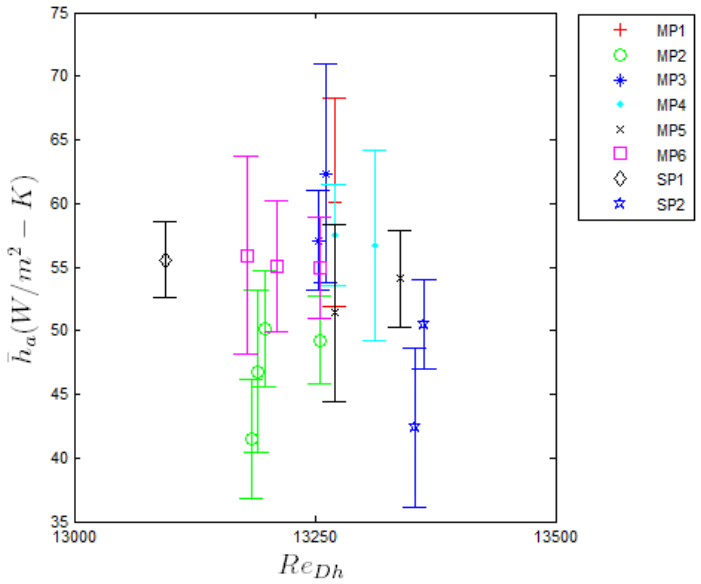

Figure A-5 Average Heat Transfer Coefficient vs. Reynolds number for Evaporation Data (Re_{Dh}=18000 to 19000)

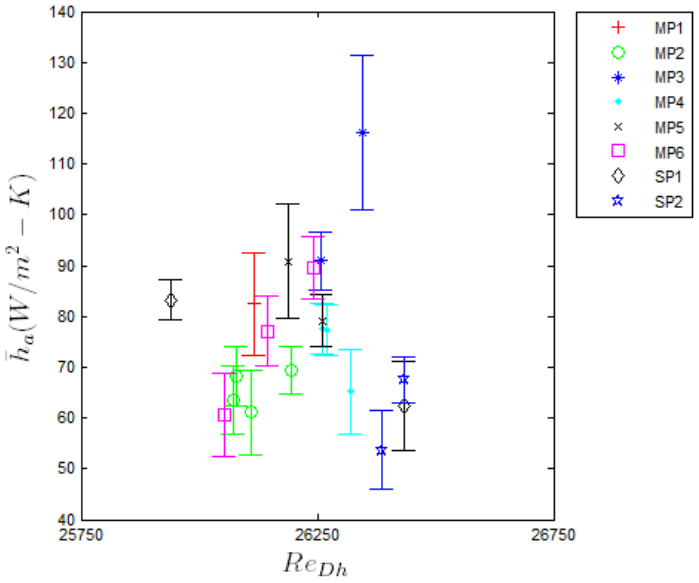

Figure A-6 Average Heat Transfer Coefficient vs. Reynolds number for Evaporation Data (Re_{Dh}=25750 to 26750)

Auxiliary Plots for Sub-Section 5.2.4

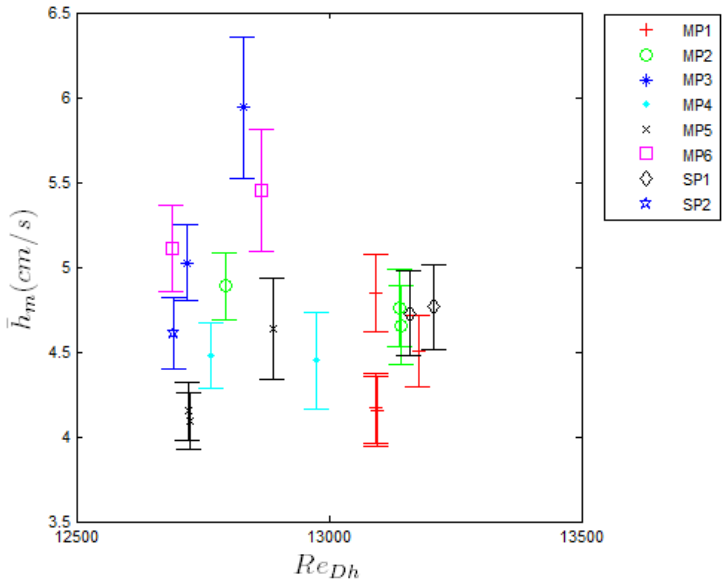

Figure A-7 Average Mass Transfer Coefficient vs. Reynolds number for Condensation Data (Re_{Dh}=12500 to 13500)

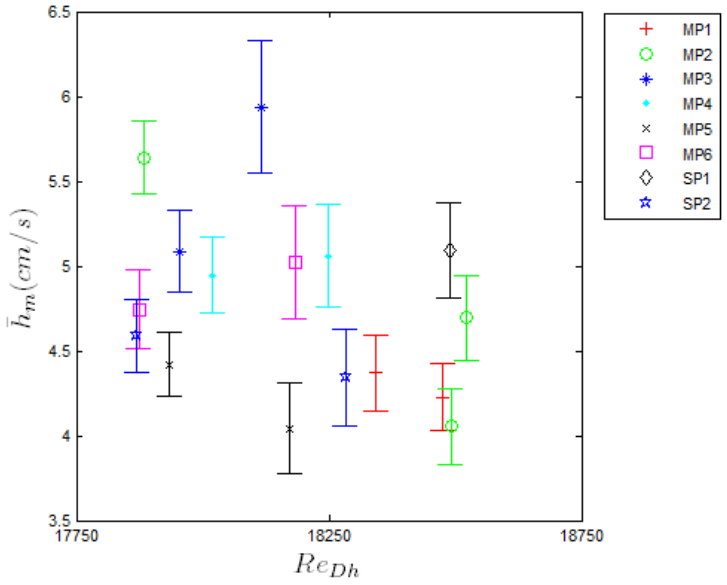

Figure A-8 Average Mass Transfer Coefficient vs. Reynolds number for Condensation Data (Re_{Dh}=17750 to 18750)

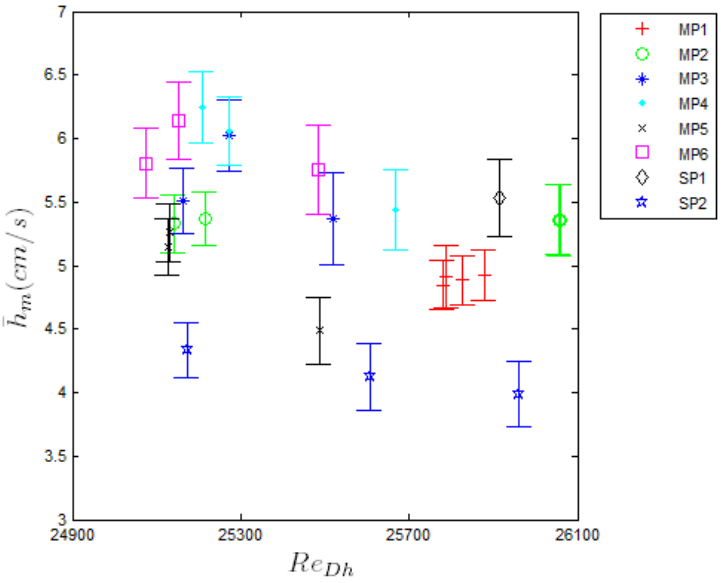

Figure A-9 Average Mass Transfer Coefficient vs. Reynolds number for Condensation Data (Re_{Dh}=24900 to 26100)

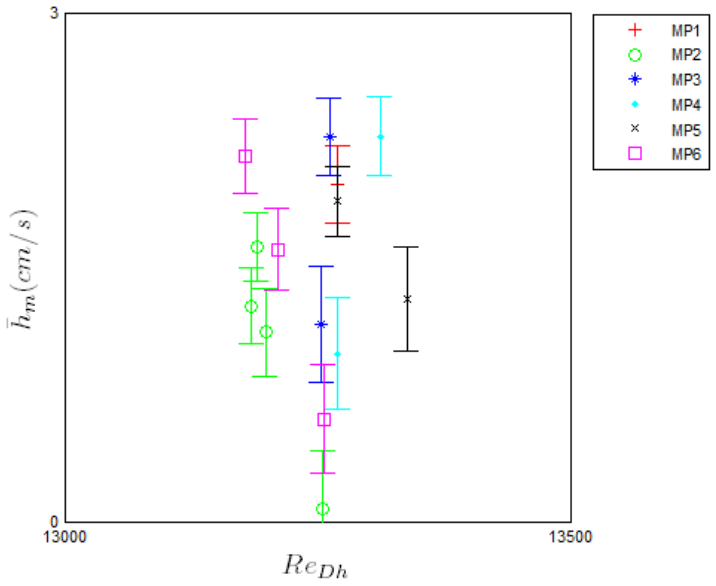

Figure A-10 Average Mass Transfer Coefficient vs. Reynolds number for Evaporation Data (Re_{Dh}=13000 to 13500)

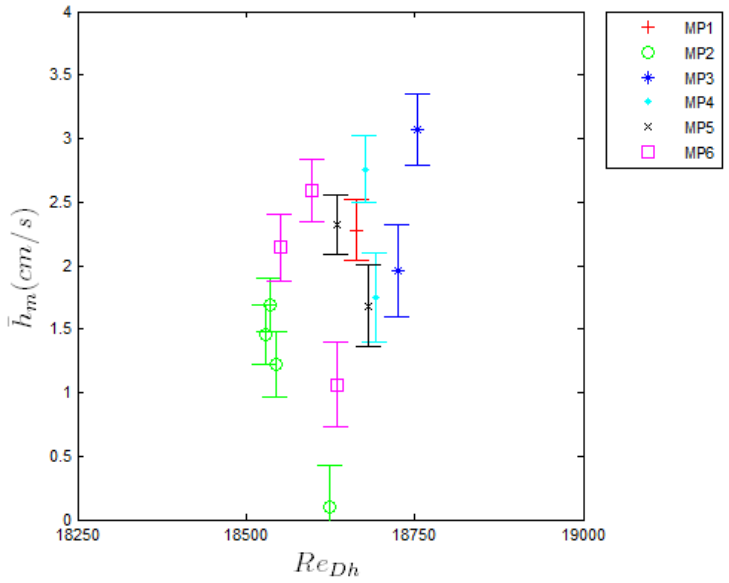

Figure A-11 Average Mass Transfer Coefficient vs. Reynolds number for Evaporation Data (Re_{Dh}=18250 to 19000)

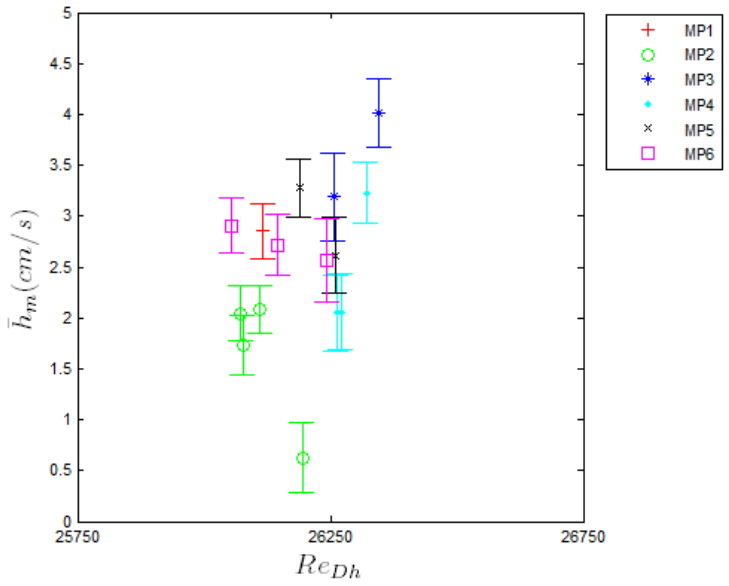

Figure A-12 Average Mass Transfer Coefficient vs. Reynolds number for Evaporation Data (Re_{Dh}=25750 to 26750)

Auxiliary Plots for Section 5.3.3

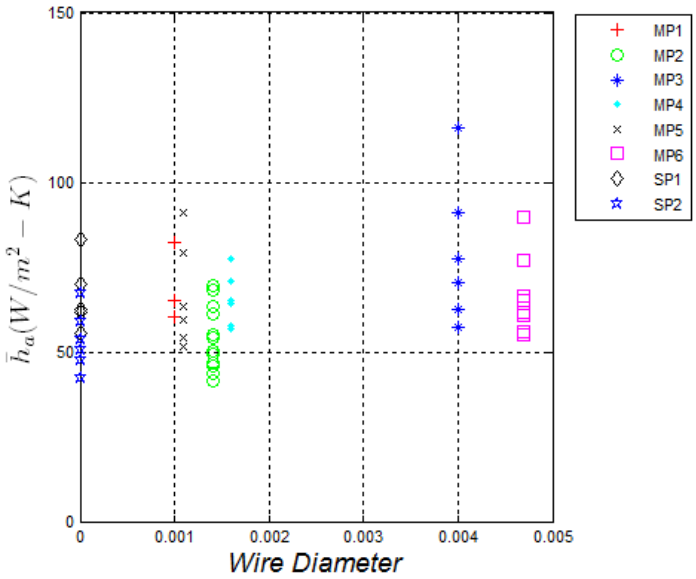

Figure A-13 Average Convective Heat Transfer Coefficient vs. Wire Diameter for Evaporation Data Points

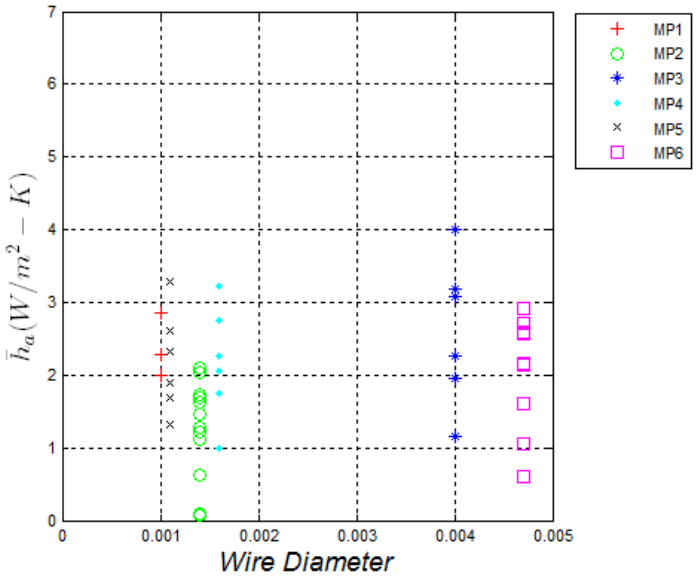

Figure A-14 Average Convective Mass Transfer Coefficient vs. Wire Diameter for Evaporation Data Points

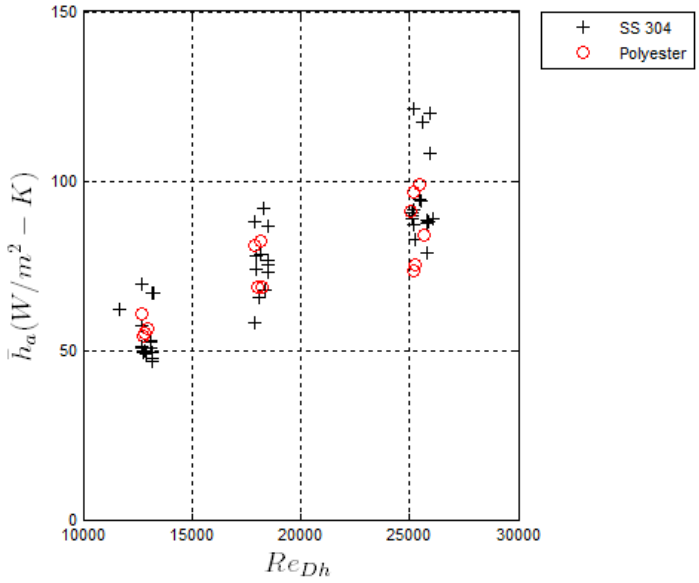

Figure A-15 Average Convective Heat Transfer Coefficient for Condensation Data Points

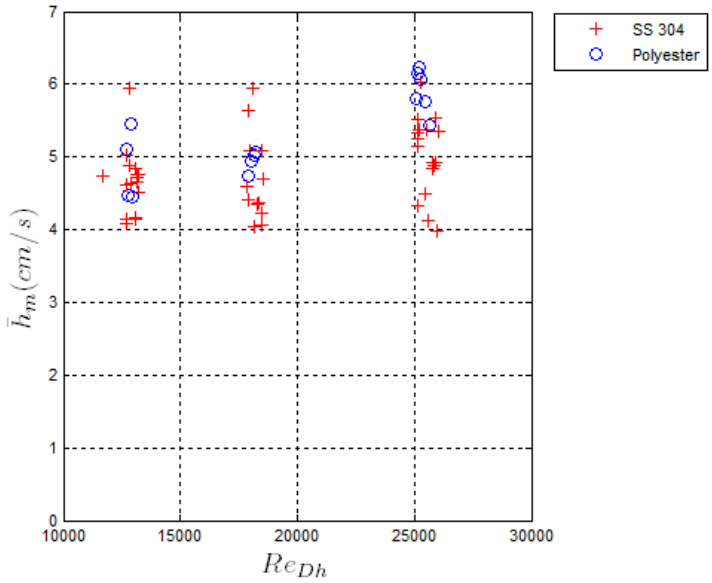

Figure A-16 Average Convective Mass Transfer Coefficient for Condensation Data Points

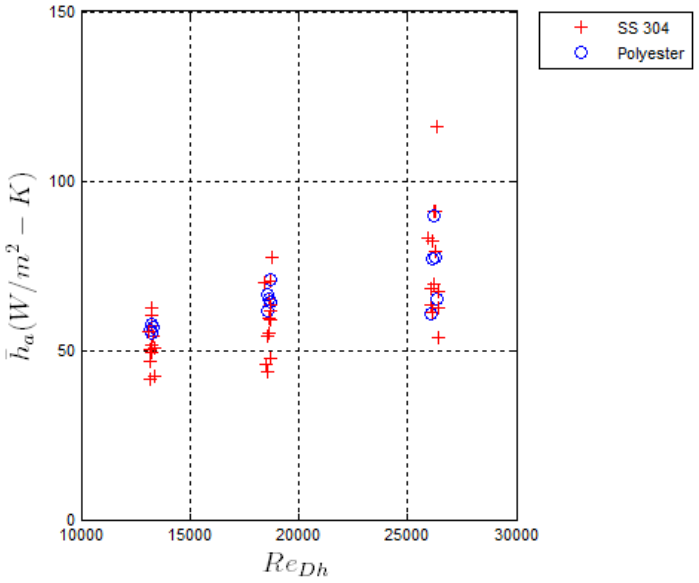

Figure A-17 Average Convective Heat Transfer Coefficient for Evaporation Data Points

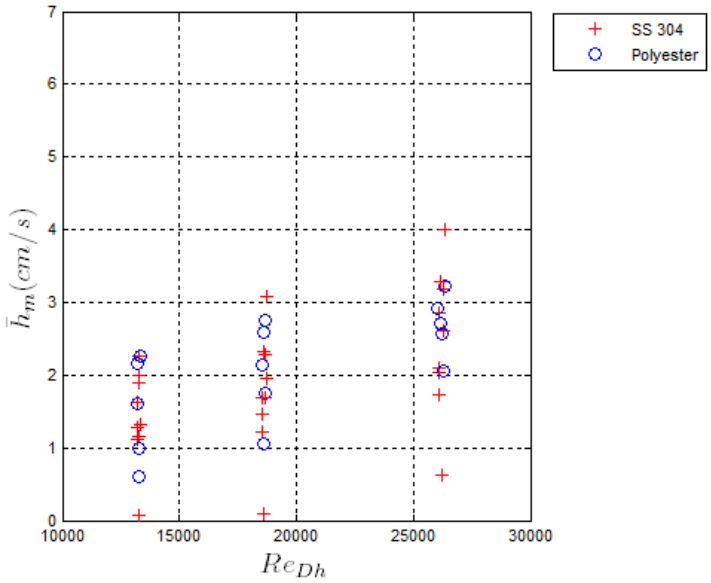

Figure A-18 Average Convective Heat Transfer Coefficient for Evaporation Data Points

Appendix B

Appendix B displays the part drawings of the base plate, back plate and mesh plate gasket parts. The dimensions in the drawings are shown in inches.

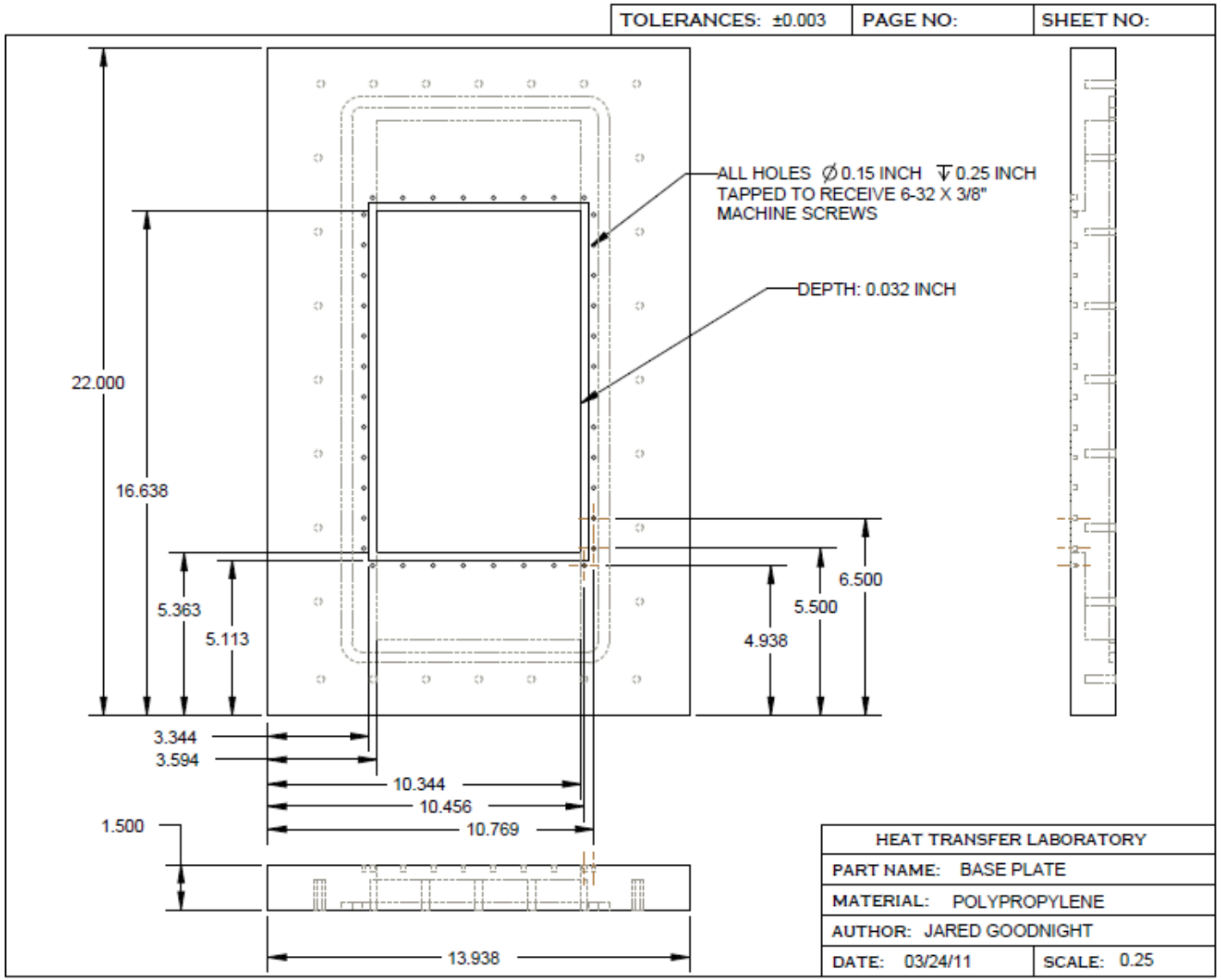

Figure B-1 Base Plate Part Drawing (Front Surface)

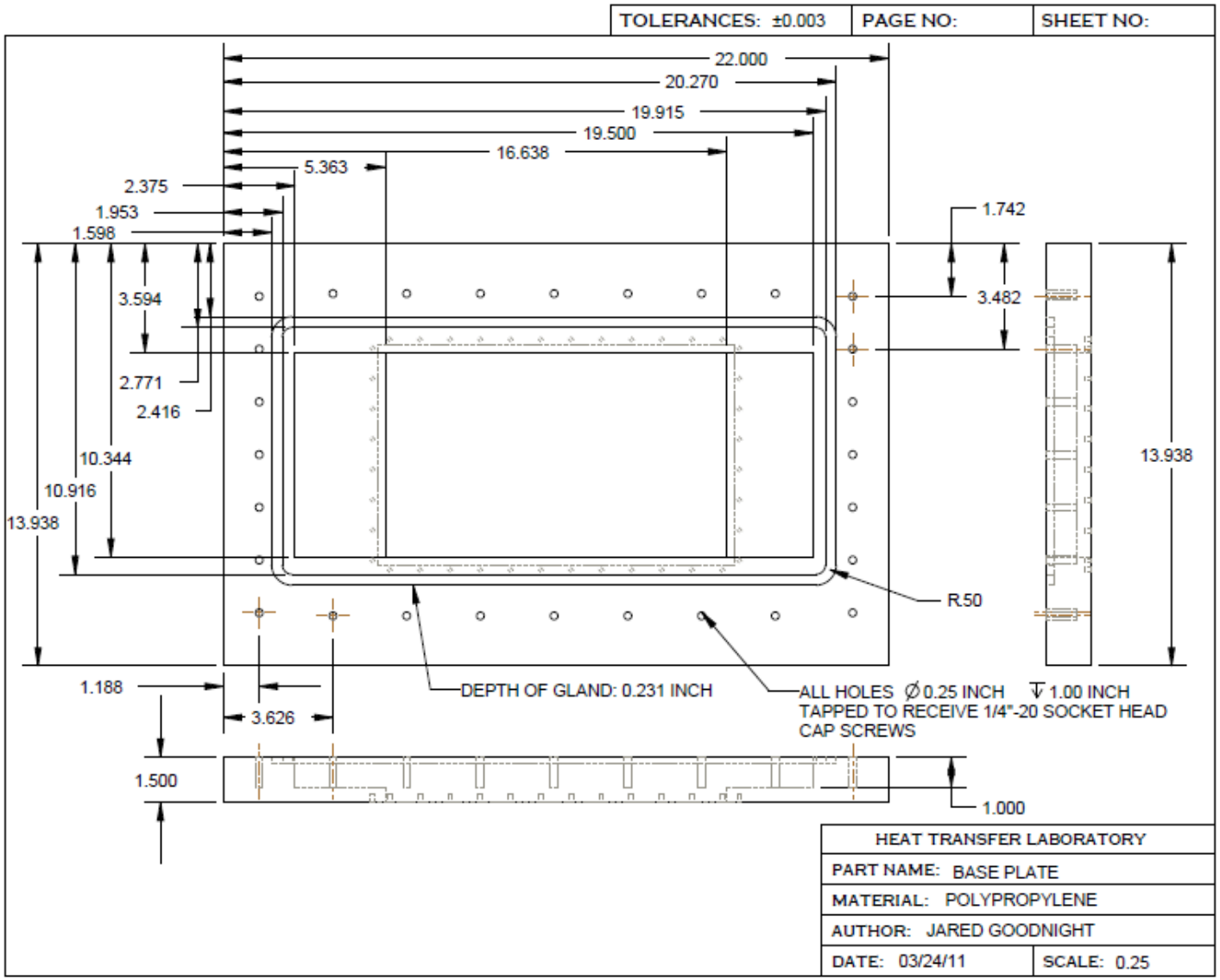

Figure B-2 Base Plate Part Drawing (Back Surface)

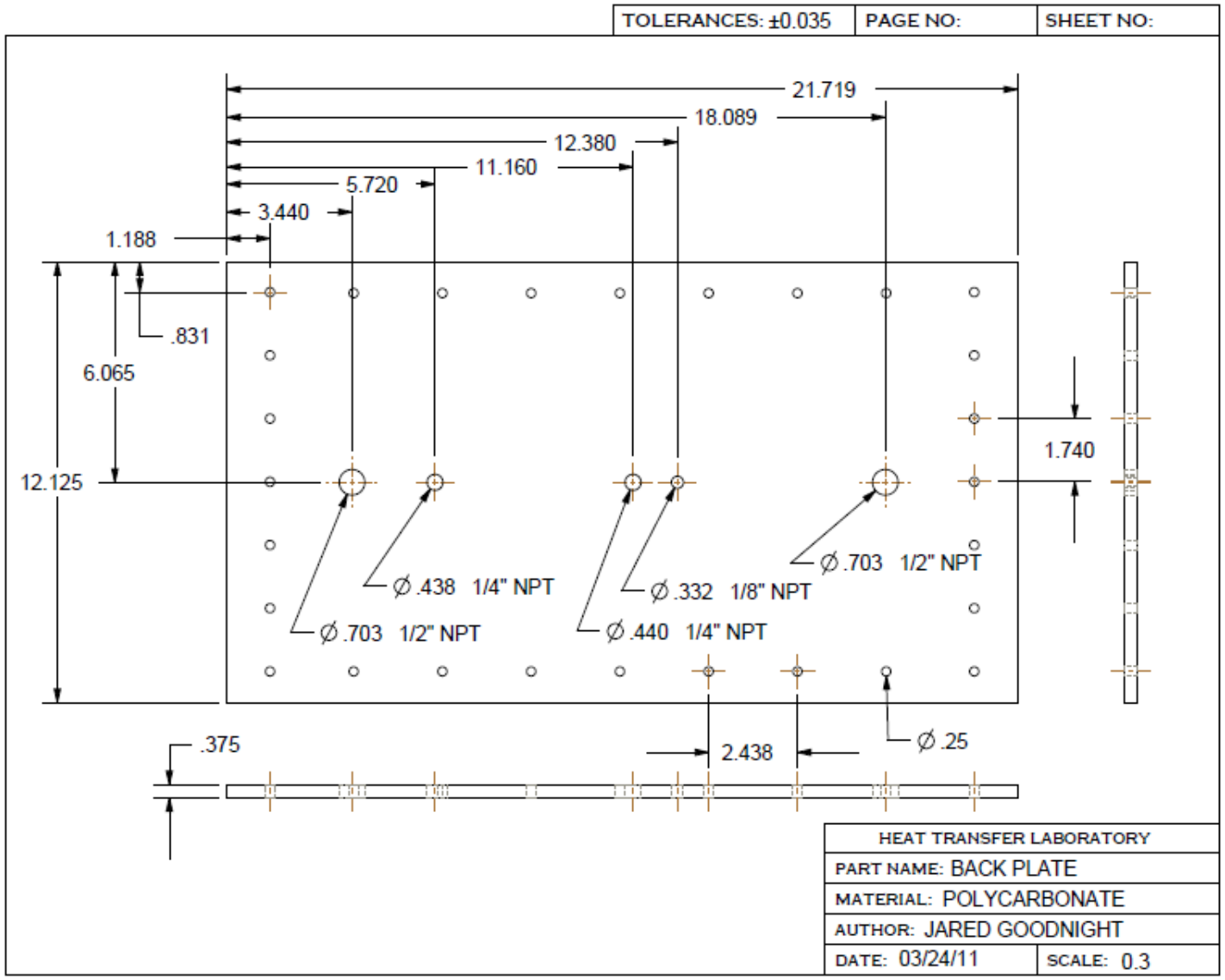

Figure B-3 Back Plate Part Drawing

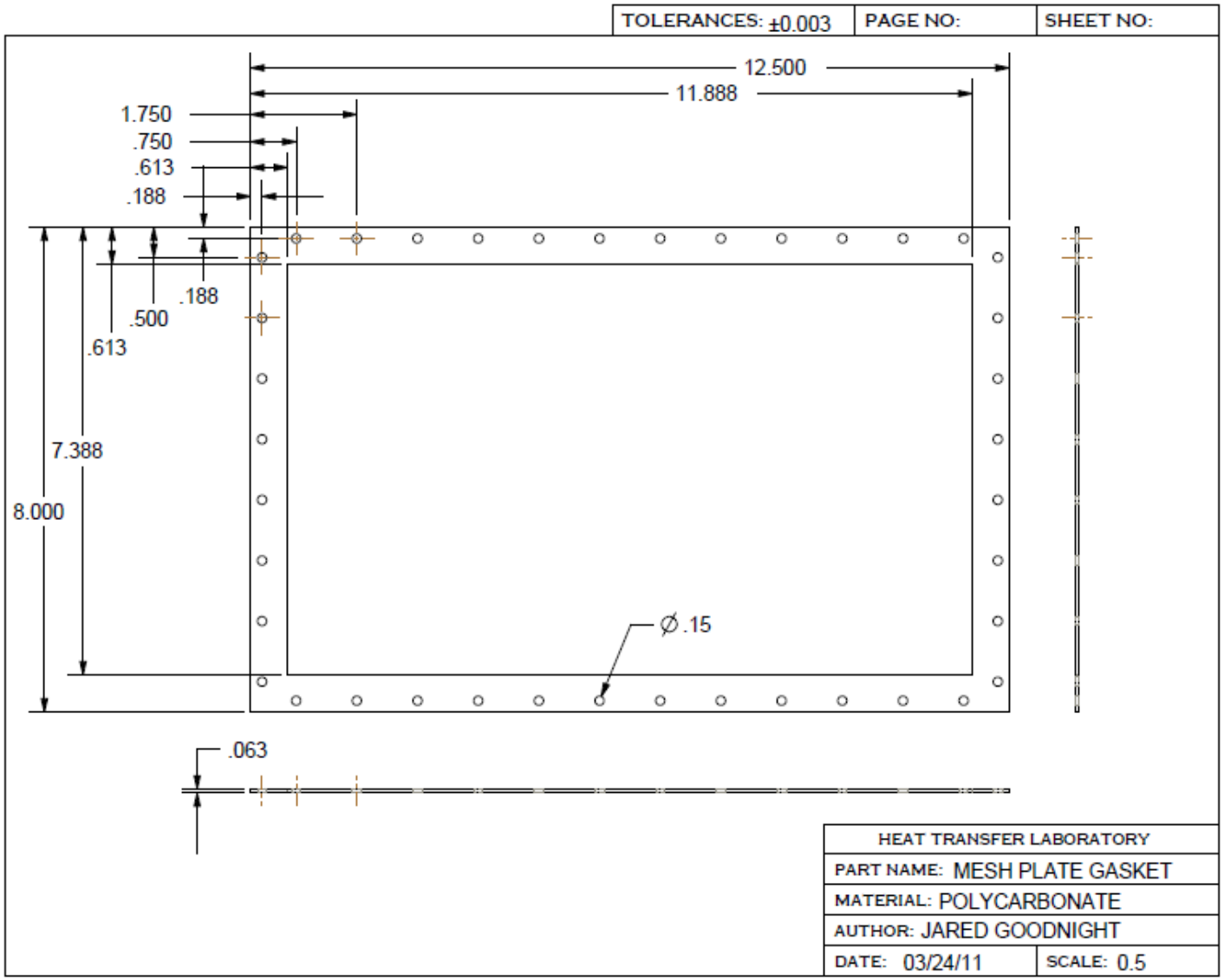

Figure B-4 Mesh Plate Gasket Part Drawing

Appendix C

This appendix contains the Mathcad program developed to determine the uncertainty in all the calculations presented in Chapter 4. This program is used to calculate the uncertainty for every data point shown in Chapter 5. The uncertainty analysis program is shown for an arbitrary datapoint selected from the MP6 data.

Uncertainty Analysis

Input data vector from the data analysis spreadsheet

Data :=

	0
0	$9.775 \cdot 10^4$
1	319.267
2	319.214
3	320.573
4	321.097
5	52.13
6	55.535
7	0.611
8	0.997
9	0.055
10	0.102
11	995.85
12	...

Define all the measurments collected from facility as variables

Inlet and outlet water thermistors

$T_{w.out} := Data_{17} - 273.15$ C

$T_{w.in} := Data_{18} - 273.15$ C

Mass flow rate of water

$m_w := Data_{16}$ $\frac{g}{s}$

Outlet air thermistors

$T_{203} := Data_1 = 319.267 \quad K$

$T_{204} := Data_2 = 319.214 \quad K$

Inlet air thermistors

$T_{205} := Data_3 = 320.573 \quad K$

$T_{207} := Data_4 = 321.097 \quad K$

Surface temperature thermistor

$T_{206} := Data_{21} = 289.2899 \quad K$

$T_s := T_{206}$

Inlet and outlet relative humidity

$\phi_{in} := Data_5 = 52.1304 \quad \%$

$\phi_{out} := Data_6 = 55.5347 \quad \%$

Atmposheric pressure measurement

$P_{atm} := Data_0 = 97752 \quad Pa$

Pressure drop across orifice

$\Delta p := Data_{11} = 995.8503 \quad Pa$

Define the uncertainty of the input measurements determined from calibration and/or the manufactuer specifications

$uTw := .0103\,K \qquad uT_s := 1 \quad K \qquad um_w := .002 \cdot m_w + 0.066667 = 0.170996 \quad \frac{g}{s}$

$uTa := 0.017 \; K \qquad u\Delta p := 13 \; Pa$

$u\phi := 1 \quad \%$

Define a function which averages two temperature measurements

$$AVE(T1, T2) := \frac{T1 + T2}{2}$$

Define average inlet and outlet air temperatures

$T_{ave.air.in} := AVE(T_{205}, T_{207}) = 320.8346 \quad K$

$T_{ave.air.out} := AVE(T_{203}, T_{204}) = 319.2407 \quad K$

Calculate uncertainty of average inlet and outlet air temperatures

$$uT_{ave.in} := \sqrt{\left(\frac{d}{dT_{205}} AVE(T_{205}, T_{207})\right)^2 \cdot uTa^2 + \left(\frac{d}{dT_{207}} AVE(T_{205}, T_{207})\right)^2 \cdot uTa^2}$$

$$uT_{ave.out} := \sqrt{\left(\frac{d}{dT_{203}} AVE(T_{203}, T_{204})\right)^2 \cdot uTa^2 + \left(\frac{d}{dT_{204}} AVE(T_{203}, T_{204})\right)^2 \cdot uTa^2}$$

$uT_{ave.air} := uT_{ave.in} = 0.012021 \quad K$

Enter the vector of constant coefficients used to calculate the saturation pressure of water vapor

$$C := \begin{pmatrix} -5800.2206 \\ 1.3914993 \\ -0.048640239 \\ 0.000041764768 \\ -0.000000014452093 \\ 6.5459673 \end{pmatrix}$$

Define saturation pressure of water vapor as a function of temperature

$$P_{ws}(T) := \exp\left(\frac{C_0}{T} + C_1 + C_2 \cdot T + C_3 \cdot T^2 + C_4 \cdot T^3 + C_5 \cdot \ln(T)\right)$$

Determine the saturation pressure of water vapor for the inlet and outlet average air temperatures and the surface temperature

$$P_{ws.in} := P_{ws}(T_{ave.air.in}) = 10999 \quad Pa \qquad P_{ws.out} := P_{ws}(T_{ave.air.out}) = 10144 \quad Pa$$

$$P_{ws.s} := P_{ws}(T_s) = 1835 \quad Pa$$

Calculate the uncertainty in the calculations of the saturation pressures of water vapor at the various locations

$$uP_{ws.in} := \sqrt{\left(\frac{d}{dT_{ave.air.in}} P_{ws}(T_{ave.air.in})\right)^2 \cdot uT_{ave.air}{}^2} = 6.67 \quad Pa$$

$$uP_{ws.out} := \sqrt{\left(\frac{d}{dT_{ave.air.out}} P_{ws}(T_{ave.air.out})\right)^2 \cdot uT_{ave.air}{}^2} = 6.2222 \quad Pa$$

$$uP_{ws.s} := \sqrt{\left(\frac{d}{dT_s} P_{ws}(T_s)\right)^2 \cdot uT_s{}^2} = 117.113 \quad Pa$$

Define partial pressure of water vapor as a function of saturation pressure and relative humidity

$$P_w(P, \phi) := P \cdot \frac{\phi}{100}$$

Calculate the partial pressure of water vapor for the inlet and outlet air stream

$$P_{w.in} := P_w(P_{ws.in}, \phi_{in}) = 5733.752 \quad Pa \qquad P_{w.out} := P_w(P_{ws.out}, \phi_{out}) = 5633.687 \quad Pa$$

Calculate the uncertainty in the partial pressure of water vapor for the inlet and outlet air stream

$$uP_{w.in} := \sqrt{\left(\frac{d}{dP_{ws.in}} P_w(P_{ws.in}, \phi_{in})\right)^2 \cdot uP_{ws.in}{}^2 + \left(\frac{d}{d\phi_{in}} P_w(P_{ws.in}, \phi_{in})\right)^2 \cdot u\phi^2} \quad Pa$$

$$uP_{w.out} := \sqrt{\left(\frac{d}{dP_{ws.out}} P_w(P_{ws.out}, \phi_{out})\right)^2 \cdot uP_{ws.out}{}^2 + \left(\frac{d}{d\phi_{out}} P_w(P_{ws.out}, \phi_{out})\right)^2 \cdot u\phi^2} \quad Pa$$

$$\frac{uP_{w.in}}{P_{w.in}} = 0.019 \qquad \frac{uP_{w.out}}{P_{w.out}} = 0.018$$

Define the humidity ratio as a function of the partial and atmospheric pressures

$$\omega(P) := 0.62198 \cdot \frac{P}{P_{atm} - P}$$

Calculate the humidity ratio of inlet and outlet air stream

$$\omega_{in} := \omega(P_{w.in}) = 0.038756 \qquad \omega_{out} := \omega(P_{w.out}) = 0.038038$$

Calculate uncertainty and percent uncertainty in humidity ratio of inlet and outlet air

$$u\omega_{in} := \sqrt{\left(\frac{d}{dP_{w.in}}\omega(P_{w.in})\right)^2 \cdot uP_{w.in}^{\,2}} \qquad u\omega_{out} := \sqrt{\left(\frac{d}{dP_{w.out}}\omega(P_{w.out})\right)^2 \cdot uP_{w.out}^{\,2}}$$

$$u\omega_{in} = 0.00079 \qquad u\omega_{out} = 0.000727$$

$$\frac{u\omega_{in}}{\omega_{in}} = 0.02 \qquad \frac{u\omega_{out}}{\omega_{out}} = 0.019$$

Define humidity ratio difference as a function of inlet and outlet humidity ratio

$$d\omega(\omega 1, \omega 2) := \omega 1 - \omega 2$$

$$\Delta\omega := d\omega(\omega_{in}, \omega_{out}) = 0.0007177$$

Calculate uncertainty and percent uncertainty of humidity ratio difference

$$u\Delta\omega := \sqrt{\left(\frac{d}{d\omega_{in}}d\omega(\omega_{in}, \omega_{out})\right)^2 \cdot u\omega_{in}^{\,2} + \left(\frac{d}{d\omega_{out}}d\omega(\omega_{in}, \omega_{out})\right)^2 \cdot u\omega_{out}^{\,2}} = 0.001074$$

$$\frac{u\Delta\omega}{\Delta\omega} = 1.496244970362$$

note: The uncertainty in the humidity ratio difference is too high !!!

Define the molar fractions of air and water as functions of the humidity ratio

$$X_a(\omega) := \frac{1}{1 + 1.607793 \cdot \omega} \qquad X_w(\omega) := \frac{\omega}{0.62197058 + \omega}$$

Calculate the molar fractions of air and water for the inlet and outlet conditions

$$X_{a.in} := X_a(\omega_{in}) = 0.941 \qquad X_{w.in} := X_w(\omega_{in}) = 0.059$$

$$X_{a.out} := X_a(\omega_{out}) = 0.942 \qquad X_{w.out} := X_w(\omega_{out}) = 0.058$$

Calculate the uncertainty and percent uncertainty of the molar fractions of air and water for the inlet and outlet conditions

$$uX_{a.in} := \sqrt{\left(\frac{d}{d\omega_{in}} X_a(\omega_{in})\right)^2 \cdot u\omega_{in}^2} \qquad uX_{w.in} := \sqrt{\left(\frac{d}{d\omega_{in}} X_w(\omega_{in})\right)^2 \cdot u\omega_{in}^2}$$

$$uX_{a.out} := \sqrt{\left(\frac{d}{d\omega_{out}} X_a(\omega_{out})\right)^2 \cdot u\omega_{out}^2} \qquad uX_{w.out} := \sqrt{\left(\frac{d}{d\omega_{out}} X_w(\omega_{out})\right)^2 \cdot u\omega_{out}^2}$$

$$\frac{uX_{a.in}}{X_{a.in}} = 0.001196 \qquad \frac{uX_{w.in}}{X_{w.in}} = 0.019192$$

$$\frac{uX_{a.out}}{X_{a.out}} = 0.001102 \qquad \frac{uX_{w.out}}{X_{w.out}} = 0.018017$$

Define the molecular weight of the air and water mixture at the inlet and outlet conditions as a function of molecular weight and molar fraction of air and water

$$M_a := 28.9645 \ \frac{g}{mol} \qquad M_w := 18.016 \ \frac{g}{mol}$$

$$M(Xa, Xw) := M_a \cdot Xa + M_w \cdot Xw$$

Evaluate the molecular weight of air and water mixture for inlet and outlet conditions

$$M_{in} := M(X_{a.in}, X_{w.in}) \qquad M_{out} := M(X_{a.out}, X_{w.out})$$

Determine the uncertainty and percent uncertainty of molecular weight of air and water mixture at inlet and outlet conditions

$$uM_{in} := \sqrt{\left(\frac{d}{dX_{a.in}} M(X_{a.in}, X_{w.in})\right)^2 \cdot uX_{a.in}^{\,2} + \left(\frac{d}{dX_{w.in}} M(X_{a.in}, X_{w.in})\right)^2 \cdot uX_{w.in}^{\,2}}$$

$$uM_{out} := \sqrt{\left(\frac{d}{dX_{a.out}} M(X_{a.out}, X_{w.out})\right)^2 \cdot uX_{a.out}^{\,2} + \left(\frac{d}{dX_{w.out}} M(X_{a.out}, X_{w.out})\right)^2 \cdot uX_{w.out}^{\,2}}$$

$$\frac{uM_{in}}{M_{in}} = 0.001 \qquad \frac{uM_{out}}{M_{out}} = 0.001$$

Define the mass fraction as a function of molecular weight and mass fraction

$$mf(M1, M2, X1, X2) := \frac{M1 \cdot X1}{M1 \cdot X1 + M2 \cdot X2}$$

Evaluate the mass fractions of air and water for the inlet conditions

$$mf_{a.in} := mf(M_a, M_w, X_{a.in}, X_{w.in}) = 0.963$$

$$mf_{w.in} := mf(M_w, M_a, X_{w.in}, X_{a.in}) = 0.037$$

Determine the uncertainty and percent uncertainty for the mass fractions of air and water

$$umf_{a.in} := \left[\left(\frac{d}{dX_{a.in}} mf(M_a, M_w, X_{a.in}, X_{w.in}) \right)^2 \cdot uX_{a.in}^2 \ldots + \left(\frac{d}{dX_{w.in}} mf(M_a, M_w, X_{a.in}, X_{w.in}) \right)^2 \cdot uX_{w.in}^2 \right]^{\left(\frac{1}{2}\right)}$$

$$umf_{w.in} := \left[\left(\frac{d}{dX_{a.in}} mf(M_w, M_a, X_{w.in}, X_{a.in}) \right)^2 \cdot uX_{a.in}^2 \ldots + \left(\frac{d}{dX_{w.in}} mf(M_w, M_a, X_{w.in}, X_{a.in}) \right)^2 \cdot uX_{w.in}^2 \right]^{\left(\frac{1}{2}\right)}$$

$$\frac{umf_{a.in}}{mf_{a.in}} = 0.000717 \qquad \frac{umf_{w.in}}{mf_{w.in}} = 0.019$$

Define the concentration of water vapor in air as a function of the partial pressure, molecular weight and temperature (ideal gas law).

$$\rho_a(P, M, T) := \frac{P}{\frac{8314}{M} \cdot T} \qquad \frac{kg}{m^3}$$

Evaluate the concentration of water vapor in the air at the inlet, outlet and surface conditions

$$\rho_{a.in} := \rho_a(P_{w.in}, M_w, T_{ave.air.in}) = 0.038726 \quad \frac{kg}{m^3}$$

$$\rho_{a.out} := \rho_a(P_{w.out}, M_w, T_{ave.air.out}) = 0.03824 \quad \frac{kg}{m^3}$$

$$\rho_s := \rho_a(P_{ws.s}, M_w, T_s) = 0.013743 \quad \frac{kg}{m^3}$$

$\frac{u\rho_{a.in}}{\rho_{a.in}} = 0.01919229$ $\frac{u\rho_{a.out}}{\rho_{a.out}} = 0.0179277196$ $\frac{u\rho_s}{\rho_s} = 0.064$

Input the parameters from the data vector used in the calculation of the mass flow rate of air in the data analysis spreadsheet

$C1 := Data_7 = 0.611058$

$\varepsilon := Data_8 = 0.997225$

$d := Data_9 = 0.055 \ m$

$D := Data_{10} = 0.1016 \ m$

$\beta := \frac{d}{D} = 0.542$

$\Delta p := Data_{11} = 995.8503 \ \frac{N}{m^2}$

$\rho 1 := Data_{12} = 1.043513 \ \frac{kg}{m^3}$

$k := Data_{13} = 1.4$

$p_1 := Data_{14} \ \frac{N}{m}$

Mass flow rate of air calculated in data analysis spreadsheet

$m_a := Data_{15} = 0.069112$

Verify the calculation from spreadsheet by determining the mass flow rate from the given input parameters

$qm := \frac{C1}{\sqrt{1-\beta^4}} \cdot \varepsilon \cdot \frac{\pi}{4} \cdot d^2 \cdot \sqrt{2 \cdot \Delta p \cdot \rho 1} = 0.069112 \ \frac{kg}{s}$

Uncertainty in the discharge coefficient

$uC1 := 0.0005 \cdot C1 = 0.00030553$

Uncertainty of the expansibility factor

$u\varepsilon := \frac{3.5 \cdot \frac{\Delta p}{k \cdot p_1}}{100} \cdot \varepsilon = 0.00025454$

Uncertainty and percent uncertainty in the pressure drop across orifice

$u\Delta p := 13 \ \text{Pa}$

$$\frac{u\Delta p}{\Delta p} = 0.013$$

Uncertainty and the percent uncertainty in the density of air

$$\rho_{mix.out} := \rho_a\left(P_{atm}, M_{out}, T_{ave.air.out}\right) = 1.043513$$

$$u\rho 1 := \left[\left(\frac{d}{dM_{out}}\rho_a\left(P_{atm}, M_{out}, T_{ave.air.out}\right)\right)^2 \cdot uM_{out}^{\,2} \ldots + \left(\frac{d}{dT_{ave.air.out}}\rho_a\left(P_{atm}, M_{out}, T_{ave.air.out}\right)\right)^2 \cdot uT_{ave.air}^{\,2}\right]^{\left(\frac{1}{2}\right)}$$

$$\frac{u\rho 1}{\rho 1} = 0.001251$$

Define the mass flow rate of air as a function of the input parameters

$$q_m(C1, \varepsilon, d, D, \Delta p, \rho 1) := \frac{C1}{\sqrt{1 - \left(\frac{d}{D}\right)^4}} \cdot \varepsilon \cdot \frac{\pi}{4} \cdot d^2 \cdot \sqrt{2 \cdot \Delta p \cdot \rho 1}$$

Determine the uncertainty and percent uncertain of the mass flow rate of air

$$uq_m := \left[\begin{array}{l} \left(\frac{d}{dC1}q_m(C1, \varepsilon, d, D, \Delta p, \rho 1)\right)^2 uC1^2 + \left(\frac{d}{d\varepsilon}q_m(C1, \varepsilon, d, D, \Delta p, \rho 1)\right)^2 \cdot u\varepsilon^2 \ldots \\ + \left(\frac{d}{dd}q_m(C1, \varepsilon, d, D, \Delta p, \rho 1)\right)^2 \cdot ud^2 + \left(\frac{d}{dD}q_m(C1, \varepsilon, d, D, \Delta p, \rho 1)\right)^2 \cdot uD^2 \ldots \\ + \left(\frac{d}{d\Delta p}q_m(C1, \varepsilon, d, D, \Delta p, \rho 1)\right)^2 \cdot u\Delta p^2 + \left(\frac{d}{d\rho 1}q_m(C1, \varepsilon, d, D, \Delta p, \rho 1)\right)^2 \cdot u\rho 1^2 \end{array}\right]^{\left(\frac{1}{2}\right)}$$

$uq_m = 0.0012169837 \quad \frac{kg}{s}$

$\frac{uq_m}{qm} = 0.017608927435$

Calculate the uncertainty in mass flow rate of condensate based on the measured humidity difference

$m_a = 0.069 \quad \frac{kg}{s} \qquad \Delta\omega = 0.000718 \quad \frac{kg_{wv}}{kg_{da}}$

Define the mass flow rate of condensate as a function of the mass flow rate of air and humidity ratio difference

$m_c(ma, d\omega) := ma \cdot d\omega$

$um_a := uq_m = 0.001217 \quad \frac{kg}{s} \qquad u\Delta\omega = 0.001074 \quad \frac{kg_{wv}}{kg_{da}}$

Evaluate the mass flow rate of condensate from the air flow rate and humidity ratio difference

$mc := m_c(m_a, \Delta\omega) = 0.0000496 \quad \frac{kg}{s}$

Calculate uncertainty and percent uncertainty in mass flow rate of condensate

$um_c := \sqrt{\left(\frac{d}{dm_a} m_c(m_a, \Delta\omega)\right)^2 \cdot um_a^2 + \left(\frac{d}{d\Delta\omega} m_c(m_a, \Delta\omega)\right)^2 \cdot u\Delta\omega^2} = 0.0000742 \quad \frac{kg}{s}$

$\frac{um_c}{mc} = 1.4963485843$

note: the high uncertainty comes from the humidity difference measurement and proves that this measurement cannot be used to determine the mass flow rate of condensate

Define the specific heat of air and the specific heat of water vapor as a function of temperature

Const :=

	0	1	2	3	4
0	4.07	$-1.108\cdot10^{-3}$	$4.152\cdot10^{-6}$	$-2.964\cdot10^{-9}$	$8.07\cdot10^{-13}$
1	3.653	$-1.337\cdot10^{-3}$	$3.294\cdot10^{-6}$	$-1.913\cdot10^{-9}$	$2.763\cdot10^{-13}$

$$Cp_{wv}(T) := \left(Const_{0,0} + Const_{0,1}\cdot T + Const_{0,2}\cdot T^2 + Const_{0,3}\cdot T^3 + Const_{0,4}\cdot T^4\right)\cdot\left(\frac{8.314}{18.016}\right)\ \frac{J}{g-K}$$

$$Cp_{air}(T) := \left(Const_{1,0} + Const_{1,1}\cdot T + Const_{1,2}\cdot T^2 + Const_{1,3}\cdot T^3 + Const_{1,4}\cdot T^4\right)\cdot\left(\frac{8.314}{28.9645}\right)\ \frac{J}{g-K}$$

Calculate the uncertainty in mass flow rate of condensate based on the energy balance

Define the heat transfer measured by the water side ($q_{w.1}$) as a function of the mass flow rate, , temperature change and specific heat

$$q_{w.1}(m, c, dt) := m\cdot c\cdot dt$$

Define the mass flow rate of water and the uncertainty in the mass flow rate of water

$$m_w := Data_{16} = 52.164\ \frac{g}{s} \qquad um_w := .002\cdot m_w + 0.0666667 = 0.170996\ \frac{g}{s}$$

Define the temperature difference between the inlet and outlet water and the uncertainty in the temperature difference (inlet and outlet temperatures must be defined in deg C in order to calculate specific heat of water)

$$\Delta T_w := T_{w.out} - T_{w.in} = 1.26\ C \qquad u\Delta T_w := \sqrt{2\cdot uTw^2} = 0.015\ C$$

Define the specific heat of water evaluated at the average water temperature and the uncertainty in specific heat of water

$$T_{w.ave} := \frac{T_{w.out} + T_{w.in}}{2} \quad C \qquad uT_{w.ave} := \sqrt{\frac{1}{2}} \cdot uTw = 0.007283 \quad C$$

Table of coefficients for the 4th order polynomial curve-fit used to approximate the specific heat of liquid water

$A :=$

	0	1	2	3	4
0	4.22	$-3.432 \cdot 10^{-3}$	$1.21 \cdot 10^{-4}$	$-2.355 \cdot 10^{-6}$	$2.219 \cdot 10^{-8}$

Define the 4th order polynomial curve-fit used to estimate the specific heat of water as a function of temperature in deg C

$$Cp_w(T) := A_{0,0} + A_{0,1} \cdot T + A_{0,2} \cdot T^2 + A_{0,3} \cdot T^3 + A_{0,4} \cdot T^4 \qquad \frac{J}{g - C}$$

Uncertainty from curve fit approximation (uCpcf = t-estimator x standard error)

$$uCpcf := 0.0000584527566895323 \qquad \frac{J}{g - C}$$

Uncertainty and the percent uncertainty in the specific heat of liquid water

$$uCp_w := \sqrt{\left(\frac{d}{dT_{w.ave}} Cp_w\left(T_{w.ave}\right)\right)^2 uT_{w.ave}^{\,2} + uCpcf^2} \qquad \frac{J}{g - C}$$

$$Cpw := Cp_w\left(T_{w.ave}\right) = 4.19157121 \qquad \frac{J}{g - C}$$

$$\frac{uCp_w}{Cpw} = 0.000014$$

Determine the uncertainty and percent uncertainty in the component of heat transfer from air to water ($q_{w.1}$)

$$uq_{w.1} := \left[\left(\frac{d}{dm_w} q_{w.1}(m_w, Cpw, \Delta T_w) \right)^2 \cdot um_w^{\,2} + \left(\frac{d}{dCpw} q_{w.1}(m_w, Cpw, \Delta T_w) \right)^2 \cdot uCp_w^{\,2} \ldots \right.$$
$$\left. + \left(\frac{d}{d\Delta T_w} q_{w.1}(m_w, Cpw, \Delta T_w) \right)^2 \cdot u\Delta T_w^{\,2} \right]^{\left(\frac{1}{2}\right)} \quad W$$

$$qw1 := q_{w.1}(m_w, Cpw, \Delta T_w) = 275.607 \quad W$$

$$\frac{uq_{w.1}}{qw1} = 0.012$$

Find the uncertainty in the mean of the average inlet and outlet air temperatures

$$T_{ave.air} := AVE(T_{ave.air.in}, T_{ave.air.out}) = 320.038 \quad K$$

$$uT_{ave.a} := \left[\left(\frac{d}{dT_{ave.air.in}} AVE(T_{ave.air.in}, T_{ave.air.out}) \right)^2 uT_{ave.air}^{\,2} \ldots \right.$$
$$\left. + \left(\frac{d}{dT_{ave.air.out}} AVE(T_{ave.air.in}, T_{ave.air.out}) \right)^2 uT_{ave.air}^{\,2} \right]^{\left(\frac{1}{2}\right)} = 0.0085 \quad K$$

Define the sensible component of heat transfer from the dry air (q_{s1}) as a function of the mass flow rate of air, specific heat of air and temperature drop in the air.

$$q_{a.1}(m, c, dt) := m \cdot c \cdot dt \cdot 1000 \quad W$$

Define specific heat of dry air and its uncertainty (uncertainty from curve fit is considered negligible)

$$Cp_a := Data_{25} = 1.005 \quad \frac{J}{g - K}$$

$$Cpa := Cp_{air}(T_{ave.air}) \quad \frac{J}{g - K}$$

$$uCp_a := \sqrt{\left(\frac{d}{dT_{ave.air}} Cp_{air}(T_{ave.air})\right)^2 \cdot uT_{ave.a}{}^2} = 5.363 \times 10^{-7} \quad \frac{J}{g - K}$$

Define the temperature drop between the inlet and oulet air and it's uncertainty

$$\Delta T_a := T_{ave.air.in} - T_{ave.air.out} = 1.594 \quad K$$

$$m_a = 0.069$$

$$u\Delta T_a := \sqrt{2} \cdot uT_{ave.air} = 0.017 \ K$$

Calculate uncertainty and percent uncertainty in sensible component of heat transfer from dry air

$$uq_{a.1} := \left[\left(\frac{d}{dm_a} q_{a.1}(m_a, Cpa, \Delta T_a)\right)^2 \cdot um_a{}^2 + \left(\frac{d}{d\Delta T_a} q_{a.1}(m_a, Cpa, \Delta T_a)\right)^2 \cdot u\Delta T_a{}^2 \ldots + \left(\frac{d}{dCp_a} q_{a.1}(m_a, Cpa, \Delta T_a)\right)^2 \cdot uCp_a{}^2\right]^{\left(\frac{1}{2}\right)} \quad W$$

$$uq_{a.1} = 2.28$$

$$qa1 := q_{a.1}(m_a, Cpa, \Delta T_a) = 110.754 \quad W$$

$$\frac{uq_{a.1}}{qa1} = 0.021$$

Define the sensible component of heat transfer from the water vapor in air ($q_{a.2}$) as a function of the mass flow rate, the specific heat and the temperature drop of water vapor in air.

$$q_{a.2}(m, \omega, c, dt) := m \cdot \omega \cdot c \cdot dt \cdot 1000 \quad W$$

Define the specific heat of water vapor in the air evaluated at the average air temperature and determine its uncertainty (the uncertainty from curve fit is considered negligible)

$$Cp_{wv.tave} := Data_{23} = 1.87 \quad \frac{J}{g - K}$$

$$Cp_{wv.tave} := Cp_{wv}(T_{ave.air}) = 1.87 \quad \frac{J}{g - K}$$

$$uCp_{wv.tave} := \sqrt{\left(\frac{d}{dT_{ave.air}} Cp_{wv}(T_{ave.air})\right)^2 \cdot uT_{ave.a}{}^2} = 2.921 \times 10^{-6} \quad \frac{J}{g - K}$$

Determine the uncertainty and the percent uncertainty of the sensible component of heat transfer from the water vapor in air.

$$uq_{a.2} := \left[\begin{array}{l} \left(\frac{d}{dm_a} q_{a.2}(m_a, \omega_{out}, Cp_{wv.tave}, \Delta T_a)\right)^2 \cdot um_a{}^2 \ldots \\ + \left(\frac{d}{d\omega_{out}} q_{a.2}(m_a, \omega_{out}, Cp_{wv.tave}, \Delta T_a)\right)^2 \cdot u\omega_{out}{}^2 \ldots \\ + \left(\frac{d}{d\Delta T_a} q_{a.2}(m_a, \omega_{out}, Cp_{wv.tave}, \Delta T_a)\right)^2 \cdot u\Delta T_a{}^2 \ldots \\ + \left(\frac{d}{dCp_{wv.tave}} q_{a.2}(m_a, \omega_{out}, Cp_{wv.tave}, \Delta T_a)\right)^2 \cdot uCp_{wv.tave}{}^2 \end{array}\right]^{\left(\frac{1}{2}\right)} \quad W$$

$$qa2 := q_{a.2}(m_a, \omega_{out}, Cp_{wv.tave}, \Delta T_a) = 7.835 \quad W$$

$$\frac{uq_{a.2}}{qa2} = 0.028$$

Define the temperature difference between the inlet air temperature and the surface temperature and find the uncertainty in the temperature difference.

$$\Delta T_{a.i.s} := T_{ave.air.in} - T_s \quad K$$

$$u\Delta T_{a.i.s} := \sqrt{uT_{ave.air}^{2} + uT_s^{2}} = 1.00007 \quad K$$

Define the latent heat of vaporization as a function of temperature. The function below is a first order linear curve fit for a given range of temperature data (30-45 deg C incremented by 1 deg C)

$$h_{fg}(T) := -2.38724999999942 \cdot (T - 273.15) + 2501.45124999999 \quad \frac{J}{g}$$

Define the uncertainty of the curve fit ($uh_{fg.cf}$ = t-estimator x standard error)

$$uh_{fg.cf} := 0.0278338336628666$$

Determine the uncertainty and the percent uncertainty of the latent heat of vaporization evaluated at the surface temperature

$$uh_{fg} := \sqrt{\left(\frac{d}{dT_s} h_{fg}(T_s)\right)^{2} \cdot uT_s^{2} + uh_{fg.cf}^{2}} = 2.387 \quad \frac{J}{g}$$

$$hfg := h_{fg}(T_s) = 2462.92137 \quad \frac{J}{g}$$

$$\frac{uh_{fg}}{hfg} = 0.000969$$

Define the temperature difference between the outlet water temperature and the surface temperature and determine the uncertainty in the temperature difference

$$\Delta T_{w.o.s} := T_{w.out} + 273.15 - T_s \quad K$$

$$u\Delta T_{w.o.s} := \sqrt{uTw^{2} + uT_s^{2}} = 1.000053 \quad K$$

Define the specific heat of water vapor in air and its uncertainty evaluated at the average between the inlet air and surface temperatures

$$Cp_{wv.is} := Data_{24} = 1.865 \quad \frac{J}{g - K}$$

$$T_{ave.is} := AVE(T_{ave.air.in}, T_s) = 305.062 \quad K$$

$$Cp_{wv.is} := Cp_{wv}(T_{ave.is}) = 1.865 \quad \frac{J}{g - K}$$

$$uT_{ave.is} := \sqrt{\frac{uT_{ave.air}^2}{2} + \frac{uT_s^2}{2}} = 0.707 \quad K$$

$$uCp_{wv.is} := \sqrt{\left(\frac{d}{dT_{ave.is}} Cp_{wv}(T_{ave.is})\right)^2 \cdot uT_{ave.is}^2} = 2.25 \times 10^{-4} \quad \frac{J}{g - K}$$

Define the specific heat of water vapor in air and its uncertainty evaluated between the average of outlet water temperature and surface temperatures

$$Cp_{w.os} := Data_{22} = 4.189 \quad \frac{J}{g - C}$$

$$Ts := T_s - 273.15 \quad C$$

$$T_{ave.os} := AVE(T_{w.out}, Ts) = 14.736 \quad C$$

$$Cp_{w.os} := Cp_w(T_{ave.os}) = 4.189 \quad \frac{J}{g - C}$$

$$uT_{ave.os} := \sqrt{\frac{uTw^2}{2} + \frac{uT_s^2}{2}} = 0.707 \ C$$

$$uCp_{w.os} := \sqrt{\left(\frac{d}{dT_{ave.os}} Cp_w(T_{ave.os})\right)^2 \cdot uT_{ave.os}^2} = 7.8876 \times 10^{-4} \quad \frac{J}{g - C}$$

Define the mass flow rate of the condensate based on the energy balance

$$m_c(q1, q2, q3, \Delta T1, h_{fg}, \Delta T2, Cp1, Cp2) := \frac{q1 - q2 - q3}{Cp1 \cdot \Delta T1 + h_{fg} - Cp2 \cdot \Delta T2}$$

Determine the uncertainty and the percent uncertainty of the mass flow rate of condensate based on the energy balance equation

$$um_c := \left[\begin{aligned} &\left(\frac{d}{dqw1} m_c(qw1, qa1, qa2, \Delta T_{a.i.s}, hfg, \Delta T_{w.o.s}, Cp_{wv.is}, Cp_{w.os})\right)^2 \cdot uq_{w.1}{}^2 \ldots \\ &+ \left(\frac{d}{dqa1} m_c(qw1, qa1, qa2, \Delta T_{a.i.s}, hfg, \Delta T_{w.o.s}, Cp_{wv.is}, Cp_{w.os})\right)^2 \cdot uq_{a.1}{}^2 \ldots \\ &+ \left(\frac{d}{dqa2} m_c(qw1, qa1, qa2, \Delta T_{a.i.s}, hfg, \Delta T_{w.o.s}, Cp_{wv.is}, Cp_{w.os})\right)^2 \cdot uq_{a.2}{}^2 \ldots \\ &+ \left(\frac{d}{d\Delta T_{a.i.s}} m_c(qw1, qa1, qa2, \Delta T_{a.i.s}, hfg, \Delta T_{w.o.s}, Cp_{wv.is}, Cp_{w.os})\right)^2 \cdot u\Delta T_{a.i.s}{}^2 \ldots \\ &+ \left(\frac{d}{dhfg} m_c(qw1, qa1, qa2, \Delta T_{a.i.s}, hfg, \Delta T_{w.o.s}, Cp_{wv.is}, Cp_{w.os})\right)^2 \cdot uh_{fg}{}^2 \ldots \\ &+ \left(\frac{d}{d\Delta T_{w.o.s}} m_c(qw1, qa1, qa2, \Delta T_{a.i.s}, hfg, \Delta T_{w.o.s}, Cp_{wv.is}, Cp_{w.os})\right)^2 \cdot u\Delta T_{w.o.s}{}^2 \ldots \\ &+ \left(\frac{d}{dCp_{wv.is}} m_c(qw1, qa1, qa2, \Delta T_{a.i.s}, hfg, \Delta T_{w.o.s}, Cp_{wv.is}, Cp_{w.os})\right)^2 \cdot uCp_{wv.is}{}^2 \ldots \\ &+ \left(\frac{d}{dCp_{w.os}} m_c(qw1, qa1, qa2, \Delta T_{a.i.s}, hfg, \Delta T_{w.o.s}, Cp_{wv.is}, Cp_{w.os})\right)^2 \cdot uCp_{w.os}{}^2 \end{aligned} \right]^{\left(\frac{1}{2}\right)}$$

$$mc := m_c(qw1, qa1, qa2, \Delta T_{a.i.s}, hfg, \Delta T_{w.o.s}, Cp_{wv.is}, Cp_{w.os}) = 0.061977$$

$$\frac{um_c}{mc} = 0.02572$$

note: the uncertainty in the mass flow is greatly reduced by using the energy balance

$$h_M := h_m(mc, \rho_{ave}, \rho_s, A) = 0.05743 \quad \frac{m}{s}$$

$$\frac{uh_m}{h_M} = 0.048384$$

Define the average air side heat transfer coefficient as a function of the sensible components of heat transfer, the difference between the average air temperature and surface temperature and the area of heat transfer

$$h_a(q1, q2, q3, \Delta T, A) := \frac{q1 + q2 + q3}{\Delta T \cdot A} \quad \frac{W}{m^2 - K}$$

Define the heat transfer of the water vapor in the humid air to the surface of interface and calculate the associated uncertainty

$$q_{a.3}(m, c, dt) := m \cdot c \cdot dt \quad W$$

$$qa3 := q_{a.3}(mc, Cp_{wv.is}, \Delta T_{a.i.s}) \quad W$$

$$uq_{a.3} := \left[\begin{array}{l} \left(\frac{d}{dmc} q_{a.3}(mc, Cp_{wv.is}, \Delta T_{a.i.s}) \right)^2 \cdot um_c^{\,2} \ldots \\ + \left(\frac{d}{d\Delta T_{a.i.s}} q_{a.3}(mc, Cp_{wv.is}, \Delta T_{a.i.s}) \right)^2 \cdot u\Delta T_{a.i.s}^{\,2} \ldots \\ + \left(\frac{d}{dCp_{wv.is}} q_{a.3}(mc, Cp_{wv.is}, \Delta T_{a.i.s}) \right)^2 \cdot uCp_{wv.is}^{\,2} \end{array} \right]^{\left(\frac{1}{2}\right)} \quad W$$

$$\frac{uq_{a.3}}{qa3} = 0.041$$

Determine the uncertainty of the temperature difference between the average of the inlet and outlet air and the surface temperature

$$\Delta T(T1, T2) := T1 - T2$$

$$\Delta T_s := \Delta T(T_{ave.air}, T_s)$$

$$u\Delta T_s := \sqrt{uT_{ave.a}^{\,2} + uT_s^{\,2}} = 1.0000361$$

Determine uncertainty and percent uncertainty in average air convective heat transfer coefficient

$$h_{a.ave} := h_a(qa1, qa2, qa3, \Delta T_s, A) = 91.135 \quad \frac{W}{m^2 - K}$$

$$uh_a := \left[\begin{array}{l} \left(\frac{d}{dqa1} h_a(qa1, qa2, qa3, \Delta T_s, A)\right)^2 \cdot uq_{a.1}{}^2 \ldots \\ + \left(\frac{d}{dqa2} h_a(qa1, qa2, qa3, \Delta T_s, A)\right)^2 \cdot uq_{a.2}{}^2 \ldots \\ + \left(\frac{d}{dqa3} h_a(qa1, qa2, qa3, \Delta T_s, A)\right)^2 \cdot uq_{a.3}{}^2 \ldots \\ + \left(\frac{d}{d\Delta T_s} h_a(qa1, qa2, qa3, \Delta T_s, A)\right)^2 \cdot u\Delta T_s{}^2 \ldots \\ + \left(\frac{d}{dA} h_a(qa1, qa2, qa3, \Delta T_s, A)\right)^2 \cdot uA^2 \end{array} \right]^{\left(\frac{1}{2}\right)} \quad \frac{W}{m^2 - K}$$

$$\frac{uh_a}{h_{a.ave}} = 0.03757$$

Define the average water side convective heat transfer coefficient as a function of the net heat rate, the temperature difference between the outlet water and surface, and the area of heat transfer

$$h_w(q1, q2, \Delta T, A) := \frac{q1 + q2}{\Delta T \cdot A} \quad \frac{W}{m^2 - K}$$

Determine uncertainty in component of heat transfer to the water side

$$q_{w.2}(m, c, dt) := m \cdot c \cdot dt \quad W$$

$$qw2 := q_{w.2}(mc, Cp_{w.os}, \Delta T_{w.o.s}) = -0.729 \quad W$$

$$uq_{w.2} := \left[\left(\frac{d}{dmc} q_{w.2}\left(mc, Cp_{w.os}, \Delta T_{w.o.s}\right) \right)^2 \cdot um_c^{\,2} \ldots + \left(\frac{d}{d\Delta T_{w.o.s}} q_{w.2}\left(mc, Cp_{w.os}, \Delta T_{w.o.s}\right) \right)^2 \cdot u\Delta T_{w.o.s}^{\,2} \ldots + \left(\frac{d}{dCp_{w.os}} q_{w.2}\left(mc, Cp_{w.os}, \Delta T_{w.o.s}\right) \right)^2 \cdot Cp_{w.os}^{\,2} \right]^{\left(\frac{1}{2}\right)} \quad W$$

Define the temperature difference between the average inlet and outlet water and the surface and its associated uncertainty

$$\Delta T_{w.as} := Ts - T_{w.ave} = 3.439 \quad C$$

$$u\Delta T_{w.as} := \sqrt{uT_s^{\,2} + uTw^2} = 1.000053 \; C$$

Calculate uncertainty and percent uncertainty in average water side convective heat transfer coefficient

$$h_{w.ave} := h_w\left(qw1, qw2, \Delta T_{w.as}, A\right) = 1832.38 \quad \frac{W}{m^2 - K}$$

$$uh_w := \left[\left(\frac{d}{dqw1} h_w\left(qw1, qw2, \Delta T_{w.as}, A\right) \right)^2 \cdot uq_{w.1}^{\,2} \ldots + \left(\frac{d}{dqw2} h_w\left(qw1, qw2, \Delta T_{w.as}, A\right) \right)^2 \cdot uq_{w.2}^{\,2} \ldots + \left(\frac{d}{d\Delta T_{w.as}} h_w\left(qw1, qw2, \Delta T_{w.as}, A\right) \right)^2 \cdot u\Delta T_{w.as}^{\,2} \ldots + \left(\frac{d}{dA} h_w\left(qw1, qw2, \Delta T_{w.as}, A\right) \right)^2 \cdot uA^2 \right]^{\left(\frac{1}{2}\right)}$$

$$\frac{uh_w}{h_{w.ave}} = 0.291$$

Calculate the uncertainty and the percent uncertainty in sensible component of heat transfer

$$q_{sensible}(q1, q2, q3) := q1 + q2 + q3 \quad W$$

$$Q_{sensible} := q_{sensible}(qa1, qa2, qa3) = 122.235 \ W$$

$$uQ_{sensible} := \left[\begin{array}{l} \left(\frac{d}{dqa1} q_{sensible}(qa1, qa2, qa3) \right)^2 \cdot uq_{a.1}{}^2 \ldots \\ + \left(\frac{d}{dqa2} q_{sensible}(qa1, qa2, qa3) \right)^2 \cdot uq_{a.2}{}^2 \ldots \\ + \left(\frac{d}{dqa3} q_{sensible}(qa1, qa2, qa3) \right)^2 \cdot uq_{a.3}{}^2 \end{array} \right]^{\left(\frac{1}{2}\right)} \quad W$$

$$\frac{uQ_{sensible}}{Q_{sensible}} = 0.0188$$

Calculate uncertainty and percent uncertainty in latent component of heat transfer

$$q_{latent}(m, h) := m \cdot h \quad W$$

$$Q_{latent} := q_{latent}(mc, hfg) = 152.643 \quad W$$

$$uQ_{latent} := \sqrt{\left(\frac{d}{dmc} q_{latent}(mc, hfg) \right)^2 \cdot um_c{}^2 + \left(\frac{d}{dhfg} q_{latent}(mc, hfg) \right)^2 \cdot uh_{fg}{}^2} = 3.929 \ W$$

$$\frac{uQ_{latent}}{Q_{latent}} = 0.0257 \quad W$$

Calculate the uncertainty and the percent uncertainty in net heat rate

$$q_{net}(q1, q2) := q1 + q2 \quad W$$

$$Q_{net} := q_{net}(qw1, qw2) \quad W$$

$$uQ_{net} := \sqrt{\left(\frac{d}{dqw1} q_{net}(qw1, qw2)\right)^2 \cdot uq_{w.1}{}^2 + \left(\frac{d}{dqw2} q_{net}(qw1, qw2)\right)^2 \cdot uq_{w.2}{}^2} \quad W$$

$$\frac{uQ_{net}}{Q_{net}} = 0.012 \quad W$$

Calculate the uncertainty in percent of sensible and latent components of heat transfer

$$\%Q(q1, q2) := \frac{q1}{q2} \cdot 100$$

$$\%Q_{sensible} := \%Q(Q_{sensible}, Q_{net}) = 44.469 \quad \%$$

$$u\%Q_{sensible} := \left[\left(\frac{d}{dQ_{sensible}} \%Q(Q_{sensible}, Q_{net})\right)^2 \cdot uQ_{sensible}{}^2 \ldots + \left(\frac{d}{dQ_{net}} \%Q(Q_{sensible}, Q_{net})\right)^2 \cdot uQ_{net}{}^2\right]^{\left(\frac{1}{2}\right)} = 1 \quad \%$$

$$\frac{u\%Q_{sensible}}{\%Q_{sensible}} = 0.022$$

$$\%Q_{latent} := \%Q(Q_{latent}, Q_{net}) = 55.531 \quad \%$$

$$u\%Q_{latent} := \sqrt{\left(\frac{d}{dQ_{latent}} \%Q(Q_{latent}, Q_{net})\right)^2 \cdot uQ_{latent}{}^2 + \left(\frac{d}{dQ_{net}} \%Q(Q_{sensible}, Q_{net})\right)^2 \cdot uQ_{net}{}^2} \quad \%$$

$$\frac{u\%Q_{latent}}{\%Q_{latent}} = 0.028$$

Output all the desired uncertainties to summary spreadsheet

$Output1_0 := uQ_{net}$ $\quad Output1_3 := \frac{u\%Q_{sensible}}{100}$ $\quad Output2_1 := uh_a$

$Output1_1 := uQ_{sensible}$ $\quad Output1_4 := \frac{u\%Q_{latent}}{100}$ $\quad Output2_2 := uh_w$

$Output1_2 := uQ_{latent}$ $\quad Output2_0 := um_c$ $\quad Output2_3 := uh_m \cdot 100$

$$Output1 = \begin{pmatrix} 3.3999540502359173 \\ 2.2955338926928945 \\ 3.928837948893077 \\ 0.00999971083202608 \\ 0.01531481807750816 \end{pmatrix} \qquad Output2 = \begin{pmatrix} 0.00159406255887156 \\ 3.423717664327632 \\ 533.3433859823203 \\ 0.2778624161467792 \end{pmatrix}$$

$Output3 := stack(Output1, Output2)$

$$Output3 = \begin{pmatrix} 3.3999540502359173 \\ 2.2955338926928945 \\ 3.928837948893077 \\ 0.00999971083202608 \\ 0.01531481807750816 \\ 0.00159406255887156 \\ 3.423717664327632 \\ 533.3433859823203 \\ 0.2778624161467792 \end{pmatrix}$$

The Output3 vector is then copied and pasted into a summary spreadsheet

Appendix D

Appendix D contains the code of the Matlab script used to analyze the various images of the wire mesh.

```
clear all; close all
%% Inputs
name='MP2_a';
file='.jpg';
filename=strcat(name,file);
wire_dia=0.0014;
%% Read in image to be analyzed display info in command space
A=imread(filename);
info=imfinfo(filename)
imshow(A)
%% Convert image to grayscale
B=rgb2gray(A);
imshow(B)
%% Show Image histogram
figure;imhist(B)
%% set threshold value and convert to bw image
thresh=43/255
C=im2bw(B,thresh);
imshow(C)
%% Invert image
D=1-C;
imshow(D)

%% remove small objects and fill holes
E=bwareaopen(D,1200);
E=imfill(E,'holes');
imshow(E)
%% Remove objects that touch border or less than full cell
EF=imclearborder(E);

imshow(EF)
%% Calculate horizontal wire length vector (in pixels)

dim=size(EF); % Assign dimensions of image to variable
imax=dim(1);  % Set maximum number of rows
jmax=dim(2);  % Set maximum number of columns
n=0;  % Initialize vector of horizontal wire lengths
```

```
% Sub-routine counts the length of every horizontal wire
for i=1:imax
    k=0;
    S=0;
    for j=1:jmax-1
        if EF(i,j)==1 && EF(i,j+1)==0
            S=1;
            n=n+1;
        end
        if S==1
            h_wire_length(n)=k;
            k=k+1;
        end
        if EF(i,j)==0 && EF(i,j+1)==1
            S=0;
            k=0;
        end
    end
end

figure,hist(h_wire_length,1000) % Plots histogram of all counted horizontal
                                % wire lengths
%% Keep only relevant samples from user specified Range
Upper=40; % Set upper limit of range
Lower=15; % Set lower limit of range
N=length(h_wire_length); % Set number of counted wires equal to N
r=1;
% Sub-routine keeps only wire lengths within specified range and assigns
% them to a new vector
for t=1:N
    X=h_wire_length(t);
    if (Lower<=X)&&(X<=Upper)
        H_wire(r)=X;
        r=r+1;
    end
end

figure,hist(H_wire,10)%Plot histogram of new wire length vector
%% Calculate horizontal pixel length in microns
Ave_H_wire=mean(H_wire)% pixels
fprintf('The average horizontal wire length is %2.4f pixels\n',Ave_H_wire)
Std_H_wire=std(H_wire)
H_pixel_len=25400*wire_dia/Ave_H_wire;
fprintf('The horizontal length of one pixel is %2.4f microns\n',H_pixel_len)
```

```
%% Calculate Vertical wire length vector (in pixels)

s=size(EF);
imax=s(1);
jmax=s(2);
n=0;
for j=1:jmax
    k=0;
    S=0;
    for i=1:imax-1
        if EF(i,j)==1 && EF(i+1,j)==0
            S=1;
            n=n+1;
        end
        if S==1
            v_wire_length(n)=k;
            k=k+1;
        end
        if EF(i,j)==0 && EF(i+1,j)==1
            S=0;
            k=0;
        end
    end
end
figure,hist(v_wire_length,100)
%% Keep only relevant samples from user specified Range
Upper=40;
Lower=20;
N=length(v_wire_length);
r=1;

for t=1:N
    X=v_wire_length(t);
    if (Lower<=X)&&(X<=Upper)
        V_wire(r)=X;
        r=r+1;
    end
end

figure,hist(V_wire,10)
%% Calculate Vertical pixel length in microns
Ave_V_wire=mean(V_wire)
Std_V_wire=std(V_wire)

V_pixel_len=25400*wire_dia/Ave_V_wire

%% Use morphological operation
%  EE=imopen(EF,strel('disk',10));
%  imshow(EE)

%% Identify and label open areas
[F,L]=bwboundaries(EF,'holes');
  NumRegions=max(L(:));
 G=label2rgb(L);
 imshow(G)
```

```
%% Calculate open areas
 stats=regionprops(L,'Area');
%% Calculate Average Cell Opening
% dim=size(E);
% open_area=bwarea(E)/(dim(1)*dim(2))
cell=[stats.Area];
H=H_pixel_len;
V=V_pixel_len;
leng=sqrt(cell*H*V);
figure, plot(leng);

ave_length=mean(leng)
std_length=std(leng)

%% Eliminate Outliers
Upper=60;  %Set the upper limit
Lower=40;  %Set the lower limit
i=1;
for k=1:length(leng)

    if leng(k)<Upper & leng(k)>Lower
        length_v(i)=leng(k);
        i=i+1;
    end
end

figure, plot(length_v);

ave_length=mean(length_v)
std_length=std(length_v)
%% Calculate Percent Open Area based on Cell Opening
Percent_Open_Area=ave_length^2/(ave_length+wire_dia*25400)^2
%% Impose calclated cells over original image

for i=1:imax
    for j=1:jmax

        if G(i,j,:)==255
            U(i,j,:)=A(i,j,:);

        else
            U(i,j,:)=G(i,j,:);
        end
    end
end



imshow(U)
```

```
%% Calculate horizontal opening length vector (in pixels)
n=1;
k=1;
s=size(EF);
imax=s(1);
jmax=s(2);
for i=1:imax
    for j=1:jmax
        if EF(i,j)==1
            h_length(n)=k;
            k=k+1;
        elseif EF(i,j)==0 && k~=1
            n=n+1;
            k=1;
        end
    end
end

figure, hist(h_length,50)


%%  Keep only relevant samples from user specified Range
Upper=56;
Lower=46;
N=length(h_length);
r=1;

for t=1:N
    X=h_length(t);
    if (Lower<=X)&&(X<=Upper)
        h_len(r)=X;
        r=r+1;
    end
end

figure, hist(h_len,10)
H_len=H*h_len;
Ave_h_len_pixels=mean(h_len)
Ave_hor_length=mean(h_len)*H
Std_hor_length=std(h_len)*H
```

```
%% Calculate vertical opening length vector (in pixels)

n=1;
k=1;
s=size(EF);
imax=s(1);
jmax=s(2);
for j=1:jmax
    for i=1:imax
        if EF(i,j)==1
            v_length(n)=k;
            k=k+1;
        elseif EF(i,j)==0 && k~=1
            n=n+1;
            k=1;
        end
    end
end

figure, hist(v_length,20)
%% Keep only relevant samples from user specified Range
Upper=54;
Lower=38;
N=length(v_length);
r=1;

for t=1:N
    X=v_length(t);
    if (Lower<=X)&&(X<=Upper)
        v_len(r)=X;
        r=r+1;
    end
end
figure, hist(v_len,10)
V_len=V*v_len;
Ave_ver_length=mean(v_len)*V
Std_ver_length=std(v_len)*V
%% Calculate average opening length percent open area based on opening
vectors
ave_opening=sqrt(Ave_hor_length*Ave_ver_length)
Percent_Open_Area_2=ave_opening^2/(ave_opening+wire_dia*25400)^2
summary=[ave_length;std_length;Percent_Open_Area;Ave_hor_length;

Std_hor_length;Ave_ver_length;Std_ver_length;ave_opening;Percent_Open_Area_2;
thresh]
%% Write results to .xls
xlswrite(name,summary,'summary');
xlswrite(name,H_wire','horizontal wire length(pixels)');
xlswrite(name,V_wire','vertical wire length (pixels)');
xlswrite(name,cell','Cell Area (pixels)');
xlswrite(name,leng','Sqrt Root length (microns)');
xlswrite(name,length_v','Sqrt Len. out. elim. (microns)');
xlswrite(name,H_len','Horz. Opening Length(microns)');
xlswrite(name,V_len','Vert. Opening Length(microns)');
```